Daniela Penas da Silva

Mestre em Biotecnologia

Structural and Mechanistic Studies of Prokaryotic Ferritins

Dissertação para obtenção do Grau de Doutor em
Biofísica e Bioquímica das Radiações,
Especialidade em Bioquímica Física

Orientador: Prof. Doutora Alice S. Pereira,
Professora Auxiliar, Faculdade de Ciências e Tecnologia – Universidade Nova de Lisboa

Co-orientador: Prof. Doutor Pedro Tavares,
Professor Auxiliar, Faculdade de Ciências e Tecnologia – Universidade Nova de Lisboa

Júri:

Presidente: Prof. Doutor Paulo Manuel Assis Loureiro Limão-Vieira

Arguente(s): Prof. Doutora Maria da Conceição Santos Silva Rangel Gonçalves
Doutora Ana Isabel Faria Ribeiro

Vogais: Prof. Doutor Gustavo Garcia Gómez-Tejedor
Prof. Doutora Alice S. Pereira
Doutor David George Norman

FACULDADE DE CIÊNCIAS E TECNOLOGIA
UNIVERSIDADE NOVA DE LISBOA

Setembro 2018

Universidade Nova de Lisboa
Faculdade de Ciências e Tecnologia

Daniela Penas da Silva

Mestre em Biotecnologia

Structural and Mechanistic Studies of Prokaryotic Ferritins

Dissertação para obtenção do Grau de Doutor em
Biofísica e Bioquímica das Radiações,
Especialidade em Bioquímica Física

Setembro 2018

Structural and Mechanistic Studies of Prokaryotic Ferritins

To my Parents,

Brother and

Husband

Acknowledgements

The work presented in this Thesis was mainly performed in the Molecular Biophysics Group (REQUIMTE/UCIBIO, FTC-UNL). I would like to express my special thanks to everyone who, directly or indirectly, contributed to making this Thesis possible.

To my supervisors, Professor Alice S. Pereira and Professor Pedro Tavares, I would like to thank, not only the opportunity that they gave me to perform this work but also, for all the guidance, advice and assistance throughout the years. I am grateful for all the shared knowledge, availability, friendship and encouragement. For all my personal and scientific development, as well as, for sharing many invaluable memories, thank you!

To Dr David G. Norman (Nucleic Acid Structure Research Group, College of Life Sciences-University of Dundee, Scotland) I would like to thank the kind and friendly reception to his lab. For all the help in data acquisition and interpretation, which is a very important part of this Thesis. For all the good moments and for the scientific exchange, thanks, it was a pleasure to work with him!

I would like to thank also Dr Hassane El-Mkami for running all my PELDOR samples and helping with data processing. To Dr David Keeble and Dr Bela Bode for all the help and availability to use their CW-EPR spectrometers.

Many thanks to the Radiation Biology and Biophysics Doctoral Training Programme (RaBBiT) and to Fundação para a Ciência e Tecnologia, Ministério da Educação e Ciência (FCT-MCES) for granting me the PhD fellowship (SRFH/BD/52535/2014).

I would like to thank my past and present friends in the Molecular Biophysics Group. Particularly, Dr Cristina Timóteo and Nídia Almeida for all the friendship, companionship and support provided at all times. Thank you!

To all undergraduate students that I had the pleasure to supervise, I would like to thank the support and interest in this work.

To Dr Michael Stevens, I would like to thank the warm welcoming to David´s lab, also all the friendship, support and especially the funny moments. Thank you, Michael!

To Joshua Wort, Dr Adam El-Qmache, Claire L. Motion, Anouki Shah and Sonia Chabbra, I would like to thank them for the friendship. Thanks!

I would like to thank my closest friends and family for all their support and for being present in my life. Especially, my parents and brother all the support, patience, encouragement and for believing in me. I am very grateful for everything, this Thesis is for you!

Last, but not least, I would like to thank my dearest husband, Fábio, for all the unconditional support, inspiration, encouragement, patience, companionship and love through this journey. To him, I am very grateful. Thank you!

Abstract

Prokaryotic ferritins are specialised proteins used by cells to uptake, oxidize and store iron. These proteins are composed by identical subunits forming a hollow spherical structure. Ftns and Bfrs are composed by 24 subunits that can store up to 4500 iron atoms. Dps (DNA-binding protein from starved cells) proteins are composed by 12 subunits and can store up to 500 iron atoms per shell. Ferritins contribute to iron homeostasis through three main processes: ferroxidation reaction, using H_2O_2 or O_2; mineralization; and iron release in the ferrous form, essential for various cellular processes.

In this Thesis, Bfr from *D. vulgaris* and Dps from *M. hydrocarbonoclasticus*, were characterized structurally and mechanistically. In general, Dps proteins use H_2O_2 to oxidize Fe^{2+} ions, while Bfr proteins use O_2. We have proved that *D. vulgaris* Bfr is more catalytically efficient when uses H_2O_2 for the ferroxidation reaction, storing up to 600 Fe^{2+} ions per protein, and has the ability to bind DNA, a feature common to some Dps proteins but unknown in Ftns and Bfrs.

DNA-binding activity was also investigated for Dps protein, which contains a flexible positively charged N-terminus. EMSA results showed that Dps binds to DNA with a K_d of ~6 μM, that this interaction is dependent on the N-terminus, and it is inhibited when the protein contains the mineral core. Dps protein uses preferentially H_2O_2 to oxidize Fe^{2+} ions and can store 500 Fe^{2+} ions. The oxidation of 24 Fe^{2+}/protein results in the formation of a small core, as demonstrated by Mössbauer spectroscopy. Additionally, using this technique and a mixture of $^{56}Fe^{2+}/^{57}Fe^{2+}$, it was possible to observe a characteristic never reported for this ferritin proteins. In the absence of oxidant, the mineral core can oxidize Fe^{2+} ions and promote its incorporation.

Keywords: Bacterioferritin; Dps; ferroxidation and biomineralization; DNA-binding and protection; Mössbauer spectroscopy; Structural dynamics and spin-labelling; EPR and PELDOR spectroscopies.

Resumo

As ferritinas procarióticas são proteínas especializadas, usadas pelas células para armazenar ferro. Estas proteínas são homopolímeros, em forma de esfera oca. As Ftns e Bfrs são constituídas por 24 subunidades e podem armazenar até 4500 átomos de ferro. As Dps (*DNA-binding protein from starved cells*) são constituídas por 12 subunidades e podem armazenar até 500 átomos de ferro. As ferritinas contribuem para a homeostasia do ferro através de três processos: reação de ferroxidação, usando H_2O_2 ou O_2; mineralização; e libertação de ferro na forma ferrosa, essencial para diversos processos celulares.

A Bfr de *D. vulgaris* e a Dps de *M. hydrocarbonoclasticus* foram caracterizadas a nível estrutural e mecanístico. Geralmente, as proteínas Dps usam H_2O_2 para oxidar os iões Fe^{2+}, enquanto que as Bfrs usam O_2. No entanto, neste trabalho verificou-se que a Bfr de *D. vulgaris* é mais eficiente cataliticamente quando usa H_2O_2, incorporando até 600 iões Fe^{2+}, e que tem a capacidade de se ligar a moléculas de DNA, uma característica comum em algumas proteínas Dps.

A atividade de ligação ao DNA foi também estudada na Dps, possuindo uma região N-terminal flexível carregada positivamente. Os resultados obtidos por EMSA mostraram que a Dps se liga ao DNA com um K_d de ~6 μM, sendo a ligação dependente da presença do N-terminal, e que quando a proteína contém o mineral férrico deixa de se ligar ao DNA. A Dps usa preferencialmente H_2O_2 para oxidar os iões Fe^{2+}, armazenando 500 Fe^{2+}. A oxidação de 24 Fe^{2+}/proteína resulta na formação de um pequeno mineral férrico, como demonstrado por espectroscopia de Mössbauer. Usando esta espectroscopia e uma mistura de isótopos $^{56}Fe^{2+}/^{57}Fe^{2+}$ foi possível observar uma nova atividade associada ao mineral férrico, totalmente nova em sistemas biológicos. O mineral férrico tem a capacidade de oxidar iões Fe^{2+} e incorporá-los, na ausência de qualquer oxidante.

Palavras-chave: Bacterioferritina; Dps; ferroxidação e biomineralização; ligação e proteção ao DNA; espectroscopia de Mössbauer; dinâmica estrutural e sondas de spin; espectroscopia de EPR e PELDOR.

Contents

List of Figures

List of Tables

List of Abbreviations and Symbols

ΔE_Q	Quadrupole splitting
τ_c	Correlation time
3D	Three-dimensional
4′-amino TEMPO	4'-amino-2,2,6,6-tetramethylpiperidinooxy
AFM	Atomic Force Microscopy
APS	Ammonium persulphate
BCA	Bicinchoninic acid
Bfd	Bacterioferritin-associated ferredoxin
Bfr	Bacterioferritin
bp	Base Pair
BSA	Albumin from Bovine Serum
CW-EPR	Continuous Wave-Electron Paramagnetic Resonance
Da	Dalton
dNTPs	Deoxyribonucleotides triphosphate
Dps	DNA-binding protein from starved cells
dsDNA	Double-stranded DNA
DTT	Dithiothreitol
EMSA	Electrophoretic Mobility Shift Assay
EPR	Electron Paramagnetic Resonance
ESE	Electron Spin Echo
FOCs	Ferroxidase centres
Ftn	Classical Ferritin

H-subunit	Heavy-chain subunit
HP-NAP	Neutrophil-Activating Protein from *Helicobacter pylori*
HuHF	Heavy-chain subunit from Human Ferritin protein
ICP-AES	Inductively coupled plasma atomic emission spectroscopy
IHF	Integration Host Factor
IPTG	Isopropyl β-D-thiogalactopyranoside
L-subunit	Light-chain subunit
LB medium	Luria-Bertani medium
LMW	Low molecular weight
M-subunit	Middle-chain subunit
MD	Molecular Dynamics
MMTS	S-methyl methanethiosulfonate
MOPS	3-(N-morpholino)propanesulfonic acid
Mt	Mitochondrial
MTSL	(1-Oxyl-2,2,5,5-tetramethyl-Δ3-pyrroline-3-methyl) methanethiosulfonate
MW	Molecular Weight
MWCO	Molecular Weight Cut-Off
NI	Nucleic sites Type I
NII	Nucleic sites Type II
PCR	Polymerase Chain Reaction
PDB	Protein Data Bank
PELDOR	Pulsed Electron-electron Double Resonance
pI	Isoelectric point
RFQ	Rapid Freeze-Quench

ROS	Reactive Oxygen Species
SDS	Sodium Dodecyl Sulphate
SDS-PAGE	Sodium Dodecyl Sulphate-Polyacrylamide Gel Electrophoresis
SDSL	Site-Directed Spin Labelling
SEC	Size Exclusion Chromatography
SU	Subunits
T_B	Blocking Temperature
T_m	Phase memory time
UniProtKB	UniProt Knowledgebase
Ve	Elution volume
Vo	Void volume
WT	Wild-type
δ	Isomer shift

1

Introduction

1.1 Iron – an essential micronutrient

Iron is the fourth most common element on Earth and is an important micronutrient for living organisms. It is required for the growth and development of almost all organisms through biochemical events such as oxygen transport, serving as a cofactor for several enzymes, electron transfer, DNA synthesis and photosynthesis [1,2]. Some strains of *Lactobacillus*, i.e. lactic acid bacteria which converts sugar to lactic acid, are the exception. These bacteria grow in absence of iron, using manganese or cobalt [3,4].

In solution, iron exists in two stable oxidation states, ferrous iron (Fe^{2+}) and ferric iron (Fe^{3+}), which can donate and accept electrons, respectively. These characteristics make iron a useful mediator in a variety of biochemical processes. However, at physiological oxygen concentrations the stable form is the ferric iron, which has a poor solubility in water, ~10^{-18} M, and easily forms precipitates preventing its availability as an iron source [5,6]. The excess of free iron has been associated with neurodegenerative diseases and apoptosis. Importantly, free iron has the ability to generate reactive oxygen species (ROS), such as hydroxyl radical ($OH^{\bullet}$), that cause damage to membranes, proteins and nucleic acids [7-9].

The reaction of Fe^{2+} with molecular oxygen (O_2) results in the superoxide radical ($O_2^{\bullet -}$) and hydrogen peroxide (H_2O_2), through the following equations:

$$Fe^{2+} + O_2 \rightarrow Fe^{3+} + O_2^{\bullet -} \quad (1.1)$$

$$2O_2^{\bullet -} + 2H^+ \rightarrow H_2O_2 + O_2 \quad (1.2)$$

In turn, the $O_2^{\bullet -}$ radical can reduce the Fe^{3+} (equation 1.3) originating Fe^{2+} and O_2, and consequently inducing the catalytic cycle well-known as Haber-Weiss-Fenton reaction, generating the harmful $OH^{\bullet}$ radical [9-12]. The Haber-Weiss-Fenton reaction is described by equation 1.4 (Fenton reaction) and equation 1.5 (Haber-Weiss reaction).

$$Fe^{3+} + O_2^{\bullet -} \rightarrow Fe^{2+} + O_2 \quad (1.3)$$

$$Fe^{2+} + H_2O_2 \rightarrow Fe^{3+} + OH^- + OH^{\bullet} \quad (1.4)$$

$$O_2^{\bullet -} + H_2O_2 \rightarrow O_2 + OH^- + OH^{\bullet} \quad (1.5)$$

To prevent cellular damage by ROS, organisms have developed defence mechanisms by means of specific enzymes, such as superoxide dismutases that act on superoxide radical, as well as, catalases and peroxidases that act on hydroxyl radical [13]. To cope with the poor solubility, bioavailability and toxicity of iron, organisms have established intracellular reserves of iron via iron storage proteins. These proteins, called ferritins represent a ubiquitous family, which store iron in a non-toxic form that will be released when external iron supplies are limited [14,15].

1.2 Ferritin family

The ferritin family belongs to an extensive Ferritin-like superfamily, characterized by the presence of a common four-helical bundle structural domain. This superfamily contains more than eleven distinct families with diverse functions such as rubrerythrin and manganese catalase, involved in redox-stress resistance by acting as peroxidases, di-Fe monooxygenase, involved in the catabolism of phenols and methylated derivatives, or the small subunit of ribonucleotide reductase, involved in the DNA synthesis [16].

Proteins from the ferritin family are present in the three kingdoms of life and are the principal iron storage proteins for maintaining iron homeostasis in living organisms. Despite sharing a highly conserved three-dimensional structure, amino acid sequences vary up to 80% in sequence similarity within this family, which has diverged into three distinct sub-families (Figure 1.1): the classical ferritins (Ftn), the bacterioferritins (Bfr) and the DNA-binding protein from starved cells (Dps) [16,17].

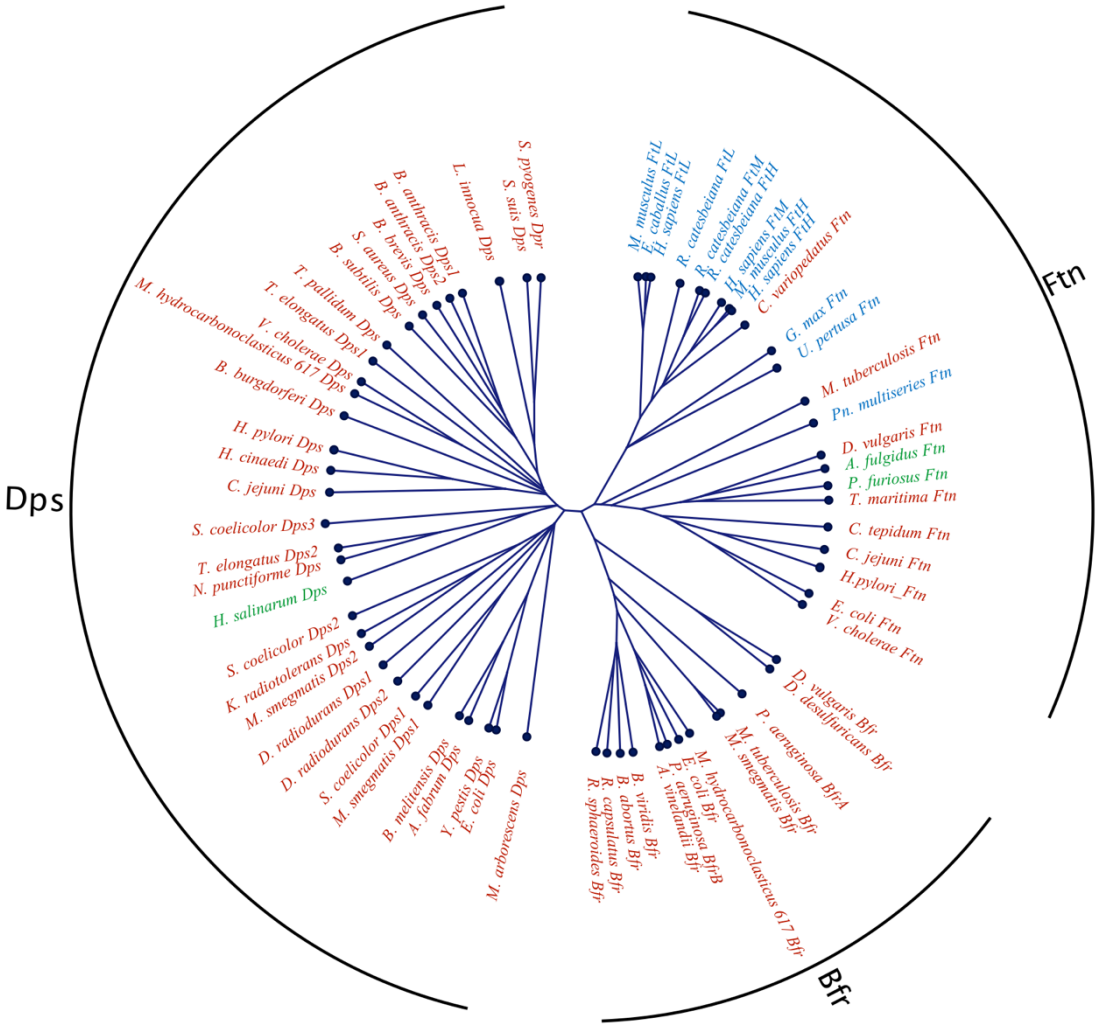

Figure 1.1: Phylogenetic relationship of selected ferritin family members. Sequence alignment and tree construction were generated with Clustal Omega [28] and the tree displayed with CLC Sequence Viewer 7.8.1 (https://www.qiagenbioinformatics.com/). The eukaryote ferritin proteins are shown in blue, the archaea ferritins are shown in green and the bacteria ferritin proteins are shown in red. Amino acid sequences were retrieved from the UniProtKB database [29]: *Agrobacterium fabrum* Dps (Q8UCK6); *Bacillus anthracis* Dps1 (Q8RPQ1); *Bacillus anthracis* Dps2 (Q8RPQ2); *Bacillus subtilis* Dps (P37960); *Borrelia burgdorferi* Dps (O51633); *Brevibacillus brevis* Dps (P83695); *Brucella melitensis* biotype 1 Dps (Q8YE98); *Campylobacter jejuni* ATCC700819 Dps (Q0P891); *Deinococcus radiodurans* Dps1 (Q9RS64); *Deinococcus radiodurans* Dps2 (Q9RZN1); *Escherichia coli* Dps (P0ABT2); *Halobacterium salinarum* Dps (Q9HMP7); *Helicobacter pylori* Dps (P43313); *Kinecoccus radiotolerans* Dps (A6WG04); *Listeria innocua* serovar 6a Dps (P80725); *Marinobacter hydrocarbonoclasticus* ATCC 49840 Dps (H8W6M5); *Microbacterium arborescens* Dps (Q1X6M4); *Mycobacterium smegmatis* Dps1 (P0C558); *Mycobacterium smegmatis* Dps2 (A0QXB7); *Nostoc punctiforme* Dps (B2J981); *Staphulococcus aureus* Dps (A0A0H2X069); *Streptococcus pyogenes* serotype M1 Dpr (Q5XAZ8); *Streptococcus suis* Dps (P0CB53); *Streptomyces coelicolor* Dps1 (Q9R408); *Streptomyces coelicolor* Dps2 (O86816); *Streptomyces coelicolor* Dps3 (Q9K3L0); *Thermosynechococcus elongatus* Dps1 (Q8DG54); *Thermosynechococcus elongatus* Dps2 (Q8DL82); *Treponema pallidum* Dps (P16665); *Vibrio cholerae* serotype O1 Dps (Q9KVK4); *Yersinia pestis* Dps (Q7CJ65); *Azotobacter vinelandii* Bfr (P22759); *Blastochloris viridis* Bfr

(K7N5M0); *Brucella abortus* Bfr (Q2YKI4); *Desulfovibrio desulfuricans* Bfr (Q93PP9); *Desulfovibrio vulgaris* Bfr (Q72C87); *Escherichia coli* Bfr (P0ABD3); *Marinobacter hydrocarbonoclasticus* ATCC 49840 Bfr (H8WD40); *Mycobacterium smegmatis* Bfr (A0QY79); *Mycobacterium tuberculosis* Bfr (P9WPQ9); *Pseudomonas aeruginosa* BfrA (Q9HWF9); *Pseudomonas aeruginosa* BfrB (Q9HY79); *Rhodobacter capsulatus* Bfr (Q59738); *Rhodobacter sphaeroides* Bfr (Q3J696); *Archaeoglobus fulgidus* Ftn (O29424); *Campylobacter jejuni* Ftn (Q46106); *Chlorobaculum tepidum* Ftn (Q8KBP5); *Desulfovibrio vulgaris* Ftn (Q72BR6); *Equus caballus* FtL (P02791); *Escherichia coli* Ftn (P0A998); *Glycine max* Ftn (Q948P5); *Helicobacter pylori* Ftn (P52093); *Homo sapiens* FtH (P02794); *Homo sapiens* FtL (P02792); *Homo sapiens* FtM (Q8N4E7); *Rana catesbeiana* FtH (P07229); *Rana catesbeiana* FtL (P07797); *Rana catesbeiana* FtM (P07798); *Mus musculus* FtH (P09528); *Mus musculus* FtL (P29391); *Mycobacterium tuberculosis* Ftn (P9WNE5); *Pseudo-nitzschia multiseries* Ftn (B6DMH6); *Pyrococcus furiosus* Ftn (Q8U2T8); *Thermotoga maritima* Ftn (Q9X0L2); *Ulva pertusai* Ftn (H7CGH2); *Vibrio cholerae* serotype O1 Ftn (Q9KVR1).

These families are hollow spherical proteins composed by similar subunits (organized in dimers), which consists of a closed four-helical bundle (the common domain present in the Ferritin-like superfamily). However, based on slight differences on the subunits, the number of subunits per protein and the protein function, the ferritin sub-families can be classified as maxi-ferritins and mini-ferritins.

The maxi-ferritins, comprising the Ftn and Bfr proteins, are composed by 24 subunits (~500 kDa). Each subunit is made up of a four-helical helix (designated A, B, C and D helices) with a short fifth helix (E helix) at the C-terminal region (Figure1.2A). The monomers assemble an octahedral spherical cage (with 432 symmetry) able to accommodate up to ~4500 Fe atoms within the hollow cavity (inner diameter of ~8 nm). The mini-ferritins, comprised by Dps proteins, are composed by 12 subunits (~250 kDa) and the monomer lacks the E helix in the C-terminus but have a short helix (BC helix) between the B and C helices (Figure 1.2B). Dps proteins have a tetrahedral spherical cage (23 symmetry) with a central cavity of ~5 nm which can accommodate up to ~500 Fe atoms [18,19].

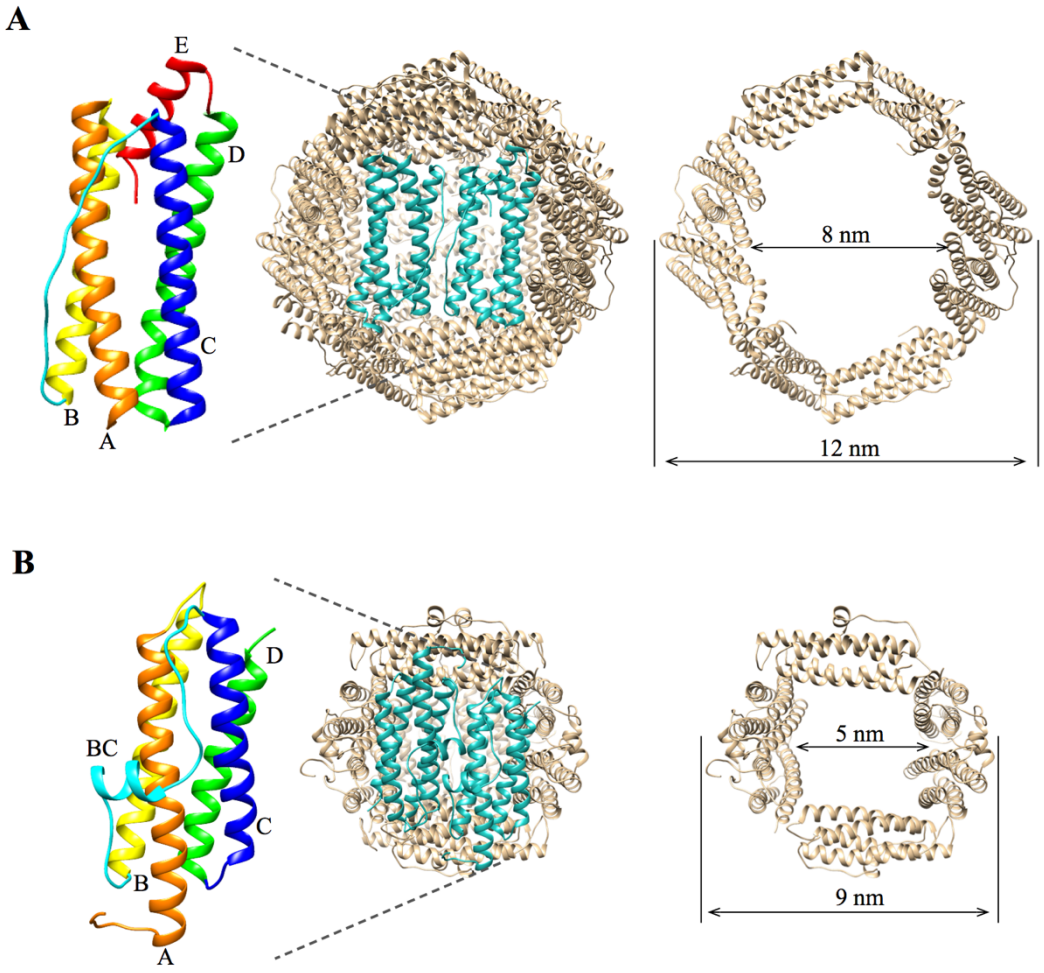

Figure 1.2: Typical three-dimensional structures of maxi-ferritin and mini-ferritin. (A) Octahedral maxi-ferritin (PDB ID: 1EUM). (B) Tetrahedral mini-ferritin (PDB ID: 1DPS). On the left, the monomer is depicted as ribbons (helix A in orange; helix B in yellow, the loop between the B and C helices in the maxi-ferritin (A), and the short helix BC in mini-ferritin (B) in cyan; helix C in blue; helix D in green; and helix E in maxi-ferritin (A) in red. In the middle, the protein cage is represented with dimers in light sea green. On the right, the sizes of the external surface and the inner cavity are shown. Structures were generated with UCSF Chimera [30].

The main function of proteins from the ferritin family is to store iron atoms in the cavity as a ferric oxyhydroxide mineral, also known as core, by three processes described as (1) ferroxidation – the iron entry and oxidation at the ferroxidase centres (FOCs); (2) mineralization – the production of mineral core at the protein cavity; (3) the iron release. Mini-ferritins are also associated to detoxification function due to their preferences by using H_2O_2 as a co-substrate for the ferroxidation, instead of O_2 used by maxi-ferritins. Another difference between these two groups is the location of the FOCs, while in maxi-

ferritins these are located in the middle of each four-helical bundle, in mini-ferritins they are located at the interface between two-fold related subunits (dimers) [20-24].

When the proteins are formed without the mineral core, these are designated by apo-ferritins. Apo-ferritins can be isolated from recombinant growth or after dissolving the mineral and chelating the iron under physiological conditions. The apo-ferritin shell is very stable due to the large numbers of intra- and inter-subunit salt bridges and hydrogen bonds. When the proteins contain the mineral core within the cavity, they are called holo-proteins.

The mineral core can have different amounts of phosphate (ratios of Fe:P~1:1, in plants and microorganisms; and ratios of Fe:P~8:1, in animals) in its composition, which changes the core crystallinity owed to the local concentration of phosphate during the mineral formation. High concentrations of phosphate lead to a more amorphous and disordered mineral, whereas low concentrations of phosphate promote crystallinity [17,20,25-27].

1.2.1 Ftn proteins

The Ftn proteins are found in all three kingdoms of life. The eukaryotic ferritins can be assembled by three types of homologous subunits: the light-chain subunit (L-subunit), the middle-chain subunit (M-subunit), and the heavy-chain subunit (H-subunit) [31].

The mammalian ferritins called cytosolic ferritins are mostly heteropolymers constituted by H- and L-subunits, with H:L ratios dependent on the tissue type and physiologic status of the cell. This ratio can also be modified by inflammatory and infectious conditions, and in response to xenobiotic stress [32]. H- and M-subunits have a conserved FOC (located on the middle of the four-helical bundle), which catalyses the fast iron oxidation, while in the L-subunits the FOC is replaced by a salt bridge that stabilizes the structure. The L-subunits are involved in the nucleation of the iron core in the inner cavity. Thus, organs that accumulate iron have a higher L-subunit content (such as liver and spleen), and organs that require iron detoxification have higher H-subunit content (e.g. heart and brain) [27,33].

Mammals also have mitochondrial (Mt) ferritins that are homopolymers constituted by 24 subunits, with a high homology with the cytosolic H-subunits but significant differences in their iron oxidation. Additionally, Mt ferritins have a long amino acid N-terminal extension for mitochondrial import, which is cleaved during processing. In humans, the Mt ferritins are found in testis, spermatozoa and in the sideroblasts of patients with sideroblastic anaemia [33-36].

In bacteria, Ftn proteins are homopolymers denominated archetypal ferritins, composed by 24 subunits identical to the eukaryotic H-subunit [23].

1.2.2 Bfr proteins

Bacterioferritin proteins were first identified in bacteria and are very similar to bacterial ferritins, sharing the same iron storage role. However, Bfr proteins possesses a non-covalently bound haem group at the two-fold related subunits interface (in the middle of the dimers), axially coordinated by methionine residues from the adjacent subunits (Figure 1.3) [27]. The haem group is of the protoporphyrin IX-type, with the exception of *Desulfovibrio desulfuricans* Bfr, which contains the haem as iron-coproporphyrin III [37]. These 12 haem cofactors appear to be involved in the Fe^{3+} reduction and the realising mechanism from the cavity [38,39].

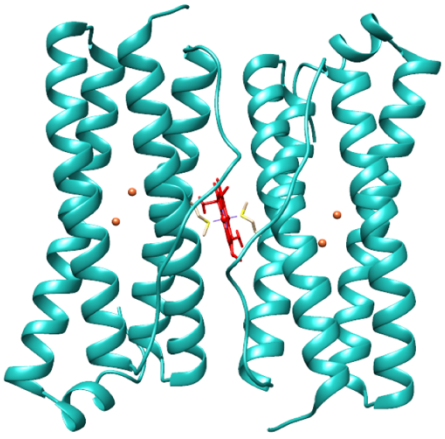

Figure 1.3: Two-fold related subunits of *Escherichia coli* Bfr (PDB ID: 1BFR). The haem group (red) is ligated by methionine residues (grey and yellow) from the two adjacent monomers. The orange spheres represent the catalytic FOCs in each subunit. The figure was generated with UCSF Chimera [30].

1.2.3 Dps proteins

Dps protein was first isolated in 1992 by Almirón and colleagues from a three-day old culture of *Escherichia coli* [40]. The authors observed that *in vitro* the isolated protein formed stable complexes with DNA, without an apparent sequence specificity, and consequently they named the protein as Dps (DNA-binding protein from starved cells). They also noticed that three-old day wild-type cells were not affected when treated with H_2O_2, whereas the mutant cells lacking the *dps* gene did not synthesize some proteins (beyond the Dps) and in the presence of H_2O_2 the cells died. These observations suggested that Dps protein has an important role in gene expression and DNA protection during stationary phase [40].

Dps proteins are largely distributed in the prokaryotes, where about 97% are found in bacteria and 3% in archaea [41]. Typically, bacterial genomes encode for one Dps protein, but some genomes encode for two (e.g. *Mycobacterium smegmatis*, *Deinococcus radiodurans* and *Bacilus anthracis*), or encode for three proteins (e.g. *Streptomyces coelicolor*) [42-46].

Dps protein from *E. coli* is predominantly expressed in the stationary phase or under oxidative stress. Ali Azam and colleagues have found that during the exponential growth phase there are about 6,000 Dps molecules per cell, reaching a maximum of about 180,000 molecules per cell at the stationary phase, where the cells are experiencing low availability of nutrients [47].

Regulation of Dps protein expression is complex and dependent upon the growth phase in which it is being expressed. During exponential growth, if the cells are exposed to H_2O_2, the OxyR regulator is activated, which induces the expression of σ^{70} RNA polymerase and consequently the expression of *dps*. In the stationary phase, the protein expression is activated by σ^{s} and the histone-like integration host factor (IHF), which is found within the *dps* promoter [48].

The downregulation of *dps* expression occurs during the exponential phase, in the absence of oxidative stress, by the nucleoid-associated proteins Fis and H-NS when their levels are high. Fis and H-NS bind at adjacent sites within the *dps* promoter, and while Fis levels are low in the stationary phase, the H-NS levels are significant. The H-NS binds to the promoter region preventing the binding of σ^{70}, but the repression can be overcome

by binding of σ^s (the stationary phase RNA polymerase). Fis binds to the *dps* promoter and forms a complex with the σ^{70} that blocks the transcription by σ^s [49,50].

In addition to protecting cells from iron toxicity and oxidative stress, which are also a feature of Ftn and Bfr proteins, Dps proteins protect cells from UV and gamma irradiation, thermal stress and acid and base shock. The cellular protection is accomplished by unique Dps proprieties in DNA-binding, metal incorporation, ferroxidase activity and regulation of gene expression [51-53].

The first crystal structure of Dps protein from *E. coli* was reported by Grant and colleagues [54] proving the initial comparison between Dps protein and maxi-ferritins (Ftn and Bfr proteins) (Figure 1.4).

At the N-terminal regions, the subunits form pores with 3-fold symmetry axes, which are lined by negatively charged residues allowing the entry and exit of iron into the cavity, similarly to the ones present in the Ftn and Bfr proteins, and thus called "Ferritin-like" pores. At the C-terminal regions, the subunits assemble creating a second type of 3-fold axes instead of 4-fold axes in Ftn and Bfr proteins, due to the lack of the fifth helix. Due to its uniqueness, these second 3-fold pores are designated "Dps-like" pore, and their function is still unknown [42,55].

The electrostatic potential surface of Dps dodecamer is dominated by the concentration of negative charge around the two types of 3-fold channels, mainly around the "Ferritin-like" pore. One exception is the surface of the neutrophil-activating protein (HP-NAP), which is predominantly positively charged. Additionally, the internal cavity is highly negative, which is ideal for the iron mineralization [54,56].

Despite the fact that the electrostatic surface characteristics of Dps are not regarded as suitable for DNA binding, the N-terminal region has been suggested to be important for DNA binding. The N-terminal region can have variable lengths and be highly flexible. This N-terminal extension, consisting in a variable number of positively charged residues, can extend perpendicularly from the core into the solvent, and stabilize the assembled dodecamer, as well as, interacting with DNA [57,58]. Moreover, the C-terminal region can also have variable lengths and promotes the interaction with DNA [59].

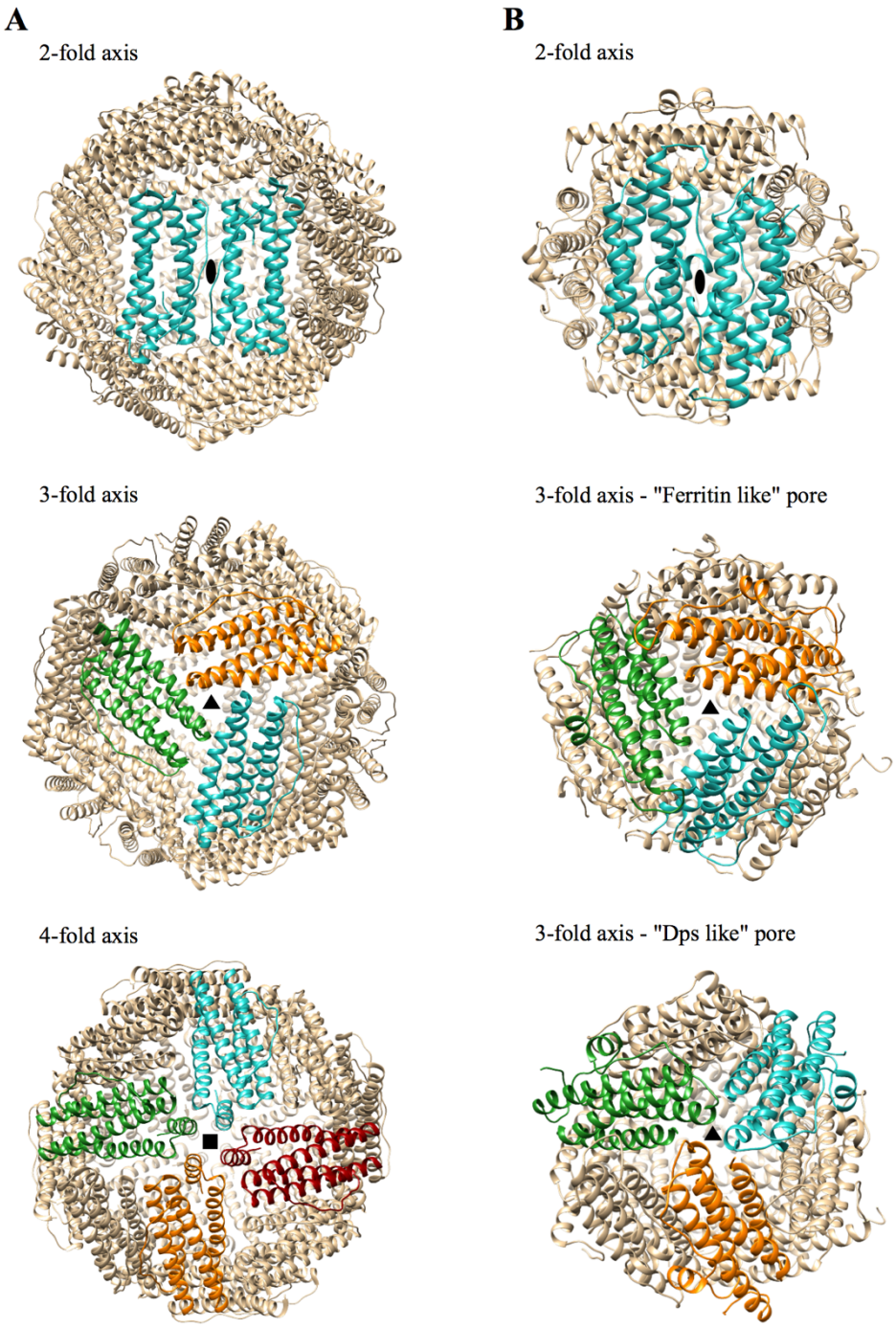

Figure 1.4: Structural comparison between maxi-ferritin (432 symmetry) and mini-ferritin (23 symmetry) from *E. coli*. (A) Quaternary structure of Ftn protein (PDB ID: 1EUM) with the 2-fold (top), 3-fold (middle) and 4-fold (bottom) channels. (B) Quaternary structure of Dps protein (PDB ID: 1DPS) with the 2-fold (top), 3-fold ("Ferritin-like" pore, middle) and 3-fold ("Dps-like" pore, bottom) channels. The oval, triangle and square symbols highlight the symmetry related subunits. Structures were generated with UCSF Chimera [30].

1.3 Molecular mechanism of Ferritins

1.3.1 Catalytic centre

As mentioned before, the main function of the ferritin family is to maintain the iron homeostasis in the cells and protect them from ROS. This function is only possible due to ferritin's ability to oxidize Fe^{2+} and to form the mineral core within the cavity.

1.3.1.1 Maxi-ferritins

The catalytic site of maxi-ferritins has been described based on the observation of the X-ray crystal structure of ferritins containing metal-ions, as being located in each subunit, where there are three metal binding sites. Two sites in the middle of the four-helical bundle, sites A and B forming a di-nuclear metal ion binding, designated as the ferroxidase centre (FOC), and a third site (site C) in the vicinity, close to the inner surface of the protein [60]. The exception is the L-subunit of eukaryotic ferritins where the FOC is absent. However, L-subunits can oxidize Fe^{2+} with a rate slightly above the rate of background oxidation of free aqueous Fe^{2+} by O_2 [61-63].

FOCs, where fast oxidation of Fe^{2+} occurs, are highly conserved among Ftn and Bfr proteins. Regarding site C, which is not conserved and whose function is a matter of some controversy, has been proposed to be a gateway site, responsible for translocation of Fe^{2+}/Fe^{3+} into/out of the ferroxidase centre [64]. Moreover, both subfamilies share a highly conserved tyrosine residue within 4-5 Å of the FOC which may play an important role on catalysis [60].

In Ftn, site A of the FOC is coordinated by a histidine and glutamate residues, and a glutamate and glutamine residues that act as a bridge ligand for the iron in site B. The iron in site B is also coordinated by a glutamate residue and another not conserved glutamate residue. Site C can have different conformations since the iron ligands at this site are not conserved among ferritins [65-67]. The FOC of Ftn is represented in Figure 1.5A.

Bfr proteins have a FOC similarly to the Ftn one, except for the oxo-bridge, which in Bfr is mediated by two glutamate residues, and the iron in the site B is also coordinated by a histidine residue (Figure 1.5B).

Although these three metal binding sites were observed in different X-ray crystal structures, their occupancy varies and so no structure has been so far determined with the sites fully occupied [68-71].

1.3.1.2 Mini-ferritins

The localization of the catalytic centre in the Dps proteins represents the most distinctive structural feature of this subfamily of proteins. Unlike the maxi-ferritins, site C is not present. The catalytic FOC is in the interface of the 2-fold symmetry axis, except in *Lactococcus lactis* Dps where it is located in the four-helical bundle [57].

Dps FOC was first identified in the X-ray crystal structure of *Listeria innocua* where a single iron atom was bound. The recognized metal ligands are a glutamate and aspartate residues, from one subunit, and two histidine residues from the adjacent subunit (Figure 1.5C) [72]. Therefore, at each interface between the subunits, the dimer accommodates two FOCs at a distance of ~2 nm [55].

The iron coordinating residues are highly conserved in the Dps subfamily, however, such as in maxi-ferritins, their occupancy varies significantly [41,42]. The X-ray structures of Dps proteins from *L. innocua* and *Agrobacterium tumefaciens* show an iron ion in one FOC site and a water molecule at a distance of 3 Å, leading to the suggestion that the later could be replaced by a second metal ion [56,72,73]. Three-dimensional structures of proteins from *Deinococcus radiodurans* and *Bacillus brevis* identified two iron ion atoms at FOCs [74,75].

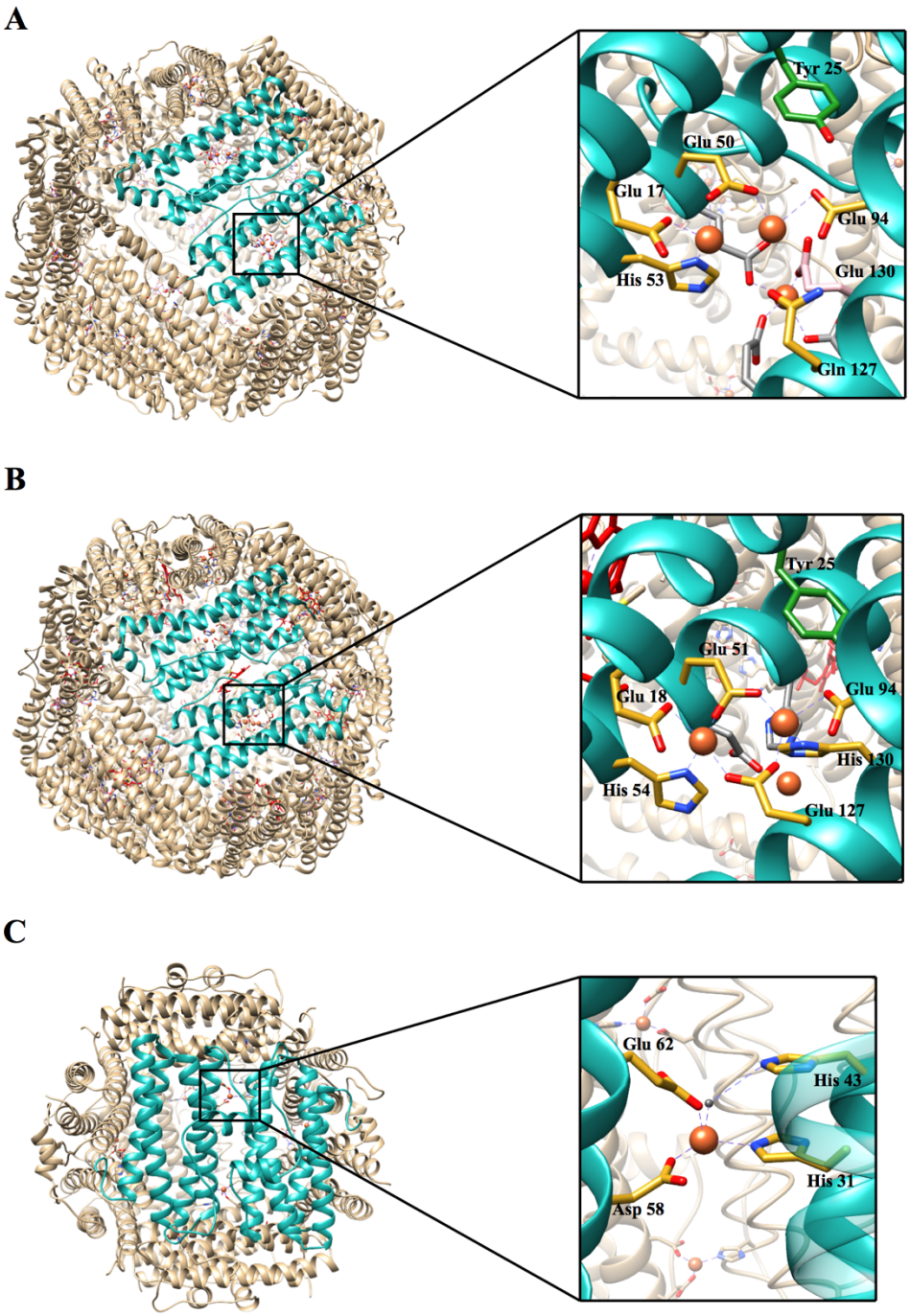

Figure 1.5: Structures of ferritin proteins and their catalytic centre. (A) *P. furiosus* Ftn (PDB ID: 2JD7). (B) *E. coli* Bfr (PDB ID: 1E1M). (C) *L. innocua* Dps (PDB ID: 1QGH). Conserved residues of the FOC are coloured in yellow. The non-conservative amino acid residue at Ftn site B is coloured in pink. Site C binding residues are shown in grey, and the residue highly conserved tyrosine in Ftn and Bfr proteins is coloured in green. The orange spheres represent the iron atoms and the grey sphere represents the water molecules. 3D structures were generated with UCSF Chimera [30].

1.3.2 Iron uptake

1.3.2.1 Maxi-ferritins

The exact pathway of Fe^{2+} transfer to the FOC of Ftn and Bfr proteins is not fully understood.

In eukaryotic Ftns, the 3-fold channels (at the 3-fold symmetry axis) have been proposed as the main entry path of Fe^{2+} ions and consequent translocation to the FOC [76-79]. Electrostatic calculations in human H-subunit ferritin protein (HuHF) showed the electrostatic gradient created at the 3-fold symmetry due to the presence of positively charged residues in the outer surface surrounding the 3-fold axis and negatively charged residues inside the channel [80]. However, molecular dynamics (MD) simulations studies in HuHF suggested a complementary Fe^{2+} entry pathway through the ferroxidase channel, a channel where Fe^{2+} ion reaches directly the FOC, in addition to the 3-fold channel [81]. Furthermore, the X-ray crystal structure of bullfrog M ferritin protein has revealed the presence of Fe^{2+}/Fe^{3+} in both the 3-fold and 4-fold (at the 4-fold symmetry axis) channels, suggesting multiple Fe^{2+} entry pathways [82].

Bacterial and archaeal Ftns have similar channels to the ones in eukaryotic proteins. While in the eukaryotic, both 3-fold and 4-fold channels are hydrophilic, in the bacterial and archaeal proteins the 3-fold channel is hydrophobic and the 4-fold channel is hydrophilic [83]. Besides, mutations in site C binding site decreased the rate of Fe^{2+} oxidation suggesting an important role in iron uptake [60].

In Bfr proteins, three different channels have been proposed as Fe^{2+} entry pathways. One channel is the 4-fold channel, where different metal atoms were observed in the X-ray crystal structure of some Bfr proteins [69-71]. The second channel, observed in the X-ray crystal structures, is the ferroxidase channel, where similarly to the Ftns, the Fe^{2+} reaches directly the FOCs [69,70,84]. The third channel, at a specific junction between three subunits, called B pores channel, was predicted by MD simulations to be involved in the Fe^{2+} entry into the cavity [71].

Thus, due to the proteins 432 symmetry, four types of channels through the protein shell were suggested (Figure 1.6): (1) 3-fold channel; (2) 4-fold channel; (3) B pore channel in Bfr; and (4) ferroxidase channel. If the Fe^{2+} ions enter a ferroxidase channel it

reaches directly the FOC; while if Fe^{2+} enters through the 3-fold, 4-fold and B pores channels, the site C at the catalytic centre may act as a transient site in grabbing Fe^{2+} to the oxidase centre.

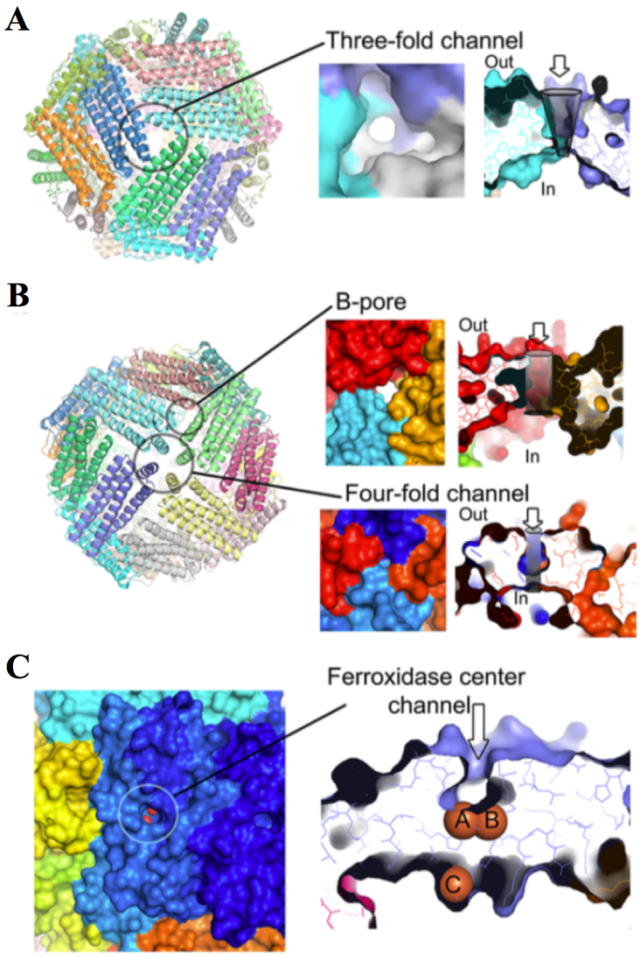

Figure 1.6: Iron uptake pathways of Ftn and Bfr proteins. (A) Funnel-shaped structure of the 3-fold channel of ferritins, and cross-section view of the 3-fold channel showing a possible path of metal ion entry. (B) B-pore and 4-fold channels. (C) Ferroxidase channel showing a pathway directly connecting the outside environment to the FOC. Adapted from reference [60].

1.3.2.2 Mini-ferritins

In Dps proteins, the Fe^{2+} entry pathway has been proposed to occur mostly through the "Ferritin-like" pore due to its similarity in 3-fold symmetry and guiding residues with the 3-fold channel in Ftns [55]. This "Ferritin-like" pore with ~1 nm is usually negatively

charged and constitute the initial part of the type I channel. The channel typically contains three conserved aspartate or glutamate residues, which are involved in the translocation process [54,85].

Two iron atoms were recently identified into the type I channel in *Microbacterium arborescens* Dps [86]. The two atoms appeared as hexa-aquo iron complexes, coordinated by aspartate residue, via side chain water interactions. Its translocation to the FOC was mediated through a glutamine and a second aspartate residue (Figure 1.7).

Another iron uptake path, called type II channel, was observed for *Halobacterium salinarum* DpsA [87]. Here, it was described as a narrow channel formed at the non-symmetrical interface of three subunits, which allows iron translocation to the FOC in two steps (Figure 1.7). A total of 12 channels were observed in the protein shell, leading to the same number of FOCs. Three Fe^{2+} were identified, coordinated by residues from three adjacent subunits, not related by symmetry. As type I channels, type II channels are negatively charged at the outer surface, with glutamine and histidine residues associated to iron translocation inside the channel. Since the distance from the exit of the channel to FOC is ~8 Å, iron migration through type II channels can be achieved by two translocation steps, whereas in the case of type I channels, the channel exit is ~ 2 nm away from FOCs [55].

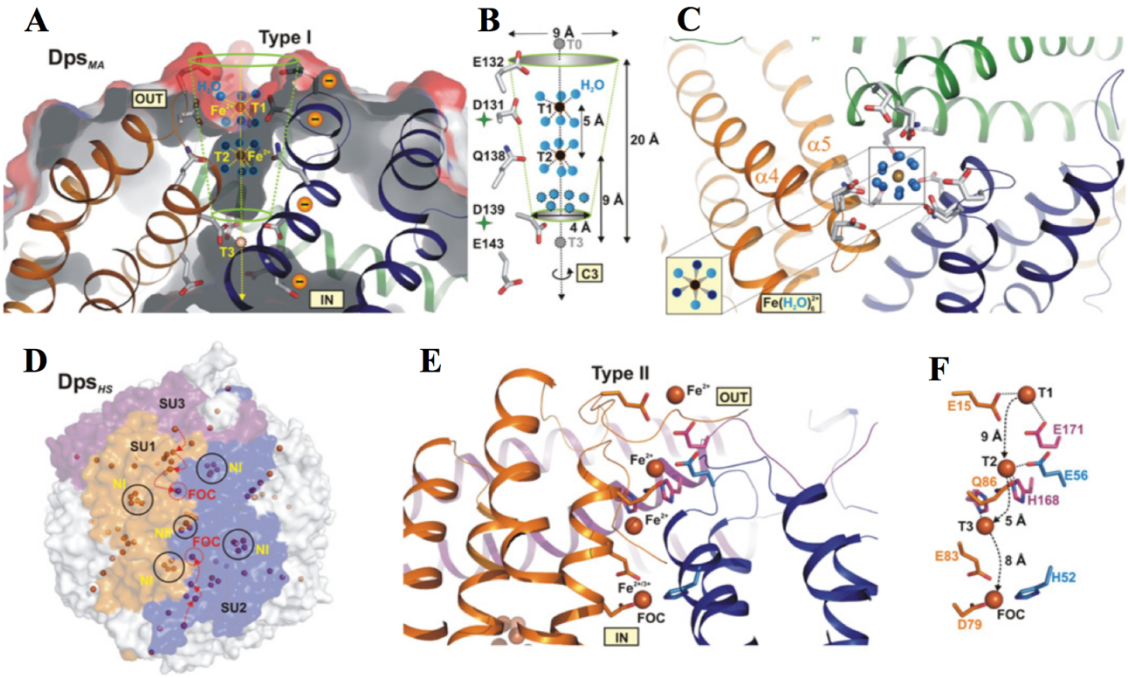

Figure 1.7: Iron uptake pathways in Dps proteins. (A) Cross-section view of type I channel of *M. arborescens* Dps showing a possible pathway of the metal ion entry. The hexa-aquo iron complexes are diffusing from outside to the inner cavity of the protein following the yellow arrow. T1 and T2 represent sites of the two hexa-aquo iron complexes; T3 is a putative translocation site located at the entry of the cavity. (B) Schematic view of the uptake channel as shown in (A). (C) Top view of the type I channel with the hexa-aquo iron complex. Ligating residues are represented as sticks. The geometry of one hexa-aquo iron complex is marked in detail as an inlet with iron in black and three water molecules located in an upper (dark blue) and a lower (light blue) plane. (D) Surface structure of *H. salinarum* DpsA showing the ion metal pathway through type II channel. Three subunits are coloured in orange (SU1), blue (SU2) and magenta (SU3). SU1 and SU2 are related by 2-fold symmetry. Full iron occupation of the dodecameric protein is shown with iron represented as small brown spheres. Iron-translocation sites are located at the interface between SU1, SU2 and SU3. These translocation channels disembogue directly into the FOCs. Two translocation pathways containing three translocation sites are marked with brown red arrows. (E) Iron entry from the outside to the inside cavity via a type II channel. (F) Schematic view of the iron translocation as shown in (E). Adapted from reference [55].

1.3.3 Ferroxidase activity

1.3.3.1 Maxi-ferritins

As mention before, the ferroxidase reaction occurs at FOCs. Ftn and Bfr proteins use predominantly O_2 as co-substrate for the ferroxidation reaction, which results in the formation of H_2O_2 (reaction is represented in equation 1.6).

Stoichiometric studies of the ferroxidase reaction consumption of O_2 and formation of H_2O_2 in eukaryotic and archaeal ferritins have revealed that when two Fe^{2+} are added per FOC, these react with one molecule of oxygen and release a molecule of hydrogen peroxide (equation 1.6) [88-91]. In bacterial ferritin a stoichiometry of three Fe^{2+} per molecular oxygen was observed with realising of water molecules (equation 1.7) [92].

$$2Fe^{2+} + O_2 + 2H^+ \rightarrow 2Fe^{3+} + H_2O_2 \quad (1.6)$$

$$3Fe^{2+} + O_2 + 4H^+ + e^- \rightarrow 3Fe^{3+} + 2H_2O \quad (1.7)$$

The third Fe^{2+} in equation 1.7 was suggested to be oxidized in site C via a redox reaction together with two Fe^{2+} in the FOC or by the H_2O_2 that is produced in the FOC. It was also suggested that the fourth electron for the reduction of the O_2 to water is provided by a tyrosine in the vicinity of site B [88]. This tyrosine residue is highly conserved among the Ftn and Bfr proteins, and it is represented in Figure 1.5A and B.

When the protein is loaded with more than 48 Fe^{2+} per 24-mer, the stoichiometry of Fe^{2+} oxidized per O_2 increases gradually until it reaches a value of about 4 [89,90,93]. In human H-subunit ferritin and in *E. coli* FtnA proteins, the stoichiometry was attributed to Fe^{2+} oxidation by the Fe^{3+} mineral core according to equation 1.8 [89,93].

$$2Fe^{2+} + O_2 + 6H_2O \rightarrow 4[FeO(OH)]_{core} + 8H^+ \quad (1.8)$$

Moreover, in *E. coli* Bfr, regardless of the Fe^{2+} concentration added to the protein, a stoichiometry of 4 Fe^{2+} per molecular oxygen was determined. Despite the fact that the ferroxidation mechanism is not consensually established, it is postulated that the H_2O_2 produced at some FOCs is rapidly consumed at the other FOCs to produce water molecules [60,94,95].

In Ftn proteins, several ferroxidation reaction intermediates have been observed, a blue intermediate, a radical intermediate, and dinuclear oxo-species. The radical intermediate was only observed by EPR spectroscopy in eukaryotic and archaeal Ftns. It was suggested that this species was formed by one-electron oxidation of the conserved tyrosine residue close to site B of the FOC [60,88].

The blue intermediate also called peroxo- or perhydroxo-differric species whose colour varies slightly among Ftns, has a UV-visible absorbance between 500 and 800 nm, with a maximum absorbance in the range of 550 to 650, depending on the Ftn protein

[64,93,96]. It is known that this is the first catalytic intermediate to be formed and that it decays into diferric-oxo dimers, as revealed by Mössbauer spectroscopy [97,98].

Accordingly, a model was suggested to simulate the first phase of the mechanism of Fe^{2+} oxidation (Figure 1.8), considering the distribution of Fe^{2+} among three sites (i.e. FOC and site C) [88]. This model considers two pathways: (1) two Fe^{2+} bind to the FOC, with no Fe^{2+} in site C. In this case, two Fe^{2+} are oxidized simultaneously via the blue intermediate and H_2O_2 is released; (2) two Fe^{2+} bind to the FOC, and a third Fe^{2+} binds to the site C. Here, the two Fe^{2+} are oxidized simultaneously to form the blue intermediate, as in pathway (1). The third Fe^{2+} either reacts with this blue intermediate or it is oxidized by H_2O_2, released with the decay of the blue intermediate. For complete reduction of O_2 to water, the fourth electron is proposed to be delivered by the conserved tyrosine residue near site B.

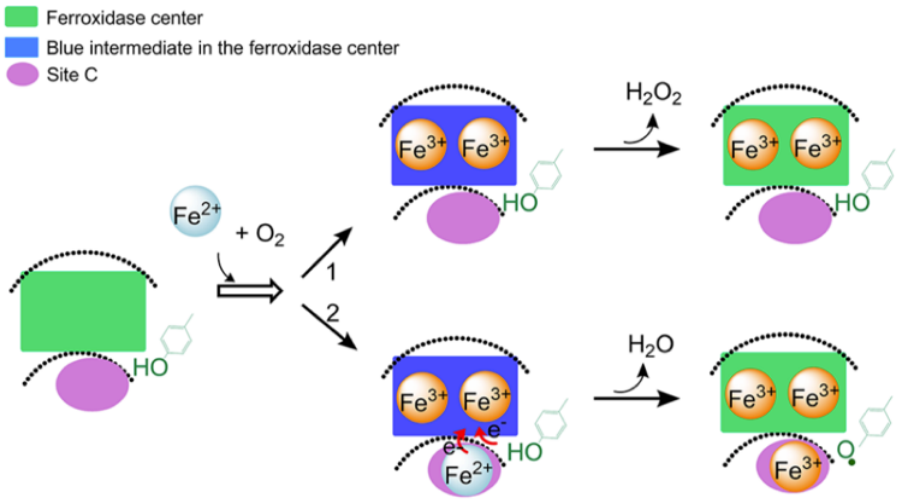

Figure 1.8: Mechanism of Fe^{2+} oxidation by Ftn via two pathways. (1) FOC is occupied with two Fe^{2+} and site C is empty. (2) FOC is occupied with two Fe^{2+} and site C binds a third Fe^{2+}. Adapted from reference [60].

After the fast initial oxidation, the first intermediates are conserved into oxo/hydroxo-diferric species (Fe^{3+}–O(H)–Fe^{3+}), Fe^{3+} monomers, trimers or small clusters ($\geq 3Fe^{3+}$) [97-103].

1.3.3.2 Mini-ferritins

As maxi-ferritins, Dps proteins oxidize Fe^{2+} to Fe^{3+} in the FOC using H_2O_2 or O_2. However, the ferroxidation reaction with H_2O_2 can be up to 100-fold faster than with O_2. This preference for H_2O_2 as iron oxidant prevents the formation of hydroxyl radical, protecting the cells against oxidative stress [42]. Therefore, it is proposed that Dps proteins perform the so-called fast ferroxidation reaction (using H_2O_2) and slow ferroxidation (using O_2), represented in the following reactions [41]:

$$2Fe^{2+} + P^{Z} \rightarrow [Fe_2 - P]^{Z+2} + 2H^{+} \quad (1.9)$$

$$[Fe_2 - P]^{Z+2} + H_2O_2 + H_2O \rightarrow [Fe_2O_2(OH - P)]^{Z} + 3H^{+} \quad (1.10)$$

$$2Fe^{2+} + H_2O_2 + 2H_2O \rightarrow 2FeOOH + 4H^{+} \quad (1.11)$$

(Fast ferroxidation reaction)

$$[Fe_2 - P]^{Z+2} + {}^{1}/_{2}\,O_2 + H_2O \rightarrow [Fe_2(OH)_2 - P]^{Z} + 2H^{+} \quad (1.12)$$

$$4Fe^{2+} + O_2 + 8H_2O \rightarrow 8FeOOH + 8H^{+} \quad (1.13)$$

(Slow ferroxidation reaction)

where, P^{Z} represents the apo-protein and $[Fe_2 - P]^{Z+2}$ the dinuclear iron complex at FOCs. The $[Fe_2O_2(OH - P)]^{Z}$ and $[Fe_2(OH)_2 - P]^{Z}$ correspond to the Fe^{3+} complex in the FOC by using H_2O_2 (equation 1.10) and O_2 (equation 1.12) as oxidant, respectively, and FeOOH corresponds to the mineralization of Fe^{3+} as hydrous ferric oxide.

The analysis of X-ray crystal structures of *H. salinarum* DpsA in its low- and high-iron states revealed three iron atoms in the FOC [87]. In the high-iron state structure, site 1, that coordinates the first iron by an aspartate and glutamate residues from one subunit

(A) and a histidine residue from the adjacent subunit (B) is 3.2 Å apart from site 2, which coordinates the second iron by a glutamate residue from one subunit (A) and a histidine residue from the adjacent subunit (B). The distance between the two iron atoms reflects the formation of μ-oxo diferric species. Moreover, a third iron coordinated by two glutamate residues in the same monomer was identified. The functional role of this third site is currently not clear, while the second site is involved in the ferroxidation reaction through H_2O_2.

1.3.4 Mineralization

1.3.4.1 Maxi-ferritins

Iron mineralization in ferritins is the mechanism for the mineral core growth in the cavity, starting with the nucleation of Fe^{3+}. The nucleation step in Ftns and Bfrs is not well understood, and there are two proposed mechanisms: the substrate site model and the Fe^{3+} displacement model (Figure 1.9A and B, respectively).

The first model, the substrate site model, suggests that the two Fe^{2+} in the FOCs are oxidized to form μ-oxo/hydroxo dinuclear ferric clusters, that migrate through nucleation channels to the inner cavity. In these channels, dimers can interact to form tetramers. Once in the cavity, the four tetramers from the four nucleation channels will nucleate and form a young core of 16 Fe^{3+} ions [24,97,104,105].

In the Fe^{3+} displacement model, it is suggested that after oxidation of Fe^{2+} in the FOC, the oxidized Fe^{3+} in FOC centres stay metastable until it is pushed to the protein cavity by new incoming Fe^{2+} [64].

As mentioned before, the L-subunits in eukaryotic Ftns are slow ferrous iron oxidizers but seems to be essential for storage of Fe^{3+} as mineral core [106-108].

Fewer studies have been performed with Bfr proteins. The best characterized is *E. coli* Bfr, where FOC is proposed to act as a true cofactor site (Figure 1.9C). In this model, two Fe^{2+} are oxidized in the FOCs, and extra Fe^{2+} bind to a third binding site to be oxidized via electron transfer reaction to Fe^{3+} mineral. Once FOC are saturated, the excess of Fe^{2+} enters the central cavity through one or more channels in the protein coat and

binds at the internal nucleation sites. Here Fe^{2+} are oxidized to Fe^{3+}, and the resulting electrons are transferred back to the FOC, where they can recycle the Fe^{3+} ions in the site to Fe^{2+}. The resulting Fe^{2+} in the FOC can react again with the oxidant (O_2 or H_2O_2) and continually cycles its oxidation state until all iron has been mineralized. During mineralization, the ferric core will act as a conducting wire to channel electrons from the oxidation of the incoming Fe^{2+} to the FOC [68,109].

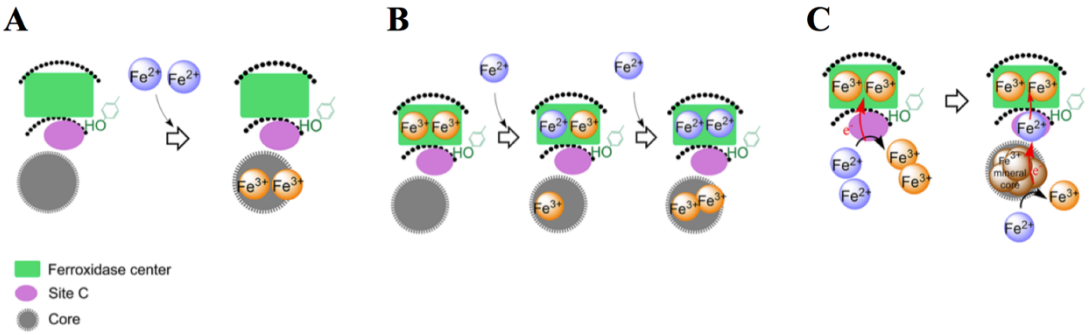

Figure 1.9: Models for iron mineralization in Ftn and Bfr. (A) Substrate site model for Ftn. (B) Fe^{3+} displacement model for Ftn. (C) Co-factor site model for Bfr. Adapted from reference [60].

1.3.4.2 Mini-ferritins

As for to maxi-ferritins, mineralization in Dps proteins starts with the nucleation of Fe^{3+} ions. Only the X-ray crystal structure of *H. salinarum* Dps has, so far, shown nucleation sites, at the 2- and 3-fold symmetry axes, at approximately 13 and 12 Å from the FOC, respectively [87].

Moreover, studies in *L. innocua* Dps have shown that the strength of the electrostatic gradient at 3-fold channel ("Ferritin-like" pore) modulates the rate of iron uptake, resulting in differences in size distribution of the mineral core. Also, negatively charged residues (such as glutamate and aspartate residues) in the 2-fold symmetry axis, in the FOC, participate in both the iron oxidation and nucleation processes [72,85].

1.3.5 Iron release

The mechanism of iron release from the cavity of both maxi- and mini-ferritin proteins is poorly understood. *In vitro* iron release from ferritin proteins can be followed by chemical reduction and complexation with a chelating agent, such as 2,2'-bipyridyl. Different reducing agents have been used for Fe^{3+} reduction, as small molecules such as dithionite, thiols, dihydroflavin, or large molecules, such as flavoproteins [110-112].

In this mechanism, it is still not understood the location of electron transfer that reduces the mineral core and where the biological chelators bind, or the route of Fe^{2+} release. However, studies in Ftns have demonstrated that the 3-fold channels in ferritins are mostly closed to minimize uncontrolled reactions between the mineral core and the cytoplasmic reductants, and small changes in conserved amino acid residues in these channels or variation in physiological concentration of urea lead to unfolding of the channel, and consequently higher iron releases [113-115].

Studies in Dps protein have also shown that the "Ferritin-like" pore in Dps are the putative pathway for iron release [85]. Iron release in Ftns and Dps proteins was described as biphasic, with the first phase corresponding to iron release from the mineral surface (fast kinetics), and the second phase involving iron reduction from the inside of mineral core (slow kinetics) [73,116,117].

In Bfr proteins, it has been proposed that the haem group is responsible for the electron transfer mechanism, with the bacterioferritin-associated ferrodoxin (Bfd) as a possible reducing agent. Bfd contains a [2Fe-2S] cluster and is encoded by the gene *bfd*, located upstream of the gene *bfr* [118,119]. The X-ray crystal structure of the *P. aeruginosa* Bfr-Bfd complex showed that Bfd was bound on top of the haem group, at the 2-fold symmetry axis of Bfr. Thus, electrons would flow from the [2Fe-2S] to the mineral core through the haem group [38,39].

1.4 DNA-binding by Dps protein

DNA-binding ability by Dps protein was discovered by Almirón and colleagues, that identified stable Dps-DNA complexes without any apparent sequence specificity, or

specific DNA size or topology. Complexes were detected *in vitro*, after incubation of Dps with supercoiled plasmid or linear DNA [40].

This DNA-binding ability is not a common feature of all Dps proteins, since their surface is dominated by negative charges that repel negatively charged DNA molecules, only the proteins with specific structural elements have this activity. The X-ray crystal structure of *E. coli* Dps demonstrated that the interaction between Dps protein and the DNA molecule is promoted by the three lysine residues in the mobile N-terminal region, which protuberate from the surface of the protein into the solvent and interact with the phosphate groups on DNA [54]. Electrophoretic mobility shift assay (EMSA) and atomic force microscopy (AFM) have been used to assess the formation of Dps-DNA complexes. At physiologic pH values, *E. coli* Dps forms large complexes with DNA, demonstrating the DNA condensation function of the protein. DNA condensation results from aggregation of Dps molecules bound to the same or neighbouring DNA molecules (Figure 1.10). This condensation ability seems to be associated with the number of lysine residues in the N-terminus and is affected by variation of the pH, i.e. fewer lysine residues and higher pH will deprotonate the lysine residues promoting DNA-binding with no condensation [120].

Besides the presence of lysine residues, the flexibility of N-terminus revealed to be important for the interaction. While *A. tumefaciens* Dps [73], which has the N-terminus positively charged and immobilized in the protein surface did not show any DNA-binding, *L. lactis* MG1363 Dps, isoforms A and B, showed DNA-binding activity, however only to long stretches of linearized DNA (>4,000 bp). Both proteins, DpsA and DpsB, have in their N-terminus folded into an α-helix, which is less mobile than the typical N-terminal region, in an extended conformation [57].

DNA-binding through the positively charged N-terminus was also observed on *M. smegmatis* Dps2 and on *D. radiodurans* Dps-1 [43,58,121].

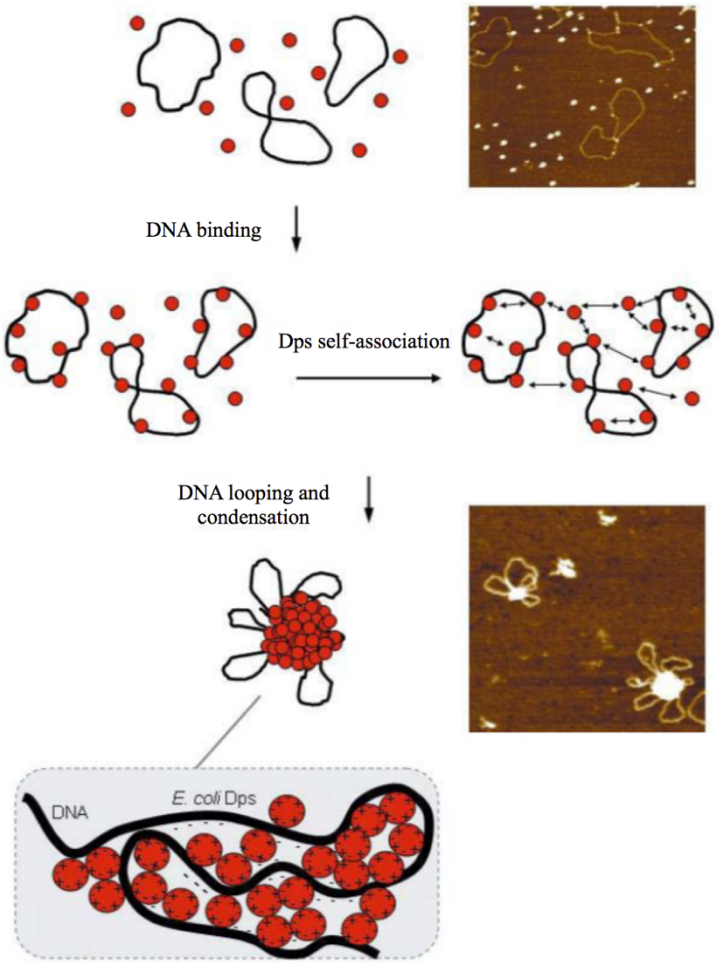

Figure 1.10: Model and demonstrative AFM images of the interaction between *E. coli* Dps with DNA at pH 6.5. The positively charged lysine residues at the N-terminus lead to DNA condensation as they interact concomitantly with DNA and with negatively charged regions of adjacent Dps molecules. Adapted from reference [125].

However, two other types of interactions were identified in Dps proteins. *M. smegmatis* Dps1, that lacks the positively charged N-terminus and has a long C-terminal region containing five positively and four negatively charged residues, binds to DNA using the C-terminus, but without DNA condensation due to the compensatory effect of the negatively charged residues on the C-terminus [59,122,123].

In *Helicobacter pylori* neutrophil-activating Dps protein (HP-NAP, also named Dps), the ability to bind DNA molecules was attributed to the electrostatic interaction between the protein surface and DNA. HP-NAP protein does not possess either the flexible positively charged N-terminus or the long C-terminus, however, at physiologic

pH the protein surface is mostly positively charged and forms large Dps-DNA complexes with DNA condensation. At higher pH, such as pH 8.0, HP-NAP still binds to DNA, but instead of condensing, the protein binds randomly to DNA, forming complexes with a "beads-on-a-string" morphology (Figure 1.11) [124].

Dps proteins provide a multifaceted protection to prokaryotic cells based on DNA-binding activity, that physically protects DNA, on iron sequestration and its ferroxidase activity. This enzymatic activity, besides concentrating and storing iron within the protein, also detoxifies the cellular environment by using H_2O_2 as preferential co-substrate, avoiding the production of hydroxyl radical via Fenton reactions [41,49].

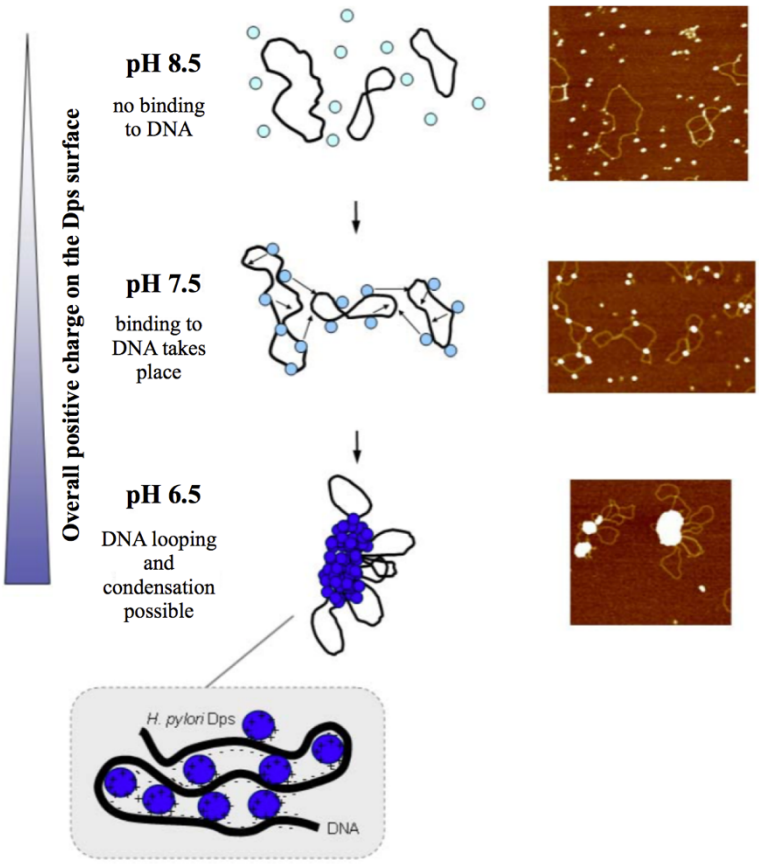

Figure 1.11: Model and AFM images demonstrating the interaction between *H. pylori* Dps and DNA and its pH-dependence. At pH 7.5 Dps-DNA complexes have the so-called "beads-on-a-string" morphology. Adapted from reference [125].

1.5 Biotechnological and medical applications

Proteins from the Ferritin superfamily have been exploited in the field of biotechnology, molecular imaging and drug delivery due to the properties of their structure, which is symmetrically placed with hydrophilic ion channels, the capacity to form mineral cores with different sizes and their thermal and chemical stabilities [24].

In vitro, ferritins can incorporate a variety of metals besides Fe, such as Co, Mg, Cr, Ni, Cd, Zn, Tb, Ca, Mn, Pb, Rh, most likely by the 3-fold channel, producing uniform nanoparticles limited in size by the interior of the cavity. Maxi- and mini-ferritins produce nanoparticle with maximum diameters of ~8 nm, and ~5 nm, respectively [126,127]. In some cases, the incorporation of additional metal ions depends on mutations on the structure. The introduction of negatively charged residues on the internal cavity surface has enhanced the formation of Ag and Au nanoparticles [128]. Due to this flexibility, ferritins have been used as templates for metal oxide nanoparticles, metal oxide semiconductors and as building blocks for the fabrication of electronic devices [127,129].

Ferritin proteins have also been studied for water treatments due to ferritin's capacity to incorporate phosphate during iron mineralization, and its stability at different temperatures and salinity [130].

In molecular imaging and drug delivery, small molecules can be introduced in the cavity by normal diffusion via the 3-fold channel (preferentially positive charged metal complexes), or by disassembly of ferritin nanocage at low pH and reassembly at neutral pH. Additionally, the external protein surface can be modified genetically or chemically in order to attach specific ligands/peptides for the drug delivery or imaging agents [131-134].

1.6 Overview of this Thesis

Proteins from the ferritin family are present in all the three kingdoms of life, where the main role is to store iron in their inner cavity as mineral core. In bacteria, the co-expression of different proteins from the ferritin family is common. While Ftns and Bfrs are currently associated to iron storage, Dps proteins are mostly responsible for cellular

detoxification and DNA protection due to their ability to use H_2O_2 for ferroxidation, thus removing toxic species, and to bind DNA, shielding it from damages.

The main aim of this thesis is to contribute for a better understanding and characterization of ferritin family proteins, focusing in the physiological role of Bfr and in the catalytic and DNA-binding mechanisms of Dps protein from a halophilic bacterium.

Chapter 2 explores the physiological role of Bfr from *Desulfovibrio vulgaris* Hildenborough, a sulphate reducer that can survive long periods of air exposure [135], and co-expresses Ftn and Bfr, but does not produce a Dps protein. Since, both Ftn and Bfr proteins have, based on the current knowledge, the same iron storage function, the co-expression seemed redundant and needed elucidation.

The remaining Chapters are dedicated to the characterization of Dps protein. As mentioned before, Dps proteins use preferentially H_2O_2 as co-substrate to oxidase Fe^{2+} and some Dps proteins bind DNA for protection and shaping. However, the ferroxidation and mineralization mechanisms, as well as the iron release process are not fully understood, and the DNA binding mode is still unknown. The Dps protein studied in this work was produced in *E. coli* cells using an overexpression system that carries the encoding gene from the bacterium *Marinobacter hydrocarbonoclasticus* 617, a gram-negative bacterium found in seawater able to degrade petroleum hydrocarbons [136].

Chapter 3 describes the production, purification and characterization of Dps protein, wild-type (WT) and variants, in a soluble and iron-free form. The variants here produced were used in structural and DNA-binding studies.

The ferroxidase activity of Dps using H_2O_2 as oxidant in the absence of O_2 was analysed by Mössbauer spectroscopy. The ability of the protein to incorporate Fe^{2+} in the absence of any oxidant was also investigated and is described in Chapter 4.

M. hydrocarbonoclasticus Dps contains a flexible N-terminus that, in homologous proteins, has been described to be involved in DNA-binding. Therefore, in Chapter 5, the DNA-binding activity of this protein was evaluated by electrophoretic mobility shift assays (EMSAs). Dps variants, with deleted N-terminus (Dps-Δ15), and a glutamine replaced by a glutamate residue (Dps-Q14E), and also core-containing proteins were used to answer this question.

In Chapter 6, Continuous Wave (CW)-EPR spectroscopy was used to investigate the structural and dynamic properties of the Dps-DNA complexes. Here, a Dps variant containing a single cysteine residue bound to a spin label, prepared by site-directed spin labelling (SDSL), was used.

Chapter 7 is dedicated to the characterization of the N-terminus of Dps using the variant obtained by SDSL combined with pulsed electron-electron double resonance (PELDOR). This technique could allow us to accurately determine the distance distribution of the N-terminus in the Dps structure and determine if these distances change upon DNA-binding.

Finally, Chapter 8 summarizes the main conclusions of work carried out in this thesis and discusses potential future work.

2

Bacterioferritin from *Desulfovibrio vulgaris* Hildenborough

The work described in this Chapter was included in the following publication:

- Timóteo C.G., Guilherme M., Penas D., Folgosa F., Tavares P., Pereira A.S., (2012) *Desulfovibrio vulgaris* bacterioferritin uses H_2O_2 as a co-subtrate for iron oxidation and reveals DPS-like DNA protection and binding activities. *Biochem. J.* **446**, 125-133.

2.1 Overview

Desulfovibrio vulgaris is a sulphate reducer bacterium that can be found in soil, animal intestines, and fresh and salt water. *D. vulgaris* has been described for a long time as an obligate anaerobe, but later studies have shown that *D. vulgaris* can survive long periods of air exposure and in some cases is able to reduce oxygen to water [135,137].

Analysis of the *D. vulgaris* Hildenborough genome allowed the identification of bacterioferritn (Bfr) and ferritin (Ftn) encoding genes. However, the physiological role of Bfr in an organism that co-express a Ftn is not yet elucidated. This work describes the investigation of the detoxifying role by *D. vulgaris* Hildenborough Bfr, and its putative ability to protect DNA against hydroxyl radical.

2.2 Experimental procedure

2.2.1 General procedures

2.2.1.1 Transformation of *E. coli* BL21(DE3) competent cells

E. coli BL21(DE3) competent cells (NZYTech) were used for production of Bfr protein, Dps protein and variants. Transformation of these overexpression cells was generally performed as described in the manufacturer's protocol.

Competent cells were incubated with the plasmid of interest on ice for 30 min. Heat-shock was performed at 42 ºC for 40 s, and incubation on ice for 2 min. 900 µL LB medium were later added to the transformation suspensions and incubated at 37 ºC for 1 h, at 200 rpm. Cells were plated on LB/Agar medium plates containing 100 µg/mL ampicillin and incubated overnight at 37 ºC.

2.2.1.2 Transformation of *E. coli* NZY5*α* competent cells

E. coli NZY5*α* competent cells (NZYTech) are designed for general cloning to increase the insert stability and the quality of plasmid. In this work, competent cells were

used for plasmid DNA isolation. The transformation procedure was the same as the one described for the *E. coli* BL21(DE3) competent cells.

2.2.1.3 Isolation of plasmid DNA

Plasmid DNA preparations from *E. coli* NZY5*α* cultures were obtained by using the NZYMiniprep kit (NZYTech) or the NZYMidiprep kit (NZYTech), depending on the required plasmid yields. The isolation was performed according to the manufacturer's instructions [138,139].

2.2.1.4 Electrophoresis

SDS-PAGE electrophoresis

Sodium dodecyl sulphate polyacrylamide gel electrophoresis (SDS-PAGE) is a technique widely used for determination of apparent molecular mass of proteins and evaluation of protein purity. This method is based on the technique developed by Laemmli U. [140], and here it was mainly used for purity evaluation. Tables 2.1 and 2.2 describe the solutions used to prepare the SDS-PAGE gels. The electrophoresis was carried out at constant voltage (200 V) for a typical running of about 50 min in 1x Tris-Glycine buffer pH 8.3.

Table 2.1: Preparation of gels for SDS-PAGE gel electrophoresis.

Solution	% Acrylamide							
	Stacking gel	Running gel						
	5	5	7.5	10	12.5	15	17.5	20
I (mL)	—	0.75	0.75	0.75	0.75	0.75	0.75	0.75
II (mL)	0.45	—	—	—	—	—	—	—
III (mL)	0.3	1.25	1.33	1.67	2.08	2.5	2.92	3.33
10% SDS (mL)	0.018	0.05	0.05	0.05	0.05	0.05	0.05	0.05
dH_2O (mL)	0.94	2.93	2.85	2.51	2.1	1.66	1.24	0.84
10% APS (µL)	13.5 µL	38	38	38	38	38	38	38
TEMED (µL)	2.0 µL	2.5	2.5	2.5	2.5	2.5	2.5	2.5

Table 2.2: Stock solutions used in SDS-PAGE gel electrophoresis.

Solutions	Components	Preparation	Observations
Running gel buffer (Solution I) [1]	2.5 M Tris Base Concentrated HCl H_2O	30.3 g until pH 8.8 up to 100 mL	pH 8.8 – 9.0 Dilute 1:2 prior to use
Stacking gel buffer (Solution II) [1]	0.5 M Tris Base Concentrated HCl H_2O	6.06 g until pH 6.8 up to 100 mL	pH 6.6 – 6.8
Acrylamide/Bisacrylamide (30:0.8) (Solution III) [1]	Acrylamide Bisacrylamide H_2O	30 g 0.8 g up to 100 mL	—
10% SDS	SDS H_2O	10 g up to 100 mL	—
10% APS	Ammonium Persulfate H_2O	0.5 g up to 5 mL	Prepare prior to use
Tris-Glycine buffer	0.25 M Tris Base 1.92 M Glycine SDS H_2O	30.3 g 144.1 g 10 g up to 100 mL	pH 8.3 Dilute 1:10 prior to use
Sample buffer	Solution II 10% SDS ß-mercaptoethanol Glycerol Bromophenol Blue	5 mL 8 mL 1 mL 2 mL 4 mg	Add 1:1 to the sample
Coomassie Brilliant Blue R-250 staining solution	Coomassie Blue R-250 Glacial Acetic Acid Methanol H_2O	1 g 15 mL 90 mL up to 200 mL	—
Destaining solution	Glacial Acetic Acid Methanol H_2O	75 mL 450 mL up to 1000 mL	—

[1] Solutions I, II and III should be kept at 4 ºC and protected from light.

In addition to hand-cast gels, some samples were analysed in a mini-gel system from GE Healthcare Life Sciences. This system is compatible with standard Laemmli buffers and consists in a horizontal electrophoresis tank (Amersham ECL Gel Box) using pre-cast gels called Amersham ECL Gel. In this system, the gels were run for approximately 1 h at 160 V.

Typically, 5 µL of sample buffer is added to each sample, except for samples from overexpression, were 50 µL of sample buffer are used to resuspend the pellet obtained

from the cells corresponding to an optical density of 1.2, and 8 μL of this solution is loaded into the gel.

To reveal the protein bands, gels were stained with Coomassie Brilliant Blue R-250 staining solution for 30 min and destained with destaining solution. Alternatively, gels were stained with BlueSafe solution (NZYTech) for 25 min and destained with water. Gels were photographed under white light with a Gel Logic 100™ Imaging System (Kodak).

Low molecular weight (LMW) standard protein marker from NZYTech (Appendix A.2.1) was used in all gels unless otherwise stated.

Agarose gel electrophoresis

Agarose gel electrophoresis allows to determine the molecular weight of DNA or RNA fragments and to assess DNA conformation and purity.

All gels used in this work were 0.8% (w/v) in agarose. Samples were prepared by adding BlueJuice™ Gel Loading Buffer (Invitrogen) in a 1:1 ratio to DNA samples.

Electrophoresis was performed at 80 V for 1 h 20 min in 1x TAE buffer (40 mM Tris-acetate buffer pH 8.0, 0.1 mM EDTA). Gels were stained with SYBR Safe solution (Invitrogen) for 30 min, and then imaged with Safe Imager™ (Invitrogen) and photographed under blue light with Gel Logic 100™ (Kodak).

2.2.1.5 Iron quantification

Both ferrous sulphate solutions or ferrous chloride solutions, used in this work, were quantified by the colorimetric assay based on the reaction between the ferrous iron (Fe^{2+}) and the 1,10-phenanthroline reagent. This reaction produces a stable complex, $Fe(Fen)_3^{2+}$, with an orange-red colour, which can be followed by UV-visible spectroscopy at 510 nm [141,142].

Iron quantification was performed by using a standard Fe^{2+} solution (Sigma-Aldrich) and following the procedure described in Table 2.3. The standard iron solution, as well as the ferrous sulphate solution, was prepared with Milli-Q water at pH 3.0.

Samples were prepared like the standard solutions (Table 2.3) with three different dilutions. Samples and standard solutions were prepared in triplicate.

A typical calibration curve obtained for the iron quantification is represented in Figure 2.1.

Table 2.3: Solutions and experimental procedure used to prepare the calibration curve for iron quantification by the 1,10-phenanthroline colorimetric assay.

Reagent	**Eppendorf (µL)**											
Fe^{2+} standard solution (0.01 mg/mL)	0	40	80	160	200	240	300	400	—	—	—	—
$FeSO_4$ sample	—	—	—	—	—	—	—	—	30	50	100	150
Milli-Q water	500	460	420	340	300	260	200	100	470	450	400	350
	Mix (vortex)											
10% Hydroxylamine	80	80	80	80	80	80	80	80	80	80	80	80
	Mix (vortex)											
0.3% 1,10-Phenanthroline	80	80	80	80	80	80	80	80	80	80	80	80
	Mix (vortex) and incubate for 10 min at room temperature											
Milli-Q water	340	340	340	340	340	340	340	340	340	340	340	340
	Absorbance measurement at 510 nm											

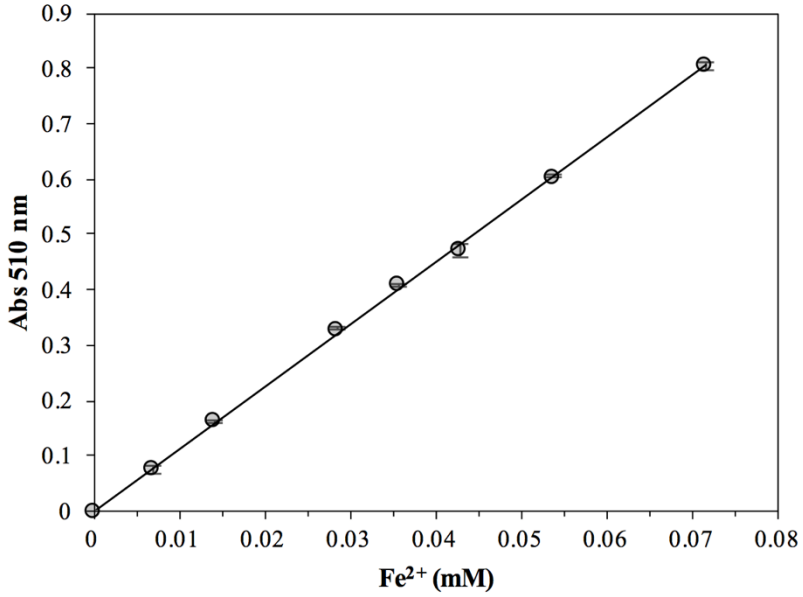

Figure 2.1: Typical calibration curve obtained with a Fe^{2+} standard solution. The trend line equation is $Abs_{510nm}=11.251\times[Fe^{2+}]$ ($R^2 = 0.9995$). Each experimental point represents the mean of three replicates.

2.2.1.6 Hydrogen peroxide quantification

Hydrogen peroxide (H_2O_2) solutions were freshly prepared and quantified by UV-visible spectroscopy at 240 nm, from three different dilutions, using the molar extinction coefficient of 43.6 $M^{-1}cm^{-1}$ [143].

2.2.2 Protein production and purification

Genomic DNA of *D. vulgaris* Hildenborough was isolated with a standard cetyltrimethylammonium bromide (CTAB)-DNA precipitation method [144]. The Bfr coding sequence was amplified using two specific oligonucleotide primers homologous to the 5'- and 3'-ends, which also included restriction enzyme recognition sites (NdeI in the forward primer and EcoRI in the reverse primer). The PCR product was purified from 0.8% agarose gels with GFX PCR DNA and a Gel Band Purification kit (GE Healthcare) and then cloned into pET-21c(+) (Novagen). The resulting overexpression vector was used to transform *E. coli* BL21(DE3) competent cells. Cells were grown in 500 mL 2× YT medium containing 100 µg/mL ampicillin at 37 ºC, at 180 rpm, until reaching an

optical density of 2.0 at 600 nm. Protein expression was induced with 0.1 mM isopropyl β-D-thiogalactopyranoside (IPTG), and 500 mL of fresh growth medium was added to the culture. The culture was grown overnight at 37 ºC, at 180 rpm. Cells were harvested by centrifugation at 11,000 × g for 10 min at 4 ºC and resuspended in 20 mM MOPS buffer pH 7.0. After disruption with a French Press, and centrifugation at 8,000 × g for 20 min at 4 ºC, the soluble extract was recovered through ultracentrifugation at 186,000 × g (Beckman Coulter type 45 Ti rotor) for 90 min at 4 ºC.

Purification of recombinant Bfr (rBfr) was carried out at 4 ºC and pH 7.0. Protein concentration steps were performed in a Diaflo apparatus with an Ultracel Y50 membrane (Amicon). The purity of rBfr was assessed by SDS-PAGE (12.5% polyacrylamide) and UV-visible spectroscopy. The dialysed ultracentrifuged supernatant was applied on to a DEAE Sepharose Fast Flow column (GE Healthcare), equilibrated with 20 mM MOPS buffer pH 7.0. Protein was eluted with a linear gradient of 20 mM MOPS buffer pH 7.0, 500 mM NaCl. Fractions containing the rBfr were pooled together, concentrated, dialysed against 20 mM MOPS buffer pH 7.0 and applied to a Q-Sepharose Fast Flow column (GE Healthcare), equilibrated with 20 mM MOPS buffer pH 7.0. Elution of rBfr was performed with a linear gradient of 20 mM MOPS buffer pH 7.0, 700 mM NaCl.

2.2.3 Protein and iron determination

Protein determination was performed with a BCA (bicinchoninic acid) kit (Sigma-Aldrich) using BSA as a standard. The molar absorption coefficient of apo-protein at 280 nm was determined through the method developed by Gill and von Hippel [145]. The sequence of the first 20 amino acids of the N-terminal region of the purified protein was confirmed by Edman degradation on an automatic sequenator (Applied Biosystem model LC491, Analytical services laboratory at Requimte). ICP-AES (inductively coupled plasma atomic emission spectroscopy) (Analytical services laboratory at Requimte) and a 2,4,6-tripyridyl-s-triazine (Sigma) assay as described by Fischer and Price [146] were used for iron content analysis.

2.2.4 Spectroscopic methods

For UV-visible measurements a Shimadzu UV-265 split-beam spectrophotometer connected to a computer was used. To acquire Mössbauer spectra, a weak-field spectrometer, operating in transmission geometry in a constant acceleration mode, was used. The zero velocity of the Mössbauer spectrum is referred to the centroid of the room temperature spectrum of a metallic iron foil. The spectrometer is equipped with a Janis Closed Cycle He gas Refrigerator cryostat with sample temperature range from 4.5 K to 325 K. Mössbauer spectra analysis was performed using the program WMOSS (SEE co.).

2.2.5 Rapid freeze-quench (RFQ) Mössbauer sample preparation

RFQ Mössbauer samples were prepared using a Bio-Logic SFM-300 equipment, controlled by an MPS 60 unit also from Bio-Logic, fitted with custom-made ageing hoses from Update Instrument. The concentrations of protein, H_2O_2 an ^{57}Fe solutions after mixing were 40 μM, 4 mM and 1.44 mM, respectively. The protein solution was prepared in 200 mM MOPS buffer pH 7.0, 200 mM NaCl. ^{57}Fe and H_2O_2 solutions were prepared in Milli-Q water. The protein, H_2O_2 and ^{57}Fe solutions were loaded into 10 mL syringes, pushed through the mixer and ageing hose, and sprayed into a quenching bath containing isopentane at -140 ºC. After spraying into the funnel containing the cold isopentane, the sample was allowed to stand for approximately 10 min, allowing the crystals to settle. The frozen ice crystals of the reaction mixture were then packed firmly into a Mössbauer sample cell. The temperature of the isopentane bath was monitored with a K-Type Thermocouple (Bioblock Scientific), and maintained by both constant stirring and addition of liquid nitrogen to the outer jacket of the quench bath. The device used to collect the crystals to the Mössbauer sample cell was similar to the one described previously by Ravi et al. [145]. During sample handling, Mössbauer sample cell was kept in contact with viscous isopentane. Control samples were prepared without H_2O_2. ^{57}Fe solutions were prepared from a ^{57}Fe-enriched $FeSO_4$ stock solution (≥ 95% enrichment made from an enriched metal foil). When judged necessary, a glove box system was used (less than 1 ppm; UNILab, MBraun).

2.2.6 Iron uptake assays

Iron uptake by rBfr was monitored at 310 nm in an 8453 UV-visible spectrophotometer (Agilent Technologies) connected to a computer using UV-visible ChemStation software (Agilent technologies). To determine the preferential oxidant, 1.5 μM rBfr, in 200 mM MOPS buffer pH 7.0, 200 mM NaCl, was reacted with oxygenated buffer or with 575 μM H_2O_2, and a molar excess of 240 of a freshly prepared acidic $FeCl_2$ solution. To determine the maximum iron load, stepwise additions of 12 μM $FeCl_2$ followed by 72 μM H_2O_2 were made under aerobic conditions to a 3 mL-stirred quartz cuvette containing 0.5 μM rBfr in 200 mM MOPS buffer pH 7.0, 200 mM NaCl. The maximum iron oxidation/storage capacity was determined by plotting the absorbance at 310 nm as a function of the Fe^{2+}/protein molar ratio.

2.2.7 Electrophoretic mobility-shift assay (EMSA)

The ability of *D. vulgaris* rBfr to bind DNA was tested using supercoiled plasmid pUC19 (vector map present in Appendix A.3.1), and a synthetic 20-bp single-stranded DNA (5'-AAACCCGAGAGAGTACGAAC-3' and complementary oligonucleotide (STABVida)) by EMSA. To prepare the 20-bp duplex DNA form, equimolar amounts of complementary oligonucleotides were heated at 95 ºC for 2 min and slowly cooled down to room temperature. The supercoiled plasmid pUC19 was obtained and purified with the NZYMiniprep kit (NZYTech) according to the manufacturer's instructions [138].

The electrophoretic images were processed and analysed (free DNA and protein-DNA complex bands) using ImageJ [147]. All the EMSAs were performed, at least, in triplicate.

2.2.7.1 EMSA with supercoiled plasmid DNA

Supercoiled pUC19 (10 nM) was incubated with rBfr (between 0.25 and 12 μM) for 10 min at room temperature, in 50 mM MOPS buffer pH 7.0, 50 mM NaCl, in a total volume of 10 μL. As a control reaction, rBfr was replaced by BSA protein (4.4 μM).

EMSA (5 µL of each reaction) was performed using 1% agarose gels in 1× TAE buffer, run at 80 V for 1 h 45 min at room temperature. The gels were stained with SYBR Safe solution (Invitrogen) and imaged with Safe Imager™ (Invitrogen) in a Gel Logic 100™ Imaging System (Kodak).

2.2.7.2 EMSA with short DNA duplex

Short DNA duplex (20-bp DNA, 0.83 µM) was incubated with rBfr (between 5.75 – 23 µM) in 50 mM MOPS buffer pH 7.0, 50 mM NaCl, in a total volume of 10 µL for 10 min at room temperature. The reaction was analysed in an E-Gel® CloneWell™ SYBR Safe system (Invitrogen) with 2% agarose gels, run at room temperature for 1 h. The results were imaged with Safe Imager™ (Invitrogen) in a Gel Logic 100™ Imaging System (Kodak).

2.2.8 DNA protection assay

The *in vitro* DNA protein assays against hydroxyl radical activity and DNase were performed using the plasmid DNA pGEX-6P-1 (GE Healthcare; Appendix A.3.2).

2.2.8.1 Protection against hydroxyl radical activity

Plasmid pGEX-6P-1 (12 nM) was allowed to react with 6 µM of rBfr, 100 Fe^{2+} ions-loaded rBfr and an excess of H_2O_2, or rBfr pre-incubated with 12 haems per protein molecule, for 10 min at room temperature, in 200 mM MOPS buffer pH 7.0, 200 mM NaCl. After the incubation, Fenton reactions were promoted by adding 76 µM $FeCl_2$ and 1.15 mM H_2O_2, and the resulting mixture was incubated at room temperature for 10 min. The reaction was stopped by addition of 2% SDS followed by heating at 85 ºC for 2 min. In a control reaction, no rBfr was added to the mixture.

2.2.8.2 Protection against DNase

Plasmid pGEX-6P-1 (15 nM) was incubated with rBfr (13 µM) in 200 mM MOPS buffer pH 7.0, 200 mM NaCl, for 10 min at room temperature, followed by addition of 1.2 µg/µL DNase I (Sigma). The mixture was incubated for 10 min, at room temperature, and stopped by the addition of 3 mM EDTA and incubated for 5 min at 65 ºC. The control was made with no rBfr. Results were analysed by 1% agarose gel electrophoresis, stained with SYBR Safe solution (Invitrogen) and imaged with Safe Imager™ (Invitrogen) in a Gel Logic 100™ Imaging System (Kodak).

2.3 Results and discussion

2.3.1 rBfr characterization

Amino acid sequence analysis of *D. vulgaris* Bfr and comparison with other Bfr primary structures (Figure 2.2) revealed that the residues identified as axial haem ligands and the iron ferroxidase centre were all conserved.

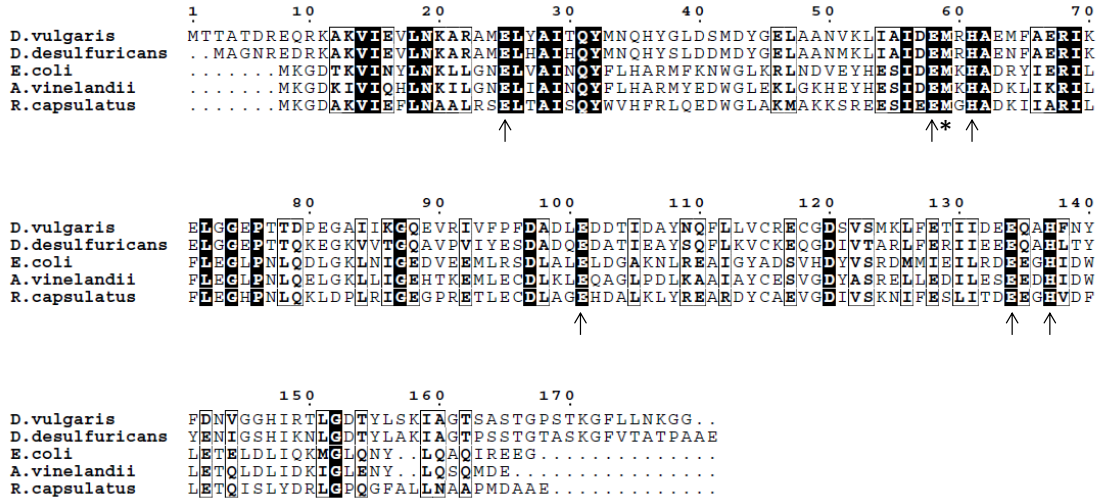

Figure 2.2: Bfr amino acid sequence comparison. Amino acid sequence alignment, prepared using ClustalX and ESPript [152,153], of *D. vulgaris* Bfr (GenBank® accession number YP_010616) with other known Bfrs (*D. desulfuricans* PDB code 1NFV, *E. coli* PDB code 1BCF, *A. vinelandii* GenBank® accession number AAA22121 and *Rhodobacter capsulatus* GenBank® accession number ADE84678). Conserved residues involved in the ferroxidase centre are marked with arrows; the conserved methionine haem ligand is marked with an asterisk.

Based on homology with *E. coli* Bfr [148,149], M59 was assumed as the haem axial ligand in *D. vulgaris* Bfr (M52 in *E. coli* Bfr), and E25, E58, H61, E101, E134 and H137 as non-haem iron ligands at the ferroxidase centre. There is also conservation of Y32 (*D. vulgaris*) that is hydrogen bounded to E94 in *E. coli* Bfr. Also, the primary sequence of *D. vulgaris* Bfr has a higher degree of similarity with the sequence of *D. desulfuricans* protein than with any other Bfr proteins.

rBfr was purified in the apo-form, as described in Section 2.2.2, since there is a maximum of 0.4 haems per protein molecule, judged by SDS-PAGE. The ICP-AES only detected less than six Fe atoms.

Protein quantification by the BCA method suffered from severe interference probably due to Cu^{2+} chelation by rBfr. The molar absorption coefficient at 280 nm for the oxidized rBf, determined by Gill and von Hippel [145] is 2.6 $x10^5$ $M^{-1}cm^{-1}$ per oligomeric protein. This is similar to the theoretical one of 2.5 $x10^5$ $M^{-1}cm^{-1}$ obtained using the ExPASy ProtParam tool [150]. Thus, the later was used to determine rBfr concentration of all preparations.

The UV-visible spectrum of rBfr exhibits a major absorption band at 280 nm. Two other small bands, corresponding to the haem, are visible at 414 nm (Soret band) and round 535 nm. Upon reduction with sodium dithionite, the Soret band is shifted to 427 nm and the band at 535 nm originates α and β bands, with an absorption maximum at 559 nm and 529 nm, respectively. This spectroscopic behaviour is in agreement with the one described for *E. coli* Bfr, which is one of the most well-studied of this class of enzymes [151].

2.3.2 Iron oxidation mechanism

The iron uptake assays using H_2O_2 and O_2 as co-substrate are shown in Figure 2.3. These assays indicate that rBfr is able to oxidize Fe^{2+} ions by using H_2O_2 (black curve, Figure 2.3A). In contrast, in the presence of O_2, the oxidation is residual (grey curve, Figure 2.3A). The use of H_2O_2 by rBfr as co-substrate resembles to Dps proteins.

Moreover, in the tested conditions, rBf could incorporate around 600 Fe^{2+} ions (Figure 2.3B). This value is small when compared with the theoretical maximum number

of iron atoms of 4500 that can be accommodated in the mineral core into the cavity of the mammalian Ft [27,154]. Some Fts and Bfrs, though, have been reported to store a lower than theoretical number of ions [27].

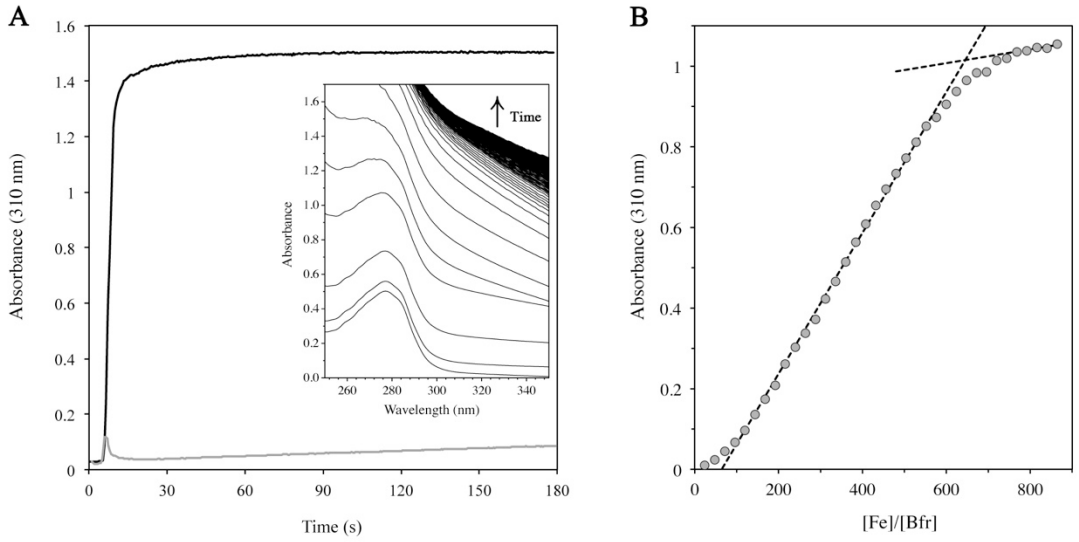

Figure 2.3: Fe^{2+} oxidation by rBfr in 200 mM MOPS buffer pH 7.0, 200 mM NaCl. (A) Kinetics of Fe^{2+} oxidation by rBfr in the presence of H_2O_2 and O_2. Reaction of 1.5 µM rBfr with a molar ratio of 240 Fe^{2+}/protein and 575 µM H_2O_2 (black curve) or atmospheric concentration of O_2 (grey curve). The reaction was started at 6 s by addition of the $FeCl_2$ solution. The inset shows the absorption spectra as a function of the reaction time (up to 180 s, bottom to top). (B) rBfr iron loading in the presence of an excess H_2O_2. Reaction of 0.5 µM rBfr with Fe^{2+} ions and H_2O_2. Each point represents an addition of 24 Fe^{2+}/rBfr and H_2O_2. Dashed lines are computed tangents to the initial (excluding three initial ratios) and end regions of the curve. The lines intersect at a Fe^{2+}/protein molar ratio of 645.

The iron oxidation mechanism was investigated by preparation of RFQ Mössbauer samples (between 25 ms and 2 min) using *D. vulgaris* rBfr in the presence of H_2O_2.

rBfr pre-loaded with 36 Fe^{2+} ions data have shown that after 25 ms of reaction time with H_2O_2, most of the Fe^{2+} were oxidized. Spectrum A (Figure 2.4) represents the Fe^{2+} pre-loaded rBfr at the starting reaction. Spectrum B (Figure 2.4) represents the Fe^{2+} ions after 25 ms of reaction, showing that most of the Fe^{2+} quadrupole doublet (high-energy lines position marked by a vertical solid line) was already oxidized. Simultaneously, a broad doublet increased in intensity in the middle of the spectra, as can be observed in

both spectra B and C (Figure 2.4), corresponding to 25 ms and 2 min of reaction, respectively.

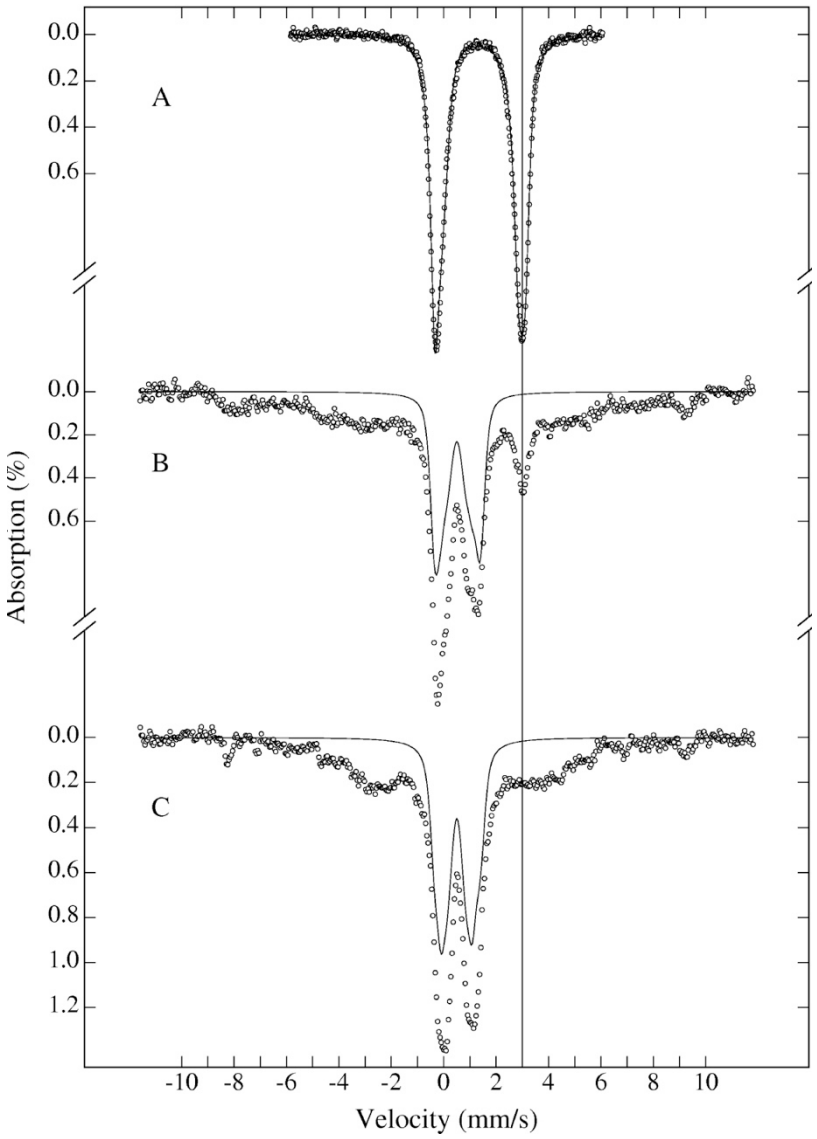

Figure 2.4: Mössbauer spectra of RFQ samples from reaction of rBfr with Fe^{2+} and H_2O_2. (A) rBfr reacted with 36 $^{57}Fe^{2+}$ ions. (B) rBfr reacted with 36 $^{57}Fe^{2+}$ ions and H_2O_2 for 25 ms. (C) rBfr reacted with 36 $^{57}Fe^{2+}$ ions and H_2O_2 for 2 min. The solid lines are superimpositions of theoretical simulations of iron species previously observed in other fast Fts. Spectrum A was fitted with two quadrupole doublets of equal percentage using the following apparent Mössbauer parameters, typical of high-spin ferrous iron: site I, ΔE_Q = 3.24 ± 0.03 mm/s and δ = 1.46 ± 0.02 mm/s; and site II, ΔE_Q = 3.20 ± 0.03 mm/s and δ = 1.22 ± 0.02 mm/s; line widths = 0.50 mm/s. Spectrum B is composed of 9 ± 2% of the previously described ferrous iron species; by the three diferric intermediates described for the H-type ferritin oxidation reaction of Fe^{2+} in the presence of O_2 using the following parameters: 15 ± 3% of dimer 1.7 (ΔE_Q = 1.73 ± 0.03 mm/s and δ = 0.53 ± 0.03 mm/s), 11% of dimer 1.2 (ΔE_Q = 1.20 ± 0.03 mm/s and δ = 0.50 ± 0.03 mm/s) and 7 ± 2% of dimer 0.7 (ΔE_Q = 0.70 ± 0.03 mm/s and δ = 0.50 ± 0.03 mm/s). Spectrum C contains 9 ± 3%

of dimer 1.7, 20 ± 3% of dimer 1.2 and 12 ± 3% of dimer 0.7. In both spectra B and C a large magnetic species representing the ferric mineral increases with reaction time. Data were recorded at 4.2 K, with a 60 mT magnetic field applied parallel to the γ-beam.

The solid lines plotted on top of experimental spectra B and C are the superimposition of theoretical simulations with variable intensities of 0.7 mm/s, 1.2 mm/s and 1.7 mm/s quadrupole doublets representing the three oxy-dimers observed on the rapid aerobic oxidation of Fe^{2+} ions by recombinant bullfrog H-type subunit Ft [97]. These catalytic intermediates have been spectroscopically characterized and were attributed to dinuclear Fe^{3+} species formed during Fe^{2+} oxidation by bullfrog Ft using O_2. The additional broad feature extending from -9 mm/s to 9 mm/s gains intensity at longer reaction times and was explained as a superparamagnetic species designated by the authors as "young core", corresponding to a small sized Fe^{3+} mineral.

A Mössbauer sample containing 240 $^{57}Fe^{2+}$ ions pre-loaded into rBfr in an excess of H_2O_2 was analysed at two different temperatures. While at 6 K the spectrum (spectrum A, Figure 2.5) can be described as a magnetic sextet, increasing the acquisition temperature to 150 K leads to a conversion of the magnetic sextet into quadrupole doublets (spectrum B, Figure 2.5). This behaviour is typical of superparamagnetic systems and can be associated to the formation of the iron mineral core [155].

Also, the high-temperature spectrum of the 2 min-reacted sample (spectrum C, at 4.2 K, Figure 2.4) is represented in Figure 2.6. In this case, the fit was obtained with two components: 41 ± 3% corresponding to a set of three quadrupole doublets representative of the three diferric intermediates used in the interpretation of spectra B and C in Figure 2.4, and the remaining absorption can be explained by the spectral shape of spectrum B in Figure 2.5.

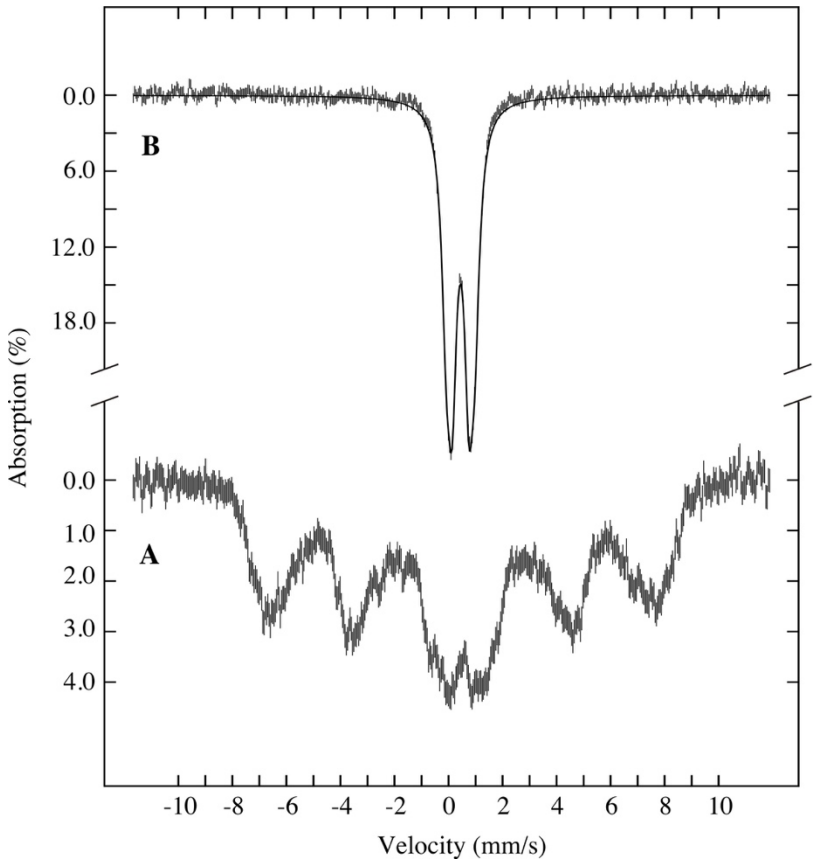

Figure 2.5: Mössbauer spectra of a 240 $^{57}Fe^{2+}$/rBfr sample reacted with H_2O_2 for 3 h. (A) Spectrum recorded at 6 K with 60 mT magnetic field applied parallel to the γ-beam. (B) Spectrum recorded at 150 K in the absence of an external magnetic field; Fitted with two quadrupole doublets of equal percentage using the following apparent Mössbauer parameters: δ = 0.44 ± 0.01 mm/s and ΔE_Q = 0.61 ± 0.02 mm/s and 1.05 ± 0.02 mm/s, line widths = 0.40 mm/s. A concentration of 55 µM rBfr and a 15× molar excess of H_2O_2 was used. The sample was in 200 mM MOPS buffer pH 7.0, 200 mM NaCl.

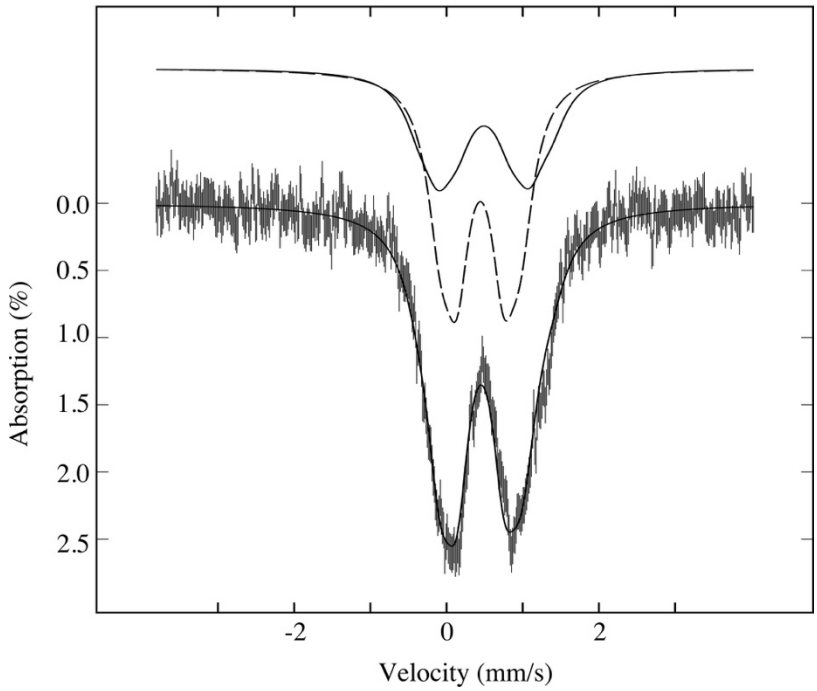

Figure 2.6: High-temperature Mössbauer spectrum of a RFQ sample of rBfr reacted with 36 $^{57}Fe^{2+}$/protein and H_2O_2 for 2 min. Data were recorded at 150 K in the absence of an external magnetic field. The experimental spectra (vertical bars) was fit using three quadrupole doublets corresponding to the three diferric intermediates (solid line superimposed to the experimental spectrum) with the following parameters: 9 ± 3% of ΔE_Q = 1.73 ± 0.03 mm/s and δ = 0.51 ± 0.03 mm/s; 20% of ΔE_Q = 1.20 ± 0.03 mm/s and δ = 0.49 ± 0.03 mm/s; and 12 ± 2% of ΔE_Q = 0.70 ± 0.03 mm/s and δ = 0.49 ± 0.03 mm/s (theoretical solid line on the top) and 59% of two quadrupole doublets corresponding to the spectral shape attributed to the mineral core (theoretical broken line on the top).

Based on the Mössbauer results, the catalytic mechanism for the Fe^{2+} oxidation with H_2O_2 by *D. vulgaris* rBfr was proposed to be similar to the one described for the H-type Ft ferroxidation reactions [97]. Free Fe^{2+} in solution entry the protein shell and forms a diferrous centre at the ferroxidase site that is oxidized to diferric-oxo/hydroxo complexes in the presence of H_2O_2, and subsequently in small superparamagnetic Fe^{3+} clusters and finally in large ferrihydrite mineral.

2.3.3 DNA binding studies

Due to the observation that Bfr oxidizes Fe^{2+} more efficiently in the presence of H_2O_2, as with Dps, and to further understand why an anaerobic bacterium such as *D.*

vulgaris can co-express more than one type of ferritin, a DNA protection function was hypothesized for Bfr to bind DNA.

EMSA experiments were performed using supercoiled plasmid pUC19 in 50 mM MOPS buffer pH 7.0, 50 mM NaCl. A representative EMSA gel is shown in Figure 2.7.

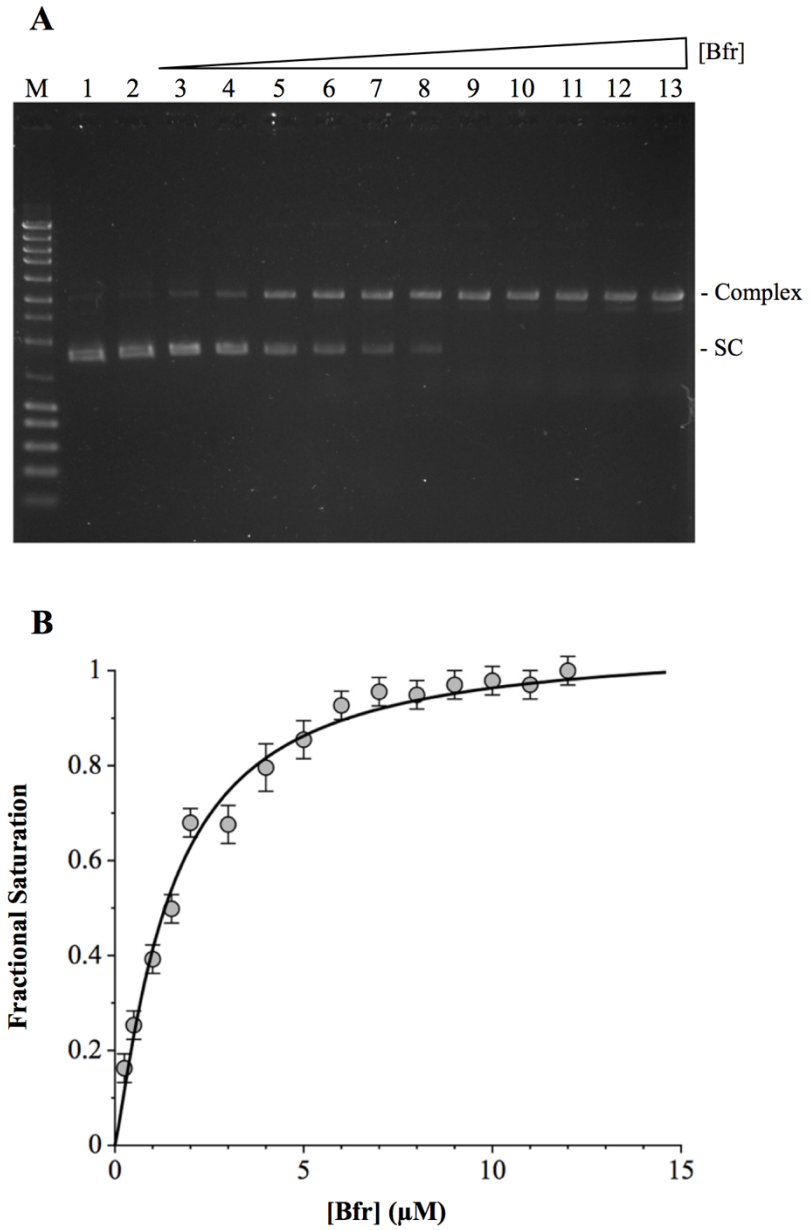

Figure 2.7: Analysis of Bfr-DNA binding by EMSA (1% agarose gel in 1x TAE buffer). (A) Binding of rBfr to supercoiled plasmid pUC19. M – NZYLadder III; 1 – Supercoiled plasmid pUC19 (10 nM); 2 – Binding reaction of BSA (4.4 µM) to supercoiled pUC19 (10 nM); 3 to 13 – Binding of rBfr (0.25, 0.50, 1.50, 3.0, 4.0, 5.0, 7.0, 9.0, 10, 11 and 12 µM) with 10 nM of supercoiled pUC19. The free supercoiled plasmid pUC19 band (SC) and the protein-pUC19 band

(Complex) are indicated on the right. (B) Hill plot of DNA binding by rBfr resulting from three sets of EMSA experiments using increasing protein concentrations, between 0.25 μM and 12 μM, and 10 nM of supercoiled pUC19.

By analysing the EMSA profile it is possible to observe the binding of rBfr to supercoiled plasmid by the formation of large protein-DNA complexes, which migrate slower than the free supercoiled plasmid (Figure 2.7A). With the increasing of protein concentration, there is a shift from the entire population of free plasmid to protein-DNA complex, with apparent saturation around 5 μM rBfr. DNA binding is specific to rBfr, since substitution with BSA (a protein that does not bind DNA) did not show any retardation on the free DNA band.

The fractional complex formation for rBfr-pUC19 complexes was fit to the Hill equation (Figure 2.7B), according to:

$$f = \frac{f_{max}[\text{Protein}]^n}{(K_\text{d} + [\text{Protein}]^n)},$$

where f is the fractional saturation, f_{max} corresponds to 100% complex formation, [Protein] is the concentration of binding protein, n is the Hill coefficient, and K_d represents the macroscopic apparent dissociation constant and is a measure of the affinity of the protein to DNA.

In the experimental conditions, the apparent dissociation constant and the Hill coefficient were K_d = 1.5 ± 0.3 μM, and n = 1.3 ± 0.2, respectively. The Hill coefficient is comparable with the values reported in the literature for binding of *Deinococcus radiodurans* DPS-1 to a 26-bp DNA duplex, indicating a positive co-operativity on DNA binding [156].

To explore the ability of rBfr to bind short linear DNA duplex, protein was incubated with 20 bp-double stranded DNA, with a normal G + C content, in 50 mM MOPS buffer pH 7.0, 50 mM NaCl. The EMSA showed that rBfr binds short DNA duplex with lower affinity when compared with supercoiled plasmid, since no sharp bands with higher molecular mass are observed. In its place, a smear of the protein-DNA complexes is observed (Figure 2.8A), indicating the possible instability of the complex, and probably dissociation during electrophoresis. However, the densiometric quantification (Figure

2.8B) shows a higher-intensity band of protein-DNA complex for higher rBfr concentrations, demonstrating the ability of rBfr to bind DNA. Although, under these conditions, the results have shown preferential binding of rBfr to supercoiled plasmid.

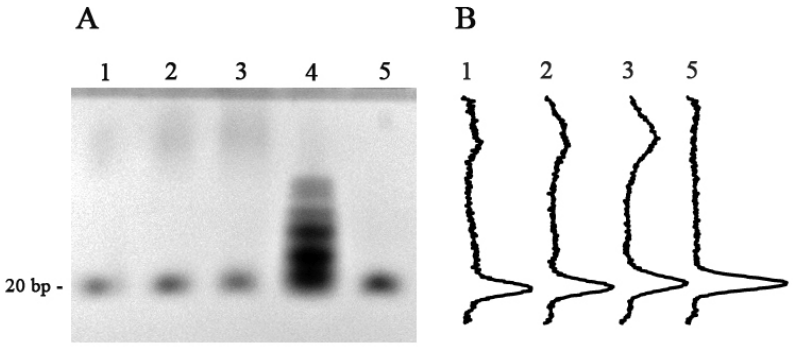

Figure 2.8: Binding of *D. vulgaris* rBfr to 20 bp-double stranded DNA in 50 mM MOPS buffer pH 7.0, 50 mM NaCl. (A) Binding of rBfr to short DNA duplex. 1 to 3 – Binding of rBfr (5.75, 11.5 and 23 μM) to 20 bp-DNA (0.83 μM); 4 – HyperLadder V (Bioline); 5 – 20 bp-double stranded DNA (0.4 μM). (B) The densitometric quantification of free 20 bp-DNA (lower band) and complex band (upper band).

The apparent dissociation constant determined, K_d of about 1 μM, is in the same micromolecular range of the values reported for the HP-NAP from *Helicobacter pylori*, a neutrophil-activating protein from the Dps family, ranging from about 3 to 10 μM for binding to linearized and to a 27 bp-short double-stranded DNA, respectively [124]. Also, *Trichodesmium erythraeum* Dps have reported a K_d of around 16 μM for a binding with pUC19 plasmid [157]. Besides these proteins, also HU histone-like proteins and IHF (integration host factor) from *E. coli* have reported low values of apparent dissociation constant. K_d of 0.2-2.5 μM for HU histone-like proteins, and K_d of 20-30 μM for *E. coli* IHF [158]. However, a direct comparison of K_d values is difficult because the affinity depends on several experimental conditions, such as the sequence, size and topology of the DNA, pH, ionic strength, temperature, or presence of divalent metals in the binding reaction.

The single sharp band of the protein-supercoiled plasmid DNA complex can be explained as a change of the topology of the plasmid DNA due to the binding of rBfr, such as relaxation of the supercoiled form, or a different mechanism of condensation of

circular DNA when compared with those of *E. coli* Dps, which involves DNA condensation and self-aggregation of the protein [124]. Ceci and colleagues [120] demonstrated by EMSA and atomic force microscopy (AFM) that, at pH 6.3, *E. coli* Dps self-aggregated and condensed DNA, whereas the Dps-Δ18 variant, lacking the positively charged amino acid at the N-terminal region did bind, but was unable to condense DNA. In this case, Dps molecules bound to DNA randomly and appeared as "beads-on-a-string". Therefore, by comparison with the *E. coli* Dps DNA-binding behaviour and in the experimental conditions used: (i) *D. vulgaris* rBfr binds plasmid DNA, but does not condensate it; or (ii) rBfr binds DNA with a different mechanism when compared with the one proposed for *E. coli* Dps.

2.3.4 DNA protection assay

The studies about the potential DNA protection of rBfr were performed by DNase I hydrolysis assays and binding reactions in the presence of hydroxyl radicals, that can prompt breaks in the DNA double helix, assessed by agarose gels.

When DNase I reacted with plasmid DNA (pDNA) complete hydrolysis occurred, as can be observed in Figure 2.9A. Contrarily, when plasmid was pre-incubated with rBf followed by exposure to DNase I no hydrolysis was observed. These results indicate that the formation of Bfr-DNA complexes prevented the physical accessibility of DNase to DNA.

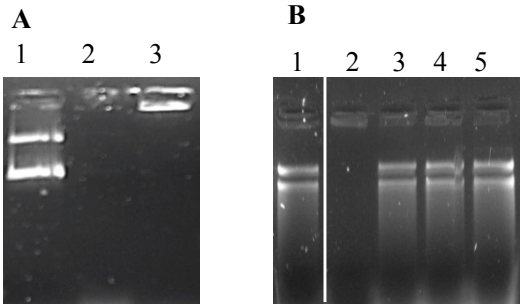

Figure 2.9: DNA protection assays. (A) Protection against DNase cleavage. 1 – pDNA (15 nM); 2 – Reaction of pDNA with DNase I (1.2 μg/μL); 3 – Reaction of pDNA with DNase I (1.2 μg/μL) pre-incubated with rBfr (13 μM in 200 mM MOPS buffer pH 7.0, 200 mM NaCl). (B) Protection assay against hydroxyl radical-induced damage. 1 – pDNA (12 nM); 2 – pDNA exposed to an excess of Fe^{2+} ions and H_2O_2; 3 to 5 – pDNA pre-incubated with apo-rBfr, rBfr loaded with 100 Fe per protein and rBfr with 12 haems per protein, respectively, in the presence of Fe^{2+} and H_2O_2.

For the DNA protection tests against hydroxyl radical-induced damage, pDNA was exposed to Fe^{2+} and H_2O_2 after pre-incubation with apo-rBfr, rBfr pre-loaded with 100 Fe^{2+}/protein, and haem-reconstituted rBfr (Figure 2.9B). Unlike the EMSAs, the reaction was stopped by incubation with SDS at 85 ºC, resulting in disruption of protein-DNA complex, which allows pDNA to migrate in the gel as the free form.

As Figure 2.9B shows, pDNA exposed to hydroxyl radicals in the absence of rBfr resulted in its complete degradation. Whereas, upon pre-incubation with rBfr, pDNA protection was observed, independently of the protein iron or haem contents. This activity to prevent DNA damage in the presence of hydroxyl radical can be related to rBfr ability to use H_2O_2 to rapidly oxidize iron, as shown in Section 2.3.2, rather than with its DNA-binding activity.

In conclusion, *D. vulgaris* bacterium expresses a Ft, which uses O_2 to oxidize iron rapidly, and co-expresses rBfr which has a Dps-like function. As such, Bfr preferentially uses H_2O_2 as the co-substrate, binds and protects DNA as the Dps protein.

3

Dps protein from *Marinobacter hydrocarbonoclasticus* 617 and variants

3.1 Overview

This chapter describes the production and purification of the Dps protein from *Marinobacter hydrocarbonoclasticus 617* and its variants. The recombinant plasmid containing the *Dps* gene was originally produced by Guilherme M. [159]. The protocol for overexpression and purification of Dps-WT was first described by Guilherme M., and optimized in this work as detailed in this Chapter.

Dps variants are the Dps-Q14E, Dps-Δ15 (protein with deletion of the first 15 amino acids, corresponding to the N-terminus), Dps-T10C and Dps-F5C, which were used for structural, spectroscopic and DNA binding studies.

3.2 Experimental procedure

3.2.1 General procedures

3.2.1.1 Protein concentration determination

Protein concentration was determined by UV-visible spectroscopy by measuring three samples prepared with serial different dilutions. The molar absorption coefficient of Dps-WT protein and variants at 280 nm (2.93 $x10^5$ $M^{-1}cm^{-1}$) was used for all quantifications [159].

Protein concentration was performed using a Vivacell 70 concentrator (100 kDa MWCO, Sartorius) or a Vivaspin 20 concentrator (100 kDa MWCO, Sartorius).

3.2.1.2 Catalase activity test

The catalase test consists in testing the protein for potential catalase contaminations. To perform the test, 100 µL of protein was incubated, for a few minutes, with four drops of 30% (w/v) hydrogen peroxide (H_2O_2). The presence of catalase was evaluated quantitatively by observing the formation of bubbles in the sample upon addition of H_2O_2.

3.2.2 Production and Purification of Dps-WT protein

E. coli BL21(DE3) cells harbouring the pET-21c–Dps-WT plasmid were used for large-scale production of Dps-WT protein. For the overexpression, 5 mL LB medium containing 100 µg/mL ampicillin was inoculated with a single isolated *E. coli* BL21(DE3) transformant. After growing for 8 h at 37 ºC, at 220 rpm, 1 mL of this culture was used to inoculate 100 mL LB medium containing 100 µg/mL ampicillin. The culture was grown overnight at 37 ºC, at 220 rpm. Subsequently, 10 mL of this culture was used to inoculate 1 L LB medium containing 100 µg/mL ampicillin that was grown at 37 ºC, at 200 rpm, until reaching an optical density at 600 nm of 0.5. Expression was induced by addition of 0.5 mM IPTG. Cells were incubated to grow for 3 h at 37 ºC, at 200 rpm and harvested by centrifugation at 11,000 × g for 10 min at 6 ºC (Z 36 HK, HERLME LaborTechnik); the pellet was resuspended in 10 mM Tris-HCl buffer pH 7.6. To enhance cell disruption, cells were submitted to three cycles of freeze-thaw and incubated with DNase I (Roche). The cell lysis was performed by sonication using an ultrasonic homogenizer equipped with a 7-mm probe (LABSONIC M, Sartorius). Cells were then sonicated on ice for 3 min, with an amplitude of 80%, followed for 90 s of rest on ice, this process was repeated 4 times. DNase I was further added to reduce the viscosity of the extract. To remove cell debris, the suspension was centrifuged at 10,000 × g for 10 min at 6 ºC (Z 36 HK, HERLME LaborTechnik). The soluble fraction (here designated soluble crude extract) was collected after ultracentrifugation at 181,000 × g for 1 h 10 min at 4 ºC (Beckman Coulter type 70 Ti rotor), which was dialysed overnight at 4 ºC against 10 mM Tris-HCl buffer pH 7.6.

Immediately before protein purification, the soluble protein extract was centrifuged at 10,000 × g for 10 min at 6 ºC (Z 36 HK, HERLME LaborTechnik), and filtered with a 0.45 µm membrane filter (polyethersulfone, VWR).

Dps-WT protein purification followed a two-steps purification protocol. In the first step, the soluble extract was loaded onto a DEAE Sepharose Fast Flow column (2.6 x 30 cm, GE Healthcare Life Sciences) previously equilibrated with 10 mM Tris-HCl buffer pH 7.6, and washed with the same buffer. Absorbed proteins were eluted with a discontinuous gradient of 500 mM NaCl in 10 mM Tris-HCl buffer pH 7.6 (elution buffer) using a flow rate of 5 mL/min and collecting fractions of 12 mL. Fractions

containing Dps-WT protein were dialysed overnight at 4 ºC against 10 mM Tris-HCl buffer pH 7.6 and further purified in a second purification step, after dialysis, centrifugation and filtration as previously described.

The second purification step was performed using a Resource Q column (6 mL, GE Healthcare Life Sciences) equilibrated with 10 mM Tris-HCl buffer pH 7.6. The protein-rich fraction was loaded onto the column with a flow rate of 4 mL/min and washed with the equilibration buffer. The elution of proteins was done with a discontinuous gradient as in the first chromatographic step. A flow rate of 1 mL/min was used and 2 mL fractions were collected.

Cellular fractionation and purification processes were assessed by SDS-PAGE. The final fractions were tested for catalase contamination, dialysed against 200 mM MOPS buffer pH 7.0, 200 mM NaCl, overnight at 4 ºC, and stored at -80 ºC.

3.2.3 Production and Purification of Dps-Q14E and Dps-Δ15 proteins variants

The overexpression vectors carrying the genes that codify for Dps-Q14E and Δ15 variants, pET-21c–Dps-Q14E and pET-21c–Dps-Δ15, respectively, were available in the group. The expression of both genes, *Dps-Q14E* and *Dps-Δ15*, was performed as described for the WT protein (Section 3.2.2). The purification procedure was also similar to the one described for the WT, with some modifications in the second chromatographic step. Elution and adsorbed proteins from the Resource Q column was achieved using a linear gradient for 45 min with the same buffer system, in the case of Dps-Q14E, and for 30 min for the Δ15 variant, at a flow rate of 4 mL/min and collecting 3 mL fractions.

Both pure protein fractions were tested for catalase contamination, dialysed against 200 mM MOPS buffer pH 7.0, 200 mM NaCl, overnight at 4 ºC, and stored at -80 ºC.

3.2.4 Production and Purification of Dps-T10C and Dps-F5C protein variants

3.2.4.1 Site-directed mutagenesis

Dps variants Dps-T10C and Dps-F5C were produced by site-directed mutagenesis using the NZYMutagenesis kit (NZYTech) following the manufacturer's protocol [160].

The oligonucleotide primers used to produce the point mutations were designed and analysed for optimization with the software Primer Premier 6.24 from PREMIER Biosoft. The primers were synthesized and purified by NZYTech (data sheets provided by NZYTech in Appendix A.4, Figure A.11 and Figure A.12). Both forward and reverse mutagenic primer sequences are shown in Table 3.1.

Table 3.1: Sequence of mutagenic primers for point mutations in Dps. Triplets coding for each mutation are underlined.

Dps Variant	Oligonucleotide Primer Forward (FF)	Oligonucleotide Primer Reverse (Rv)
Dps-T10C	5' – g aac ttt ata ggt ctc gac tgc gac aaa acc cag aag ctg g – 3'	5' – c cag ctt ctg ggt ttt gtc gca gtc gag acc tat aaa gtt c – 3'
Dps-F5C	5' – gat ata cat atg ggt aag aac tgt ata ggt ctc gac aca gac – 3'	5' – gtc tgt gtc gag acc tat aca gtt ctt acc cat atg tat atc – 3'

Site-directed mutagenesis relies on the polymerase chain reaction (PCR) for DNA amplification. Here, the PCR reaction mixture contains the reaction buffer (buffer optimized for the polymerase activity), the mixture of deoxyribonucleotides (dNTPs), the recombinant pET-21c–Dps-WT plasmid as double-stranded DNA template (dsDNA), the forward and reverse mutagenic primers and the NZYProof DNA polymerase. Tables 3.2 and 3.3 describe the PCR mixtures and the cycling parameters, respectively, in the mutagenesis. The PCR was performed in a thermocycler (Biometra, Invitrogen) and verified by agarose gel electrophoresis, followed by hydrolysis with 5 μL of *Dpn* I for 1 h at 37 ºC.

Table 3.2: Composition of the PCR mixtures (50 µL) for mutagenesis.

Component	Volume (µL)			
	Dps-T10C		Dps-F5C	
	60 ng	35 ng	60 ng	35 ng
Reaction buffer, 10x	5	5	5	5
dNTP mix	1	1	1	1
pET-21c–Dps-WT plasmid	3.02	1.76	3.02	1.76
Oligonucleotide primer FF	2.47	2.47	2.40	2.40
Oligonucleotide primer Rv	2.48	2.48	2.44	2.44
Milli-Q water	35.03	36.29	35.14	36.4
NZYProof DNA polymerase (2.5 U/µL)	1	1	1	1

[1] 60 ng and 35 ng of dsDNA template were used.

Table 3.3: PCR programme used in site-directed mutagenesis.

Segment	Description	Temperature (ºC)	Time (min)	Cycles
1	Initial denaturation	95	2	1
2	Denaturation	95	1	18
	Primers annealing	60	1	
	Extension	68	9	
3	Final extension	68	15	1

Dpn I hydrolysis products (7 µL) were used to transform ultracompetent *E. coli* cells, NZYStar (NZYTech), plated on LB/Agar medium plates containing 100 µg/mL ampicillin and incubated overnight at 37 ºC. Selected clones were analysed by DNA sequencing of plasmid DNA (sequenced by Eurofins Genomics).

3.2.4.2 Production and Purification

To optimize the overexpression conditions for both Dps-T10C and Dps-F5C variant proteins, expression tests were performed using *E. coli* BL21(DE3) (NZYTech) host

cells, analysing the effects of IPTG concentration, growth time of induction, and time after incubation. Table 3.4 shows the culture parameters considered for the expression tests, carried out at 37 ºC, at 200 rpm.

Table 3.4: Optimization of overexpression conditions.

	Optical density at 600 nm	**Concentration of IPTG (mM)**	**Incubation time after induction (h)**
LB medium	0.5	0.1	3
			16
		0.5	3
			16
		1	3
	2	0.5	3
			16

Protein expression profiles were evaluated by SDS-PAGE electrophoresis. Both proteins, Dps-T10C and Dps-F5C, were produced using the same protocol as the one used to produce the WT protein, with the following modifications.

The expression was induced by addition of 1 mM ITPG, and the culture was incubated at 37 ºC, at 200 rpm, for 3 h. After pelleting, cells were resuspended in 10 mM Tris-HCl buffer pH 7.6, 1 mM dithiothreitol (DTT). The soluble extract, collected after ultracentrifugation was dialysed overnight at 4 ºC against the same DTT-containing buffer.

For both Dps-T10C protein and Dps-F5C protein, the purification procedure was similar to the one described for the Dps-WT. In this case, however, all buffers used contained 1 mM DTT.

The efficiency of all experimental steps was assessed by SDS-PAGE. Pure protein fractions were dialysed overnight at 4 ºC against 50 mM MOPS buffer pH 7.0 containing 200 mM NaCl and 1 mM DTT, and stored at -80 ºC.

3.2.5 Spectroscopic and biochemical characterization of Dps protein and variants

3.2.5.1 Spectroscopic characterization

The UV-visible spectra of Dps-WT protein and variants were measured in an UV-visible Evolution 300 spectrophotometer (Thermo Scientific).

3.2.5.2 Biochemical characterization

Size exclusion chromatography was used to determine the molecular mass of Dps-WT and variants, Dps-Δ15, Dps-T10C and Dps-F5C.

The chromatography was performed by using a Superdex 200 10/300 GL (GE Healthcare, size exclusion of 10 – 600 kDa) equilibrated with 50 mM sodium phosphate buffer pH 7.0 containing 150 mM NaCl, and proteins used as markers were Blue Dextrane (2000 kDa), catalase (232 kDa), BSA (66 kDa), ovalbumin (44.3 kDa), carbonic anhydrase (29.4 kDa), and cytochrome c (13.2 kDa).

All protein samples were prepared identically in parallel. Each protein, 30 µL, (21.24 µM Dps-WT, 21.31 µM Dps-T10C and 21.26 µM Dps-F5C, respectively), was mixed with 3 µL of Blue Dextran (10 mg/mL) and 200 µL of 50 mM sodium phosphate buffer pH 7.0, 150 mM NaCl, and loaded onto the column. Samples were eluted with a flow rate of 0.4 mL/min. For Dps-Δ15, 150 µL of protein (21.02 µM) was mixed with 200 µL of 50 mM sodium phosphate buffer pH 7.0, 150 mM NaCl and loaded onto the column.

3.3 Results and discussion

3.3.1 Dps-WT

Dps-WT expression in *E. coli* BL21(DE) cells was performed in LB medium, where the cells were induced with 0.5 mM IPTG when an optical density at 600 nm of 0.5 was reached. An average cell yield of 2.6 g/L (wet weight) was obtained. The protein

expression profile and cell fractionation were analysed by SDS-PAGE. The resulting gel is shown in Figure 3.1.

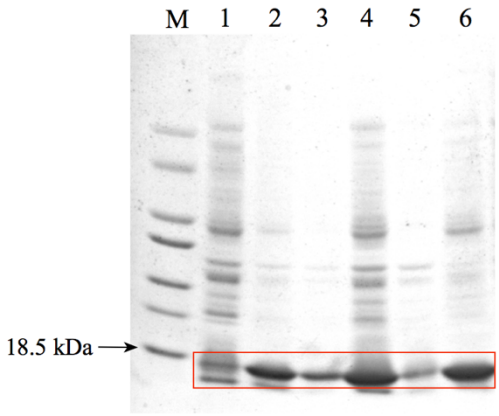

Figure 3.1: Dps-WT protein expression profile assessed by SDS-PAGE (8-12% acrylamide pre-cast gel). M – LMW Standard (NZYTech); 1 – Protein extract of the overexpression culture before induction; 2 – Protein extract after 3 h of induction with IPTG; 3 – Pellet from low-speed centrifugation; 4 – Supernatant from low-speed centrifugation; 5 – Pellet from ultracentrifugation; 6 – Supernatant from ultracentrifugation. The red box highlights the bands corresponding to Dps-WT. For comparison, samples on lanes 1 to 3 were normalized as described in Chapter2, Section 2.2.1.4.

The Dps-WT expression electrophoretic profile showed an intense band with an apparent molecular mass of 18.5 kDa, which is in agreement with the molecular mass of the Dps-WT monomer, deduced from the encoding gene [150], 18 kDa. More, the Dps-WT protein is mostly present in the soluble crude extract, which highlights the efficiency of the lysis and fractionation steps.

As determined by the ProtParam tool on the ExPASy Server [150], the isoelectric point (pI) of Dps-WT is 5.01. This is fairly acidic protein, prompted the use of anion exchange chromatography, as the main purification method. The soluble crude extract was thereby purified in two steps.

The first purification step was performed using a preparative anionic exchange column. Figure 3.2 shows the elution profile of Dps-WT and Figure 3.3 the SDS-PAGE gel prepared to evaluate the efficiency of the chromatographic separation.

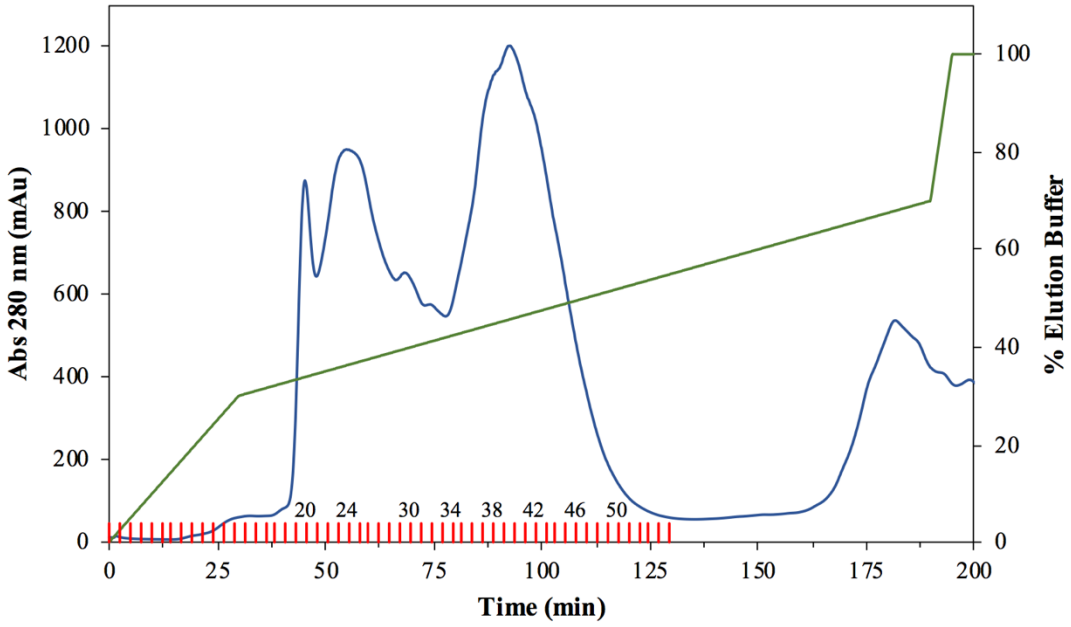

Figure 3.2: Elution profile of Dps-WT purification on DEAE Sepharose FF ion exchange chromatographic column. Protein elution was monitored at 280 nm (blue line) using a discontinuous gradient of elution buffer, 10 mM Tris-HCl buffer pH 7.6, 500 mM NaCl (green line). Eluted fractions of 12 mL are represented in red vertical bars.

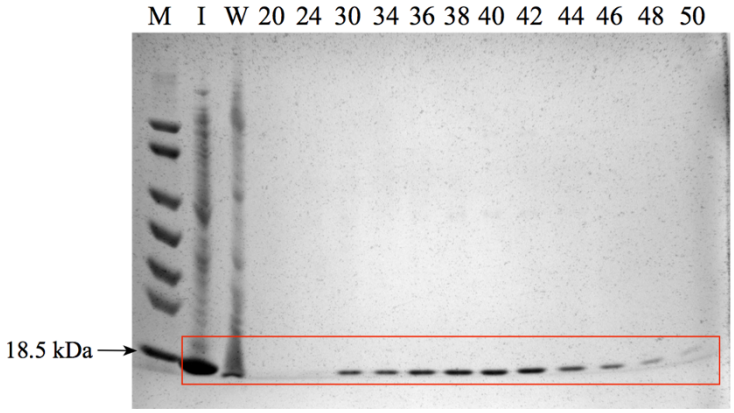

Figure 3.3: SDS-PAGE analysis of the first chromatographic step of Dps-WT purification (12% acrylamide pre-cast gel). M – LMW Standard (NZYTech); I – Soluble crude extract; W – Flow-through fraction. Numbers on top of the gel correspond to the number of eluted fractions. The red box highlights the bands corresponding to Dps-WT. 0.5 µL of each fraction was applied.

According to the chromatographic elution profile and the SDS-PAGE gel, Dps-WT protein is eluted between 200 mM and 260 mM NaCl, i.e. from 40% to 52% of elution buffer. Despite the apparent purity showed by SDS-PAGE, the fractions were tested for

the presence of catalase. Since catalase test revealed positive for all fractions, a second purification step was performed. In this case, a Resource Q column, prepacked with Source 15Q, a strong anionic exchanger for high resolution polishing purification of the protein was chosen.

Figure 3.4 shows the chromatogram of the second step of Dps-WT protein purification. Dps-WT protein elution occurred between 240 mM and 355 mM of NaCl. The purity of the eluted fractions was assessed by SDS-PAGE, as shown in Figure 3.5.

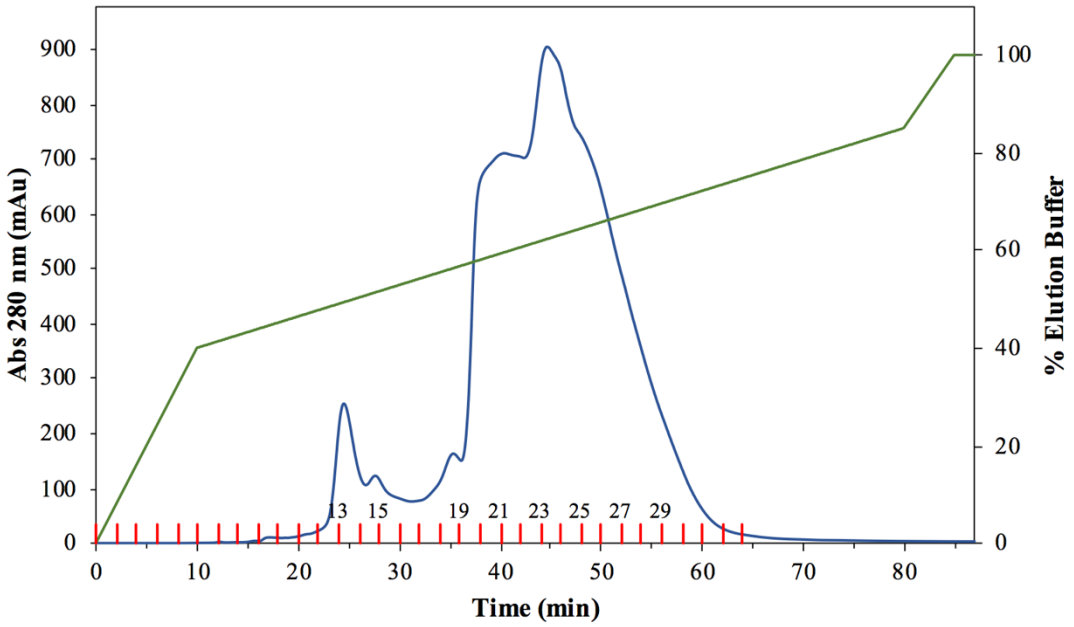

Figure 3.4: Elution profile of Dps-WT of Resource Q ion exchange chromatographic step. The blue line corresponds to the Dps-WT elution monitored at 280 nm, the green line corresponds to the gradient with 10 mM Tris-HCl buffer pH 7.6, 500 mM NaCl, and the red vertical bars represent the 2 mL fractions collected from the column.

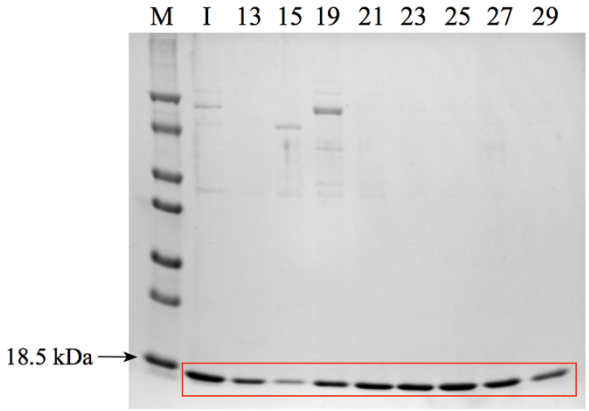

Figure 3.5: Analysis of Dps-WT purification in the Resource Q ion exchange column by SDS-PAGE (12% acrylamide pre-cast gel). M – LMW Standard (NZYTech); I – Fraction loaded onto the column; Numbers on top of the gel correspond to the fractions collected on this chromatographic step. The red box highlights the bands corresponding to the Dps-WT. 2 µL of each fraction was applied.

Fractions were pooled together based on the SDS-PAGE gel (Figure 3.5) and on the catalase test results, as a fraction deprived of catalase (pure protein) and as a fraction containing residual amounts of catalase. It is important that catalase is not a contamination in protein preparations since the co-substrate of Dps is hydrogen peroxide, which would be rapidly consumed by catalase due to its high turnover number [161]. Pure protein fraction was obtained with a yield of 37.2 mg/L (mg of protein per litre of cell culture) and used for the following studies described in this thesis.

3.3.2 Dps-Q14E

Dps-Q14E protein was produced using the same procedure described for Dps-WT protein. *E. coli* BL21(DE3) harbouring the overexpression vector that carried the gene of interest, has grown to a final yield of 3.5 g/L (wet weight). The overexpression kinetic profile and fractionation process (described in Section 3.2.3) were analysed by SDS-PAGE. The resulting gel is shown in Figure 3.6.

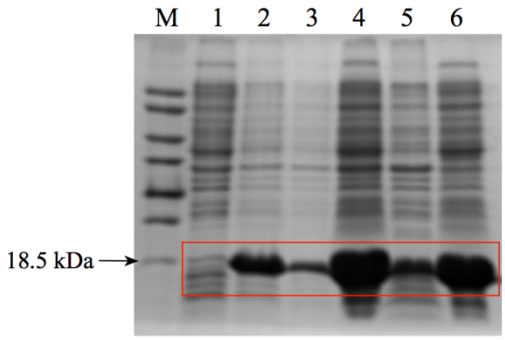

Figure 3.6: Dps-Q14E expression assessed by SDS-PAGE (12.5% acrylamide). M – LMW Standard; 1 – Protein extract of the overexpression culture before induction; 2 – Protein extract after 3 h of induction with IPTG; 3 – Pellet from low-speed centrifugation; 4 – Supernatant from low-speed centrifugation; 5 – Pellet from ultracentrifugation; 6 – Supernatant from ultracentrifugation. The red box highlights the bands corresponding to Dps-Q14E. For comparison, samples on lanes 1 to 3 were normalized as described in Chapter2, Section 2.2.1.4.

The Dps-Q14E expression electrophoretic profile showed an intense band corresponding to the protein monomer with an apparent molecular mass at around 18.5 kDa. As with WT protein, Dps-Q14E protein is mostly present in the soluble fraction.

As determined by the ProtParam tool on the ExPASy Server [150], the pI value of this variant is 4.93. Comparing with the wild-type protein, a slight decreasing of the pI was expected, since an amino acid with uncharged polar side chain (glutamine) was mutated to an amino acid with negative charged polar side chain (glutamic acid).

Purification using a DEAE ion exchange chromatography was performed as described for the Dps-WT protein. Figure 3.7 shows the elution profile obtained using a flow rate of 5 mL/min with 10 mM Tris-HCl buffer pH 7.6, 500 mM NaCl as the elution buffer.

Eluted fractions were analysed by SDS-PAGE electrophoresis (Figure 3.8) and tested for the presence of catalase.

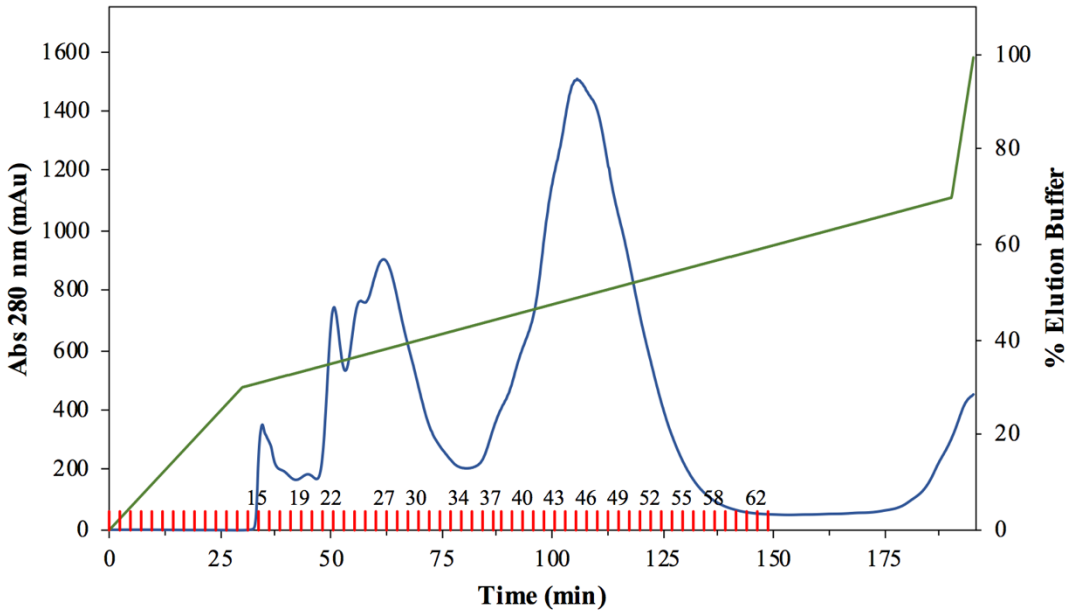

Figure 3.7: Elution profile of Dps-Q14E by DEAE ion exchange chromatography (first purification step). The blue line represents the absorption at 280 nm of eluted proteins, the green line corresponds to the gradient elution with 10 mM Tris-HCl buffer pH 7.6, 500 mM NaCl, and the red vertical bars represent the collected fractions containing 12 mL of eluted protein.

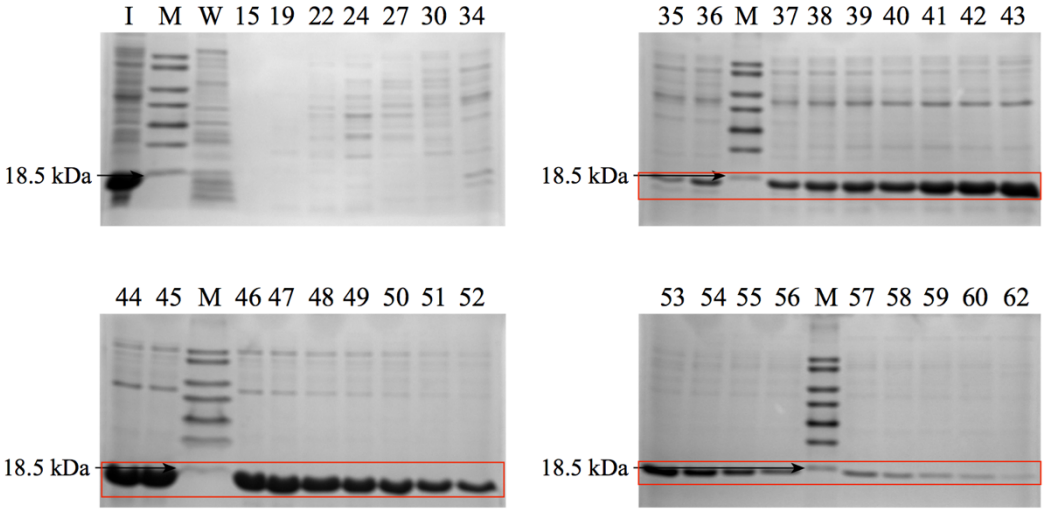

Figure 3.8: Analysis of the purity of fractions eluted from DEAE column used to purify Dps-Q14E by SDS-PAGE (12.5% acrylamide). I – Soluble crude extract; M – LMW Standard; W – Flow-through fraction; The numbers on top of each gel correspond to the number of eluted fractions. The red boxes highlight the bands which correspond to the Dps-Q14E. 4 µL of each fraction was applied.

The analysis of both, the chromatographic elution profile and the electrophoretic profile of Dps-Q14E, indicates that the protein is eluted between 220 mM and 290 mM of NaCl. Two fractions were pooled together, one containing the fractions 37 to 49 and 57 to 60, denominated Fraction I, and a second, Fraction II, containing fractions 50 to 56. Fraction II was stored at -80 ºC, while Fraction I was concentrated using a Vivacell 70 concentrator (Sartorius) and dialysed against 10 mM Tris-HCl buffer pH 7.6.

Fraction I was further purified by anion exchange chromatography, using a Resource Q column. The chromatogram is represented in Figure 3.9. Collected fractions were analysed by SDS-PAGE (Figure 3.10).

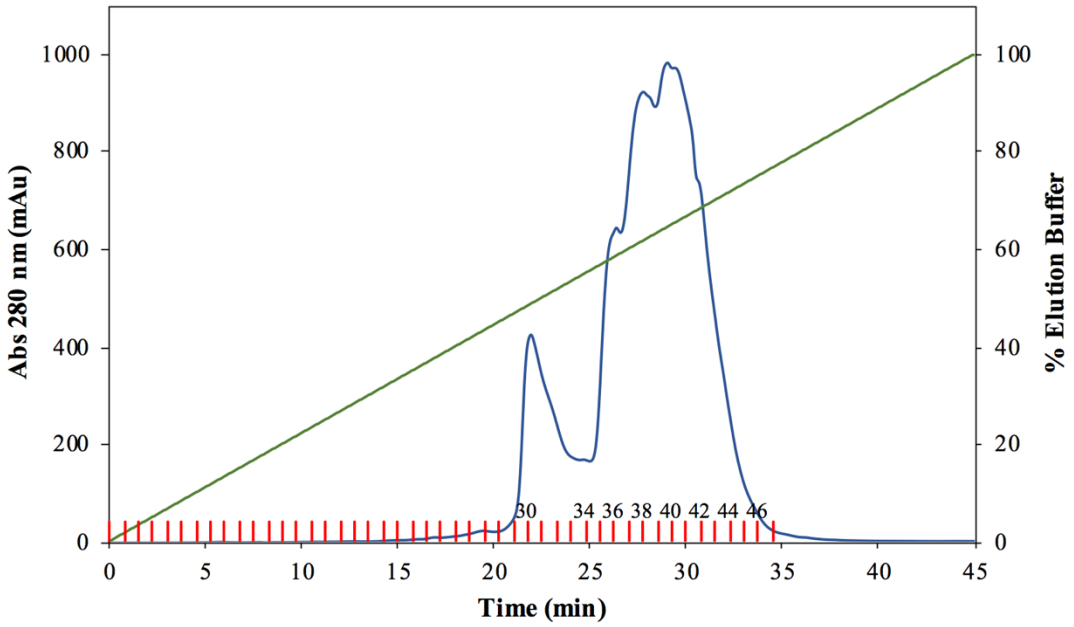

Figure 3.9: Elution profile of the second purification step of Dps-Q14E in Resource Q column. The blue line represents the absorption at 280 nm, the green line corresponds to the gradient elution with 10 mM Tris-HCl buffer pH 7.6, 500 mM NaCl, and the red vertical bars represent the collected fractions containing 3 mL of eluted protein.

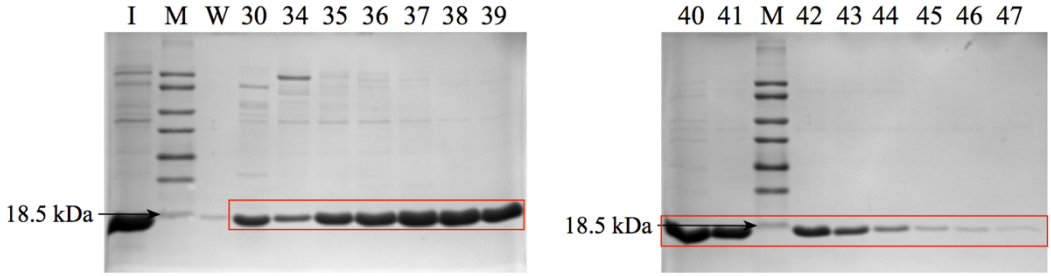

Figure 3.10: SDS-PAGE analysis of the eluted fractions from the Resource Q column for Dps-Q14E purification (12.5% acrylamide). I – Fraction loaded onto the column; M – LMW Standard; W – Flow-through fraction; The numbers on top of each gel correspond to the number of collected fractions. The red boxes highlight the bands which correspond to the Dps-Q14E. 4 µL of each fraction was applied.

In this second purification step, elution of Dps-Q14E occurred between 245 mM and 320 mM of NaCl. Based on the elution and electrophoretic profiles, fractions 35 to 43 were pooled together in one fraction, that revealed no presence of catalase, and thus considered pure. The variant protein was obtained with a yield of 112.9 mg/L (mg of protein per litre of cell culture). Pure protein was subsequently used for DNA binding studies.

3.3.3 Dps-Δ15

Dps-Δ15 protein was expressed in *E. coli* BL21(DE) using the protocol described for Dps-WT (Section 3.2.2), yielding a cell wet weight of 3.8 g /L.

Figure 3.11 shows the SDS-PAGE analysis of the expression level of the protein, as well as the protein content of soluble and membrane fractions from cell fractionation. Due to the lack of 15 amino acids residues at the N-terminal, the molecular mass of variant Dps-Δ15, deduced from the DNA sequence [150], is 16.4 kDa. Accordingly, the gel present in Figure 3.11 shows an intense band below 18.5 kDa which corresponds to the overexpressed protein, predominant in the soluble fractions (lanes 4 and 6).

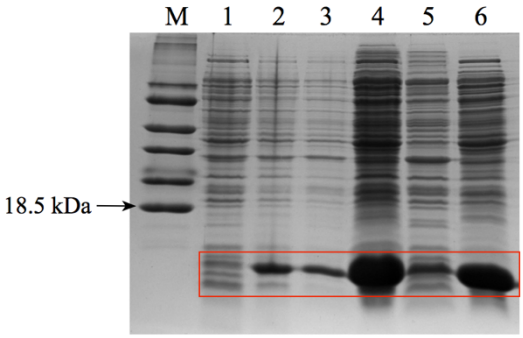

Figure 3.11: Dps-Δ15 expression profile assessed by SDS-PAGE (12.5% acrylamide). M – LMW Standard; 1 – Protein extract of the overexpression culture before induction; 2 – Protein extract after 3 h of induction with IPTG; 3 – Pellet from low-speed centrifugation; 4 – Supernatant from low-speed centrifugation; 5 – Pellet from ultracentrifugation; 6 – Supernatant from ultracentrifugation. The red box highlights the bands which correspond to the Dps-Δ15 protein. For comparison, samples on lanes 1 to 3 were normalized as described in Chapter2, Section 2.2.1.4.

With a pI of 4.88, this variant was purified by ion exchange chromatography at pH 7.6, adopting the strategy used for other Dps proteins.

Purification efficiency was judged based on the elution profile (Figure 3.12) and by SDS-PAGE (Figure 3.13).

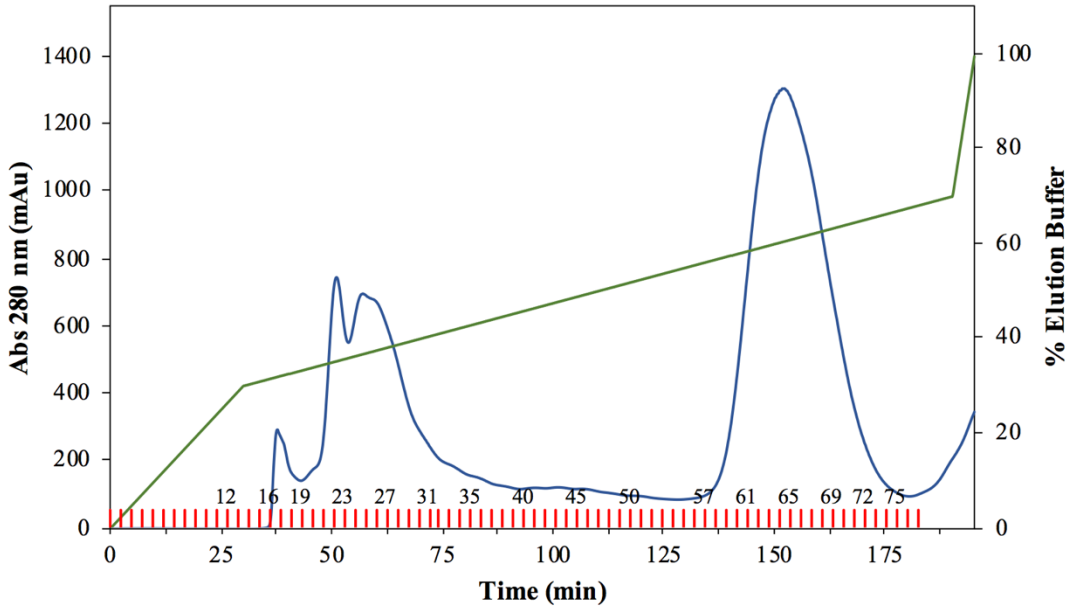

Figure 3.12: Elution profile of DEAE Sepharose ion exchange chromatography on the purification of Dps-Δ15 protein. The blue line represents the absorption at 280 nm, the green line

corresponds to the gradient elution with 10 mM Tris-HCl buffer pH 7.6, 500 mM NaCl, and the red vertical bars represent the 12 mL fractions collected from the column.

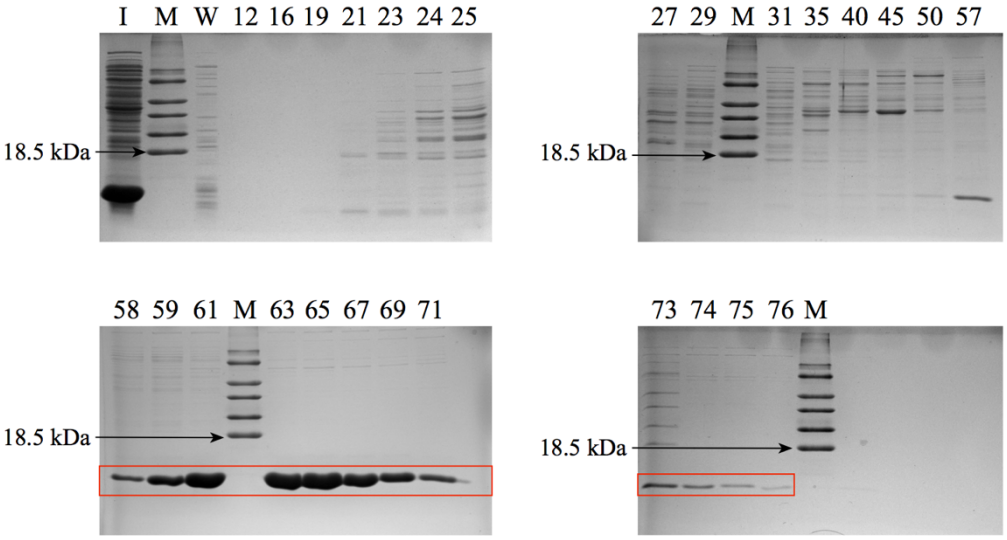

Figure 3.13: SDS-PAGE analyses of DEAE Sepharose ion exchange chromatography separation on the purification of Dps-Δ15 protein (12.5% acrylamide). I – Soluble crude extract; M – LMW Standard; W – Flow-through fraction; The numbers on top of each gel correspond to the number of fractions eluted from the column. Red boxes highlight the bands which correspond to the Dps-Δ15. 5 µL of each fraction was applied.

Dps-Δ15 was eluted between 280 mM and 335 mM of NaCl. By analysing the SDS-PAGE electrophoresis results, two final fractions were obtained, one by pooling fractions 57 to 61 (Fraction I), and a second containing fractions 62 to 76 (Fraction II). Fraction I was stored at -80 ºC, while Fraction II was applied on a second "polish" column chromatography, after concentration and dialysis (Figure 3.14).

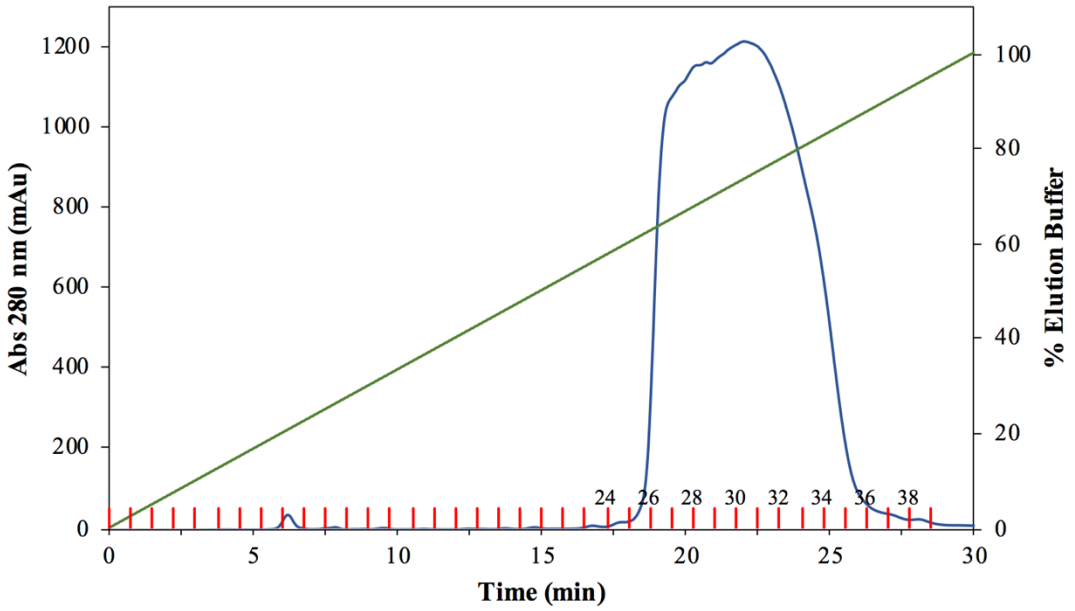

Figure 3.14: Elution profile of Resource Q ion exchange chromatography to further purify Dps-Δ15. Detection of eluted proteins was done at 280 nm (blue line), the green line corresponds to the gradient elution buffer (10 mM Tris-HCl buffer pH 7.6, 500 mM NaCl), and the red vertical bars represent the eluted protein fractions (3 mL).

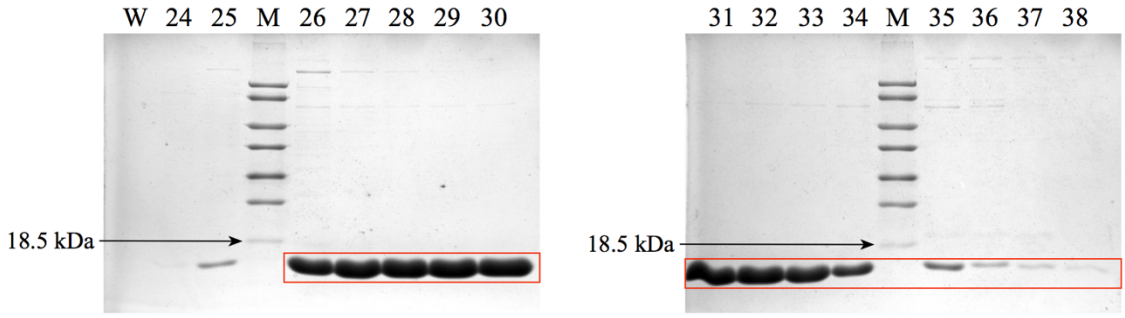

Figure 3.15: SDS-PAGE (12.5% acrylamide) analyses of the second purification step of Dps-Δ15 on a Resource Q column. W – Flow-through fraction; M – LMW Standard; Numbers on top of each gel correspond to the number of eluted fractions. The red boxes highlight the bands which correspond to the Dps-Δ15. 5 µL of each fraction was applied.

Dps-Δ15 protein was judged pure (fractions 26 to 34) according with the chromatogram, SDS-PAGE gel (Figure 3.15) and catalase test, that revealed no presence of catalase.

A purification yield of 77.97 mg/L of final pure Dps-Δ15 protein in 200 mM MOPS buffer pH 7.0, 200 mM NaCl was obtained. Similarly to the the Dps-Q14E, this protein preparation was used for DNA binding studies.

3.3.4 Site-directed mutagenesis

Dps-T10C and Dps-F5C variants were designed with the aim of performing structural and DNA binding studies. These point variants were obtained by site-directed mutagenesis [162], using the pET-21c–Dps-WT expression plasmid as template.

Point mutations were made in the nucleotide triplets coding for threonine 10 (Dps-T10C) and for phenylalanine 5 (Dps-F5C), that were replaced by cysteine residues, since these amino acids are within the N-terminal region which mediate the binding to DNA (described in Chapter 5). Moreover, the replacement of these amino acids by cysteines are not expected to affect the protein structure and possibly the binding.

After performing site-directed mutagenesis, selected DNA clones were sent for sequencing to confirm the mutation. Figure 3.16 shows the multiple alignment of Dps-WT and variant amino acid sequences translated from DNA coding sequences as determined by the Sanger method. The single point mutations were successfully introduced and importantly, no additional random mutations were produced. Therefore, these clones were used to produce and purify both Dps-T10C and Dps-F5C.

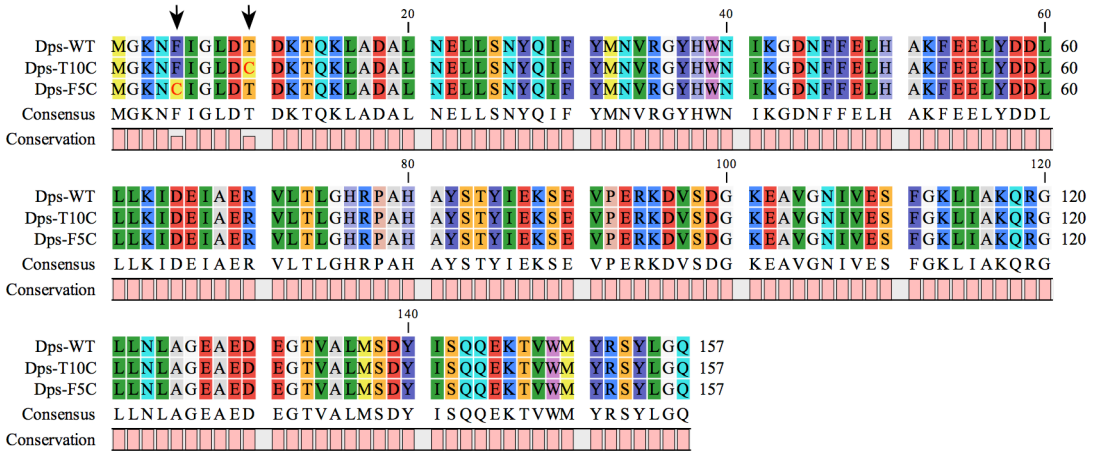

Figure 3.16: Multiple sequence alignment of Dps-WT from *M. hydrocarbonoclasticus 617* with

Dps-T10C and Dps-F5C obtained by site-directed mutagenesis. The multiple sequence alignment was generated with CLC Sequence Viewer 7.8.1 (https://www.qiagenbioinformatics.com/); the black arrows indicate the mutated amino acid residues.

3.3.5 Dps-T10C

To tune the expression of Dps-T10C protein in the soluble form in *E. coli* Bl21(DE3) cells, various expression parameters were tested in small-scale. The post-induction time courses of protein expression were analysed by SDS-PAGE as is shown in Figure 3.17.

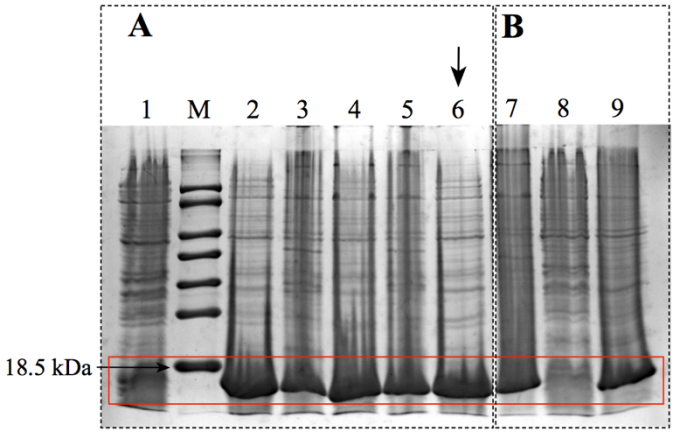

Figure 3.17: SDS-PAGE analysis of Dps-T10C protein expression in *E. coli* BL21(DE3) cells in LB medium (12.5% acrylamide). (A) Protein expression induced at $OD_{600\ nm}$ = 0.5 with 0.5 mM IPTG, *t* = 0 h, 3 h and 16 h, respectively (lanes 1 to 3); 0.1 mM IPTG, *t* = 3 h and *t* = 16 h (lanes 4 and 5); 1.0 mM IPTG, *t* = 3 h (lane 6); M – LMW Standard. (B) Protein expression induced at $OD_{600\ nm}$ = 2.0 with 0.5 mM IPTG, *t* = 16 h, 0 h and 3 h, respectively (lanes 7 to 9). The red box highlights the bands corresponding to the Dps-T10C and the black arrow indicates the selected optimal expression condition. For comparison, samples were normalized as described in Chapter2, Section 2.2.1.4.

Based on results presented in Figure 3.17, it was possible to observe that when an addition of IPTG was done at a high optical density ($OD_{600\ nm}$ of 2.0) less protein was expressed (lanes 7 and 9), when compared with the ones induced at an optical density of 0.5. However, for an optical density of 0.5 (lanes 1 to 6), the expression appeared to be more significant for the condition where cells were induced with 1 mM IPTG for 3 h.

Therefore, Dps-T10C protein expression in *E. coli* BL21(DE3) cells was performed by addition of 1 mM IPTG when cell density was around 0.5, in LB medium at 37 ºC, at 200 rpm. The cells were grown for 3 h and harvested, yielding 3 g/L of culture (wet weight).

The SDS-PAGE obtained after lysis and fractionation of cells is shown in Figure 3.18.

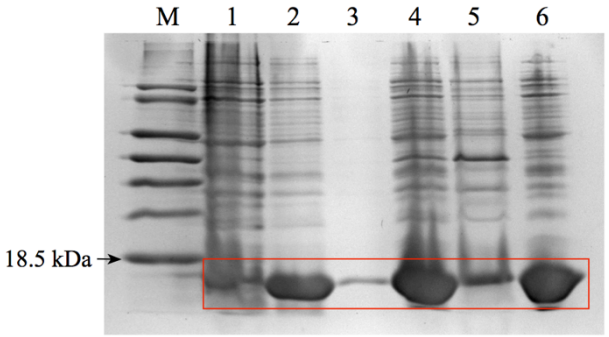

Figure 3.18: Production of recombinant Dps-T10C assessed by SDS-PAGE (12.5% acrylamide). M – LMW Standard; 1 – Protein profile before induction; 2 – Protein extract after 3 h of induction with IPTG; 3 – Pellet from low-speed centrifugation; 4 – Supernatant from low-speed centrifugation; 5 – Pellet from ultracentrifugation; 6 – Supernatant from ultracentrifugation. The red box highlights the bands corresponding to the Dps-T10C protein. For comparison, samples on lanes 1 to 3 were normalized as described in Chapter2, Section 2.2.1.4.

As with the Dps proteins, wild-type and variants, described before, Figure 3.18 shows a very high yield of Dps-T10C expression profile, mostly in the soluble form (lane 6).

Dps-T10C was also purified following the protocol described before, by two consecutive steps using anion exchange chromatography, at pH 7.6. The pI of Dps-T10C is 5.01, as determined by the ProtParam tool on the ExPASy Server [150], which is, as expected, identical to the wild-type protein since both threonine and cysteine have uncharged side chains, which would not contribute to the global charge.

To prevent formation of random intramolecular and intermolecular disulphide bonds between cysteine residues, 1 mM DTT was added to all buffers. Protein elution profile of the first chromatography on DEAE Sepharose column is shown in Figure 3.19, and purification efficiency was evaluated by SDS-PAGE (Figure 3.20).

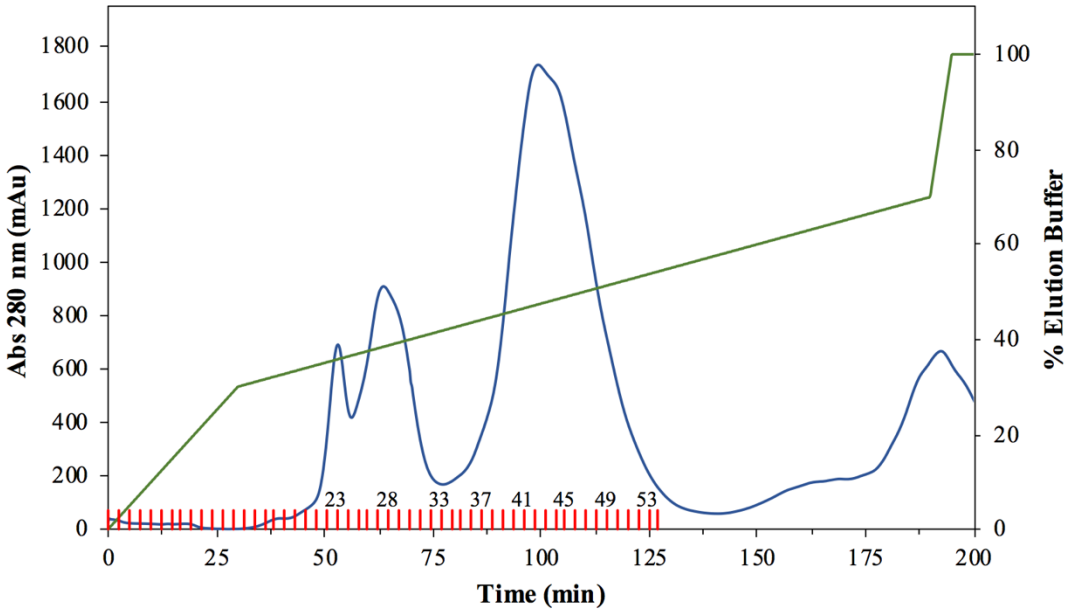

Figure 3.19: Elution profile of Dps-T10C protein by DEAE Sepharose chromatography. The blue line represents the absorption at 280 nm, the green line corresponds to the gradient elution buffer (10 mM Tris-HCl buffer pH 7.6, 1 mM DTT, 500 mM NaCl), and the red vertical bars the fractions collected (12 mL per fraction).

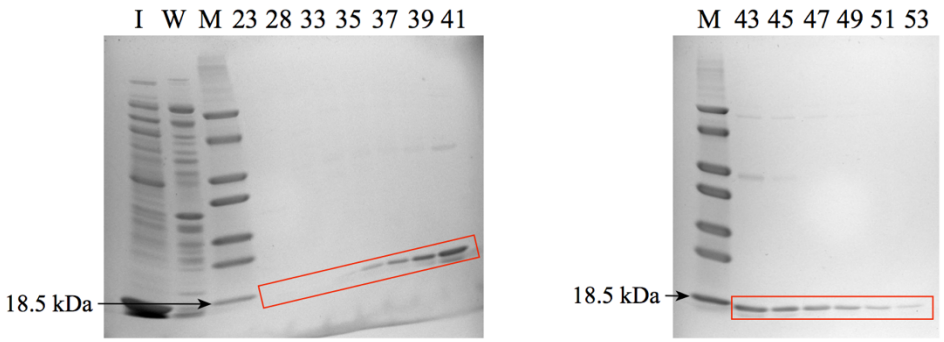

Figure 3.20: SDS-PAGE analysis of purified Dps-T10C on DEAE Sepharose chromatography (12% acrylamide pre-cast gel). I – Soluble crude extract loaded onto the column; W – Flow-through fraction; M – LMW Standard. The numbers on top of gels correspond to the number of eluted fractions. The red boxes highlight the bands which correspond to Dps-T10C. 0.5 µL of each fraction was applied.

Analysis of the protein elution profile and the corresponding electrophoretic profile indicated that Dps-T10C was eluted between 42% and 54% of elution buffer, i.e. between 210 mM and 270 mM of NaCl. Catalase was present in all eluted fractions as judged by the catalase test. Hence, a second purification step with a Resource Q ion exchange

column was performed to polish the Dps-T10C enriched fraction. The resulting chromatogram is represented in Figure 3.21, that shows the elution of the target protein between 280 mM and 355 mM of NaCl. The purity of fractions collected in this separation step was evaluated by SDS-PAGE (Figure 3.22). Fractions were pooled together according to their purity and presence of catalase. As a final step, the Dps-T10C pure protein was dialysed against 50 mM MOPS buffer pH 7.0, 200 mM NaCl, 1 mM DTT. This protein preparation was obtained with a yield of 40.6 mg of pure protein per litre of culture.

Dps-T10C was used for structural and DNA binding studies using the electron paramagnetic resonance spectroscopy (EPR spectroscopy).

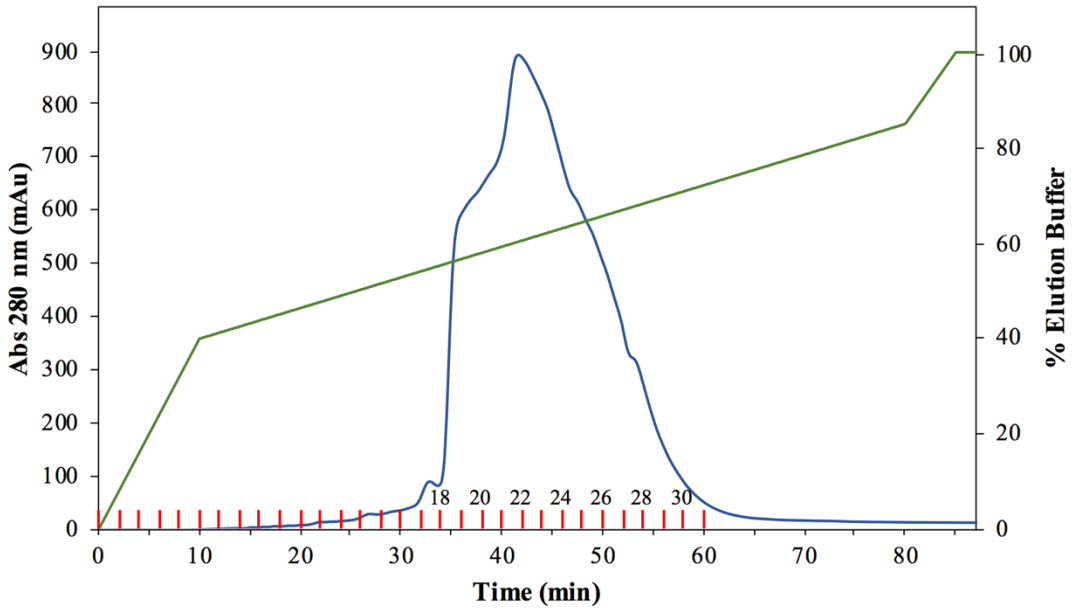

Figure 3.21: Elution profile of Dps-T10C protein second purification step on a Resource Q ion exchange chromatography. The blue line represents the absorption at 280 nm, the green line corresponds to the gradient elution buffer (10 mM Tris-HCl buffer pH 7.6, 1 mM DTT, 500 mM NaCl), and the red vertical bars represent the eluted protein fractions (2 mL).

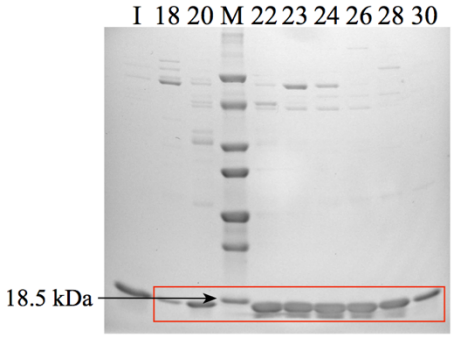

Figure 3.22: SDS-PAGE (12% acrylamide pre-cast gel) analysis of Dps-T10C eluted fractions from the Resource Q ion exchange chromatography. I – Loaded fraction collected from the first separation step; M – LMW Standard. Numbers on top of the gel correspond to the number of collected fractions. The red box highlights the bands corresponding to the Dps-T10C. 5 µL of each fraction was applied.

3.3.6 Dps-F5C

Small-scale tests were performed to choose the optimal conditions for production of Dps-F5C in *E. coli* BL21(DE3) cells. Expression tests, in LB medium at 37 ºC, at 200 rpm were performed as described for Dps-T10C, varying the concentration of IPTG (0.1 mM, 0.5 mM and 1 mM), the incubation time after induction and growth time for protein induction (0.5 and 2.0).

Figure 3.23 shows the electrophoretic profile of cell suspensions collected during growth for each expression test.

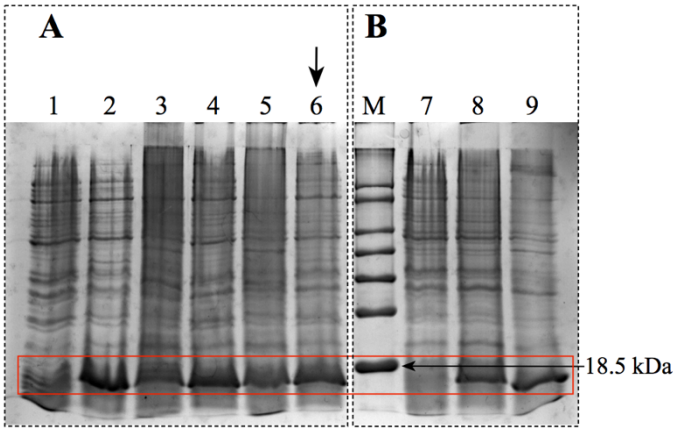

Figure 3.23: SDS-PAGE analysis of Dps-F5C in *E. coli* BL21(DE3) cells in LB medium, 37 ºC (12.5% acrylamide). (A) Protein expression induced at $OD_{600\ nm}$ = 0.5 with 0.5 mM IPTG, t = 0 h, 3 h, and 16 h, respectively (lanes 1 to 3); 0.1 mM IPTG, t = 3 h and t = 16 h (lanes 4 and 5);

1 mM IPTG, t = 3 h (lane 6). (B) Protein expression induced at $OD_{600\,nm}$ = 2.0 with 0.5 mM IPTG, t = 0h, 3 h and 16 h, respectively (lanes 7 to 9); M – LMW Standard. The red box highlights the bands corresponding to the Dps-F5C and the black arrow indicates the selected optimal expression conditions. For comparison, samples were normalized as described in Chapter2, Section 2.2.1.4.

Based on the SDS-PAGE gel shown in Figure 3.23, expression of the protein seemed to be higher when induced with 1 mM IPTG for 3 h (lane 6), in cultures with an optical density of 0.5.

Thus, Dps-F5C expression in *E. coli* BL21(DE3) cells, in LB medium at 37 ºC, and 200 rpm, with 1 mM IPTG, when the optical density at 600 nm of the culture was 2.0, resulted in cell yield of 3.5 g/L (wet weight).

The soluble crude extract prepared as described in Section 3.2.4.2, was analysed by SDS-PAGE (Figure 3.24) showing an intensive band with an apparent molecular mass around 18.5 kDa.

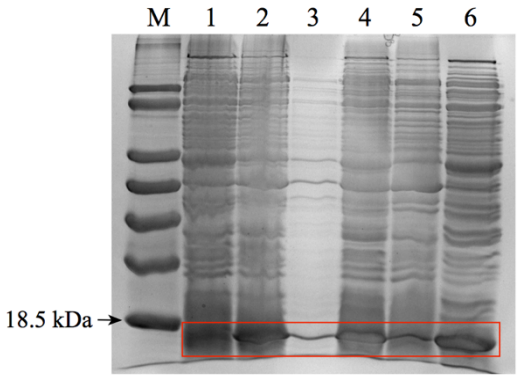

Figure 3.24: Dps-F5C expression profile assessed by SDS-PAGE (12.5% acrylamide). M – LMW Standard; 1 – Protein extract of the overexpressed culture before induction; 2 – Protein extract after 3 h of induction with 1 mM IPTG; 3 – Pellet from low-speed centrifugation; 4 – Supernatant from low-speed centrifugation; 5 – Pellet from ultracentrifugation; 6 – Supernatant from ultracentrifugation. The red box highlights the bands corresponding to the Dps-F5C protein. For comparison, samples on lanes 1 to 3 were normalized as described in Chapter2, Section 2.2.1.4.

Purification of Dps-F5C following the protocol described for the Dps-T10C variant (pI of Dps-F5C determined by the ProtParam tool on the ExPASy Server [150] is 5.01)

involved a first purification step on a DEAE Sepharose chromatography column (Figure 3.25).

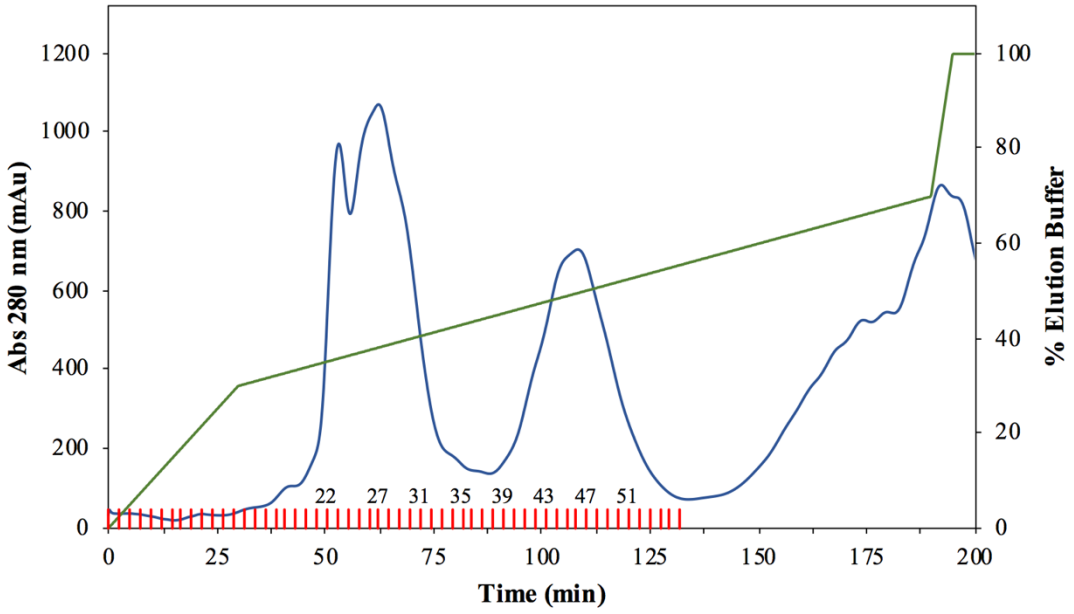

Figure 3.25: Purification of Dps-F5C on a DEAE Sepharose chromatography. The blue line represents the absorption at 280 nm; the green line corresponds to the gradient elution buffer (10 mM Tris-HCl buffer pH 7.6, 1 mM DTT, 500 mM NaCl), and the red vertical bars represent the fractions collected (12 mL/fraction).

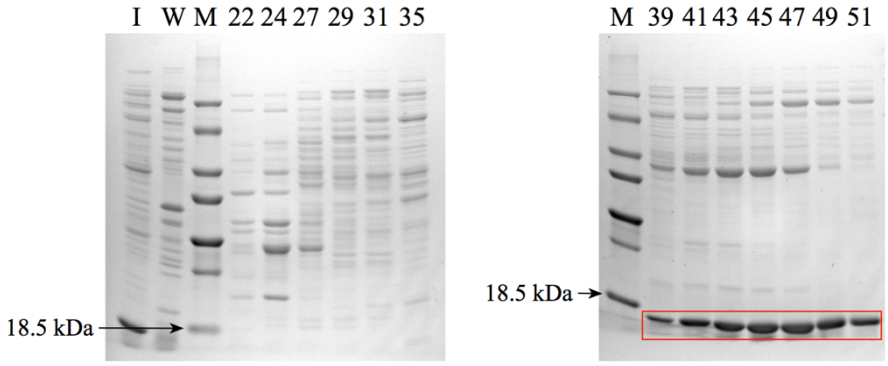

Figure 3.26: SDS-PAGE analysis of purified Dps-F5C on a DEAE Sepharose chromatography column (12% acrylamide pre-cast gel). I – Soluble crude extract loaded onto the column; W – Flow-through fraction; M – LMW Standard; Numbers on top of each gel correspond to the number of eluted fractions. The red box highlights the bands corresponding to Dps-F5C. 5 µL of each fraction was applied.

After analysis of the purity of fractions collected from the first chromatography, by SDS-PAGE (Figure 3.26), that allowed to conclude that the protein was eluted between 225 mM and 270 mM of NaCl. Fractions were pooled together in two fractions, Fraction I (fractions 39 to 48) and II (from 49 to 54), according to their purity degree.

Fraction I was further purified using a Resource Q column. The elution profile is shown in Figure 3.27; purity analysis by SDS-PAGE is presented in Figure 3.28.

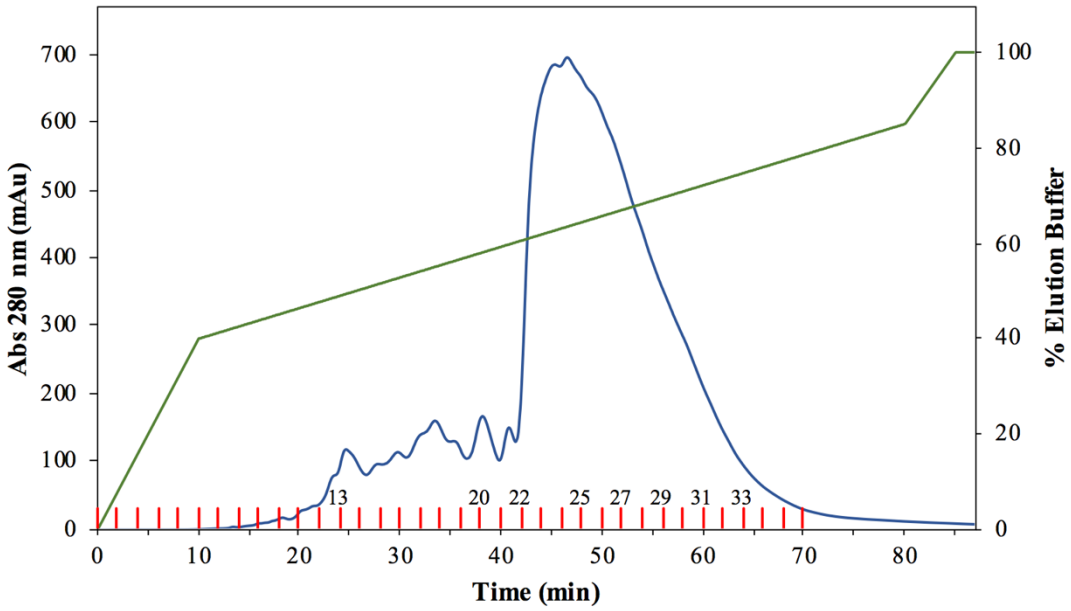

Figure 3.27: Second chromatography on a Resource Q column of Dps-F5C protein. The blue line represents the absorption at 280 nm; the green line corresponds to the elution gradient at a flow rate of 1 mL/min (10 mM Tris-HCl buffer pH 7.6, 1 mM DTT, 500 mM NaCl), and the red vertical bars represent the fractions collected from the column (2 mL each).

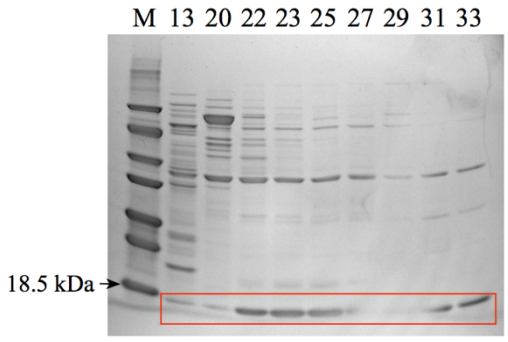

Figure 3.28: SDS-PAGE analysis of the Dps-F5C second purification step on a Resource Q

column (12% acrylamide pre-cast gel). M – LMW Standard. The numbers on top of the gel correspond to the collected fractions. Red box highlights the bands corresponding to the Dps-F5C. 5 µL of each fraction was applied.

In this case, Dps-F5C protein was eluted between 310 mM and 375 mM of NaCl. Based on the SDS-PAGE gel and the results of the catalase test, fractions 23 to 33 were pooled together. In this way, 20.17 mg of protein per litre of culture was obtained.

Similarly, to Dps-T10C protein, the Dps-F5C protein was dialysed against 50 mM MOPS buffer pH 7.0, 200 mM NaCl, 1 mM DTT for later use in EPR spectroscopy studies.

3.3.7 Spectroscopic and biochemical characterization of Dps protein and variants

The UV-visible spectra of all pure protein preparations, wild-type and variants, were collected and are represented in Figure 3.29. In all cases, a single band at 280 nm attributed to the apo-form was observed, as described by Guilherme M. [159]. This behaviour was observed in all protein preparations produced in this work.

Guilherme M., reported the presence of 0.07 to 0.17 iron atoms per protein when the apo-protein is grown in rich medium. From all protein preparations, only Dps-F5C showed a broad absorption in the range of 300 and 350 nm, indicating the presence of iron.

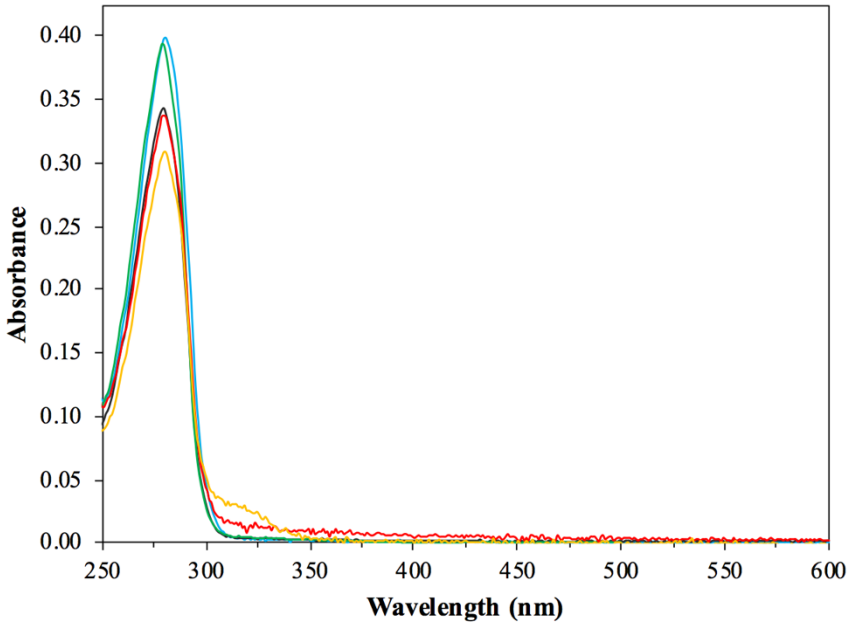

Figure 3.29: UV-visible spectra for all Dps proteins produced. UV-visible spectra of Dps-WT (blue line), Dps-Q14E (black line), Dps-Δ15 (green line), Dps-T10C (red line) and Dps-F5C (yellow line) in 200 mM MOPS buffer pH 7.0, 200 mM NaCl (and 1 mM DTT in the case of T10C and F5C variants). The proteins vary between 1.05 mM and 1.36 mM.

To verify the oligomeric state of all proteins, a size exclusion chromatography (SEC) was performed using a Superdex 200 10/300 GL (GE Healthcare), with a size exclusion between 10 kDa and 600 kDa for globular proteins, in 50 mM sodium phosphate buffer pH 7.0, 150 mM NaCl.

All proteins were loaded into the column with Blue Dextran, and eluted with a flow rate of 0.4 mL/min.

The void volume of the column was determined by the elution volume of Blue Dextran (2000 kDa) allowing the construction of a calibration curve. Figure 3.30 shows the overlapping of chromatographic profiles and the calibration curve used to calculate the molecular masses of all protein preparations studied in this work.

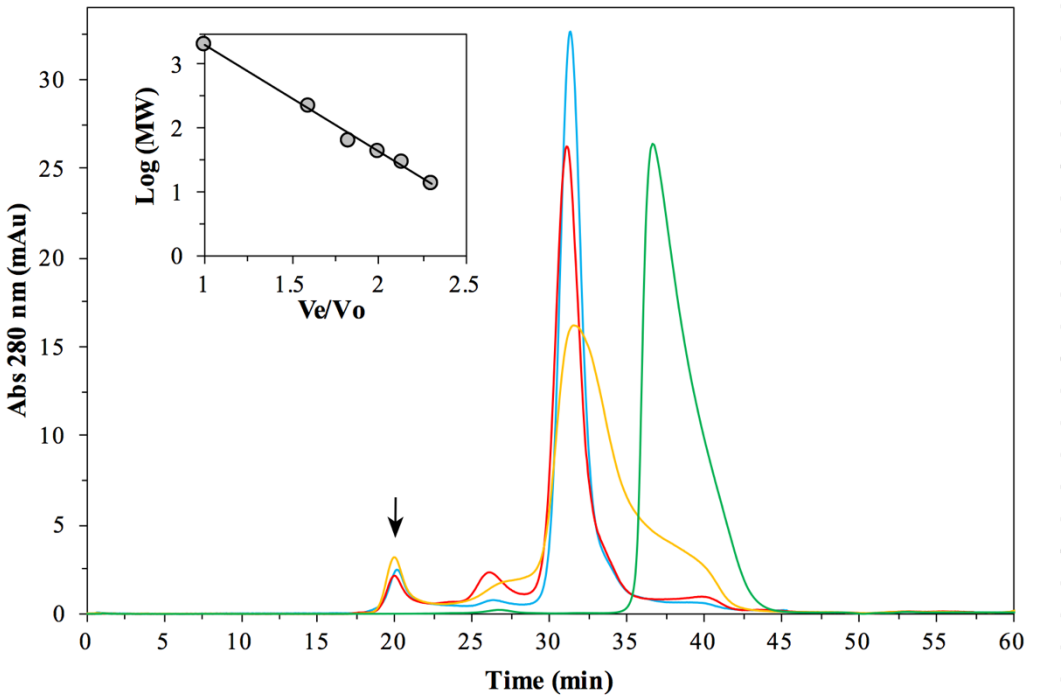

Figure 3.30: Molecular mass determination of Dps protein by SEC using Superdex 200 10/300 GL in 50 mM sodium phosphate buffer pH 7.0, 150 mM NaCl. Dps-WT in blue, Dps-Δ15 in green, Dps-T10C in red, and Dps-F5C in yellow. The black arrow indicates the elution of Blue Dextran, which was mixed with each protein. Flow rate of 0.4 mL/min was used. In inset is represented the calibration curve, where the trend line equation is Log (MW) = -1.675×Ve/Vo + 4.969 (R^2 = 0.9951).

For Dps-WT dodecamer the molecular mass determined using the calibration curve is 202 kDa, which is in agreement with the one reported by Guilherme M. (199 ± 2 kDa) [159]. The apparent molecular mass of Dps-T10C and Dps-F5C proteins is 209 kDa and 192 kDa, respectively, while the Dps-Δ15 has a molecular mass of 71 kDa. The molecular mass deduced from the DNA sequence for Dps-Δ15 was 196.8 kDa [150], which is much higher than the one determined here.

The asymmetric peak observed for Dps-Δ15 (green line in Figure 3.30) and Dps-F5C (yellow line in Figure 3.30), can be an explanation for the differences found in the molecular masses. The asymmetry can be the result of the change of the globular form of the protein as a consequence of an effect on the hydrodynamic radius. This could be due to the lack of the N-terminal region and the modified cysteine at the N-terminal, respectively. Varying the protein shape can change the retention time of the protein [163].

4

Ferroxidase activity of Dps protein from *Marinobacter hydrocarbonoclasticus* 617

The work described in this Chapter was included in a submitted publication to *Angew. Chem.*, currently under revision:

- Penas D., Pereira A.S., Tavares P. Direct evidence for ferrous ions oxidation and incorporation in absence of oxidants by Dps from *Marinobacter hydrocarbonoclasticus*.

4.1 Overview

The ferroxidase activity of Dps protein from *M. hydrocarbonoclasticus* using H_2O_2 as oxidant has been investigated by Mössbauer spectroscopy, in the absence of O_2, and will be presented in this chapter. Moreover, the ability of ferric mineral core to catalyse the oxidation of Fe^{2+} ions in the absence of any oxidants was also studied, performing mixed isotope, $^{56}Fe/^{57}Fe$, experiments. In these experiments, H_2O_2 was used as co-substrate, since the ferroxidase reaction is much faster than using O_2, as described by Guilherme M [159].

Mössbauer spectroscopy is a technique based on the Mössbauer effect discovered by Rudolph Mössbauer in 1957. In Mössbauer effect there is a recoilless resonance emission and absorption of gamma (γ) radiation by the atomic nucleus in a solid matrix [164]. The most used isotope is ^{57}Fe, which has a natural abundance of 2.2% [165], and the nuclear resonance absorption is generate by a ^{57}Co source. This spectroscopy allows to differentiate changes in the energy levels of an atomic nucleus (hyperfine interactions) using the Doppler effect. That is, the source is accelerated through a range of velocities (mm/s) to produce the Doppler effect and the spectrum recorded in discrete velocity steps [166]. Typically, three types of hyperfine interactions can be identified by this spectroscopy: the isomer shift (δ); the quadrupole splitting (ΔE_Q); and the magnetic splitting.

The isomer shift results from the interaction of nucleus (protons) with the s-electrons, which leads to an electric monopole interaction, altering the nuclear energy levels (Figure 4.1A). Thus, any difference in the s-electron environment between the source and absorber produces a shift in the resonance energy, and consequently a shift of the whole spectrum positively or negatively (in mm/s). This parameter gives information about the oxidation state, bonding properties and spin state.

The quadrupole and magnetic splitting induce splitting of the resonance lines according to the allowed transitions from the ground state to the excited state. In the case of the quadrupole splitting, the nuclear quadrupole moment in the presence of an inhomogeneous electric field splits the nuclear energy levels (Figure 4.1B). This interaction is called electric quadrupole interaction. For example, the isotope ^{57}Fe with an

angular momentum quantum number I = 3/2 excited state; the excited state is split into two substrates, $m_I = \pm 1/2$ and $m_I = \pm 3/2$, giving a doublet spectrum. ΔE_Q gives information about the oxidative state, spin state and symmetry of the metal centre.

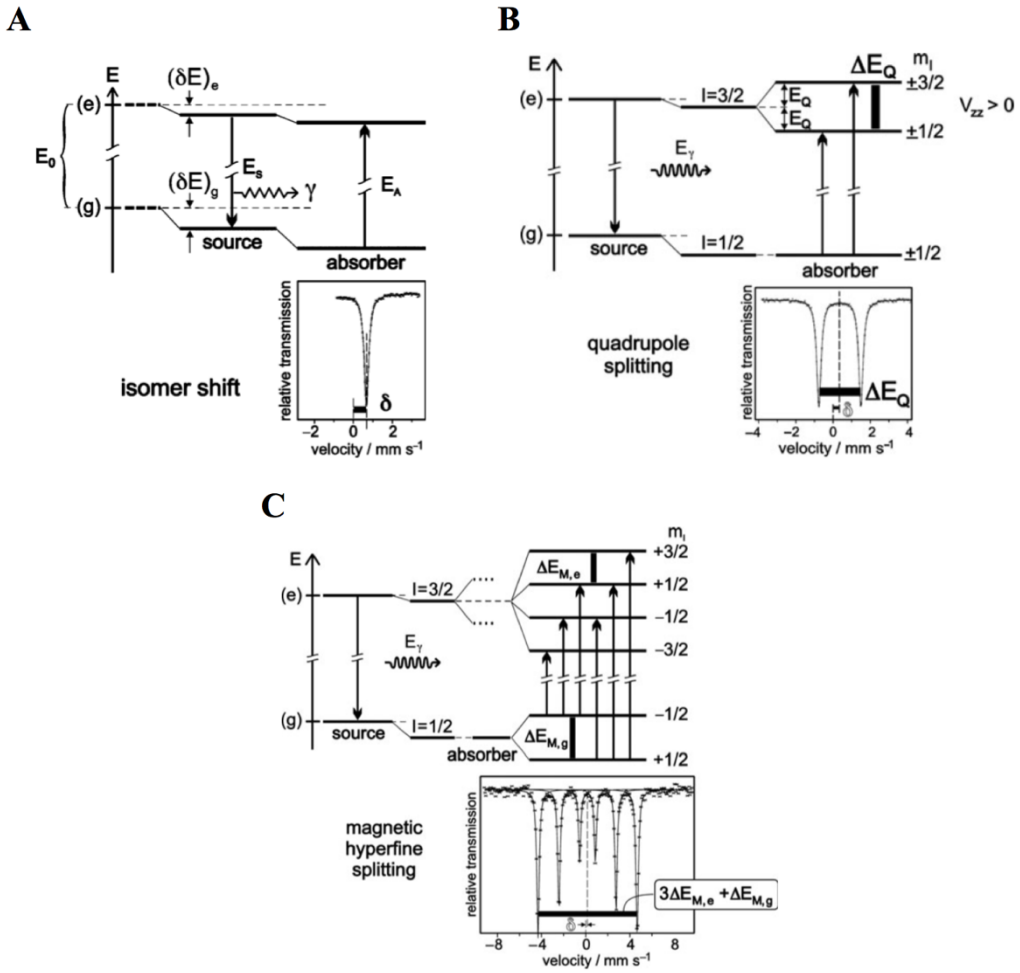

Figure 4.1: Hyperfine interactions in Mössbauer spectroscopy. (A) Isomer shift (δ) due to the energy shifting of the nuclear states as a result of the electric monopole interaction. (B) Quadrupole splitting of the excited state of ^{57}Fe with I = 3/2 and the resulting Mössbauer spectrum. The nuclear states are additionally shifted by the isomer shift. (C) Magnetic splitting in ^{57}Fe and the resulting spectrum. $\Delta E_{\mathrm{M,g}}$ and $\Delta E_{\mathrm{M,e}}$ refer to the Zeeman energies of the ground and excited states, respectively. Adapted from [167].

On the other hand, the magnetic splitting results from the magnetic dipole interaction between the nuclear magnetic dipole and the effective magnetic field at the nucleus (Figure 4.1C). This last is the sum of the applied field ($B_{applied}$) and the internal magnetic field (B_{int}) arising from a magnetic moment of the valence electrons. The

contributions for the B_{int} are the magnetic field from the spin on those electrons polarizing the spin density at the nucleus ($B_{contact}$), the magnetic field due to the orbital moment on those electrons ($B_{orbital}$), and the dipolar field due to the non-spherical distribution of the electronic spin density ($B_{dipolar}$). This hyperfine interaction gives information on the magnetic properties of the material under study [166,167].

Table 4.1 lists the typical values for δ and ΔE_Q for important compounds in bioinorganic chemistry and biochemistry, i.e. haems, iron-sulphur centres containing Fe sites in a distorted tetrahedral sulphur environment, and compounds with a hexacoordinate and pentacoordinate Fe sites with oxygen and/or nitrogen ligands [165].

Table 4.1: Values for ΔE_Q and δ for compounds of biologic interest at 4.2 K. Adapted from [165].

Oxidation State	Spin State, S	Ligand Set	ΔE_Q (mm/s)	δ (mm/s) [a]
Fe(IV)	2	Fe-(O,N)	0.5 – 1.0	0.0 – 0.1
	1	Haems	1.0 – 2.0	0.0 – 0.1
		Fe-(O,N)	0.5 – 4.3	-0.20 – 0.10
Fe(III)	5/2	Haems	0.5 – 1.5	0.35 – 0.45
		Fe-S	< 1.0	0.20 – 0.35
		Fe-(O,N)	0.5 – 1.5	0.40 – 0.60
	3/2	Haems	3.0 – 3.6	0.30 – 0.40
	1/2	Haems	1.5 – 2.5	0.15 – 0.25
		Fe-(O,N)	2.0 – 3.0	0.10 – 0.25
Fe(II)	2	Haems	1.5 – 3.0	0.85 – 1.0
		Fe-S	2.0 – 3.0	0.60 – 0.70
		Fe-(O,N)	2.0 – 3.2	1.1 – 1.3
	0	Haems	< 1.5	0.30 – 0.45

[a] The isomer shifts are relative to the centroid of Fe metal at 298 K, the standard most commonly used.

Mössbuaer spectra of magnetic nanoparticles samples (as holo-ferritins) at low temperature (4.2 K) will be dominated by the magnetic dipole interaction, where the electronic spin relaxation is slow on the Mössbauer timescale, and sextets are observed.

At higher temperatures, however, all particles have fast superparamagnetic relaxation and only doublets are observed, where only monopole and quadrupole interactions are visible [167,168].

Mössbauer spectrometer (Figure 4.2) consists in one drive, containing the ^{57}Co source, which is constantly accelerated moving periodically back and forward. The emitted γ-rays, that are absorbed and emitted by the frozen sample, arrive at the γ-detector, where are converted into electric pulses which are then amplified, shaped and selected by a chain of electronic components.

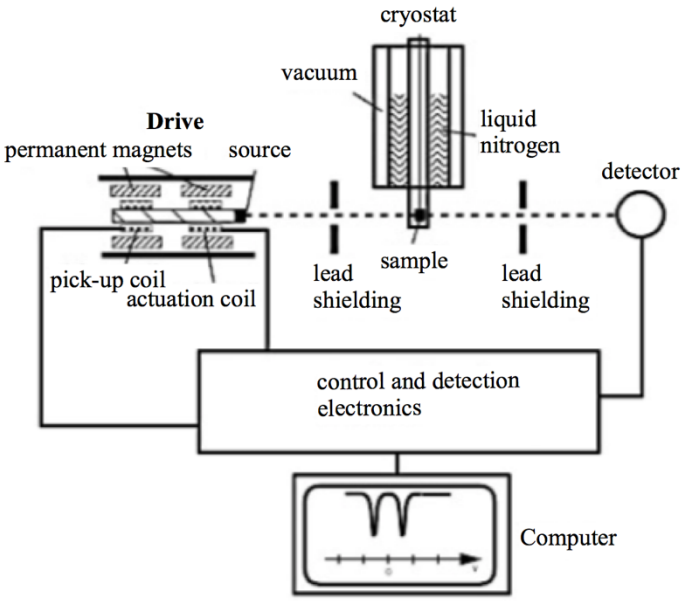

Figure 4.2: Schematic representation of a Mössbauer spectrometer. Adapted from [168].

4.2 Experimental procedure

Expression and purification of recombinant Dps-WT protein was described in Chapter 3, Section 3.2.2.

4.2.1 Iron uptake assays

Iron uptake by *M. hydrocarbonoclasticus* Dps-WT protein was monitored at 310 nm in an UV-visible spectrophotometer (Agilent technologies) at room temperature. To determine the maximum iron load, sequential additions of 24 Fe^{2+} per protein molecule, at 5 min intervals, were made to Dps protein (1 μM) in 200 mM MOPS buffer pH 7.0, 200 mM NaCl, in the presence of H_2O_2 (2-fold molar excess relative to added Fe^{2+}). The absorbance measurements were made after each addition of iron. The maximum iron oxidation/storage capacity was determined by plotting the absorbance at 310 nm as a function of Fe^{2+}/Dps molar ratio.

4.2.2 Mössbauer method

Mössbauer spectra were recorded on a week-field spectrometer operating in a constant acceleration mode in a transmission geometry as described in Chapter 2, Section 2.2.4.

4.2.3 Mössbauer sample preparation

Mössbuaer Dps-WT protein samples were prepared inside a glove box system (MBraun MBLab; <1 ppm O_2, <1 ppm H_2O_2). The ^{57}Fe solutions were prepared from a ^{57}Fe-enriched $FeSO_4$ stock solution (≥95% enrichment made from an enriched metal foil).

Dps protein (typically, 50 to 120 μM) in 200 mM MOPS buffer pH 7.0, 200 mM NaCl, was incubated for 30 min with Fe^{2+} ions at final ratios of 12, 24 and 96 Fe^{2+}/protein (molar ratio), and subsequently reacted with H_2O_2 (15-fold molar excess relative to added Fe^{2+}) for 2 h before freezing in liquid nitrogen.

In the case of mixed isotope experiments, samples were prepared using ^{56}Fe-enriched $FeSO_4$ solution as described above. As a control sample, the iron solution was

replaced by the same volume of buffer. To remove the unreacted H_2O_2, samples were washed by buffer exchange with an aqueous solution of 200 mM MOPS buffer pH 7.0, 200 mM NaCl using a Vivaspin 20 concentrator (100 kDa MWCO, GE Healthcare Life Sciences). After that, samples were anaerobically reacted as before with 12 $^{57}Fe^{2+}$/protein (molar ratio), frozen and stored in liquid nitrogen until measurement.

4.3 Results and discussion

4.3.1 Iron uptake experiments by UV-visible spectroscopy

The UV-visible spectrum of pure Dps-WT protein is dominated by a single band at 280 nm, as shown in Chapter 3, Section 3.3.7, but the spectrum of the Fe-loaded Dps-WT protein has a broad band centred at 345 nm (Figure 4.3A). The broad absorption, in the range of 300 and 450 nm, in the latest (highest Fe^{2+}/protein ratio) spectrum is a common feature of ferritin proteins, and it due to the formation of the ferric mineral core inside of protein [116,121,169].

The iron uptake experiments using H_2O_2 as oxidant indicated that Dps-WT was able to incorporate about 500 Fe^{2+} per protein molecule (Figure 4.3B). This value agrees with the data reported for this ferritin sub-family, which is limited by the size of the inner cavity [45,170-173].

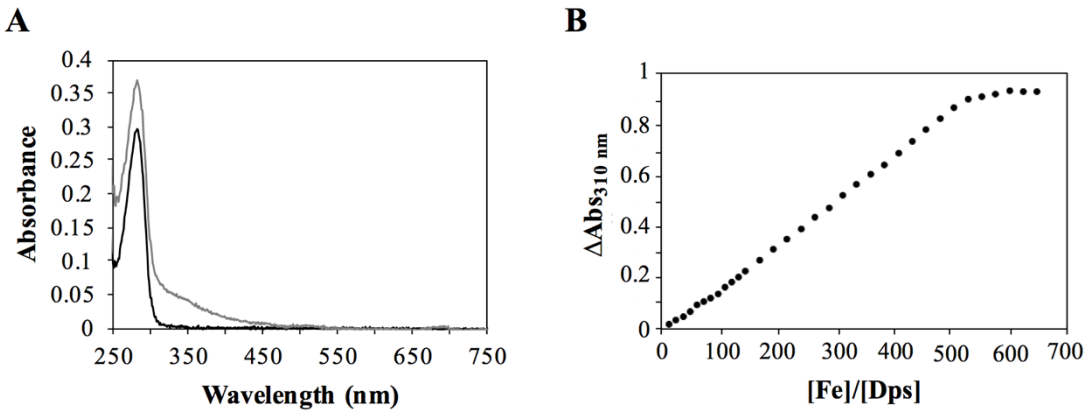

Figure 4.3: UV-visible spectra of Dps-WT and Fe-loaded Dps-WT in the presence of H_2O_2. (A) UV-visible spectra of Dps (black line) and 24 Fe-loaded Dps (grey line) in 200 mM MOPS buffer pH 7.0, 200 mM NaCl. (B) Dps protein (1 μM) iron loading in the presence of an excess of H_2O_2. Consecutive additions of 12 Fe^{2+} up until a molar ratio of 144 Fe^{2+}/protein, and of 24 Fe^{2+} for higher molar ratios.

4.3.2 Iron oxidation by Mössbauer spectroscopy

4.3.2.1 ^{57}Fe-loaded Dps protein

Dps-WT samples reacted with 12, 24 and 96 $^{57}Fe^{2+}$/protein for 20 min, under anaerobic conditions were characterized by Mössbauer spectroscopy (Figure 4.4).

The spectra obtained for samples loaded with 24 and 96 Fe^{2+}/protein molecule (Figure 4.4B and C, respectively) were simulated using two quadrupole doublets with ΔE_Q of 2.72 ± 0.03 and 3.35 ± 0.03 mm/s, and δ of 1.35 ± 0.02 mm/s. While the spectrum obtained for the sample with a molar ratio of 12 Fe^{2+}/protein (Figure 4.4A) was sharper and better fitted by a quadrupole doublet with ΔE_Q = 3.19 ± 0.04 mm/s, and δ = 1.27 ± 0.02 mm/s. These parameters are typical of high-spin Fe^{2+} and point to the existence of differences in coordination environments and local structures around Fe^{2+}.

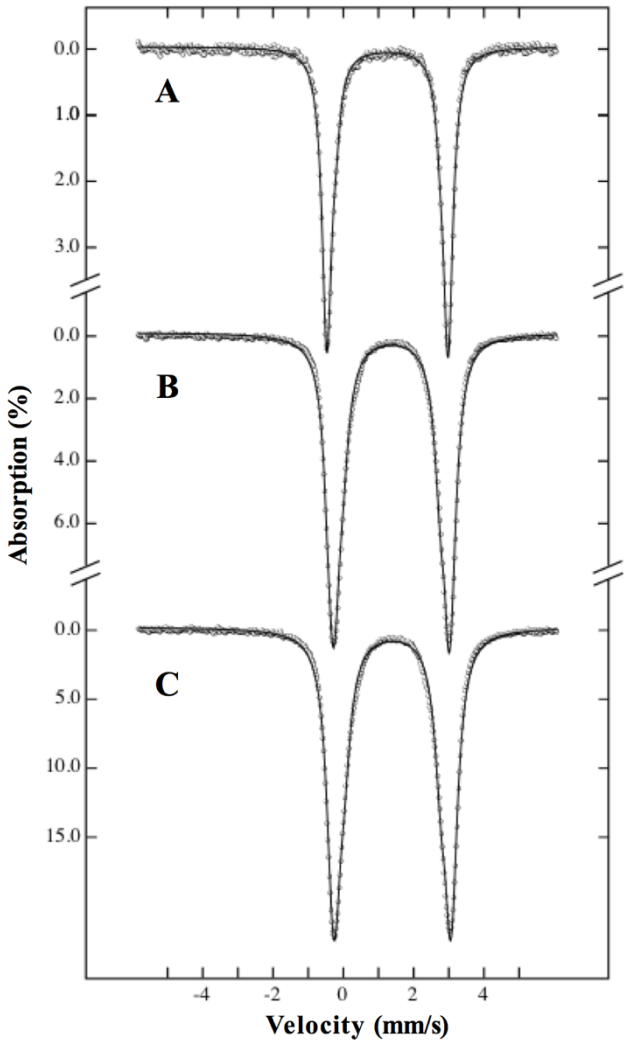

Figure 4.4: Mössbauer spectra of $^{57}Fe^{2+}$-loaded Dps-WT protein. Dps protein samples were incubated, under anaerobic conditions, with 12 (A), 24 (B) and 96 (C) $^{57}Fe^{2+}$ per protein molecule. The spectra were recorded at 4.2 K, with a 60 mT magnetic field applied parallel to the γ-beam. The solid lines are theoretical simulations using the parameters listed in Table 4.2.

When Dps protein is incubated with Fe^{2+} under anaerobic conditions no oxidation of the added Fe^{2+} occurs. However, the 12 $^{57}Fe^{2+}$ per protein molecule sample spectrum (Figure 4.4A) shows sharper lines and the low energy line is slightly shifted to lower energy (approximately 0.21 mm/s, Figure 4.5) when compared to the one obtained for the 24 and 96 $^{57}Fe^{2+}$/protein (spectra B and C in Figure 4.4).

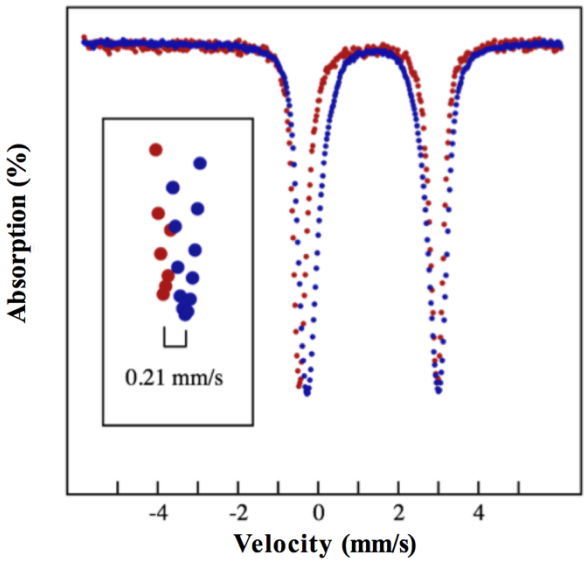

Figure 4.5: Mössbauer spectra of ^{57}Fe-loaded Dps protein. Dps samples were incubated under anaerobic conditions, with 12 (red circles) and 24 (blue circles) $^{57}Fe^{2+}$ per protein molecule. Data was recorded at 4.2 K, with 60 mT magnetic field applied parallel to the γ-beam. The inset shows the 0.21 mm/s difference between the low energy peak of both spectra.

The difference in the low energy peaks was seen in several Mössbauer samples prepared under the same conditions. Thus, it is possible to assume that the iron in the lower iron ratio sample has a more defined and slightly different coordination site, which can be due to the binding of Fe^{2+} to a specific ferroxidase centre (FOC), taking in account available structural data for Dps protein (which has twelve putative FOCs) [41,49,174].

At the FOC the Fe^{2+} is coordinated by an aspartate and a glutamate residue, from one monomer, and a histidine residue from the adjacent monomer, which generates a coordination sphere compatible with the observed Mössbauer parameters. Additional Fe^{2+} can be allocated in uptake channels either in hexa-aquo iron complex form or interacting with other polar and negatively charged residues, where the iron is in high-spin Fe^{2+} species. Mössbauer spectroscopy can identify the iron species but does not have resolution to properly quantify these.

All samples were, later, reacted with H_2O_2 for 20 min and the Mössbauer spectra recorded (Figure 4.6). The spectrum of the sample containing 12 Fe^{2+} and H_2O_2 showed a quadrupole doublet (Figure 4.6A), which was simulated using two quadrupole doublets with ΔE_Q of 1.51 ± 0.03 and 1.18 ± 0.03 mm/s, and δ of 0.52 ±0.03 and 0.54 ± 0.02 mm/s,

respectively. These parameters are indicative of high-spin Fe^{3+} compounds with oxygen/nitrogen ligands, as listed in Table 4.1. The presence of single quadrupole doublet in the spectrum indicates that it can arise from a complex with an even number of Fe^{3+} with strong antiferromagnetic exchange coupling, resulting in a system with a diamagnetic ground state. However, the presence of quadrupole doublets also can be explained by the electronic relaxation rate. If the electronic relaxation rate is much faster than the nuclear Larmor precession (~10^{-7} s for a ^{57}Fe nucleus), the magnetic splitting will be average out, causing the quadrupole doublet.

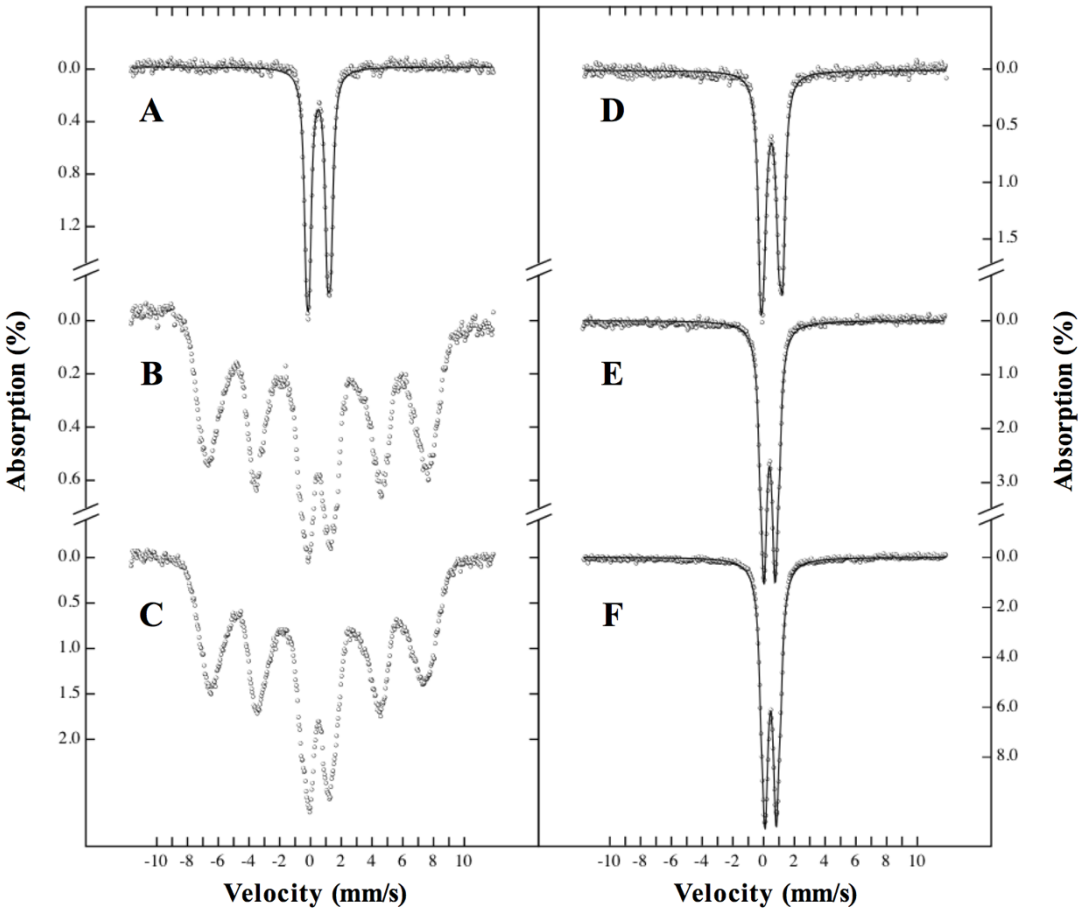

Figure 4.6: Mössbauer spectra of ^{57}Fe-loaded Dps-WT protein after reaction with H_2O_2. Samples previously incubated with 12 (A, D), 24 (B, E), and 96 (C, F) $^{57}Fe^{2+}$ per protein molecule were reacted for 20 min with H_2O_2. Spectra were recorded at 4.2 K (A to C) with a 60 mT magnetic field applied parallel to the γ-beam, or at 30 K (D to F) in the absence of an external applied magnetic field. The solid lines are theoretical simulations using the parameters listed in Table 4.2.

For the samples containing 24 and 96 Fe^{2+}/protein molecule, after oxidation (Figure 4.6B and C, respectively), low magnetic field, low temperature (4.2 K) spectra are dominated by the presence of sexts. These sexts are converted in quadrupole doublets with the increasing of acquisition temperature, above 30 K (Figure 4.6E and F). These quadrupole doublets were simulated with two quadrupole doublets with parameters of high-spin Fe^{3+} compounds (ΔE_Q = 0.57 ± 0.03 and 1.00 ± 0.03 mm/s, and δ = 0.48 ± 0.02 mm/s). This type of behaviour is typical of superparamagnetic systems and has been detected and characterized in ferritin proteins [97,175]. Additionally, it can be associated with the formation of the iron mineral core, which can be formed even for ratios of Fe^{2+}/ferritin as low as 10. For these systems the blocking temperature (T_B) is taken as the temperature at which the doublet and sextet components are of equal intensity [176,177]. T_B is linearly proportional to the particle volume and a magnetic anisotropy constant, which is a function of material characteristics. The observation that only a doublet species exists in the 30 K-spectra of these samples is indicative of small core formation in *M. hydrocarbonoclasticus* Dps.

H_2O_2 reaction of samples containing 12, 24 and 96 $^{57}Fe^{2+}$ per protein molecule resulted in full iron oxidation, but with different activities. In the case of the 12 $^{57}Fe^{2+}$/protein spectrum, oxidation originated iron species with quadrupole doublet parameters similar μ-oxo binuclear Fe^{3+} clusters found in other ferritins and other iron-containing enzymes [97,178-182]. For the higher iron ratios samples, 24 and 96 $^{57}Fe^{2+}$/protein, the spectra showed the presence of an iron core species as can be seen by the occurrence of a sextet at low temperature, which at 30 K collapses into quadrupole doublets distinct from the ones observed for the 12 $^{57}Fe^{2+}$/protein, showing lower δ and ΔE_Q, and being in accordance with previously observed core parameters [176].

4.3.2.2 $^{56}Fe/^{57}Fe$-loaded Dps protein

To investigate the fate of iron oxidation in Dps protein, a set of samples was prepared by reacting Dps protein with $^{56}Fe^{2+}$ in the molar ratios of 12, 24 and 96 Fe^{2+}/protein in presence of an excess of H_2O_2. After oxidation, unreacted H_2O_2 was removed and all samples were anaerobically reacted with additional 12 $^{57}Fe^{2+}$/ protein

molecule for 2 h and analysed by Mössbauer spectroscopy at 80 K (Figure 4.7). A control sample was prepared as above omitting the $^{56}Fe^{2+}$.

The control spectrum (Figure 4.7A) shows a single quadrupole doublet with the same characteristic parameters of high-spin Fe^{2+} species for a 12 Fe^{2+}/protein as per comparison with Figure 4.4A (listed in Table 4.2). This observation is an indication that all unreacted H_2O_2 was efficiently removed before addition of the extra 12 $^{57}Fe^{2+}$/protein, and no oxidant was present.

The Mössbauer spectrum of the sample previously incubated with 12 $^{56}Fe^{2+}$/protein molecule and further reacted with 12 $^{57}Fe^{2+}$/protein (Figure 4.7B) showed a quadrupole doublet with the parameters of high-spin Fe^{2+} species, similar to the ones in the control sample. While the spectra of samples containing 12 $^{57}Fe^{2+}$/protein, after reaction of 24 and 96 $^{56}Fe^{2+}$/protein and H_2O_2 (Figure 4.7C and D, respectively), exhibited additional quadrupole doublets with parameters identical to the ones observed in Figure 4.6E and F, attributed to the iron core containing 24 and 96 $^{57}Fe^{3+}$, respectively. These unprecedented observations reveal that a significant percentage of the added $^{57}Fe^{2+}$ ions changed oxidation state in the absence of oxidant. Hence, in the sample loaded with 24 $^{56}Fe^{2+/}$protein 44 ± 3% of the 12 $^{57}Fe^{2+/}$protein was oxidized, while the sample loaded with 96 $^{56}Fe^{2+}$/protein raised to 77 ± 2%. Table 4.2 lists all Mössbauer parameters used to fit the observed iron species and their contribution to the total spectral absorption.

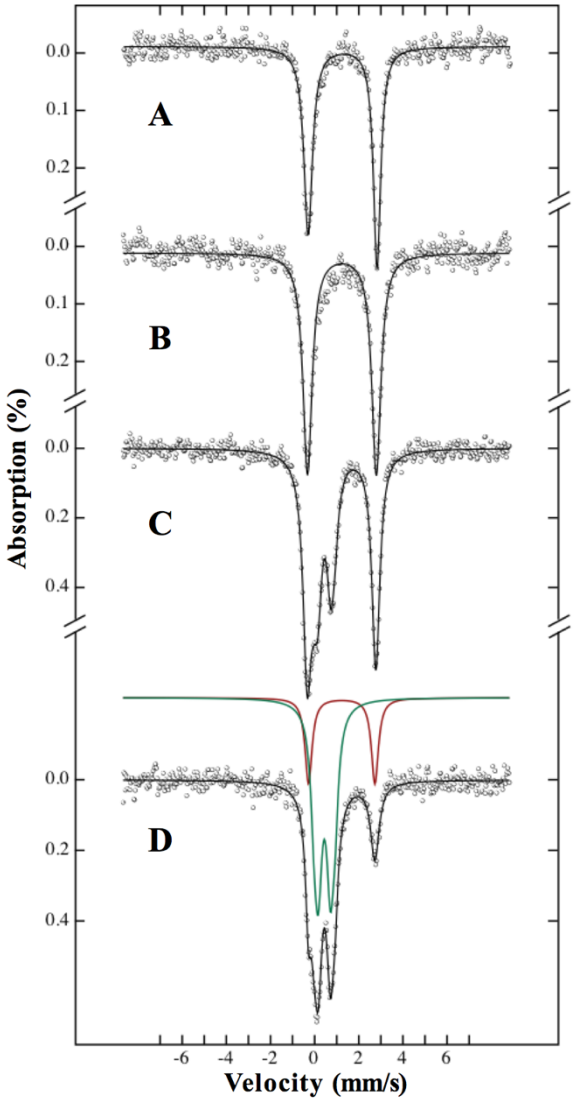

Figure 4.7: Mössbauer spectra of preloaded ^{56}Fe-loaded Dps protein after incubation with 12 $^{57}Fe^{2+}$/protein. Samples previously incubated with 0 (A), 12 (B), 24 (C), and 96 (D) $^{56}Fe^{2+}$ per protein molecule and further reacted with H_2O_2 were incubated with 12 $^{57}Fe^{2+}$ per protein molecule, after removal of unreacted H_2O_2. Data were recorded at 80 K in the absence of an external applied magnetic field. The solid lines are theoretical simulations using the parameters listed in Table 4.2. The red and green lines above spectrum D are the theoretical simulations obtained for the high-spin Fe^{2+} and Fe^{3+} components, respectively.

Table 4.2: Mössbauer parameters for iron species observed in *M. hydrocarbonoclasticus* Dps.[a]

Sample	Ferrous species			Ferric species		
	δ (mm/s)	ΔE_Q (mm/s)	%	δ (mm/s)	ΔE_Q (mm/s)	%
12 ^{57}Fe	1.27(2)	3.19(4)	100			
24 ^{57}Fe 96 ^{57}Fe	1.35(2)	2.72(3) 3.35(3)	41(3) 59(3)			
12 ^{57}Fe + H_2O_2				0.52(3) 0.54(2)	1.51(3) 1.18(3)	49(2) 51(2)
24 ^{57}Fe + H_2O_2 96 ^{57}Fe + H_2O_2				0.48(2)	0.57(3) 1.00(3)	44(3) 56(3)
0 ^{56}Fe + H_2O_2 [b] + 12 ^{57}Fe	1.27(2)	3.12(4)	100			
12 ^{56}Fe + H_2O_2 [b] + 12 ^{57}Fe	1.26(2)	3.12(4)	100			
24 ^{56}Fe + H_2O_2 [b] + 12 ^{57}Fe	1.25(2)	3.11(4)	56(3)	0.47(2)	0.58(3) 0.96(3)	44(3)
96 ^{56}Fe + H_2O_2 [b] + 12 ^{57}Fe	1.25(2)	3.01(4)	23(2)	0.48(2)	0.56(3) 0.97(3)	77(2)

[a] Values in parentheses are uncertainties of the last significant digits.
[b] Unreacted H_2O_2 was removed before anaerobic incubation with 12 $^{57}Fe^{2+}$.

The use of $^{56}Fe^{2+}$ enables the use of protein samples loaded with the same iron per protein molecule ratios, oxidation and structural state when $^{57}Fe^{2+}$ was used, but being silent for Mössbauer spectroscopy. Further addition of $^{57}Fe^{2+}$ makes possible to follow by Mössbauer spectroscopy the fate of these ones. It is expected that the $^{57}Fe^{2+}$ added enter Dps protein through the "Ferritin-like" pore and translocated in the dimer interface, and in the absence of oxidant no oxidation would occur. However, the results showed that in the presence of iron core, the oxidation of additional $^{57}Fe^{2+}$ occurs. This oxidation depends on core size, but even for small cores, such as the ones containing 24 iron atoms, it is possible to detect significant oxidation.

In the absence of iron core (Figure 4.7B) no oxidation reaction is observed. This agrees with the results obtained when only 12 $^{57}Fe^{2+}$/protein were added. The loading

experiments with $^{57}Fe^{2+}$ showed that after 20 min oxidation with H_2O_2 no core is formed. So, the Mössbauer spectrum is better explained by the presence of μ-oxo binuclear Fe^{3+} clusters. For the subsequent addition of Fe^{2+}, the Mössbauer spectrum showed that all the iron stays in the ferrous oxidation state, due to the quadrupole doublet parameters that are characteristic of high-spin Fe^{2+} with octahedral nitrogenous/oxygenous coordination, most probably chelated by the protein environment in the dimer interface or at the inner cavity.

So far, it is commonly accepted that further iron oxidation can concomitantly occur through an autocatalytic reaction for which the Fe^{2+} can enter and be oxidized at the mineral core surface in the presence of oxidant co-substrate. However, these results have shown that even in the absence of oxidant co-substrate iron uptake and mineralization was possible, and that not only the $^{57}Fe^{2+}$ was oxidized but also it was incorporated into the bulk mineral structure given the spectral similarity with the iron reacted with H_2O_2 sample. Silvester and colleagues [183] and Williams and Scherer [184] have observed this phenomenon in abiotic systems. The authors proved that Fe^{2+} ions could adsorb to the surface of synthetic minerals (goethite and hydrous ferric oxide hydrate) and be completely oxidized in anoxic environments, through electron transfer reactions from the aqueous Fe^{2+} to the solid ferric mineral.

Overall, these results provide a direct evidence of the reactivity of the ferric mineral core when the oxidant, H_2O_2 or O_2, is absent or eventually scarce, thus facilitating the biomineralization process in such conditions, which may have physiological relevance for facultative or anaerobic bacteria. This fascinating hypothesis opens the discussion of iron biomineralization by Dps and ferritins in general.

5

Dps, a DNA-binding protein

5.1 Overview

It was estimated that 2-3% prokaryotic genome encodes for DNA-binding proteins, which makes protein-DNA interactions a common physiologic process [185].

The major cellular function of Dps proteins is to detoxify the intracellular environment from the ferrous iron atoms (Fe^{2+}). However, some of these proteins can bind DNA in a non-specific manner. This chapter aims to investigate the DNA-binding ability of Dps protein from *Marinobacter hydrocarbonoclasticus* 617 using electrophoretic mobility-shift assays (EMSAs).

EMSA is a rapid and sensitive technique widely used to detect protein-nucleic acid complexes *in vitro*. Protein solutions and nucleic acid are combined together under appropriate conditions and allowing binding to occur. The mixture is then assessed by electrophoresis under native conditions in either polyacrylamide or agarose gels. Generally, the protein-nucleic acid complexes have less electrophoretic mobility than the free nucleic acid, which results in a retardation of nucleic acid when bound to protein, i.e., resulting in discrete bands above the free nucleic acid band corresponding to protein-nucleic acid complexes [186,187].

The ability of Dps protein to bind DNA was evaluated using Dps-WT and variants Dps-Q14E, Dps-Δ15, Dps-T10C and Dps-F5C. Besides, the DNA binding property of Dps-WT loaded with different amounts of iron (holo-Dps-WT), i.e., Dps-WT protein containing various amounts of ferric mineral core produced in the presence of molecular oxygen or hydrogen peroxidase, was also investigated. Additionally, DNA protection studies against Proteinase K and hydroxyl radical activities were analysed to characterize the importance of Dps-DNA complex.

5.2 Experimental procedure

5.2.1 EMSAs

All EMSAs were performed using supercoiled plasmid pUC19 (vector map in Appendix A.3.1) in 50 mM MOPS buffer pH 7.0, 50 mM NaCl (EMSA buffer). Each DNA binding test (5 μL of each reaction) was analysed in 1% agarose gels in 1x TAE buffer, run at 80 V for about 1 h 30 min at room temperature. Gels were stained with SYBR Safe solution (Invitrogen) for 30 min, and imaged with Safe Imager™ (Invitrogen) in a Gel Logic 100™ Imaging System (Kodak). Gel electrophoresis images were processed and analysed (free DNA and protein-DNA complex bands) using ImageJ [147].

5.2.1.1 Dps-WT

Supercoiled pUC19 (10 nM) was incubated with Dps-WT (between 2.5 and 13 μM) for 10 min at room temperature, in 50 mM MOPS pH 7.0, 50 mM NaCl in a total volume of 10 μL. In a control reaction, Dps-WT was replaced by BSA protein (3 μM).

To investigate the affinity for different supercoiled plasmids assays were performed replacing pUC19 with pGEX-6P-1 (vector map in Appendix A.3.2) and pET-21c (vector map in Appendix A.3.3). Supercoiled pGEX-6P-1 (0.88 nM) and supercoiled pET-21c (3.36 nM) were incubated with Dps-WT (5.0 and 13 μM) in parallel, using the experimental conditions above described.

5.2.1.2 Dps-Q14E and Dps-Δ15

EMSAs were performed as described for Dps-WT, with supercoiled pUC19 at 15 nM and varying the protein concentrations between 0.21 and 7.5 μM.

5.2.1.3 Dps-T10C and Dps-F5C

EMSAs were performed as described for Dps-WT, but in this case, the concentration of protein ranged between 3 μM and 13 μM.

5.2.1.4 Iron-loaded Dps-WT

EMSAs were performed as described for the Dps-WT, but Dps-WT was replaced by iron-loaded Dps-WT proteins (containing 12, 24, 48, 96, 192 and 384 iron atoms per protein) at a concentration of 13 μM. Iron-loaded proteins were prepared using either H_2O_2 or O_2 as co-substrate.

The ferrous sulphate solution was freshly prepared in milliQ water at pH 3.0, and H_2O_2 solution prepared in 50 mM MOPS buffer pH 7.0, 50 mM NaCl. Both ferrous sulphate solution and the H_2O_2 solution were quantified as described in Chapter 2, Section 2.2.1.5 and 2.2.1.6, respectively.

H_2O_2 as co-substrate

Dps-WT protein was loaded with 12 Fe^{2+} per protein molecule, incubated for 5 min at room temperature and reacted with a 15-fold molar excess of H_2O_2, to the concentration of ferrous iron, for 5 more min at room temperature. Stepwise additions of iron and hydrogen peroxide were performed to achieve the Fe^{2+}/protein ratios of 12, 24, 48, 96, 192 and 384. Then the protein is incubated for 30 min at room temperature.

O_2 as co-substrate

Dps-WT protein was loaded by stepwise additions of 12 Fe^{2+}/protein molecule at intervals of 5 min, until the ratios of 12, 24, 48, 96, 192 and 384 iron atoms per protein were reached. After those additions of Fe^{2+} ions, the reaction mixture was saturated with oxygen gas, every 12 h for 5 days, at 4 ºC.

5.2.2 DNA protection assays

5.2.2.1 Protease protection assays

The proteolytic resistance of the Dps-WT-DNA complex against Proteinase K was performed incubating Dps-WT (0.5 to 13 μM) with supercoiled plasmid pUC19 (10 nM), for 10 min at room temperature, in 50 mM MOPS buffer pH 7.0, 50 mM NaCl (total

volume of 10 µL), following incubation with Proteinase K (20 mg/mL) for 30 min at 37 ºC. Controls were prepared by incubating Dps-WT with Proteinase K for 30 min at 37 ºC, and then incubating with the pUC19 for 10 min at room temperature. Additionally, Dps-WT was substituted with BSA protein (13 µM) and Dps-Q14E protein (13 µM).

Reactions were analysed as described in Section 5.2.1.

5.2.2.2 DNA protection assays

DNA protection assays against hydroxyl radical were performed using supercoiled plasmid pUC19 and the proteins Dps-WT, Dps-Q14E, Dps-Δ15 and holo-Dps-WT protein containing 96 Fe^{3+}/protein, in 50 mM MOPS buffer pH 7.0, 50 mM NaCl.

First, a DNA binding reaction was prepared with pUC19 (10 nM) and protein (13 µM) following the protocol described for the WT protein (Section 5.2.1.1). Afterwards, 2.04 mM $FeSO_4 \cdot 7H_2O$ and 30.7 mM H_2O_2 were added to promote Fenton reaction for 8 min at room temperature. The reaction was stopped by addition of 10% SDS and heating at 85 ºC for 2 min.

In parallel, and after the DNA binding reaction, Proteinase K (20 mg/mL) was added to the DNA-Dps WT mixture (for 30 min at 37 ºC), following incubation with ferrous sulphate and H_2O_2.

As previously, all reactions were analysed as described in Section 5.2.1.

5.3 Results and discussion

5.3.1 EMSAs for apo-protein

To investigate the ability of Dps protein from *Marinobacter hydrocarbonoclasticus* 617 to bind DNA non-specifically, EMSAs were performed.

The results demonstrated the ability of Dps-WT to bind supercoiled plasmid pUC19 (in 50 mM MOPS buffer pH 7.0, 50 mM NaCl). A representative EMSA is shown in Figure 5.1A.

Binding of Dps-WT to supercoiled pUC19 produces larger protein-DNA complexes which migrate slower than the free form of supercoiled pUC19, seen by the shifting of the supercoiled band with increasing protein concentrations. In the tested conditions, apparent saturation is obtained at around 10 μM Dps-WT. The observed binding is specific for Dps-WT, since substitution with BSA (a protein that does not bind DNA) did not show any shift of the free form of supercoiled pUC19, as shown in Figure 5.1A.

The fractional complex formation was plotted as a function of protein concentration and fitted to the Hill equation, ($\theta = k[\text{Protein}]^n/(K_\text{d} + [\text{Protein}]^n)$, where θ is the fractional complex, k corresponds to the number of protein molecules bound to plasmid, [Protein] is the concentration of the binding protein, n is the Hill coefficient and K_d represents the macroscopic apparent dissociation constant and is a measure of the affinity of the protein to DNA (Figure 5.1B). In our experimental conditions, we calculated an apparent dissociation constant, K_d of 5.9 $\pm$ 1.0 μM and a Hill coefficient, n of 1.2 $\pm$ 0.1. The Hill coefficient indicates a modest positive cooperativity on DNA binding and is comparable with the values reported in Chapter 2 (Section 2.3.3) for *D. vulgaris* rBfr.

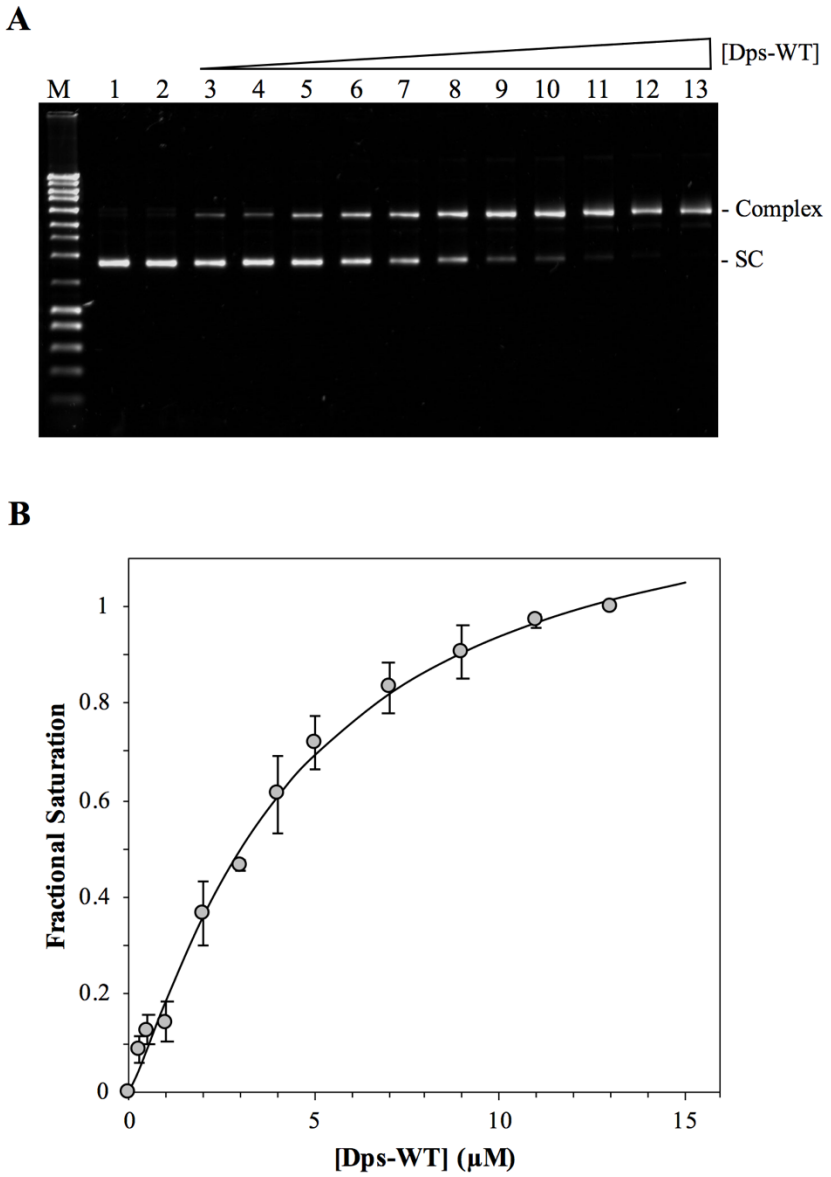

Figure 5.1: Binding of Dps-WT to supercoiled plasmid pUC19 in 50 mM MOPS buffer pH 7.0, 50 mM NaCl, analysed by EMSA. (A) EMSA on 1% agarose gel. M – NZYLadder III; 1 – Supercoiled plasmid pUC19 (10 nM); 2 – Binding reaction of BSA (3 µM) to supercoiled pUC19 (10 nM); 3 to 13 – Binding of Dps-WT (0.25, 0.50, 1.0, 2.0, 3.0, 4.0, 5.0, 7.0, 9.0, 11 and 13 µM) to supercoiled pUC19 (10 nM). The free supercoiled plasmid pUC19 band (SC) and the protein-pUC19 band (Complex) are indicated on the right. (B) Hill plot of DNA binding by Dps-WT from four sets of EMSA experiments using increasing concentrations of protein (between 0.25 µM and 13 µM) and supercoiled plasmid pUC19 (10 nM). Less than 8% uncertainty is estimated for the fractional saturation.

Besides the assays with the cloning vector, plasmid pUC19, two expression vectors were also used in binding assays with Dps-WT, pGEX-6P-1 and pET-21c. The data presented in Figure 5.2 revealed the non-specific DNA-binding ability of Dps protein.

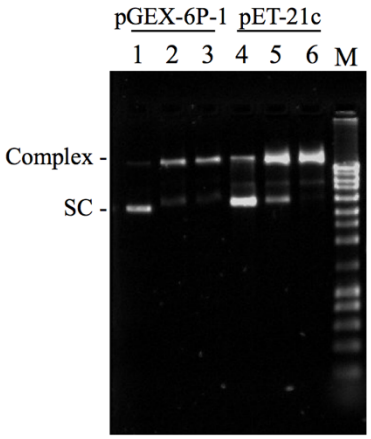

Figure 5.2: EMSA of the binding reaction of Dps-WT to supercoiled plasmid pGEX-6P-1 and pET-21c in 50 mM MOPS buffer pH 7.0, 50 mM NaCl. M – NZYLadder III; 1 – Supercoiled plasmid pGEX-6P-1 (0.88 nM); 2 and 3 – Binding of Dps-WT (5.0 and 13 µM) to supercoiled pGEX-6P-1 (0.88 nM); 4 – Supercoiled plasmid pET-21c (3.36 nM); 5 and 6 – Binding of Dps-WT (5.0 and 13 µM) to supercoiled pET-21c (3.36 nM). The free supercoiled plasmid band (SC) and the protein-plasmid band (Complex) are indicated on the left.

It has been reported that the Dps protein-DNA interactions are mediated by the flexible N-terminal region and dependent on the presence of positively charged residues [41,49,120], based on the polyanionic nature of DNA. The sequence of the N-terminal region of Dps is represented, with the positively charged residues depicted in blue:

MGKNFIGLDTDKTQK

To characterize the protein-DNA interaction two Dps variants were tested by EMSA with supercoiled plasmid pUC19 in 50 mM MOPS buffer pH 7.0, 50 mM NaCl. One variant is Dps-Q14E, in which glutamine 14 was replaced by a glutamate residue adding a negative charge at pH 7.0. The second variant is Dps-Δ15, which suffered a deletion of the first fifteen amino acid residues of the polypeptide chain.

A representative gel from the EMSA of the binding reaction of the two variants, Dps-Q14 and Dps-Δ15, with supercoiled plasmid pUC19 is shown in Figure 5.3. Results

were compared with the ones obtained with Dps-WT, as shown in Figure 5.4, where the fractional complex formation was plotted as a function of protein concentration.

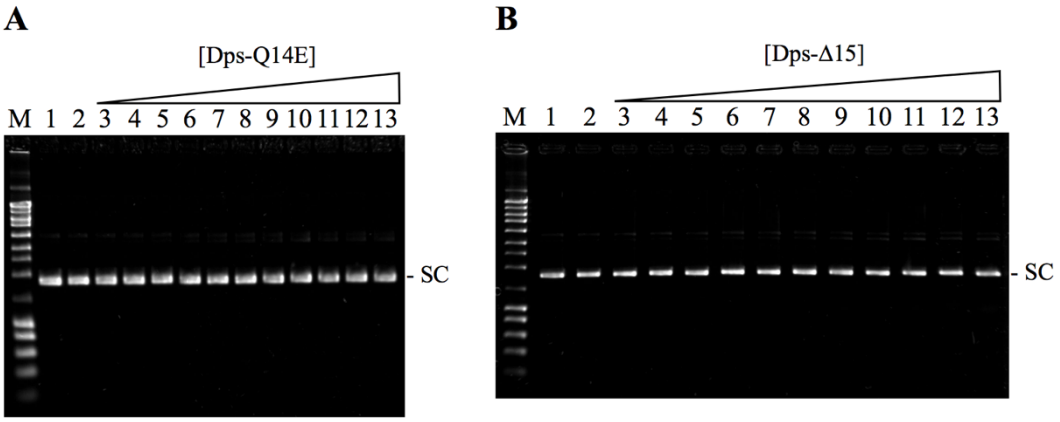

Figure 5.3: EMSA of the binding reaction of Dps-Q14E (A) and Dps-Δ15 (B) to supercoiled plasmid pUC19 in 50 mM MOPS buffer pH 7.0, 50 mM NaCl. M – NZYLadder III; 1 – Supercoiled plasmid pUC19 (15 nM); 2 – Binding reaction with BSA (3 µM); 3 to 13 – Binding reaction with each protein variant (0.21, 0.375, 0.75, 1.05, 1.5, 1.8, 2.7, 3.75, 4.5, 6.0 and 7.5 µM) and pUC19 (15 nM). The free supercoiled plasmid band (SC) is indicated on the right of each gel.

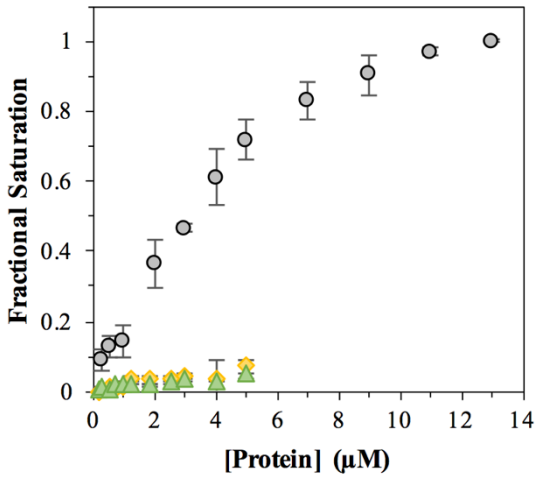

Figure 5.4: Comparison of fractional complex formation in DNA binding reactions with Dps-WT and variants. Grey circles represent the binding of Dps-WT (data from Figure 5.1); yellow diamonds correspond to Dps-Q14E (average from three sets of EMSA experiments with an estimated uncertainty of less than 6% for the fractional saturation); and the green triangles correspond to the DNA binding of Dps-Δ15 (average from two sets of EMSA experiments with an estimated uncertainty for the fractional saturation of less than 2%).

As both Figure 5.3 and Figure 5.4 show, Dps-Q14E and Dps-Δ15 were not able to bind DNA, demonstrating that a single charge residue substitution is enough to change the binding affinity and that the N-terminal region is essential for the interaction.

To further characterize the interaction between the N-terminal region and DNA, continuous wave (CW) X-band EPR spectroscopy studies were performed (Chapter 6). This analysis relied on the labelling of Dps protein with a nitroxide radical, MTSL, through a cysteine residue. Since the protein does not have any cysteine, site direct mutagenesis was performed to introduce a cysteine residue in the N-terminal region of the protein. Two variants were prepared, Dps-F5C and Dps-T10C, based on the structure of the protein (unpublished data): phenylalanine at the fifth position, located in a more flexible part of the N-terminal region, and threonine 10 positioned at the beginning of the α-helix in a more constrained part of the N-terminal region.

To assure the DNA binding capacity of these two variants, EMSAs were performed using the experimental conditions as for the WT protein (Figure 5.5).

The fractional complex formation was plotted as a function of protein concentration and compared with the Dps-WT fractional complex. Similarly, Dps-T10C binds to supercoiled pUC19 with an apparent affinity identical to the wild-type protein, unlike Dps-F5C which exhibited lower affinity for the interaction (Figure 5.5B). Even though pUC19 plasmid was not fully supercoiled (lane 2, Figure 5.5A), in these conditions, the observed binding is specific for the Dps-WT and variants, as the control in lane 3 (substitution with BSA) did not show any shift (Figure 5.5A).

Since the mutations on these two variants do not affect the net charge of N-Terminal region, no charge effects on DNA-interactions were expected. However, in these conditions, Dps-F5C has shown a lower affinity, suggesting that a potential structural change has occurred in the mobile N-terminal extension. Due to these observations, CW-EPR experiments were only performed with Dps-T10C variant.

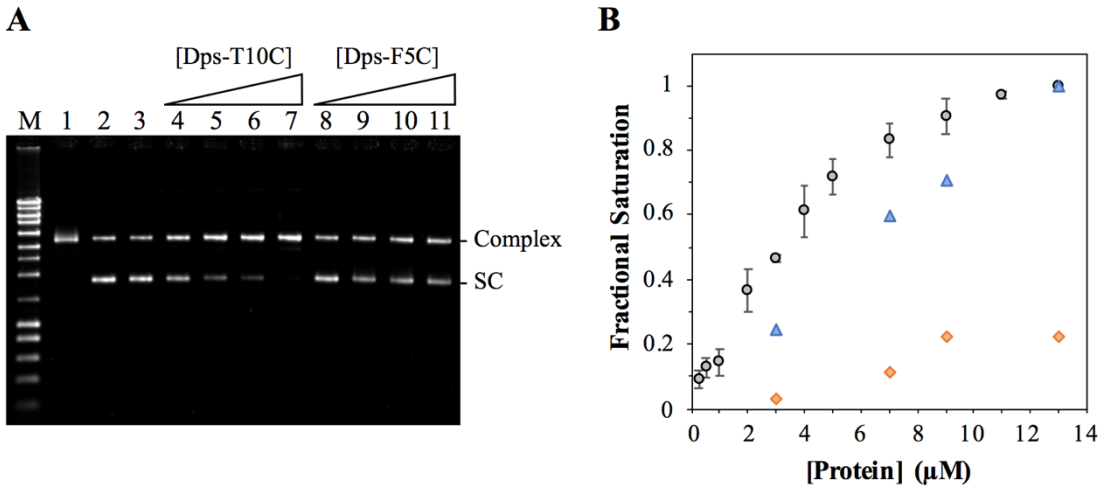

Figure 5.5: EMSA of the binding reaction of variants Dps-T10C and Dps-F5C with supercoiled plasmid pUC19 in 50 mM MOPS buffer pH 7.0, 50 mM NaCl. (A) Binding of Dps-T10C (lanes 4 to 7) and Dps-F5C (lanes 8 to 11) to plasmid pUC19 (10 nM). M – NZYLadder III; 1 – DNA binding control using Dps-WT (13 µM); 2 – Plasmid pUC19 (10 nM); 3 – Binding reaction replacing Dps protein with BSA (3 µM); Protein concentrations in the binding reactions: 3.0, 7.0, 9.0 and 13 µM. The free supercoiled plasmid band (SC) and the protein-plasmid band (complex) are indicated on the right. (B) Comparison of fractional saturation of Dps-WT (grey circles, data from Figure 5.1), Dps-T10C (blue triangles) and Dps-F5C (orange diamonds).

The single sharp band of the protein-DNA complex observed in all EMSA experiments can be explained by a change of the topology of plasmid DNA due to binding of Dps proteins, namely relaxation of the supercoiled form. The Dps-DNA complex behaviour is similar to the one observed for rBrf-DNA complex shown in Figure 2.7 (Chapter 2, Section 2.3.3), in the same experimental conditions, which could mean that the binding mechanism might be similar for these two proteins.

As mentioned before, protein-DNA binding has been reported to be mediated by positively charged residues in the N-terminal. In the case of *E. coli* Dps, the protein has the ability to self-aggregate and to condensate DNA [120]. In general, Dps proteins interact with DNA through positively charged lysine and/or arginine residues in the N-terminal region, however there are some Dps proteins able to bind through the positively charged residues in the C-terminal, as for *Mycobacterium smegmatis* Dps [123].

EMSAs with Dps-Q14E have demonstrated no interaction with supercoiled DNA, which can be explained by the presence of the negatively charged residue (glutamate

residue) in the N-terminal region, despite the presence of three positively charged residues (lysine residues), that changed the affinity for the interaction.

Moreover, Dps-Δ15 has shown the importance of this flexible extension for the interaction, showing to be essential for binding. Ceci and colleagues [120] have reported the importance of the N-terminal for DNA-binding and condensation for the *E. coli* Dps, where the lack of this extension only affects the DNA-condensation and not the binding, showing the Dps-DNA complex as "beads-on-a-string". Thus, by comparison, we can infer that *M. hydrocarbonoclasticus* 617 Dps binds supercoiled DNA non-specifically but does have the capacity to condense it, and/or Dps binds to DNA with a different mechanism when compared with the one proposed for the *E. coli* Dps.

5.3.2 EMSAs using the iron-loaded Dps proteins

To investigate the affinity to DNA of iron-loaded Dps protein, samples of holo-protein were prepared with different amounts of ferric mineral core inside the inner cavity of the protein, in the presence of H_2O_2 or O_2 in 50 mM MOPS buffer pH 7.0, 50 mM NaCl.

The DNA binding reactions were prepared as described for the apo-forms using Dps-WT loaded with increasing amounts of Fe^{2+} ions (12, 24, 48, 96, 192 and 384 Fe^{2+}/apo-protein) in the presence of the oxidant. Representative EMSAs and quantification of DNA-protein complex are presented in Figure 5.6.

Comparison with the apo-protein, the iron-loaded forms have lower affinity to DNA, decaying with higher iron loads. When the protein was loaded with sub-stoichiometric amounts of Fe^{2+} ions, between 12 and 48 Fe^{2+}/protein, some shift is observed (lanes 4 and 6 in gels from Figure 5.6), that becomes null for proteins with iron loads above 48. This observation leads us to propose that when the iron is mainly in the form of mineral core (in the inner cavity), the protein no longer has the ability to bind DNA.

Tosha and colleagues [113] have hypothesised a role for the N-terminal extensions as pore gates for the Fe^{2+} entry and exit in M ferritin from frog. These pore gates result from a network interaction which involves the conserved residues Q6 and N7 (N-

terminal), R72 (helix $\alpha 2$) and R122 (loop between helices $\alpha 2$ and $\alpha 3$) present in all eukaryotic ferritins. Although these residues are absent in the mini-ferritins, both types of ferritins share the same 3-fold symmetry channel, the so-called "ferritin-like" channels. In both families, the pore channels create an electrostatic potential, due to the presence of carboxylate residues (aspartate and glutamate residues), that promote the Fe^{2+} traffic into and from the protein cavity, down electrochemical gradient [42]. Therefore, we propose that in the presence of Fe^{2+}, the positively charged residues at the N-terminal (lysine residues in Dps protein) can establish electrostatic interactions with the negatively charged residues in the pore channels (aspartate and glutamate residues). Consequently, when the protein carries a mineral core, acting as an iron storage enzyme, subtle structural modifications will occur at the N-terminal as a channel gate, inhibiting DNA binding.

Nevertheless, some iron-loaded Dps proteins have shown the ability to bind DNA, which is the case of Dps from *Campylobacter jejuni*, *Helicobacter pylori*, and *Deinococcus radiodurans* [124,188,189].

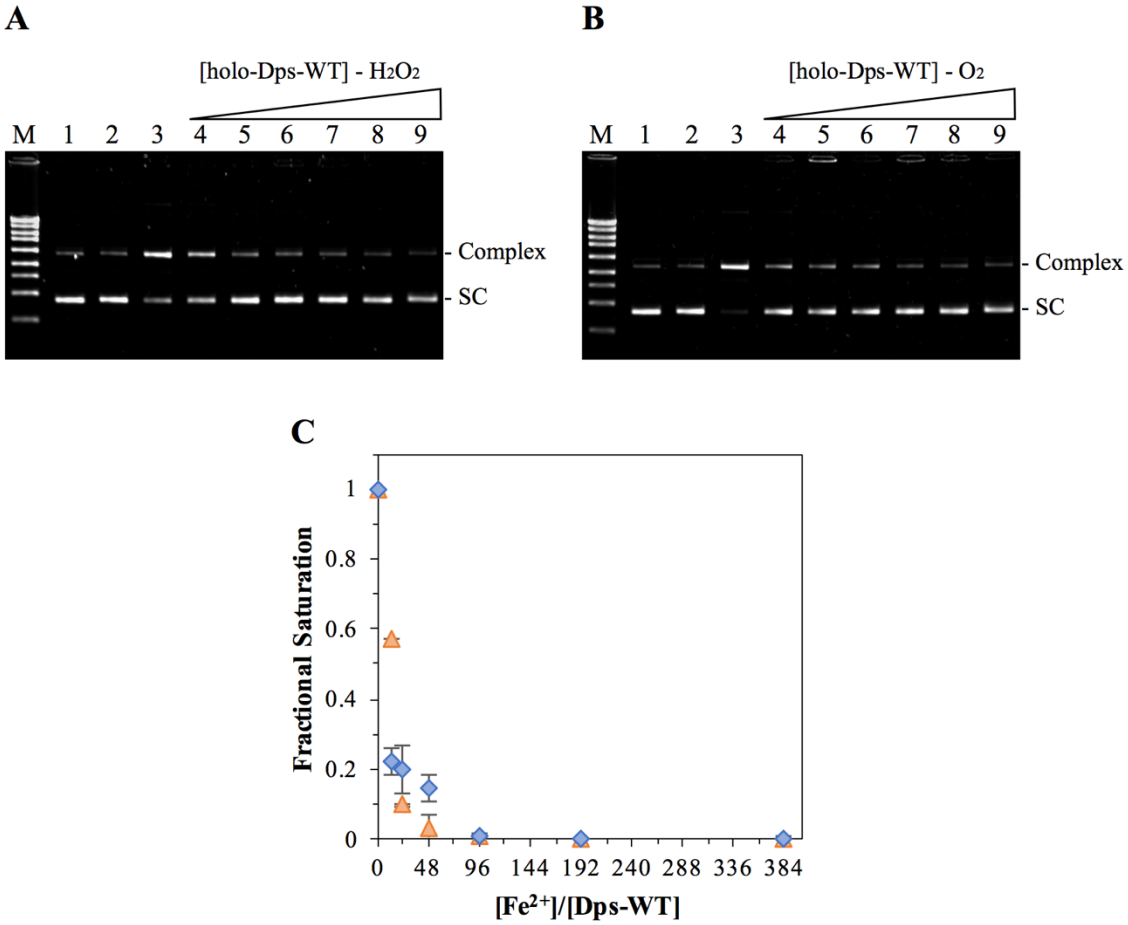

Figure 5.6: DNA binding analysis of iron-loaded Dps in 50 mM MOPS buffer pH 7.0, 50 mM NaCl by EMSA. Binding reaction with loaded Dps-WT produced in the presence of H_2O_2 (A) or O_2 (B). M – NZYLadder II (NZYTech); 1 – Plasmid pUC19 (10 nM); 2 – Binding reaction of BSA (3 µM) to plasmid pUC19 (10 nM); 3 – Binding control of apo-Dps-WT (13 µM) to plasmid pUC19 (10 nM); 4 to 9 – Binding of Dps-WT loaded with 12, 24, 48, 96, 192 and 384 Fe^{2+}/protein. The free supercoiled plasmid band (SC) and the protein-DNA band (complex) are indicated on the right. (C) Comparison of fractional saturation of iron-loaded Dps-WT produced with H_2O_2 (orange triangles) and produced with O_2 (blue diamonds), plotted as averages of two sets of EMSA experiments with an estimated uncertainty less than 7%.

5.3.3 Protection assays

To investigate DNA and protein protection by the formation of protein-DNA complexes, two different assays were performed.

Protein protection in the presence of Proteinase K

When Dps protein was incubated with Proteinase K, as expected most of the protein was hydrolysed (Figure 5.7A, lane 8, and Figure 5.7B, lane 12). The same result was obtained for BSA and Dps-Q14E protein (Figure 5.7B, lanes 2 and 4, respectively). The incubation of the protein-DNA complexes with Proteinase K (Figure 5.7A, lanes 2 to 7) did not affect the complex, while the pre-incubation of Dps-WT protein with Proteinase K prevented the formation of DNA-protein complex (Figure5.7B). Protection of the protein to proteolysis associated with the formation of protein-DNA complexes can be explained by physical shielding of the accessibility of proteinase to DNA bound protein molecules.

The bottom gels in Figure 5.7 correspond to the agarose gel stained with Coomassie Brillant Blue to detect the presence of protein. In accordance with what was described before, when protein is pre-incubated with Proteinase K, the protein is proteolyzed (Figure 5.7B, lanes 6 to 11) and unable to form the complex with DNA. While, when the Proteinase K was added after formation of complex, no proteolysis was verified (Figure 5.7A, lanes 2 to 7).

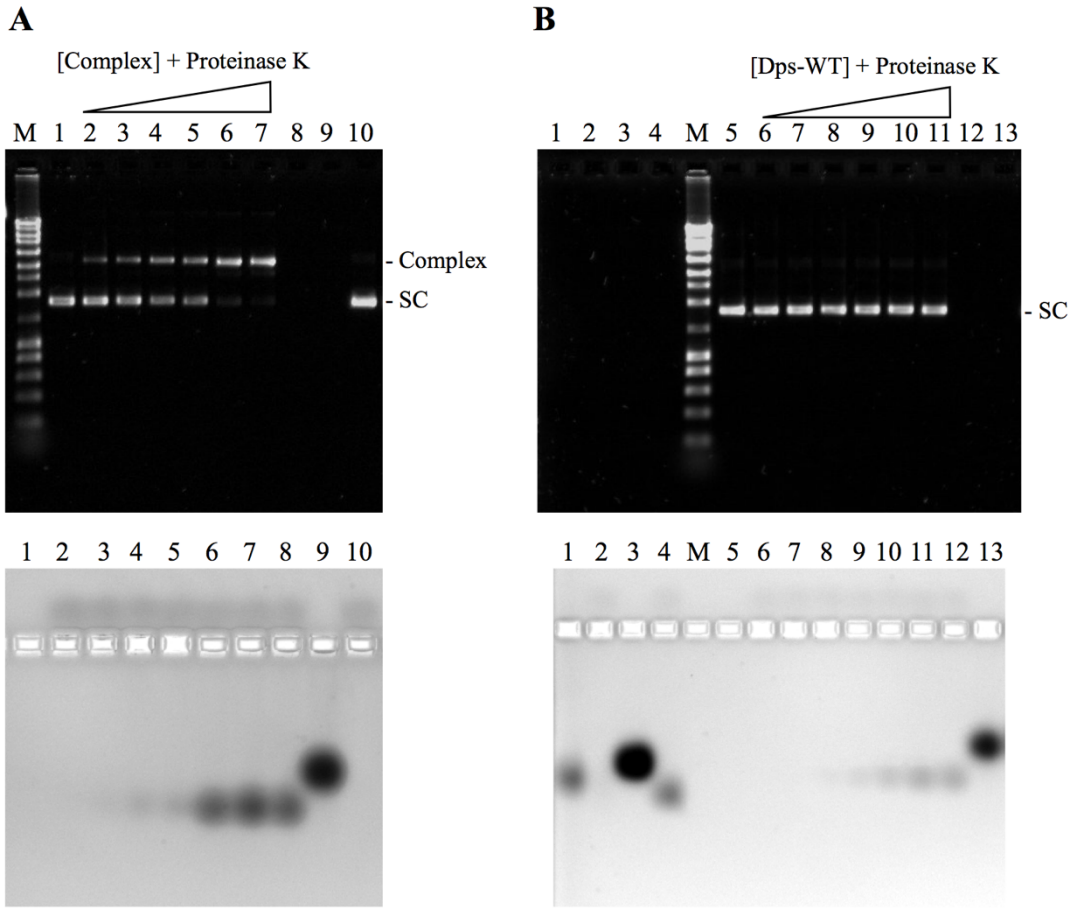

Figure 5.7: Dps protein protection assays against Proteinase K. (A) Protein-DNA complex incubated with Proteinase K. M – NZYLadder III; 1 – Plasmid pUC19 (10 nM); 2 to 7 – Binding reaction of Dps-WT (0.50, 1.0, 3.0, 5.0, 9.0 and 13 μM) to plasmid pUC19 (10 nM) incubated with Proteinase K (20 mg/mL); 8 – Dps-WT (13 μM) incubated with Proteinase K; 9 – Dps-WT (13 μM); 10 – plasmid pUC19 (10 nM) incubated with Proteinase K. (B) Binding of Dps-WT pre-incubated with Proteinase K to supercoiled plasmid pUC19. M – NZYLadder III; 1 – BSA protein (13 μM); 2 – BSA (13 μM) incubated with Proteinase K; 3 – Dps-Q14E protein (13 μM); 4 – Dps-Q14E (13 μM) incubated with Proteinase K; 5 – Plasmid pUC19 (10 nM); 6 to 11 – Binding reaction of pre-incubated Dps-WT (0.50, 1.0, 3.0, 5.0, 9.0 and 13 μM) with Proteinase K to plasmid pUC19 (10 nM); 12 – Dps-WT (13 μM) incubated with Proteinase K; 13 – Dps-WT protein (13 μM). The free supercoiled plasmid band (SC) is indicated on the right. Upper gels stained with SYBR Safe solution for detection of DNA, and lower gels stained with Coomassie Brilliant Blue to detect protein.

DNA protection in the presence of hydroxyl radical

These experiments had the aim to ascertain the protection of plasmid DNA molecule associated to the formation of Dps-DNA complexes or presence of Dps protein when exposed to an excess of deleterious ferrous ions and hydrogen radicals. Thus, supercoiled pUC19 was incubated with Dps proteins (Dps-WT, Dps-Δ15, Dps-Q14E and

iron-loaded Dps-WT (containing 96 Fe atoms per protein) in 50 mM MOPS buffer pH 7.0, 50 mM NaCl followed by exposure to an excess of Fe^{2+} and H_2O_2. The results are shown in Figure 5.8.

Supercoiled DNA was completely hydrolysed in the presence of hydroxyl radical (Figure 5.8, lane 12), while upon pre-incubation with Dps proteins, DNA protection is observed, as shown in lanes 13 and lanes 15 to 17 (Figure 5.8) of the agarose gel. However, in the presence of Proteinase K (Figure 5.8, lane 14), DNA suffered more degradation when compared with the reaction without Proteinase K (Figure 5.8, lane 13). Reactions with the hydroxyl radical were stopped by incubation with SDS at 85 ºC for 2 min, resulting in the disruption of the protein-DNA complex, and denaturation of the protein (lanes 13 to 18 on the lower gel in Figure 5.8). Comparison of the intensity of DNA band in lanes 13 and 14, data seems to indicate that when bound to DNA the protein does not oxidizes ferrous iron or does it at a slower rate. Moreover, results from lanes 15 to 17 suggest that the protection of DNA is due to the ferroxidase activity (in the presence of H_2O_2) of the enzyme Dps, and not a shielding effect by protein binding.

Thus, by observing that (i) in the presence of iron the N-terminal region can adopt an important role in controlling the entry and exit of iron atoms in the protein; and (ii) the holo-Dps-WT (containing 96 Fe per molecule) and the variants Dps-Q14E and Dps-Δ15, do not have affinity to bind DNA, but in the presence of hydroxyl radical they perform their catalytic activity, we can infer that the DNA protection activity by Dps protein relates more with its catalytic activity by rapidly oxidizing Fe^{2+} with H_2O_2 as oxidant than with its DNA-binding activity.

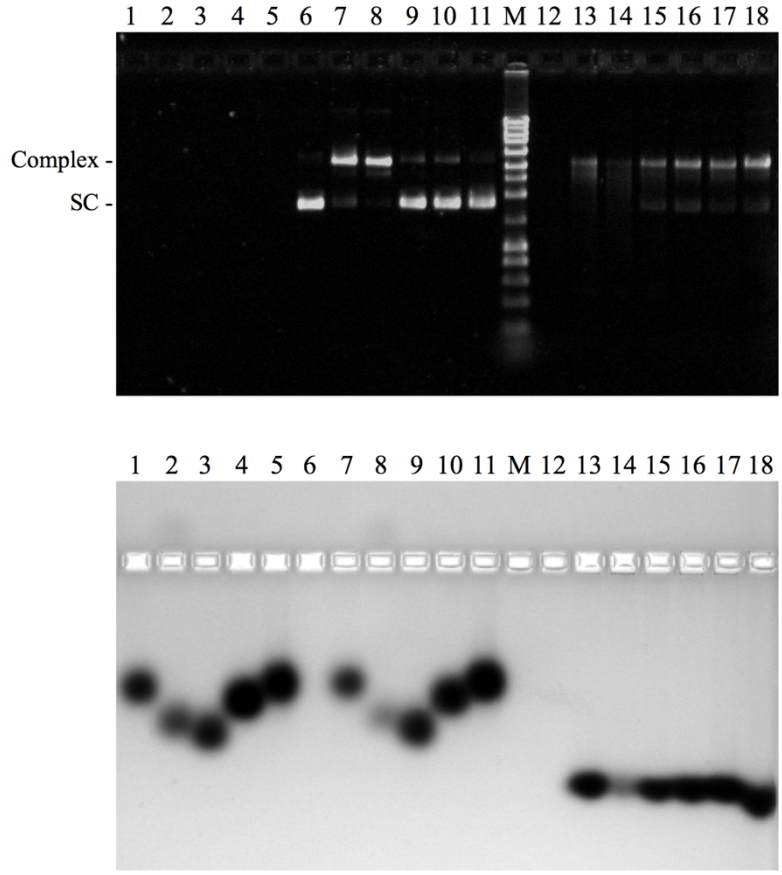

Figure 5.8: Agarose gel electrophoresis analysis of DNA protection assays against Fenton-mediated DNA damage. M – NZYLadder III; 1 – Dps-WT protein (13 µM); 2 – Dps-WT (13 µM) incubated with Proteinase K; 3 – Dps-Δ15 protein (13 µM); 4 – Dps-Q14E protein (13 µM); 5 – Dps-WT loaded with 96 Fe^{2+}/protein (13 µM); 6 – Plasmid pUC19 (10 nM); 7 – Binding of Dps-WT (13 µM) to pUC19 (10 nM); 8 – Binding reaction of Dps-WT (13 µM) to pUC19 (10 nM) incubated with Proteinase K; 9 – Binding of Dps-Δ15 (13 µM) to pUC19 (10 nM); 10 – Binding of Dps-Q14E (13 µM) to pUC19 (10 nM); 11 – Binding of Dps-WT loaded with 96 Fe^{2+}/protein (13 µM) to pUC19 (10 nM); 12 – Plasmid pUC19 (10 nM) exposed to an excess of Fe^{2+} and H_2O_2; 13 – Dps-WT-pUC19 complexes reacted with Fe^{2+} and H_2O_2; 14 – Dps-WT-pUC19 complexes pre-incubated with Proteinase K and reacted with Fe^{2+} and H_2O_2; 15 to 17 – Protein (Dps-Δ15, Dps-Q14E and iron loaded Dps-WT (containing 96 Fe atoms/protein), respectively) incubated with pUC19 and then reacted with Fe^{2+} and H_2O_2; 18 – Dps-WT-pUC19 complexes reacted with SDS. The free supercoiled plasmid band (SC) and the protein-DNA band (complex) are indicated on the left. Upper gel stained with SYBR Safe solution for detection of DNA, and lower gel stained with Coomassie Brilliant Blue to detect protein.

6

DNA-binding activity of Dps studied by site-directed spin labelling CW-EPR spectroscopy

6.1 Overview

The ability of Dps to interact with supercoiled DNA through the N-terminal region has been demonstrated in Chapter 5. To investigate the structural and dynamics properties the formation of the DNA-Dps complex was analysed by X-band Continuous Wave (CW)-EPR spectroscopy, using site-directed spin labelling (SDSL). As such, a single cysteine variant was generated replacing the threonine 10 at the N-terminal region.

SDSL consists in introducing a nitroxide side chain at selected sites using site-directed mutagenesis. Due to its reactive sulfhydryl group, cysteine is the most commonly used amino acid residue in SDSL, as it is able to react with the nitroxide reagent [190]. The most used nitroxide reagent is MTSL (also abbreviated as MTSSL), (1-Oxyl-2,2,5,5-tetramethyl-Δ3-pyrroline-3-methyl) methanethiosulfonate spin label, which generates the spin label side chain commonly designated as R1 (Figure 6.1).

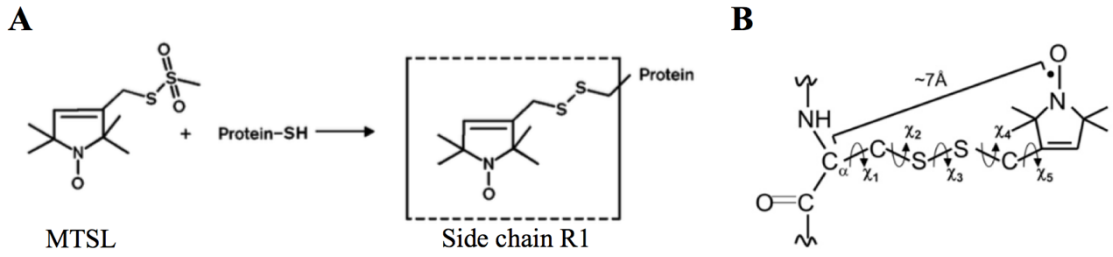

Figure 6.1: Generation of the spin label side chain R1. (A) Reaction of MTSL with cysteine to generate the spin label side chain R1. Adapted from [192]. (B) Structure of R1 showing the five torsion angles between C_α and the nitroxide ring. Depending on these torsion angles, the distance from C_α to the unpaired electron localized to the N-O bond is ~7 Å. Adapted from [191].

R1 has five torsion angles between C_α and the nitroxide ring allowing label rotation independently of the protein backbone. This feature makes MTSL adaptable to most proteins sites without disturbing either the native fold or the function of the protein. Nevertheless, the binding of MTSL and protein can be reversible. In this case, the appearance of three-line spectrum, with the same intensity, is the spectroscopic fingerprint for the release of the spin label in solution (Figure 6.2, Isotropic limit).

CW-EPR spectroscopy of spin-labelled proteins can give information about the nitroxide side chain mobility, the solvent accessibility and the distance between the side chain from either a second nitroxide or another paramagnetic centre in the system, such as a metal ion in the protein [191-193].

The line shape of R1 CW-EPR spectra at room temperature is sensitive to the reorientational motion of the nitroxide side chain due to partial motional averaging of the anisotropic components of the *g* tensor and hyperfine tensor, *A*. When R1 has high mobility the rotational diffusion (tumbling) will be high and the spectrum will be similar to that of a free nitroxide radical, i.e., the anisotropic interactions are averaged out, and only the isotropic average of the magnetic interactions is observed. Thus, the three-line spectrum is centred at a *g* value ($g_x = g_y = g_z$) and separated by an isotropic hyperfine coupling ($A_x = A_y = A_z$) (isotropic limit). The motion of a nitroxide chain is characterized by three correlation times: (i) the rotational correlation time for the entire protein, which can be neglected for soluble proteins with molecular weight above 200 kDa); (ii) the effective correlation time due to the rotational isomerization about the bonds linking the nitroxide to the backbone, that is expected to be a complex function of the spin label molecular structure and the primary, secondary, tertiary and eventually quaternary structure of the protein; and (iii) the effective correlation time for the segmental motion of the backbone with respect to the average protein structure, which is related to backbone flexibility, i.e., to the secondary structure [194].

The different motional regimes characterized by different isotropic correlation times (τ_c) for the R1 probe are represented in Figure 6.2.

The accurate *g* and *A* values can only be achieved by measuring the CW-EPR spectra at W-band (95 GHz), at low temperature, where the Zeeman interaction is fully resolved and consequently the *g* and *A* components are also resolved [193].

The slow-motion CW spectral shape of R1 sometimes can be difficult to characterize due to the presence of different populations of nitroxide in slow exchange. In these cases, the spectral components with different mobilities are labelled as ‘immobile’ and ‘mobile’ components.

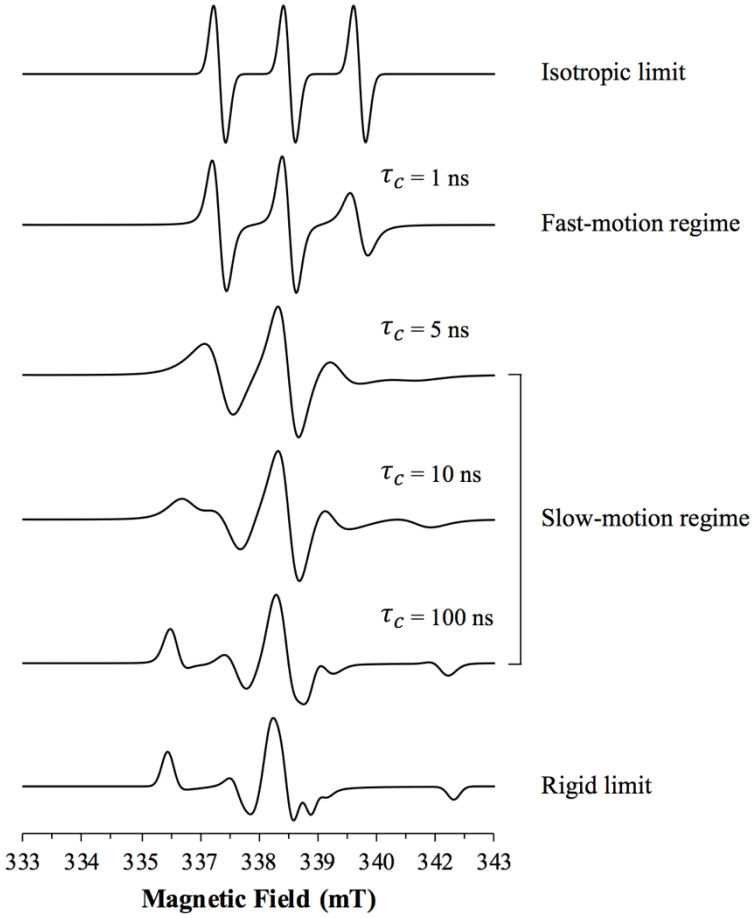

Figure 6.2: The effect of the correlation time (τ_c) on the R1 CW-EPR spectral line shape at room temperature. Spectra were simulated using the EasySpin package [197] for MATLAB with static parameters of *g* tensor of 2.008, 2.006, 2.003 and of *A* tensor of 0.7136, 0.7136, 3.0330 mT. The X-band frequency is 9.5 GHz.

The mobility of R1 can be estimated from the spectrum without simulations by measuring the peak-to-peak amplitude of the low and central field lines, denoted as h(+1)/h(0) ratio. The higher the h(+1)/h(0) ratio, the more mobile is the nitroxide, however, this parameter can only be applied when the R1 spectral line is described by one single spectral component. Another 'mobility' parameter is the inverse value of the linewidth of the central nitroxide spectral line, ΔH_0^{-1}. The smaller the linewidth, the higher is the mobility parameter. Moreover, the spectral breadth along the magnetic field, represented by the second moment of the spectrum ($\langle H^2 \rangle$), has been found to be correlated with the spectral linewidth. In the presence of multicomponent spectra, the mobility parameter ΔH_0^{-1} will be dominated by the most mobile component unless it is present in

extremely small amounts, and $\langle H^2 \rangle$ will be biased toward the less mobile component [192,195,196]. The plot of $(\langle H^2 \rangle^{-1}$ versus ΔH_0^{-1} can serve to identify the topographical location of specific residues in the protein fold, i.e., to distinguish sites buried in the protein core, in helical regions or loops. As an example, Figure 6.3B shows the plot of 'mobility' parameters for T4 Lysozyme.

However, simulations should be performed in an attempt to characterize the R1 spectral line. Here the spectral simulations were performed by using the EasySpin package [197] for MATLAB.

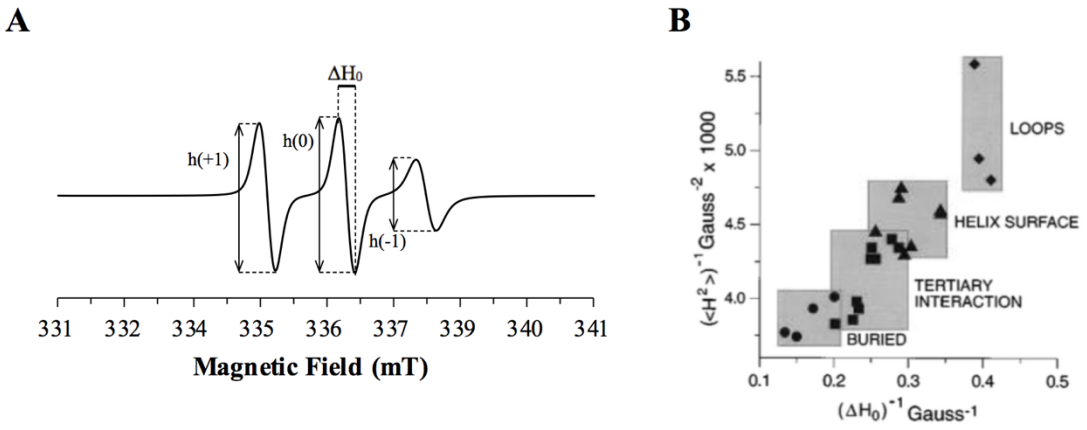

Figure 6.3: 'Mobility' parameters for nitroxide CW-EPR spectrum. (A) Nitroxide CW-EPR spectrum showing the h(+1), h(0), h(-1) and ΔH_0 parameters. (B) Plot of the inverse spectral second moments ($\langle H^2 \rangle^{-1}$) versus the inverse central line widths (ΔH_0^{-1}) for R1 side chain at twenty sites in T4 Lysozyme. Adapted from [196].

6.2 Experimental procedure

Expression and purification of Dps-T10C is described in Chapter 3, Section 3.2.4.2.

6.2.1 Labelling of Dps-T10C protein

Dps-T10C protein was incubated with 5 mM DTT at room temperature for 2 h, to ensure complete reduction of cysteine labelling site. DTT was afterwards removed by size exclusion chromatography using a Superdex 200 prep grade column (GE Healthcare Life Sciences) in 50 mM MOPS buffer pH 7.0, 200 mM NaCl. Spin labelling was

accomplished by the addition of a 10-fold molar excess of MTSL (Toronto Research Chemicals) to labelling sites at room temperature for 2 h.

Unbound MTSL was removed by dialysis against 2 L 50 mM MOPS buffer pH 7.0, 50 mM NaCl in a 12 kDa MWCO dialysis tubing membrane (Medicell Membranes Ltd) at 4 ºC; buffer was replaced after overnight dialysis, and let equilibrate for another 3 h (this last buffer exchange was repeated twice). The dialysed sample was then concentrated by using a Vivaspin 20 concentrator (100 kDa MWCO, Sartorius).

The same procedure was used for the sparsely-labelled samples, analysed in this work, except for the MTSL solution. This solution was substituted by a mixture of MTSL and S-methyl methanethiosulfonate (MMTS, Sigma-Aldrich) for the desired sparse-labelling.

The percentage of labelling was determined by a calibration curve (Figure 6.4), using three different sample concentrations. To build the calibration curve, CW-EPR spectra of the standard solutions of 4'-amino TEMPO (4-Amino-2,2,6,6-tetramethylpiperidinooxy, Fisher Scientific) were double integrated to quantify the absorption intensity for each solution. Standard solutions were prepared by serial dilutions from the 1 mM 4'-amino TEMPO. The stock solution of 4'-amino TEMPO was quantified by UV-visible spectroscopy using the molar absorption coefficient at 400 nm of 12.4 $M^{-1}cm^{-1}$ [198].

6.2.2 CW-EPR analysis

The CW-EPR measurements were carried out on a MiniScope MS 400 spectrometer (Magnettech GmbH) set-up with 9.448 GHz microwave frequency, at room temperature, with 19.9 mW microwave power, 0.1 mT modulation amplitude, and 4096 points acquired within 10 mT field sweep; or at 77 K, with the same frequency and modulation amplitude, but with 0.3 mW microwave power and 4096 points acquired within 20 mT field sweep.

CW-EPR measurements were also performed at room temperature on a Bruker EMX spectrometer set-up with 9.861 GHz microwave frequency, 10 mW microwave power, 0.1 mT modulation amplitude and 2048 points acquired with a 10 mT field sweep.

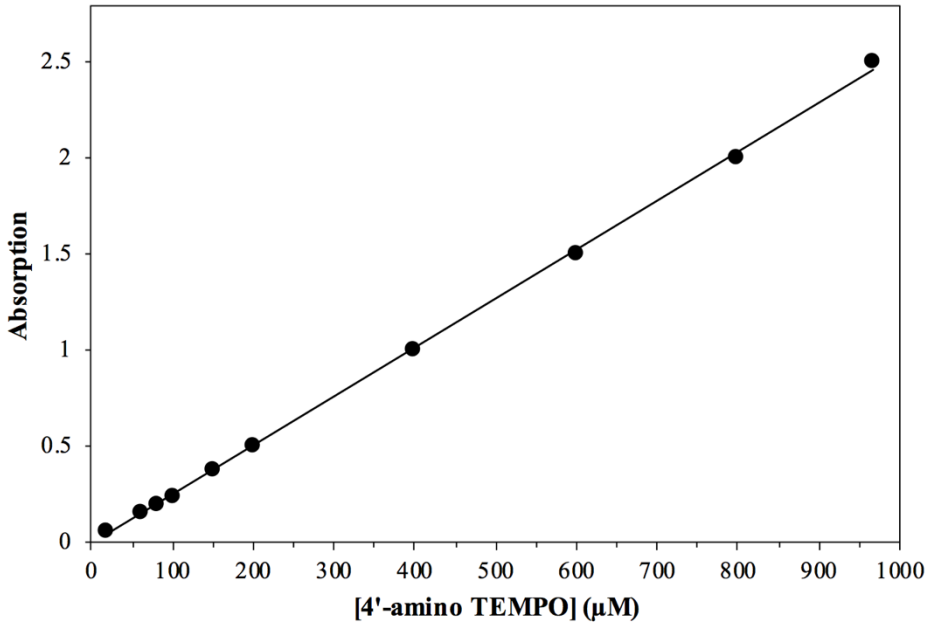

Figure 6.4: A typical calibration curve with 4'-amino TEMPO from the CW-EPR spectra. The trend line equation is Absorption=0.0025×[4'-amino TEMPO] (R^2 = 0.9994). CW-EPR spectra were recorded at room temperature on a MiniScope MS 400 spectrometer, at 9.448 GHz, a microwave power of 19.9 mW, and a modulation amplitude of 0.1 mT. The spectra were integrated by using the software ANALYSIS, provided by the Windows® ESR spectrometer software package (Magnettech GmbH).

6.2.3 CW-EPR samples preparation

The DNA binding to Dps-T10R1 experiments were performed in 50 mM MOPS buffer pH 7.0, 50 mM NaCl, using supercoiled plasmid pUC19 plasmid. Supercoiled pUC19 (105.5 nM) was incubated with Dps-T10R1 (between 1.24 and 7.04 µM) for 15 min at room temperature, in a total volume of 15 µL. Then, 10 µL of reaction were transferred to Ringcaps disposable capillaries 50 µL (Hirschmann) and sealed with Critoseal®.

In the sparse-labelled samples, Dps-T10R1 was used in 50 mM MOPS buffer pH 7.0, 200 mM NaCl. The CW-EPR samples were prepared by using 10 µL of Dps-T10R1 (between 33 and 53 µM) in capillaries as the described before.

A sample of Dps-T10R1 (16.7 μM) in 50 mM MOPS buffer pH 7.0, 50 mM NaCl was analysed at 77 K. The protein solution, 160 μL, was transferred to 2.3 mm ID quartz tube and frozen in liquid nitrogen.

6.3 Results and discussion

6.3.1 Characterization of MTSL spin-labelling

To proceed with the characterization of Dps-DNA interaction by CW-EPR spectroscopy, it is important to start by assessing the Dps-labelling efficiency, as well as to characterize the R1 spectral line.

The CW-EPR spectrum (Figure 6.5) showed that MTSL spin label was completely bound to the protein. As described in Section 6.2.1, the number of spins present in Dps protein was determined as 1.00 ± 0.06 spin per monomer, representing 100% of labelling efficiency.

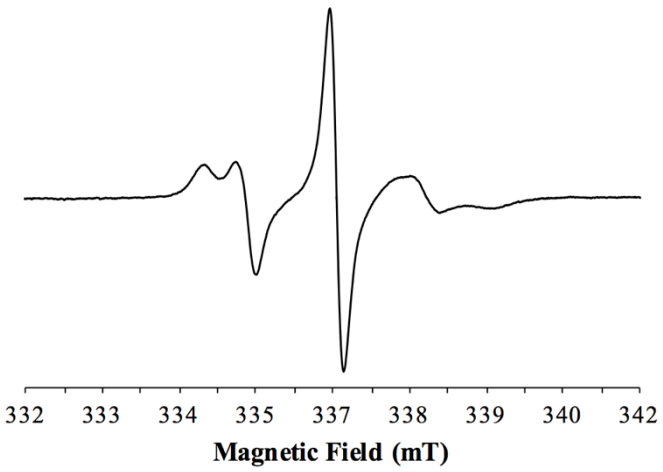

Figure 6.5: CW-EPR spectrum of Dps-T10R1 (7.07 μM) in 50 mM MOPS buffer pH 7.0, 50 mM NaCl. The spectrum was recorded at room temperature on a MiniScope MS 400 spectrometer, at 9.448 GHz, a microwave power of 19.9 mW and a modulation amplitude of 0.1 mT.

Dps-T10R1 (protein 100% labelled with MTSL) was also measured at low temperature and the EPR spectral line fitted (Figure 6.6) using the algorithm Pepper in the software EasySpin to estimate the values of *g* and *A* parameters.

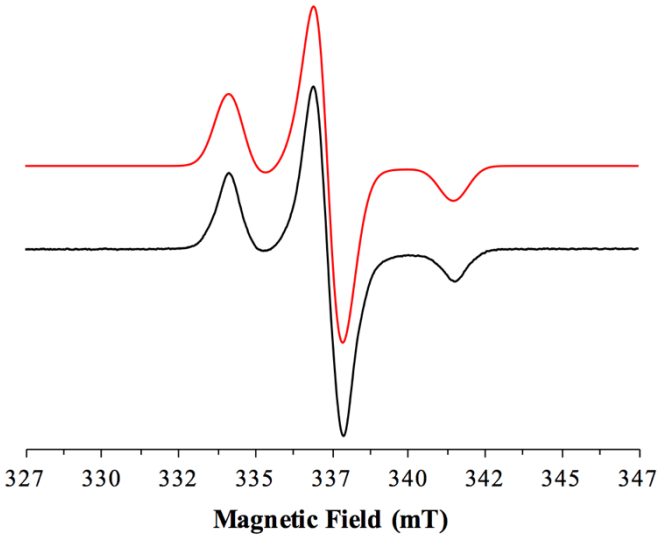

Figure 6.6: CW-EPR spectrum of Dps-T10R1 at 77 K. Black line is the experimental spectrum recorded at 9.448 GHz. The red line is the theoretical simulation of the experimental spectrum using the software EasySpin and the set of parameters listed in Table 6.3.

The set of parameters that produced the best fit the 77 K spectrum were for *g* tensor g_x = 2.0067, g_y = 2.0048, g_z = 2.0012, and *A* tensor A_x = 0.432, A_y = 0.220, A_z = 3.648 mT. These values were used to fit the CW-EPR spectrum measured at room temperature, using the algorithm Chili in EasySpin, which is the most indicated for slow-motion regimes. However, the fit was only possible assuming two components with different anisotropic correlation times, $\tau_c = \tau_x, \tau_y, \tau_z$, that were attributed to two R1 conformations with different motional regimes, fast and slow mobility. Moreover, all parameters were allowed to be adjusted during the fitting, except the *g* and *A* values that were fixed. The resulting spectroscopic parameters are listed in Table 6.3, and the theoretical simulation represented in Figure 6.7A (red line spectrum).

To gain structural/dynamics information of the N-terminal region (Chapter 7) in different experimental conditions, more samples were labelled containing between 12 spins to 1 spin per protein molecule. The spectrum of the 100% labelled sample, 12 spins

per dodecamer, was fitted following the approach above described (Figure 6.7B, red line spectrum).

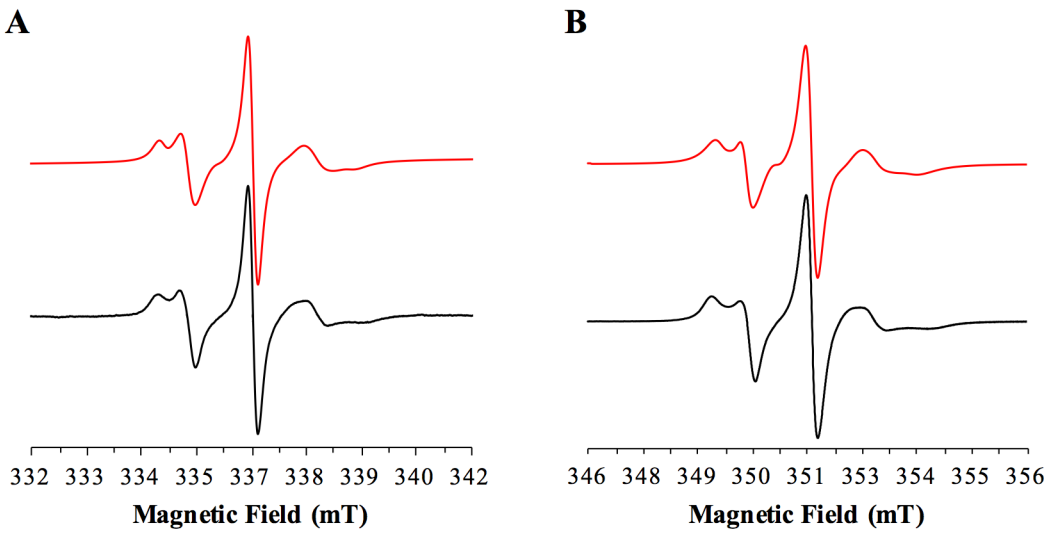

Figure 6.7: CW-EPR spectra of Dps-T10R1 100% labelled, 12 spins per protein, recorded at room temperature. (A) Experimental spectrum (black line) of Dps-T10R1 (7.04 µM) in 50 mM MOPS buffer pH 7.0, 50 mM NaCl, recorded at 9.448 GHz; and its theoretical simulation (red line). (B) Experimental spectrum (black line) of Dps-T10R1 (53.0 µM) in 50 mM MOPS buffer pH 7.0, 200 mM NaCl, recorded at 9.861 GHz; and its theoretical simulation (red line). The parameters used for the theoretical spectra in A and B are listed in Table 6.3.

Both CW-EPR spectra (Figure 6.7 A and B, black line spectra) were explained with the same g and A values (g_x = 2.0066, g_y = 2.0056, g_z = 2.0018, and A_x = 0.41, A_y = 0.18, A_z = 3.95 mT), assuming a component with fast mobility and a component with slow mobility, as before. However, in the case of the spectrum recorded at 9.448 GHz, the fast mobility component represents 71%, and in the case of the sample recorded at 9.861 GHz, this component represents 35% of the total absorption. The differences in the percentage of the fast mobility component can reflect: (i) a certain degree of plasticity of Dps-T10R1 protein which is a multimeric protein containing a total of 12 spins; (ii) different spin-labelling preparations; or (iii) the effect of the ionic strength of the buffers used in the two samples.

In summary, the 12 MTSL spin-labelling Dps spectra, acquired at room temperature, can be characterized as the superposition of two sub-spectra due to the presence of two protein populations with different motional regimes, with fast mobility

and slow mobility. The *g* and *A* values determined from the theoretical simulation of the experimental spectra are slightly smaller than the ones reported for other systems (g_x = 2.0083, g_y = 2.0061, g_z = 2.0022, and A_x = 0.464, A_y = 0.428, A_z = 3.675 mT), and can be associated with the hydrogen bonding network and the polarity of the microenvironment around of the nitroxide site. To ascertain about these effects Dps-T10R1 should be analysed at low temperature at higher magnetic fields, as W-band (95 GHz) EPR or at 360 Ghz, where the Zeeman resolution is increased and consequently facilitates the interpretation of the *g* and *A* components [193,199,200].

The sparse-labelled Dps-T10R1 samples have the same CW-EPR spectral line shape (Figure 6.8A), with different intensities depending on the number of spins per protein molecule. The effective percentage of labelling (Table 6.1) was determined through the calibration curve described in Section 6.2.1. As one can conclude from Table 6.1, the sparse-labelling was efficient, achieving the target labelling with about 6-7% of deviation, except for the sample 50:50 MTSL:MMTS.

Table 6.1: Quantification of sparse-labelling of Dps-T10R1 protein.

[MTSL]:[MMTS]	
Target Labelling (%)	**Effective Labelling (%)**
100	95 ± 5
75	69 ± 5
50	62 ± 5
25	31 ± 5
15	22 ± 1
8	11.7 ± 0.4
1	1.8 ± 0.2

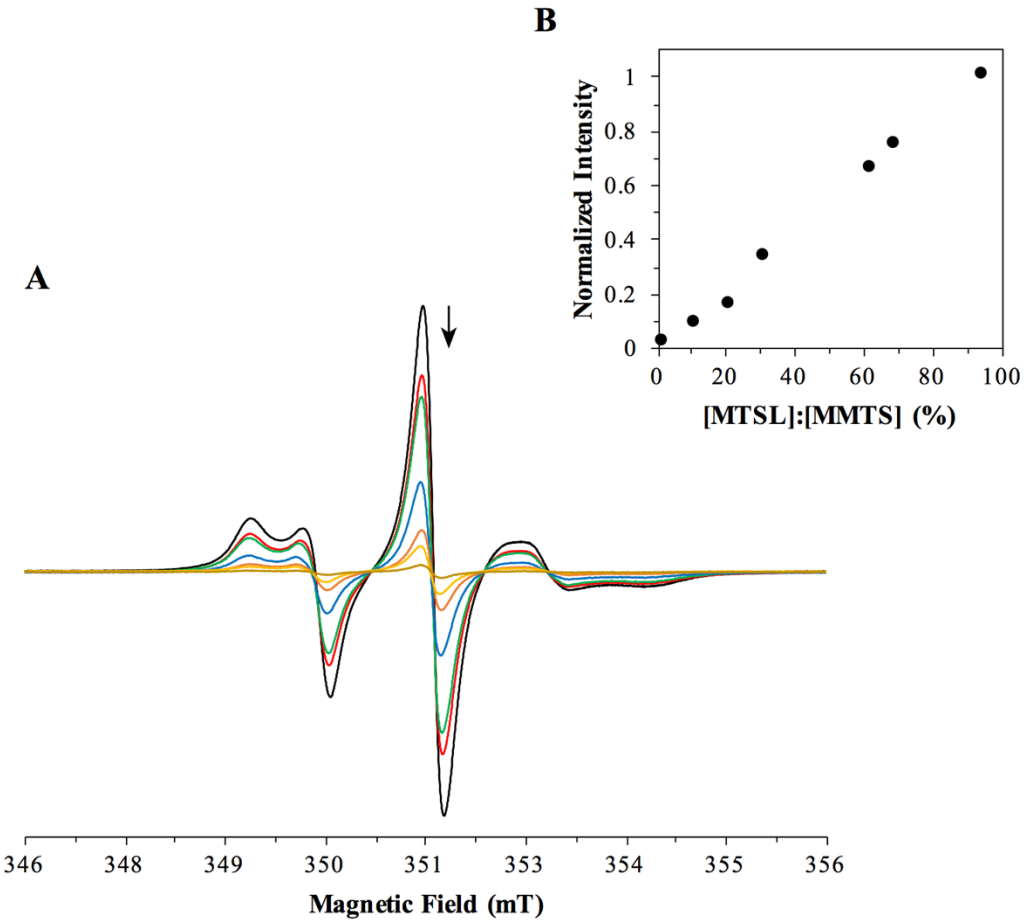

Figure 6.8: Dps-T10R1 labelled with different MTSL:MMTS ratios. (A) Room temperature CW-EPR spectra for Dps-T10R1 sparse-labelled with 100% to 1% of MTSL. The black arrow indicates the decreasing spectral intensity with the percentage of MTSL spin-label. Spectra recorded at 9.861 GHz. (B) Normalized intensity of CW-EPR spectra absorption as a function of the percentage [MTSL]:[MMTS] ratio.

6.3.2 DNA binding interaction

The DNA binding studies by CW-EPR spectroscopy were performed at room temperature, in 50 mM MOPS buffer pH 7.0, 50 mM NaCl for 15 min. The CW-EPR spectra present in Figure 6.9A showed a significant change in the spectral line shape of Dps-T10R1 owing to the presence of plasmid pUC19, with the R1 spin-label on the N-terminal region of the protein becoming more mobile. Simulation of spectra was only possible with an additional third component, attributed to the DNA-protein complex (see theoretical parameters in Table 6.3).

The contributions of the three different components to the total spectra are as R1 conformational populations in Table 6.2, i.e. the percentage of the conformational population with slow mobility, fast mobility and fast mobility in the presence of plasmid DNA.

Table 6.2: Distribution of R1 conformational populations in the different CW-EPR spectra of Dps-T10R1 reacted with plasmid DNA. The spectral line shape colour corresponds to the ones in Figure 6.9A. All parameters are listed in Table 6.3.

CW-EPR Spectrum	R1 Populations		
	Slow mobility (%)	Fast mobility (%)	Fast mobility (interacting with DNA) (%)
Dps-T10R1 (Black spectral line shape)	29	71	—
[Dps-T10R1]:[pUC19] = 67 (Yellow spectral line shape)	23	44	33
[Dps-T10R1]:[pUC19] = 47 (Blue spectral line shape)	14	42	44
[Dps-T10R1]:[pUC19] = 24 (Green spectral line shape)	8	45	47
[Dps-T10R1]:[pUC19] = 12 (Purple spectral line shape)	7	45	48

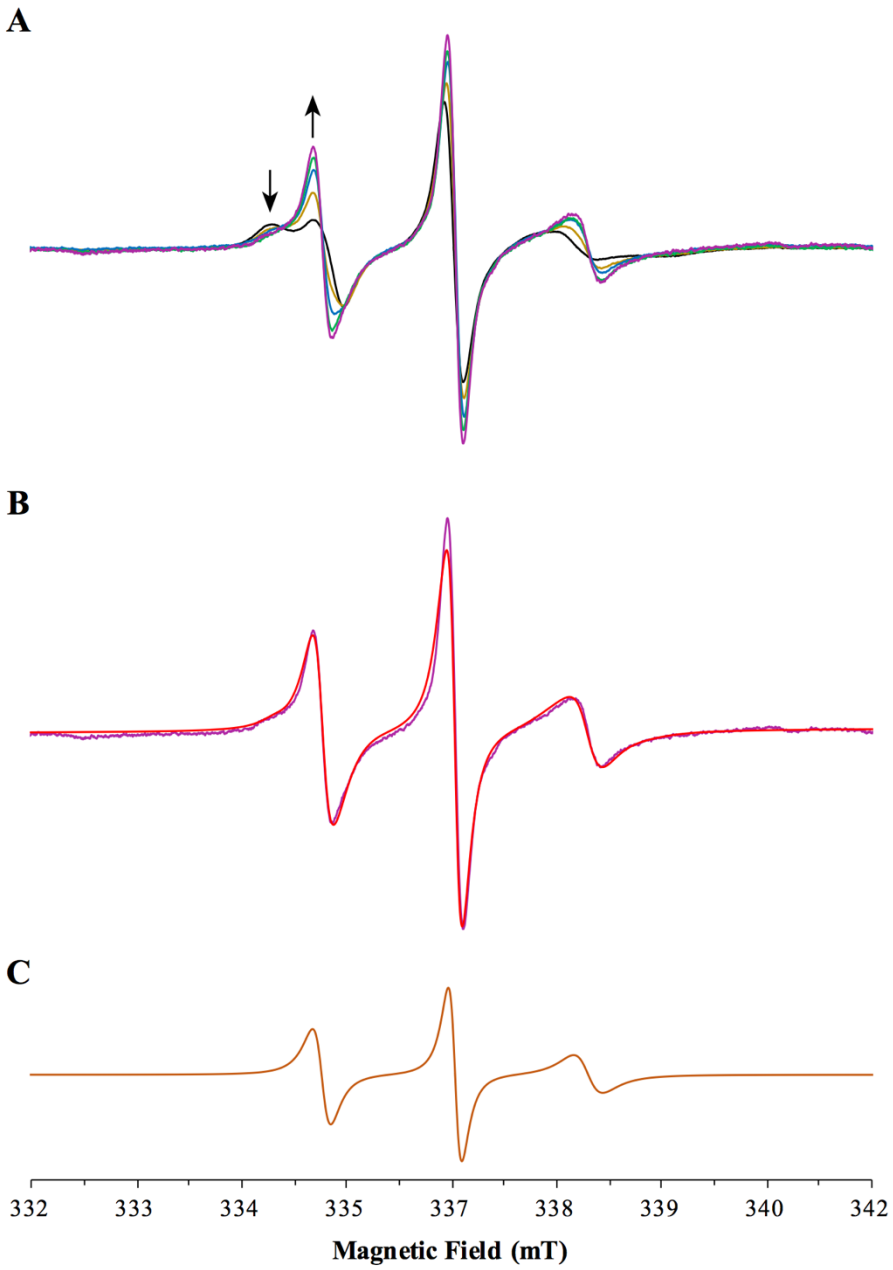

Figure 6.9: CW-EPR analysis of Dps-T10R1-DNA complex. (A) CW-EPR spectrum of Dps-T10R1 protein (7.04 µM, black line) overlaid with Dps-T10R1 (7.04 µM, yellow line; 4.96 µM, blue line; 2.48 µM, green line; 1.24 µM, purple line) reacted with supercoiled plasmid pUC19 (105.5 nM). All spectra were recorded at room temperature at 9.448 GHz. The black arrows indicate the decreasing in the intensity of the slow-mobile population and the increasing of the fast-mobile population. (B) Spectrum of Dps-T10R1 (1.24 µM) reacted with plasmid pUC19 (105.5 nM), purple line, overlaid with its theoretical spectrum simulation (red line). (C) Theoretical simulation of the new fast-mobile population, Dps-T10R1-DNA complex, that accounts for 48% of the purple line spectrum in (B). Parameters are listed in Table 6.3.

Table 6.3: EPR parameters for Dps-T10R1 (100% MTSL), at room temperature, obtained from the fitting of CW-EPR spectra using EasySpin software.[a]

	Dps-T10R1 protein					
	T = 77 K ν = 9.448 GHz	**ν = 9.448 GHz**		**ν = 9.861 GHz**		**ν = 9.448 GHz**
		Slow mobility	**Fast mobility**	**Slow mobility**	**Fast mobility**	**Fast mobility (interacting with DNA)**
g_x	2.0067(4)	2.0066(2)		2.0066(2)		2.0069(4)
g_y	2.0048(2)	2.0056(2)		2.0056(2)		2.0045(4)
g_z	2.0012(1)	2.0018(2)		2.0018(2)		2.0022(2)
A_x (mT)	0.43(3)	0.41(2)		0.41(2)		0.54(4)
A_y (mT)	0.22(2)	0.18(3)		0.18(3)		0.39(2)
A_z (mT)	3.65(4)	3.95(4)		3.95(4)		3.88(6)
lw.G [b] (mT)	0.68(2)	0.151(2)	0.061(9)	0.082(1)	0.024(3)	—
lw.L [b] (mT)	—	—	0.071(9)	0.284(9)	0.012(3)	0.027(6)
τ_x (ns)	—	11060 ± 2515	0.74(2)	51929 ± 2284	0.79(3)	
τ_y (ns)	—	0.493(2)	2.07(8)	0.60(1)	1.88(9)	0.87(3) [c]
τ_z (ns)	—	97 ± 4	0.88(8)	436 ± 252	0.30(8)	
Weight (%)	—	29	71	65	35	—

[a] Values in parentheses correspond to uncertainties of the last significant digits.
[b] Spectral linewidths were described with a Guassian (lw.G), Lorentzian (lw.L) or Voigtian (lw.G and lw.L) lineshapes.
[c] The correlation time, τ_c is isotropic.

Chapter 5 describes the DNA interaction with Dps protein with a dissociation constant, K_d of 5.9 ± 1.0 μM and a co-operativity of 1.2 ± 0.1, described by the Hill equation. The same equation was used to estimate the fractional complex observed by the CW-EPR measurements (Figure 6.10). The fractional complex, θ, was defined as $(\theta = [\text{Spins bound}]/(s \times [\text{DNA}]))$, where $[\text{Spins bound}]$ is the concentration of spins affected by the binding to DNA, s is the number of protein binding sites on the DNA, and $[\text{DNA}]$ is the total concentration of DNA.

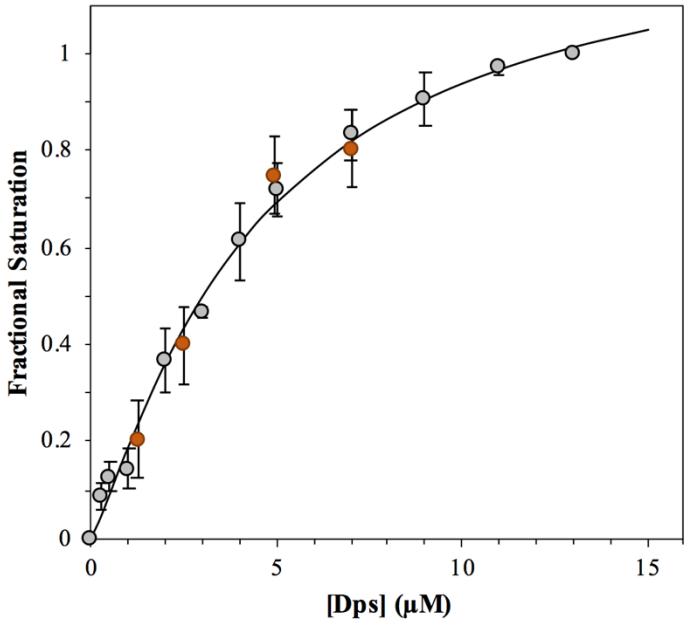

Figure 6.10: Hill plot of DNA binding by Dps protein from EMSA and CW-EPR experiments. Grey circles correspond to EMSA experiments using increasing concentrations of Dps-WT (between 0.25 μM and 13 μM) and supercoiled plasmid pUC19 (10 nM). Orange circles correspond to CW-EPR experiments using concentrations of Dps-T10R1, 100% MTSL labelling, (between 1.24 μM and 7.04 μM) and plasmid pUC19 (105.5 nM).

In the experimental conditions tested, there is a good accordance between the data obtained by EMSA and CW-EPR, explained by the same Hill parameters (with a K_d of 5.9 ± 1.0 μM and a cooperativity of 1.2 ± 0.1). In the case of EMSA, the formation of protein-DNA complexes leads to a smaller migration on the gel, which is observed whenever there is binding of at least one molecule of protein to DNA. On the other hand, the observation of variations of spin-label dynamics in CW-EPR spectra demonstrated the interaction between DNA and the N-terminus of the protein. Thus, it was possible to quantify 9–12 spins/protein affected by DNA binding, and that 21 to 28 molecules of Dps could bind to DNA. As previously suggested by Chiancone and collaborators, these data suggest that Dps protein binds along the DNA molecule, non-specifically, forming the so-called “beads-on-a-string” [124].

7

Structural study of Dps protein by PELDOR

7.1 Overview

In order to understand the functionality and DNA binding properties of Dps through the N-terminal region, site-directed spin labelling (SDSL) [190,192] combined with pulsed electron-electron double resonance (PELDOR) spectroscopy were used. PELDOR is a powerful technique for measuring long-distances in proteins, nucleic acids and protein-DNA complexes, ranging from 1.8 nm up to 8 nm [201-205]. PELDOR measures dipolar coupling between electron spins when a sample is excited by different frequencies, generally designated observer and pump. Here, the 4-pulse PELDOR sequence was used, where the observer pulse sequence sets up a refocused electron spin echo (ESE), which allows measurements outside the dead time where the signal is too weak to be read above background noise (Figure 7.1). The refocused ESE results from the pump pulse which inverts spins from the second species using a π pulse at time *t* inserted between the two π observer pulses [206]. Furthermore, this technique can be applied to chemically identical spin label pairs, which is suited for studying multimeric proteins [207].

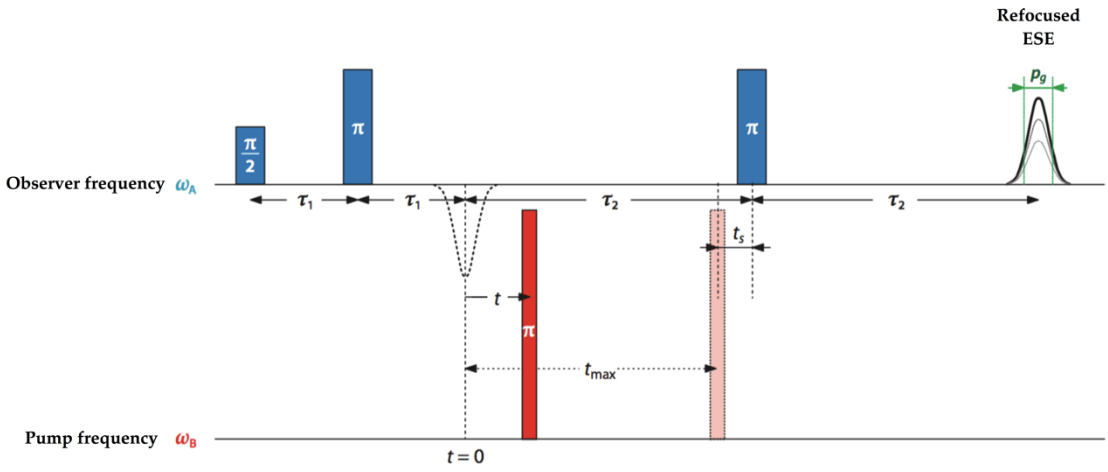

Figure 7.1: 4-pulse PELDOR sequence. Time *t* is varied from $t < 0$ to t_{max}, and variation of the integral echo intensity in the window of length p_g is recorded. Adapted from [207].

The raw PELDOR signal (V(*t*)) is the result of the contribution of the dipolar interaction between two spin labels within the same molecule ($V_{intra}(t)$) and the

contributions of the background ($V_{inter}(t)$), which comes from the dipolar interactions between spin labels on different molecules. The background contribution is usually removed during data analysis. The intra-molecular contributions are described by [208,209]:

$$V_{intra}(t) = V(0)\left(1 - \int_0^{\infty} P(r) \int_0^{\pi/2} \lambda(\theta)\,[1 - \cos(\omega_{dd} t)\sin\theta\, dr d\theta]\right),$$

$$\omega_{dd} = \frac{\mu_0 \beta_e^2 g_A g_B}{4\pi\hbar r^3}(1 - 3\cos^2\theta) \quad (1)$$

where the dipolar coupling is determined by the spin-spin distance r and the angle θ, the angle between distance r and the external magnetic field. In equation (1), g_A and g_B are the g values of the two couple spins, μ_0 is the vacuum permeability, β_e is the Bohr magneton, $V(0)$ is the initial echo intensity, $P(r)$ is the distance distribution of all distances present in the sample and $\lambda(\theta)$ is the probability of flipping the second species through the pump pulse, which is referred as the modulation depth parameter.

The modulation depth (Δ) corresponds to the difference between the intensity at the initial PELDOR echo curve and the value of the background where the PELDOR data oscillates around. It is described by [210]:

$$\Delta = 1 - \left(1 - \lambda(\theta)\right)^{n-1} \quad (2)$$

where n is the number of interacting spins. The modulation depth is used to determine the number of interacting spins in the sample, however, systems with more than two spins can generate sum and difference frequencies that are not necessarily related to a physical distance, commonly known as "ghost peaks" [211]. The multi-spin effects can be reduced by decreasing the flip angle of the pump pulse and by using sparse spin-labelling [212,213].

Moreover, the required t_{max} for the PELDOR experiments depends on the distance being measured. Therefore, the experiments are usually performed at 50 K, where the phase memory time (transverse relaxation time, T_m) for nitroxide is only caused by the fluctuations of the hyperfine field at the electron spin, dominated by the proton spin diffusion of the solvent and the biomolecules [214]. The proton concentration in the sample can be decreased by deuteration of both solvent and protein, allowing to increase the t_{max} and thus allowing measurements up to 10 nm [202].

As mentioned in Chapter 6, the most commonly used spin label (1-Oxyl-2,2,5,5-tetramethyl-Δ3-pyrroline-3-methyl) methanethiosulfonate (MTSL), which contains a nitroxide highly selective for thiol groups, was used in this work. MTSL reacts with the protein's cysteine residues, forming the chain side known as R1 [190,215]. Additionally, S-methyl methanethiosulfonate (MMTS) was used for sparse-labelling, with the aim of decreasing the labelling efficiency.

7.2 Experimental procedure

The expression and purification of protonated Dps-T10C protein is described in Chapter 3, Section 3.2.4.2.

7.2.1 R1 modelling using MTSSL-Wizard

The side chain R1 was added onto the Dps crystallographic structure (unpublished data) using the MTSSL-Wizard, which is a plug-in for PyMOL [216]. MTSSL-Wizard uses a rotamer library for dihedral angles in the leg of R1 to produce a distribution of label rotamers. A 'thorough search' with loose van der Waals restraints (3.4 Å van der Waals radius cut-off, and 3 clashes with the surrounding protein structure allowed) was performed, which produced approximately 240 different rotamers for R1. Distance distributions were produced by measuring distances between each nitroxide from one site to all rotamers at the remaining sites.

7.2.2 Transformation of *E. coli* BLR(DE3) competent cells for production of deuterated Dps-T10C

The *E. coli* BLR(DE3) competent cells (Novagen) were used for expression of Dps-T10C protein in deuterated medium. The transformation procedure was generally performed as described in the manufacturer's protocol.

Competent cells were incubated with the plasmid pET-21c–Dps-T10C on ice for 20 min. Heat-shock was performed at 42 ºC for 30 s, followed by incubation on ice for 2 min. 900 µL SOC medium was added to the transformations and these incubated at 37 ºC for 1 h, at 200 rpm. Cells were plated in LB/Agar medium plates containing 100 µg/mL ampicillin and incubated overnight at 37 ºC.

7.2.3 Expression and purification of deuterated Dps-T10C

Total protein deuteration was accomplished using bacterial growth in Spectra9 deuterated growth media (Cambridge Isotope Inc.).

E. coli BLR(DE3) competent cells containing the plasmid pET-21c–Dps-T10C were inoculated in 1 mL of Spectra9 medium containing 50 µg/mL carbenicillin. After growing overnight at 37 ºC, at 200 rpm, this culture was used to inoculate 100 mL Spectr9 medium containing 50 µg/mL carbenicillin which was grown at 37 ºC at 200 rpm, until an optical density at 600 nm of approximately 0.8 was reached. Gene expression was induced by addition of 1 mM IPTG and the culture was allowed to grow for 15 h at 37 ºC, at 200 rpm. Cells were harvested by centrifugation (at 11,000 × g for 15 min at 4 ºC), resuspended in 10 mM Tris-HCl buffer pH 7.6, 1 mM dithiothrietol (DTT). Before sonication, the cell suspension suffered three cycles of freeze-thaw and was incubated with DNase (1 U/µL, Promega) for 1 h at room temperature. Cell lysis was performed by sonication on a Fisherbrand™Q700 Sonicator (Fisher Scientific), that was equipped with a 2-mm probe. Cells were sonicated on ice for 5 s followed for 10 s of rest, in a total time of sonication of 2 min with 30% amplitude, this process was repeated 4 times with 2 min of cooling between each time. Cell debris were separated by centrifugation at 10,000 × g for 10 min at 4 ºC. The supernatant was then dialysed overnight at 4 ºC against 10 mM Tris-HCl buffer pH 7.6, containing 1 mM DTT.

The soluble crude extract was then filtered (using a 0.45 µM pore syringe filter, Sartorius) and loaded onto a HiTrap™ Q FF (5 mL, GE Healthcare Life Sciences) previously equilibrated with 10 mM Tris-HCl buffer pH 7.6, 1 mM DTT. The protein was eluted with a discontinuous linear gradient using 10 mM Tris-HCl buffer pH 7.6, 1 mM DTT, 1 M NaCl as elution buffer, at a flow rate of 1 mL/min, as follows: 5 min to reach 30% of elution buffer, 30 min until 90% of elution buffer and 25 min to reach 100% of elution buffer. Fractions were analysed by SDS-PAGE using a 15% acrylamide gel and by UV-visible spectroscopy (NanoDrop 2000 Spectrophotometer, Thermo Scientific) to assess purity and for quantification, respectively. Fractions containing the pure protein were concentrated using a Vivaspin 20 concentrator (10 kDa MWCO, Sartorius) until reaching the desired concentration.

7.2.4 Labelling of Dps-T10C protein

MTSL labelling of Dps-T10C was performed as described in Chapter 6. Briefly, the protein was pre-treated with DTT to ensure complete reduction of cysteine labelling site; removal of DTT which was accomplished by size exclusion chromatography on a Superose S12 column (Pharmacia) in 50 mM MOPS buffer pH 7.0, 200 mM NaCl. Spin labelling was achieved by the addition of a 10-fold molar excess of MTSL (Toronto Research Chemicals) to labelling sites at room temperature for 2 h.

Unbound MTSL was removed by dialysis against 2 L of PELDOR buffer (50 mM MOPS buffer pH 7.0, 200 mM NaCl) in 10 kDa MWCO membrane tubing (SnakeSkin Dialysis Tubing, Thermo Scientific) at 4 ºC; buffer was replaced after overnight dialysis, and let equilibrated for another 3 h (this last buffer exchange was replaced twice). Dialysed samples were concentrated using a Vivaspin 20 concentrator (10 kDa MWCO Sartorius) to the desired concentration.

Sparsely-labelled samples were prepared in the same way replacing the MTSL solution by a mixture of MTSL and MMTS (Sigma-Aldrich) according to the desired sparse-labelling ratio. For example, for 8% sparse-labelled sample, the mixture contains 8% MTSL and 92% MMTS.

The effective percentage of labelling was determined by a calibration curve as described in Chapter 6, Section 6.2.1.

7.2.5 Spectroscopic methods

7.2.5.1 CW-EPR

CW-EPR measurements were carried out at room temperature on a Bruker EMX spectrometer set-up with 9.861 GHz microwave frequency, 10 mW microwave power, 0.1 mT modulation amplitude, and 2048 points acquired within 10 mT field sweep.

7.2.5.2 Pulsed EPR

Q-Band Spectrometer Set-up

Q-band (34 GHz) PELDOR was carried out in 3 mm thin wall quartz EPR sample tubes (Wilmad-LabGlass) with 75 µL to 100 µL of protein. Experiments were performed using a Bruker Elexsys E530 spectrometer with a cylindrical ER 5106 QT-2w resonator, over-coupled to give a Q factor of approximately 250-300. The spectrometer was equipped with a cryogen free variable temperature cryostat (Cryogenic limited), operating in the 1.5 – 300 K temperature range. Pulses were amplified using a pulsed travelling wave tube amplifier with a nominal power output of 150 W.

PELDOR

PELDOR was performed at 50 K with samples made up to 50% glycerol-D8 (Cambridge Isotope Laboratories Inc.) to produce a frozen glass using a dead time free 4-pulse sequence. Typically, the $\pi/2$ pulse length was 16 ns and the pump π pulse had a length of 14 – 18 ns. The pump pulse was set to the highest sensitivity point within the absorption spectra with the observer pulse set at an 80 MHz offset, receiver offsets were eliminated using two steps phase cycling. Each experiment had a repetition time of 4 ms and 50 shots per point. The number of data and time points varied between samples, and

each sample was run for the number of scans required to give a suitable signal-to-noise ratio.

7.2.6 Samples preparation

7.2.6.1 CW-EPR samples

CW-EPR samples used to determine the effective percentage of protein labelling were prepared as described in Chapter 6, Section 6.2.3.

The samples consist in 10 µL of Dps-T10R1 (between 17 µM and 53 µM) in 50 mM MOPS buffer pH 7.0, 200 mM NaCl, which were transferred to 0.6 mm ID borosilicate capillary tubes (CM Scientific) and sealed with silicone gel.

7.2.6.2 PELDOR samples

Dps-T10C preparations in PELDOR buffer were exchanged for 2× PELDOR buffer in D_2O by four rounds of sequential concentration and dilution using an Amicon Ultra-0.5 centrifugal concentrator (3 kDa MWCO, Sigma-Aldrich). Samples were finally concentrated up to 50 µL – 100 µL, diluted 1:2 with glycerol-D8 (Cambridge Isotope Laboratories Inc.) and stored in liquid nitrogen until EPR measurements were performed.

7.3 Results and discussion

7.3.1 Prediction of distance distribution on Dps-T10R1 protein

A standard approach for the analysis of distances using PELDOR is to compare the predicted distance distribution of the spin label (MTSL) within the protein with the distances determined by PELDOR.

The distance distribution of the spin label bound to cysteine-10 at the N-terminal of each monomer was predicted using the MTSSL-Wizard plug-in for PyMOL. Due to the spherical symmetry of Dps protein, the prediction resulted in five unique distances with different intensities, with the shortest around 5 nm and the longest distance of

approximately 10 nm. The spatial distribution of the spin label in the Dps protein, as well as, the distance distribution, is shown in Figure 7.2.

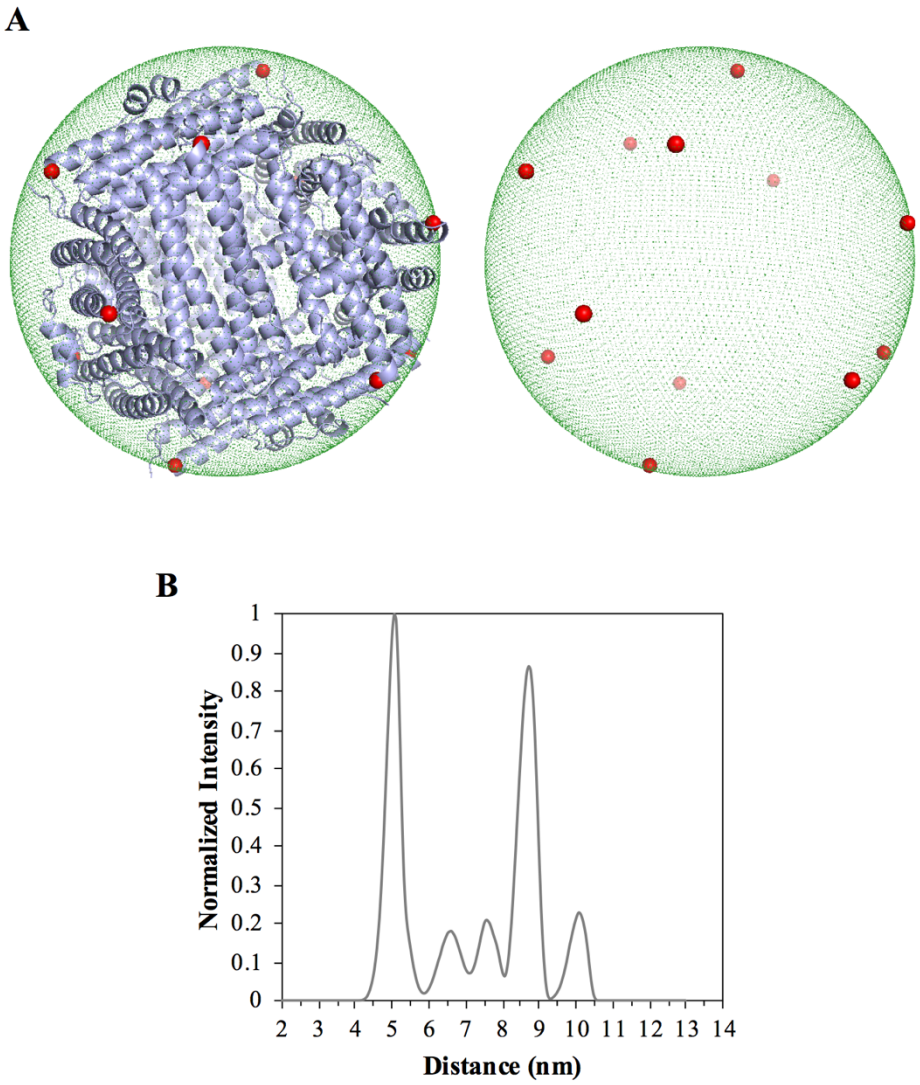

Figure 7.2: Spin label distribution on Dps from *Marinobacter hydrocarbonoclasticus* 617. (A) Dodecamer with 12 spins introduced at position 10 (red spheres) in each chain (left panel); and spatial distribution of the 12 spins (right panel). (B) Distance distribution predicted by MTSSL-Wizard.

The longest predicted distance of 10 nm would be difficult to measure by PELDOR due to the limitation of t_{max}, since we are working with a large multi-labelled protein. This limitation can be minimized by deuteration of both protein and solvent as mentioned before [202].

7.3.2 Expression and purification of deuterated Dps-T10C

Dps-T10C was produced in *E. coli* BLR (DE3) grown in Spectra9 deuterated medium, with a cell yield of 4.93 g/L (wet weight).

Figure 7.3 shows the analysis of whole cells protein profile by SDS-PAGE. The results prove the production of the protein in the soluble fraction, with an apparent molecular mass around 15 kDa, that corresponds to the Dps-T10C monomer (which has a molecular mass of around 17.8 kDa).

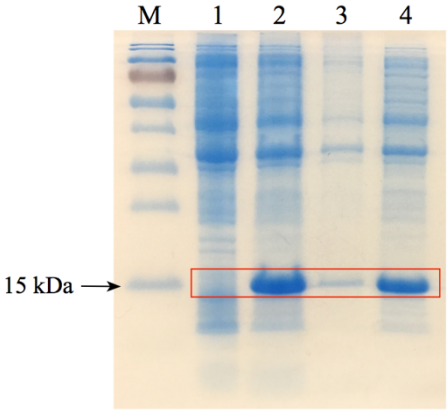

Figure 7.3: Protein Dps-T10C expression profile of deuterated Dps-T10C assessed by SDS-PAGE (15% acrylamide gel). M – PageRuler PreStained Protein Ladder (Thermo Scientific – Appendix A.2.2); 1 – Protein extract of the overexpression culture before induction; 2 – Protein extract after 15 h of induction with 1 mM of IPTG; 3 – Pellet from centrifugation; 4 – Supernatant from centrifugation. Red box highlights the band corresponding to the Dps-T10C monomer. For comparison samples were normalized as described in Chapter 2, Section 2.2.1.4.

As determined by the ProtParam tool on the ExPASy Server [150], the isoelectric point (pI) of Dps-T10C protein is 5.01. Accordingly, deuterated protein was purified by ion exchange chromatography using a HiTrap Q FF (5 mL), as described in Section 7.2.3. Figure 7.4 shows the elution profile of Dps-T10C protein using 10 mM Tris-HCl buffer pH 7.6, 1 mM DTT, 1 M NaCl as elution buffer. The purity of eluted fractions was then analysed by SDS-PAGE (15% acrylamide gel), as shown in Figure 7.5.

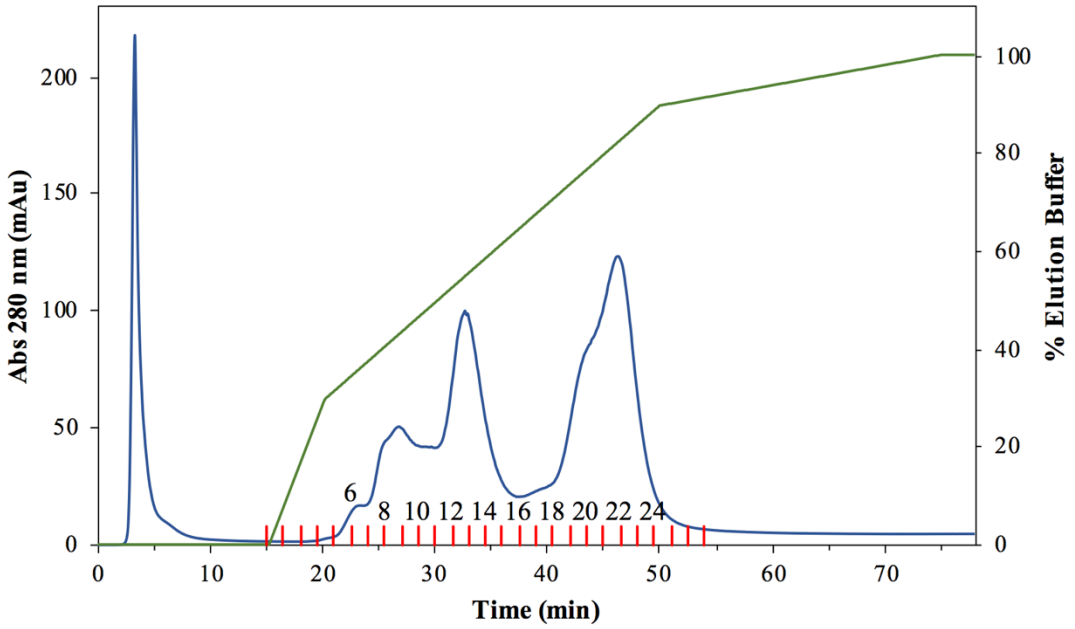

Figure 7.4: Anion exchange chromatography elution profile of deuterated Dps-T10C protein. The blue line represents the absorbance at 280 nm; the green line is the gradient of the elution buffer. Collected fractions containing 1.5 mL of eluted protein are represented in red vertical bars.

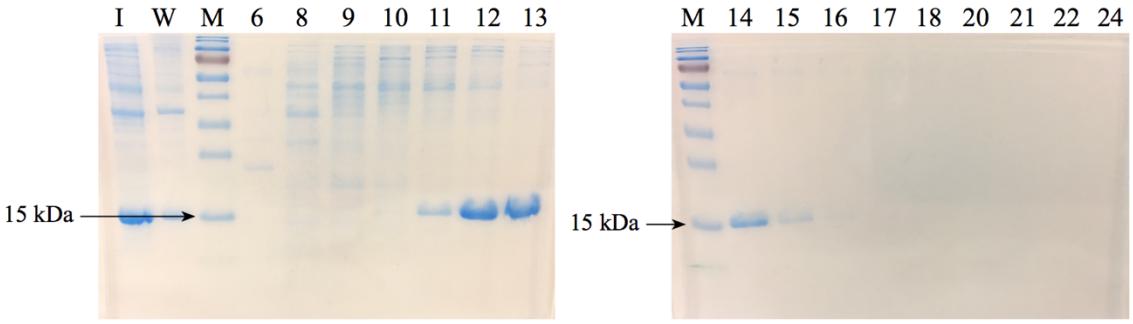

Figure 7.5: SDS-PAGE analysis of chromatographic step (15% acrylamide gel). I – Soluble crude extract (8 µL of a 1:3 dilution); W – Flow-through fraction (15 µL); M – PageRuler PreStained Protein Ladder (5 µL); numbers on top of gels represent the number of eluted fractions from the chromatographic column and marked on the chromatogram of Figure 7.4. Application of 12 µL of each fraction.

Based on the analysis of both the chromatographic elution profile and the SDS-PAGE gels, fractions 11 to 16, eluted between 490 mM and 650 mM of NaCl, were pooled together in a single fraction. This fraction was then quantified by UV-visible

spectroscopy and concentrated using a Vivaspin 20 concentrator to the desired concentration. The protein was stored at -80 ºC until labelling with MTSL.

7.3.3 Labelling of Dps-T10C protein

As mentioned before, Dps-T10C protein is a homopolymeric protein with 12 spins when fully labelled, which leads to multi-spin effects when processing the PELDOR data. To minimize these effects, sparsely-labelled samples were prepared using a mixture of MTSL/MMTS to reach 75%, 50%, 25%, 15%, 8% and 1% of MTSL as described in Section 7.2.4.

The efficiency of labelling was assessed by CW-EPR spectroscopy at room temperature as showed in Chapter 6, Section 6.3.1. Efficient spin labelling was obtained for all samples, with the spin label fully bound to the protein, which indicated that the dialysis after the labelling was effective for removing all the unbound spin probe.

The effective percentage of labelling was determined by the calibration curve (Chapter 6, Section 6.2.1) with 4'-amino TEMPO as standard. As demonstrated (Table 6.1 from Chapter 6) the labelling procedure (100% and sparse-labelling) was considered efficient, allowing to proceed with PELDOR studies.

7.3.4 PELDOR data

Since one of the major aims of this work was to characterize the Dps protein-DNA complex, it was important to start determining the PELDOR features of the protonated Dps protein in the absence of DNA. For that, distance distribution of Dps-T10R1 determined by PELDOR was compared with the one predicted in silico using MTSSL-Wizard.

Experimental PELDOR data were analysed using the DeerAnalysis 2015, a MATLAB package developed by Gunnar Jeschke [217]. For all data experiments the 'ghost suppression' option was used to minimize the "ghost peaks", due to the multimeric nature of the protein, which contains 12 spins leading to a multi-spin contribution to the dipolar coupling.

Figure 7.6 shows the different time traces (after background correction), the corresponding distances distributions (Tikhonov distribution) and the modulation depth, for each sample. Here, a decrease in the modulation depth with increasing sparse-labelling was visible, as well as, some clarification of distances distributions, especially in the low range. These results showed the decrease of multi-spin effects by sparse-labelling and consequently the decrease of modulation depth, due to the presence of fewer spins (spin dilution effect) which contribute less for the dipolar coupling [211].

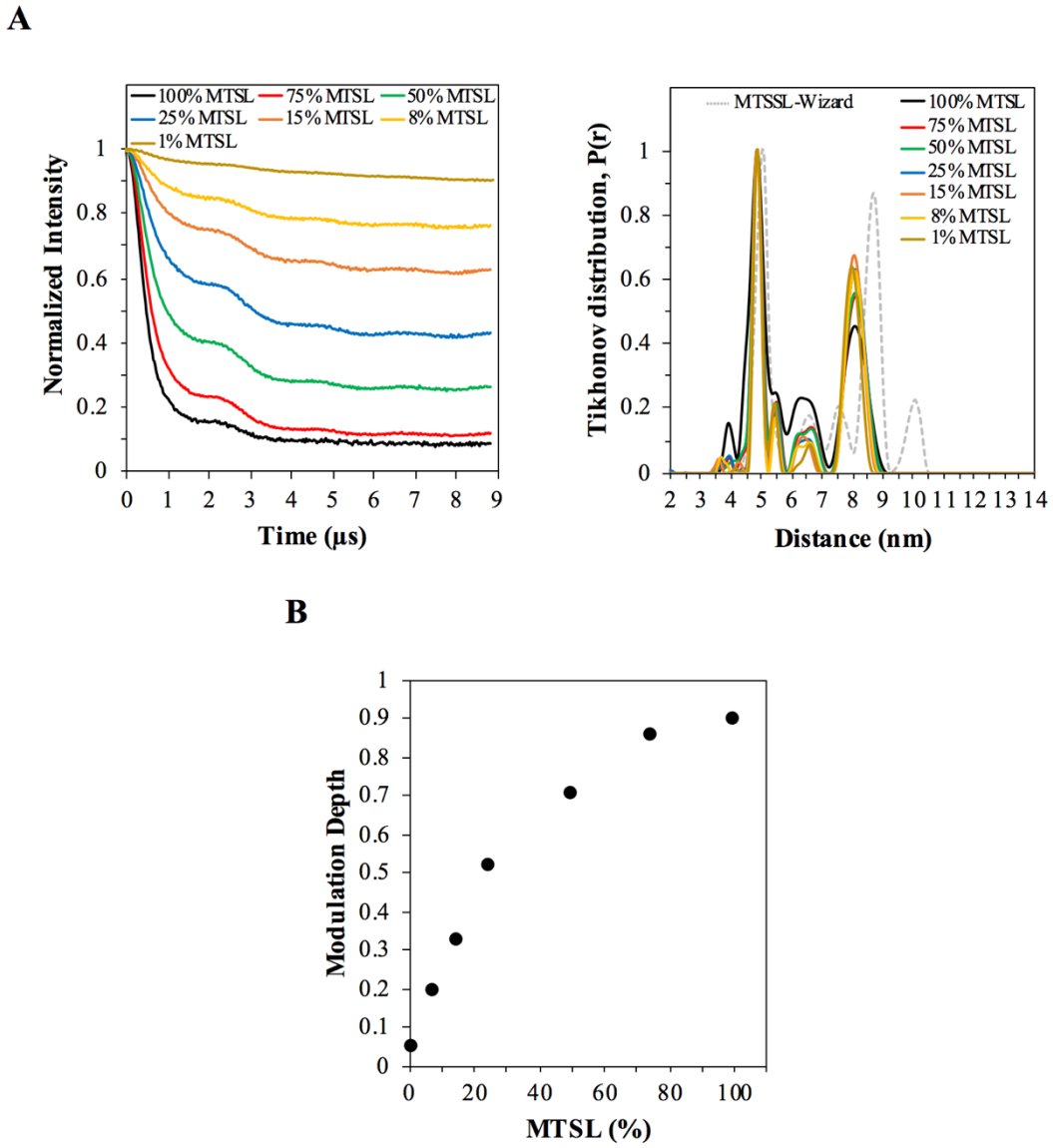

Figure 7.6: Dps-T10R1 PELDOR data for the different ratios of MTSL:MMTS labelling. (A) PELDOR time traces (with background correction). (B) Tikhonov distribution determined from each time trace on (A). (C) Modulation depth as a function of percentage of MTSL in the sparse-labelled protein samples.

For these samples (prepared with protonated protein and deuterated solvent) the t_{max} of 9 µs allowed to obtain the longest distance at about 8 nm and the shortest distance around 5 nm. The predicted distance, based on the X-ray crystal structure, for the shortest distance, was the same one determined by PELDOR, but the longest distance predicted was around 10 nm and the distances around 6.5 nm and 7.5 nm were not resolved in the Tikhonov distribution. In order to improve these results, especially the resolution of the middle and longest distances, and to extend the t_{max}, a sparsely-labelled sample was prepared using deuteration of both protein and solvent. Analysis of the data of differently sparse-labelled protonated protein samples (Figure 7.6B) lead to the conclusion that the sparse-labelling percentage with 8% MTSL showed some improvements in the middle peaks and a reasonably good signal-to-noise ratio.

It was possible to extend the PELDOR measurements to 30 µs and 50 µs for the deuterated protein, due to the extension of the T_m [202]. Comparison of distance distributions between the protonated and deuterated forms of Dps-T10R1 with 8% MTSL is shown in Figure 7.7.

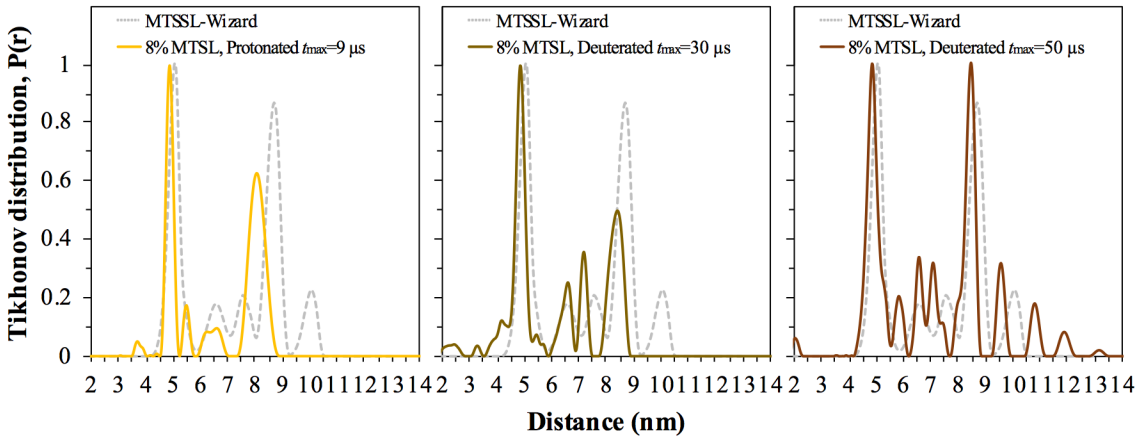

Figure 7.7: Distance distribution for protonated and deuterated Dps-T10R1 (8% MTSL) protein. The left panel is the Tikhonov distribution for the protonated form with t_{max} of 9 µs; the middle and the right panels are the Tikhonov distribution for the deuterated form with t_{max} of 30 µs and 50 µs, respectively.

For t_{max} = 30 µs (Figure 7.7, middle panel) there was a resolution improvement on the middle peaks, and the longest distance was, in this case, around 8.5 nm. When the t_{max}

was increased to 50 μs (Figure 7.7, right panel), an improvement on the resolution of the longer distances was observed, such as the one at 8.5 nm and at around 9.5nm, despite the presence of distances longer than 11 nm when the expected longest distance was 10 nm. Besides sparse-labelling with 8% and deuteration, multi-spin effects can be minimized, enhancing the resolution on the longest distances, by attenuating the PELDOR pulse [212]. Using PELDOR measurements of 20 μs, the attenuation of the pulse decreases the flip angle of the pump pulse from 180º through to 32º (Figure 7.8).

This last approach showed that for a flip angle of 180º, the shortest distance was at around 5 nm, the longest distance is a broad peak between 8 nm and 9 nm, and in the middle, there is an overlap between two peaks. By decreasing the flip angle (Figure 7.8), it was possible to observe the shortest distance at the same position (~5 nm) and a resolution improvement for the longest distances, with the longest distance at ~10 nm (observed for the flip angle of 63º and 32º).

Overall, these measurements showed that sparse-labelling, deuteration of both protein and solvent, and changing the flip angle on the pump pulse are a very good approach to suppress multi-spin contributions in a complex system such as Dps protein, a molecule with symmetric geometry that contains 12 spins. However, only the shortest distance, at 5 nm, is a reliable measurement whereas the longest distances are still not fully resolved. Characterization of the MTSL spin-label in the N-terminus of the protein (Chapter 6) has shown some structural heterogeneity in this region, which suggests that the distance distribution based on the crystal structure may not represent the real distance distribution of the N-terminus in the protein when the protein is in solution.

Nevertheless, PELDOR measurements should be made in the presence of DNA in order to understand if both, the distance distribution profile, and the shortest distance, change upon DNA binding. Unfortunately, due to time constraints, PELDOR measurements of Dps with DNA were not conducted in this work.

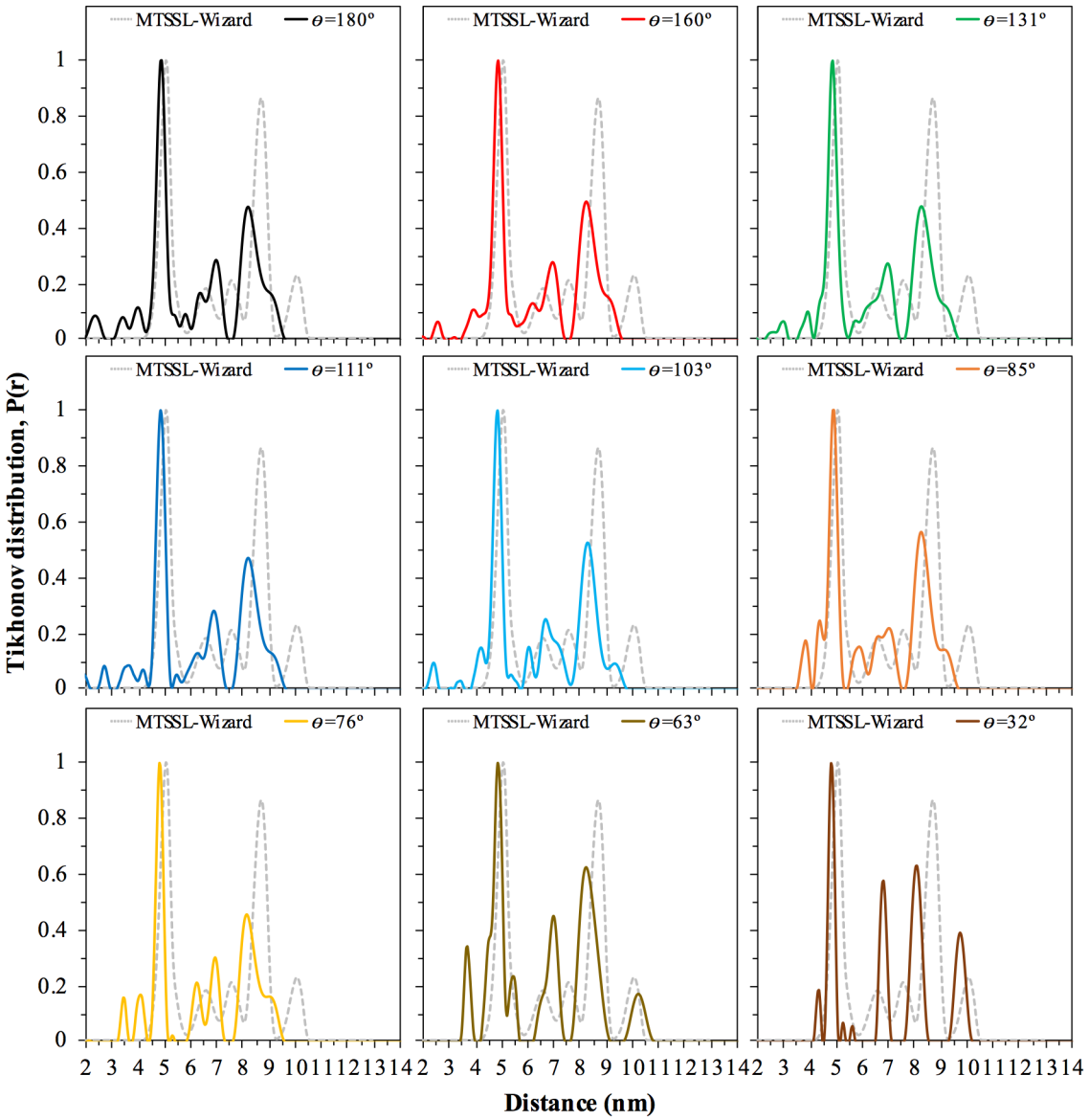

Figure 7.8: Tikhonov-derived distance distribution at decreasing flip angle on PELDOR pulse. Attenuation from 5 dB (180º) to 27 dB (32º).

8

Conclusions and Future work

The work presented in this Thesis focused on the characterization of proteins from the ferritin family, particularly centred on the physiological role of Bfr and on the catalytic and DNA-binding mechanisms of Dps, two bacterial proteins from the ferritin family. The main role of ferritin proteins is to store Fe^{2+} ions in their inner cavity in the form of mineral core, and release it to be used in a variety of vital cellular processes.

The two studied proteins are structurally different, at various levels, namely subunit composition, catalytic sites, and presence of haem group in bacterioferritin. Both share the preference of H_2O_2 as oxidant co-substrate, contrarily to the canonical maxi-ferritins.

The Bfr protein targeted in this work is from *Desulfovibrio vulgaris* Hildenborough, a sulphate reducer that can survive long periods of air exposure and co-expresses a Ftn and a Bfr. The Dps protein is from *Marinobacter hydrocarbonoclasticus* 617, a gram-negative bacterium found in seawater, able to degrade petroleum hydrocarbons. All the protein preparations used in this work were obtained in a soluble and apo-form, that allowed the study of iron uptake and oxidation mechanism with both co-substrates, H_2O_2 and O_2.

Chapter 2 was dedicated to the study of Bfr. Iron uptake assays demonstrated the preference of Bfr to use H_2O_2 as co-substrate to oxidize Fe^{2+} ions, in clear contrast with what has been reported for these proteins [218]. According to the EMSA results, *D. vulgaris* Bfr demonstrated ability to bind supercoiled plasmid DNA, with a K_d of 1.5 ± 0.3 μM, and short DNA duplex, a very important discover. The DNA-binding ability is a feature common to some Dps proteins, such as Dps proteins from *E. coli*, *M. smegmatis* and *D. radiodurans* [43,58,120]. Moreover, Bfr demonstrated the ability to protect DNA against hydroxyl radical due to its capacity to rapidly oxidize the Fe^{2+} ions by using H_2O_2 as co-substrate. Based on these results, we hypothesise that the physiological role of *D. vulgaris* Bfr is similarly to that of Dps proteins. Therefore, *D. vulgaris* expresses Ft, which uses O_2 to oxidize iron rapidly for storage purposes, and co-expresses Bfr protein which uses H_2O_2 for iron oxidation, and to bind and protect DNA.

From the ferritin family, DNA-binding activity has been only reported for Dps and for *D. vulgaris* Bfr. Nevertheless, overall, Dps proteins are those in which the ferroxidation, mineralization and releasing mechanisms are less understood.

The ferroxidase activity of *M. hydrocarbonoclasticus* Dps was investigated in Chapter 4. Iron uptake assays demonstrated the preference of this protein to rapidly oxidize iron using H_2O_2, a characteristic common among these proteins. Additionally, Mössbauer studies provided evidence that when the protein contains 12 Fe^{2+}/protein, and after oxidation with H_2O_2, the iron forms μ-oxo binuclear Fe^{3+} clusters, similarly to the ones observed for ferritins [97,175].

Mössbauer spectroscopic studies also provided evidence of the reactivity of the mineral core in the absence of oxidant, a feature which was never reported to date. These studies showed that in the absence of oxidant, and when Dps protein contains a mineral core, Fe^{2+} ions are oxidized and incorporated into the mineral core. This new ability of Dps protein to oxidize and mineralize iron ions in the absence of oxidant could have a physiological relevance for facultative or anaerobic bacteria and opens up the discussion for iron biomineralization by Dps proteins.

As mentioned before, in addition to ferrodoxidase activity, some Dps proteins have the ability to bind DNA non-specifically and protect it from oxidative damage. In Chapter 5, EMSAs were performed using wild-type Dps protein and variants. Dps variants included a N-terminal deletion of the first fifteen amino acid residues, as well as point mutation where glutamine-14 residue was replaced by a glutamate residue, since the flexible positively charged N-terminal region has been indicated as a mediator for the interaction, and *M. hydrocarbonoclasticus* Dps contains this structural element with these characteristics. EMSAs have shown the ability of *M. hydrocarbonoclasticus* Dps to bind non-specifically to supercoiled plasmid DNA with a K_d of 5.9 ± 1.0 μM. The flexible N-terminal region revealed to be essential for the interaction with DNA, as Dps variants have shown no interaction with DNA.

CW-EPR spectroscopy using site-directed spin labelling was used to complement the characterization of the DNA-binding activity, described in Chapter 6. This technique allowed to characterize the dynamic properties of a spin-label (MTSL) bound to the N-terminal region. CW-EPR experiments revealed that 9–12 spins/protein were affected by DNA binding and that 21 to 28 molecules of Dps could bind to pUC19 plasmid DNA. By comparison with *E. coli* Dps, where the lack of N-terminus only affected the DNA-condensation but not the binding [120], and HP-NAP, that binds randomly to DNA,

forming complexes with a morphology of "bead-on-a-string" at pH 8.0 [124], CW-EPR results suggest that *M. hydrocarbonoclasticus* Dps binds randomly and non-specifically to supercoiled plasmid DNA, without condensate, but forming the so-called "beads-on-a-string" complexes.

Some iron-loaded proteins have also shown the ability to bind DNA [124,188,189], however, in the experimental conditions used, iron-loaded *M. hydrocarbonoclasticus* Dps showed a weak affinity (near null) for DNA-binding. It is likely that in the presence of Fe^{2+}, the positively charged residues at the N-terminus can establish electrostatic interactions with the negatively charged residues in the "ferritin-like" pore, where is the entry and exit of iron atoms. Thus, acting as a gate for the Fe^{2+} entry and exit, similarly to what happens in M ferritin from frog [113].

Formation of protein-DNA complex showed to be important for protein protection. Assays performed with Proteinase K demonstrated that the formation of the Dps-DNA complexes could physically shield the accessibility of Proteinase K to the Dps molecules bound to DNA. On other hand, protection assays against hydroxyl radical suggest that DNA protection activity by Dps protein is probably more associated with its catalytic activity to rapidly oxidize Fe^{2+} using H_2O_2 as oxidant, than with its DNA-binding activity.

The Dps variant used for the CW-EPR experiments was also characterized structurally by PELDOR spectroscopy. PELDOR spectroscopy allows to accurately determine the distance distribution of the N-terminus in the Dps protein. Due to the hollow-spherical structure of Dps, composed by 12 monomers, there are five unique distances predicted between each N-terminal region, with the shortest and the longest distances ~5 nm and ~10 nm, respectively, and the intermediate distances ~6.5 nm, ~7.5 nm and ~8.5 nm.

The Dps protein was produced in deuterated medium and sparsely-labelled with 8% of MTSL, since a fully labelled Dps protein containing 12 spins, lead to multi-spin effects. Despite the different experiments performed with PELDOR, it was only possible to determine accurately the shortest distance of 5 nm, as predicted, whereas the intermediate and the longest distances were not resolved. However, these results are very important, giving a distance distribution profile between the N-terminus of Dps protein.

As future work, supplementary experiments should be performed by PELDOR spectroscopy using the Dps-DNA complex, in order to compare the distance distribution profile. Additionally, to complement the structural information about the interaction between protein and DNA from PELDOR, determining the high-resolution structure of Dps-DNA complex with X-ray crystallography or cryo-EM would be very elucidative. AFM microscopy could also be used to characterize the morphology and packaging of the "beads-on-a-string" complexes.

A DNA-binding activity of *D. vulgaris* Bfr should be further explored in a tentative to identify structural features or motifs involved in the binding. Variants and other forms of proteins could also be tested to understand possible regulation mechanisms. Structural and spin-labelling studies of the protein and DNA molecule could be performed.

Bibliography

1 Andrews SC (1998) Iron storage in bacteria. *Adv. Microb. Physiol.* **40**, 281–351.
2 Groves JT (2003) The bioinorganic chemistry of iron in oxygenases and supramolecular assemblies. *Proc. Natl. Acad. Sci. U.S.A.* **100**, 3569–3574.
3 Bruyneel B, Woestyne MV & Verstraete W (1989) Lactic acid bacteria: Micro-organisms able to grow in the absence of available iron and copper. *Biotechnol. Lett.* **11**, 401–406.
4 Weinberg ED (1997) The Lactobacillus Anomaly: Total Iron Abstinence. *Perspect. Biol. Med.* **40**, 578–583.
5 Ponka P (2000) Iron metabolism: Physiology and Pathophysiology. *J. Trace Elem. Exp. Med.* **13**, 73–83.
6 Ratledge C (2007) Iron metabolism and infection. *Food Nutr Bull* **28**, S515–23.
7 Christen Y (2000) Oxidative stress and Alzheimer disease. *Am. J. Clin. Nutr.* **71**, 621S–629S.
8 Crichton RR & Ward RJ (1995) Iron species in iron homeostasis and toxicity. *Analyst* **120**, 693.
9 Valko M, Rhodes CJ, Moncol J, Izakovic M & Mazur M (2006) Free radicals, metals and antioxidants in oxidative stress-induced cancer. *Chem. Biol. Interact.* **160**, 1–40.
10 Aisen P, Enns C & Wessling-Resnick M (2001) Chemistry and biology of eukaryotic iron metabolism. *Int. J. Biochem. Cell Biol.* **33**, 940–959.
11 Kehrer JP (2000) The Haber–Weiss reaction and mechanisms of toxicity. *Toxicology* **149**, 43–50.
12 Imlay JA (2003) Pathways of oxidative damage. *Annu. Rev. Microbiol.* **57**, 395–418.
13 Imlay JA (2008) Cellular defenses against superoxide and hydrogen peroxide. *Annu. Rev. Biochem.* **77**, 755–776.
14 Andrews SC, Robinson AK & Rodríguez-Quiñones F (2003) Bacterial iron homeostasis. *FEMS Microbiol. Rev.* **27**, 215–237.
15 Crichton R (2001) Intracellular Iron Storage and Biomineralization. In *Inorganic biochemistry of iron metabolism: from molecular mechanisms to clinical consequences* 2nd ed., pp. 133–165. John Wiley & Sons, LTD, Chichester, UK.
16 Andrews SC (2010) The Ferritin-like superfamily: Evolution of the biological iron storeman from a rubrerythrin-like ancestor. *Biochim. Biophys. Acta* **1800**, 691–705.
17 Theil EC (2011) Ferritin protein nanocages use ion channels, catalytic sites, and nucleation channels to manage iron/oxygen chemistry. *Curr. Opin. Chem. Biol.* **15**, 304–311.
18 Crichton RR & Declercq J-P (2010) X-ray structures of ferritins and related proteins. *Biochim. Biophys. Acta* **1800**, 706–718.
19 Zhang Y & Orner BP (2011) Self-assembly in the ferritin nano-cage protein superfamily. *Int. J. Mol. Sci.* **12**, 5406–5421.
20 Harrison PM & Arosio P (1996) The ferritins: molecular properties, iron storage function and cellular regulation. *Biochim. Biophys. Acta Bioenerg.* **1275**, 161–203.
21 Hintze KJ & Theil EC (2006) Cellular regulation and molecular interactions of the ferritins. *Cell. Mol. Life Sci.* **63**, 591–600.
22 Arosio P, Ingrassia R & Cavadini P (2009) Ferritins: a family of molecules for iron storage, antioxidation and more. *Biochim. Biophys. Acta* **1790**, 589–599.
23 Bou-Abdallah F (2010) The iron redox and hydrolysis chemistry of the ferritins. *Biochim. Biophys. Acta* **1800**, 719–731.
24 Theil EC, Behera RK & Tosha T (2013) Ferritins for Chemistry and for Life. *Coord. Chem. Rev.* **257**, 579–586.

25 Rohrer JS, Islam QT, Watt GD, Sayers DE & Theil EC (1990) Iron environment in ferritin with large amounts of phosphate, from *Azotobacter vinelandii* and horse spleen, analyzed using extended X-ray absorption fine structure (EXAFS). *Biochemistry* **29**, 259–264.
26 Aitken-Rogers H, Singleton C, Lewin A, Taylor-Gee A, Moore GR & Le Brun NE (2004) Effect of phosphate on bacterioferritin-catalysed iron(II) oxidation. *J. Biol. Inorg. Chem.* **9**, 161–170.
27 Lewin A, Moore GR & Le Brun NE (2005) Formation of protein-coated iron minerals. *Dalton Trans.*, 3597–3610.
28 Sievers F, Wilm A, Dineen D, Gibson TJ, Karplus K, Li W, Lopez R, McWilliam H, Remmert M, Söding J, Thompson JD & Higgins DG (2011) Fast, scalable generation of high-quality protein multiple sequence alignments using Clustal Omega. *Mol. Syst. Biol.* **7**, 1–6.
29 The UniProt Consortium (2017) UniProt: the universal protein knowledgebase. *Nucleic Acids Res.* **45**, D158–D169.
30 Pettersen EF, Goddard TD, Huang CC, Couch GS, Greenblatt DM, Meng EC & Ferrin TE (2004) UCSF Chimera--a visualization system for exploratory research and analysis. *J. Comput. Chem.* **25**, 1605–1612.
31 Dickey LF, Sreedharan S, Theil EC, Didsbury JR, Wang YH & Kaufman RE (1987) Differences in the regulation of messenger RNA for housekeeping and specialized-cell ferritin. A comparison of three distinct ferritin complementary DNAs, the corresponding subunits, and identification of the first processed in amphibia. *J. Biol. Chem.* **262**, 7901–7907.
32 Torti FM & Torti SV (2002) Regulation of ferritin genes and protein. *Blood* **99**, 3505–3516.
33 Friedman A, Arosio P, Finazzi D, Koziorowski D & Galazka-Friedman J (2011) Ferritin as an important player in neurodegeneration. *Parkinsonism Relat. Disord.* **17**, 423–430.
34 Bou-Abdallah F, Santambrogio P, Levi S, Arosio P & Chasteen ND (2005) Unique iron binding and oxidation properties of human mitochondrial ferritin: a comparative analysis with Human H-chain ferritin. *J. Mol. Biol.* **347**, 543–554.
35 Drysdale J, Arosio P, Invernizzi R, Cazzola M, Volz A, Corsi B, Biasiotto G & Levi S (2002) Mitochondrial Ferritin: A New Player in Iron Metabolism. *Blood Cells Mol. Dis.* **29**, 376–383.
36 Santambrogio P, Biasiotto G, Sanvito F, Olivieri S, Arosio P & Levi S (2007) Mitochondrial ferritin expression in adult mouse tissues. *J. Histochem. Cytochem.* **55**, 1129–1137.
37 Romão CV, Louro R, Timkovich R, Lübben M, Liu MY, LeGall J, Xavier AV & Teixeira M (2000) Iron-coproporphyrin III is a natural cofactor in bacterioferritin from the anaerobic bacterium *Desulfovibrio desulfuricans*. *FEBS Lett.* **480**, 213–216.
38 Weeratunga SK, Gee CE, Lovell S, Zeng Y, Woodin CL & Rivera M (2009) Binding of *Pseudomonas aeruginosa* apobacterioferritin-associated ferredoxin to bacterioferritin B promotes heme mediation of electron delivery and mobilization of core mineral iron. *Biochemistry* **48**, 7420–7431.
39 Yao H, Wang Y, Lovell S, Kumar R, Ruvinsky AM, Battaile KP, Vakser IA & Rivera M (2012) The structure of the BfrB-Bfd complex reveals protein-protein interactions enabling iron release from bacterioferritin. *J. Am. Chem. Soc.* **134**, 13470–13481.

40 Almirón M, Link AJ, Furlong D & Kolter R (1992) A novel DNA-binding protein with regulatory and protective roles in starved *Escherichia coli*. *Genes Dev.* **6**, 2646–2654.
41 Haikarainen T & Papageorgiou AC (2010) Dps-like proteins: structural and functional insights into a versatile protein family. *Cell. Mol. Life Sci.* **67**, 341–351.
42 Chiancone E & Ceci P (2010) The multifaceted capacity of Dps proteins to combat bacterial stress conditions: Detoxification of iron and hydrogen peroxide and DNA binding. *Biochim. Biophys. Acta* **1800**, 798–805.
43 Roy S, Saraswathi R, Chatterji D & Vijayan M (2008) Structural studies on the second Mycobacterium smegmatis Dps: invariant and variable features of structure, assembly and function. *J. Mol. Biol.* **375**, 948–959.
44 Reon BJ, Nguyen KH, Bhattacharyya G & Grove A (2012) Functional comparison of *Deinococcus radiodurans* Dps proteins suggests distinct in vivo roles. *Biochem. J.* **447**, 381–391.
45 Liu X, Kim K, Leighton T & Theil EC (2006) Paired Bacillus anthracis Dps (Mini-ferritin) Have Different Reactivities with Peroxide. *J. Biol. Chem.* **281**, 27827–27835.
46 Facey PD, Hitchings MD, Saavedra-Garcia P, Fernandez-Martinez L, Dyson PJ & Del Sol R (2009) *Streptomyces coelicolor* Dps-like proteins: differential dual roles in response to stress during vegetative growth and in nucleoid condensation during reproductive cell division. *Mol. Microbiol.* **73**, 1186–1202.
47 Ali Azam T, Iwata A, Nishimura A, Ueda S & Ishihama A (1999) Growth phase-dependent variation in protein composition of the *Escherichia coli* nucleoid. *J. Bacteriol.* **181**, 6361–6370.
48 Altuvia S, Almiron M, Huisman G, Kolter R & Storz G (1994) The dps promoter is activated by OxyR during growth and by IHF and σs in stationary phase. *Mol. Microbiol.* **13**, 265–272.
49 Calhoun LN & Kwon YM (2011) Structure, function and regulation of the DNA-binding protein Dps and its role in acid and oxidative stress resistance in *Escherichia coli*: a review. *J. Appl. Microbiol.* **110**, 375–386.
50 Grainger DC, Goldberg MD, Lee DJ & Busby SJW (2008) Selective repression by Fis and H-NS at the *Escherichia coli* dps promoter. *Mol. Microbiol.* **68**, 1366–1377.
51 Nair S & Finkel SE (2004) Dps Protects Cells against Multiple Stresses during Stationary Phase. *J. Bacteriol.* **186**, 4192–4198.
52 Arnold AR & Barton JK (2013) DNA Protection by the Bacterial Ferritin Dps via DNA Charge Transport. *J. Am. Chem. Soc.* **135**, 15726–15729.
53 Bellapadrona G, Ardini M, Ceci P, Stefanini S & Chiancone E (2010) Dps proteins prevent Fenton-mediated oxidative damage by trapping hydroxyl radicals within the protein shell. *Free Radic. Biol. Med.* **48**, 292–297.
54 Grant RA, Filman DJ, Finkel SE, Kolter R & Hogle JM (1998) The crystal structure of Dps, a ferritin homolog that binds and protects DNA. *Nat. Struct. Biol.* **5**, 294–303.
55 Zeth K (2012) Dps biomineralizing proteins: multifunctional architects of nature. *Biochem. J.* **445**, 297–311.
56 Zanotti G, Papinutto E, Dundon WG, Battistutta R, Seveso M, Del Giudice G, Rappuoli R & Montecucco C (2002) Structure of the Neutrophil-activating Protein from *Helicobacter pylori*. *J. Mol. Biol.* **323**, 125–130.

57 Stillman TJ, Upadhyay M, Norte VA, Sedelnikova SE, Carradus M, Tzokov S, Bullough PA, Shearman CA, Gasson MJ, Williams CH, Artymiuk PJ & Green J (2005) The crystal structures of *Lactococcus lactis* MG1363 Dps proteins reveal the presence of an N-terminal helix that is required for DNA binding. *Mol. Microbiol.* **57**, 1101–1112.

58 Bhattacharyya G & Grove A (2007) The N-terminal extensions of *Deinococcus radiodurans* Dps-1 mediate DNA major groove interactions as well as assembly of the dodecamer. *J. Biol. Chem.* **282**, 11921–11930.

59 Roy S, Saraswathi R, Gupta S, Sekar K, Chatterji D & Vijayan M (2007) Role of N and C-terminal tails in DNA binding and assembly in Dps: structural studies of *Mycobacterium smegmatis* Dps deletion mutants. *J. Mol. Biol.* **370**, 752–767.

60 Honarmand Ebrahimi K, Hagedoorn P-L & Hagen WR (2015) Unity in the biochemistry of the iron-storage proteins ferritin and bacterioferritin. *Chem. Rev.* **115**, 295–326.

61 Boyd D, Vecoli C, Belcher DM, Jain SK & Drysdale JW (1985) Structural and functional relationships of human ferritin H and L chains deduced from cDNA clones. *J. Biol. Chem.* **260**, 11755–11761.

62 Levi S, Salfeld J, Franceschinelli F, Cozzi A, Dorner MH & Arosio P (1989) Expression and structural and functional properties of human ferritin L-chain from *Escherichia coli*. *Biochemistry* **28**, 5179–5184.

63 Levi S, Luzzago A, Cesareni G, Cozzi A, Franceschinelli F, Albertini A & Arosio P (1988) Mechanism of ferritin iron uptake: activity of the H-chain and deletion mapping of the ferro-oxidase site. A study of iron uptake and ferro-oxidase activity of human liver, recombinant H-chain ferritins, and of two H-chain deletion mutants. *J. Biol. Chem.* **263**, 18086–18092.

64 Honarmand Ebrahimi K, Bill E, Hagedoorn P-L & Hagen WR (2012) The catalytic center of ferritin regulates iron storage via Fe(II)-Fe(III) displacement. *Nat. Chem. Biol.* **8**, 941–948.

65 Lawson DM, Artymiuk PJ, Yewdall SJ, Smith JM, Livingstone JC, Treffry A, Luzzago A, Levi S, Arosio P & Cesareni G (1991) Solving the structure of human H ferritin by genetically engineering intermolecular crystal contacts. *Nature* **349**, 541–544.

66 Tatur J, Hagen WR & Matias PM (2007) Crystal structure of the ferritin from the hyperthermophilic archaeal anaerobe *Pyrococcus furiosus*. *J. Biol. Inorg. Chem.* **12**, 615–630.

67 Stillman TJ, Hempstead PD, Artymiuk PJ, Andrews SC, Hudson AJ, Treffry A, Guest JR & Harrison PM (2001) The high-resolution X-ray crystallographic structure of the ferritin (EcFtnA) of *Escherichia coli*; Comparison with human H ferritin (HuHF) and the structures of the Fe^{3+} and Zn^{2+} derivatives. *J. Mol. Biol.* **307**, 587–603.

68 Crow A, Lawson TL, Lewin A, Moore GR & Le Brun NE (2009) Structural basis for iron mineralization by bacterioferritin. *J. Am. Chem. Soc.* **131**, 6808–6813.

69 Swartz L, Kuchinskas M, Li H, Poulos TL & Lanzilotta WN (2006) Redox-dependent structural changes in the *Azotobacter vinelandii* bacterioferritin: new insights into the ferroxidase and iron transport mechanism. *Biochemistry* **45**, 4421–4428.

70 Weeratunga SK, Lovell S, Yao H, Battaile KP, Fischer CJ, Gee CE & Rivera M (2010) Structural studies of bacterioferritin B from *Pseudomonas aeruginosa* suggest a gating mechanism for iron uptake via the ferroxidase center. *Biochemistry* **49**, 1160–1175.

71 Rui H, Rivera M & Im W (2012) Protein dynamics and ion traffic in bacterioferritin. *Biochemistry* **51**, 9900–9910.
72 Ilari A, Stefanini S, Chiancone E & Tsernoglou D (2000) The dodecameric ferritin from *Listeria innocua* contains a novel intersubunit iron-binding site. *Nat. Struct. Biol.* **7**, 38–43.
73 Ceci P, Ilari A, Falvo E & Chiancone E (2003) The Dps protein of *Agrobacterium tumefaciens* does not bind to DNA but protects it toward oxidative cleavage: x-ray crystal structure, iron binding, and hydroxyl-radical scavenging properties. *J. Biol. Chem.* **278**, 20319–20326.
74 Cuypers MG, Mitchell EP, Romão CV & McSweeney SM (2007) The crystal structure of the Dps2 from *Deinococcus radiodurans* reveals an unusual pore profile with a non-specific metal binding site. *J. Mol. Biol.* **371**, 787–799.
75 Ren B, Tibbelin G, Kajino T, Asami O & Ladenstein R (2003) The multi-layered structure of Dps with a novel di-nuclear ferroxidase center. *J. Mol. Biol.* **329**, 467–477.
76 Stefanini S, Desideri A, Vecchini P, Drakenberg T & Chiancone E (1989) Identification of the iron entry channels in apoferritin. Chemical modification and spectroscopic studies. *Biochemistry* **28**, 378–382.
77 Desideri A, Stefanini S, Polizio F, Petruzzelli R & Chiancone E (1991) Iron entry route in horse spleen apoferritin. Involvement of the three-fold channels as probed by selective reaction of cysteine-126 with the spin label 4-maleimido-tempo. *FEBS Lett.* **287**, 10–14.
78 Bou-Abdallah F, Arosio P, Levi S, Janus-Chandler C & Chasteen ND (2003) Defining metal ion inhibitor interactions with recombinant human H- and L-chain ferritins and site-directed variants: an isothermal titration calorimetry study. *J. Biol. Inorg. Chem.* **8**, 489–497.
79 Bou-Abdallah F, Zhao G, Biasiotto G, Poli M, Arosio P & Chasteen ND (2008) Facilitated diffusion of iron(II) and dioxygen substrates into human H-chain ferritin. A fluorescence and absorbance study employing the ferroxidase center substitution Y34W. *J. Am. Chem. Soc.* **130**, 17801–17811.
80 Douglas T & Ripoll DR (1998) Calculated electrostatic gradients in recombinant human H-chain ferritin. *Protein Sci.* **7**, 1083–1091.
81 Laghaei R, Evans DG & Coalson RD (2013) Metal binding sites of human H-chain ferritin and iron transport mechanism to the ferroxidase sites: a molecular dynamics simulation study. *Proteins* **81**, 1042–1050.
82 Bertini I, Lalli D, Mangani S, Pozzi C, Rosa C, Theil EC & Turano P (2012) Structural insights into the ferroxidase site of ferritins from higher eukaryotes. *J. Am. Chem. Soc.* **134**, 6169–6176.
83 Cho KJ, Shin HJ, Lee J-H, Kim K-J, Park SS, Lee Y, Lee C, Park SS & Kim KH (2009) The crystal structure of ferritin from *Helicobacter pylori* reveals unusual conformational changes for iron uptake. *J. Mol. Biol.* **390**, 83–98.
84 Macedo S, Romão CV, Mitchell E, Matias PM, Liu MY, Xavier AV, LeGall J, Teixeira M, Lindley P & Carrondo MA (2003) The nature of the di-iron site in the bacterioferritin from *Desulfovibrio desulfuricans*. *Nat. Struct. Biol.* **10**, 285–290.
85 Bellapadrona G, Stefanini S, Zamparelli C, Theil EC & Chiancone E (2009) Iron translocation into and out of *Listeria innocua* Dps and size distribution of the protein-enclosed nanomineral are modulated by the electrostatic gradient at the 3-fold "ferritin-like" pores. *J. Biol. Chem.* **284**, 19101–19109.

86 Pesek J, Büchler R, Albrecht R, Boland W & Zeth K (2011) Structure and mechanism of iron translocation by a Dps protein from *Microbacterium arborescens*. *J. Biol. Chem.* **286**, 34872–34882.
87 Zeth K, Offermann S, Essen L-O & Oesterhelt D (2004) Iron-oxo clusters biomineralizing on protein surfaces: structural analysis of *Halobacterium salinarum* DpsA in its low- and high-iron states. *Proc. Natl. Acad. Sci. U.S.A.* **101**, 13780–13785.
88 Honarmand Ebrahimi K, Hagedoorn P-L & Hagen WR (2013) A conserved tyrosine in ferritin is a molecular capacitor. *ChemBioChem* **14**, 1123–1133.
89 Yang X, Chen-Barrett Y, Arosio P & Chasteen ND (1998) Reaction paths of iron oxidation and hydrolysis in horse spleen and recombinant human ferritins. *Biochemistry* **37**, 9743–9750.
90 Honarmand Ebrahimi K, Hagedoorn P-L, Jongejan JA & Hagen WR (2009) Catalysis of iron core formation in *Pyrococcus furiosus* ferritin. *J. Biol. Inorg. Chem.* **14**, 1265–1274.
91 Zhao G, Bou-Abdallah F, Yang X, Arosio P & Chasteen ND (2001) Is Hydrogen Peroxide Produced during Iron(II) Oxidation in Mammalian Apoferritins? *Biochemistry* **40**, 10832–10838.
92 Treffry A, Zhao Z, Quail MA, Guest JR & Harrison PM (1998) How the presence of three iron binding sites affects the iron storage function of the ferritin (EcFtnA) of *Escherichia coli*. *FEBS Lett.* **432**, 213–218.
93 Bou-Abdallah F, Yang H, Awomolo A, Cooper B, Woodhall MR, Andrews SC & Chasteen ND (2014) Functionality of the Three-Site Ferroxidase Center of *Escherichia coli* Bacterial Ferritin (EcFtnA). *Biochemistry* **53**, 483–495.
94 Yang X, Le Brun NE, Thomson AJ, Moore GR & Chasteen ND (2000) The Iron Oxidation and Hydrolysis Chemistry of *Escherichia coli* Bacterioferritin. *Biochemistry* **39**, 4915–4923.
95 Bou-Abdallah F, Lewin AC, Le Brun NE, Moore GR & Chasteen ND (2002) Iron detoxification properties of *Escherichia coli* bacterioferritin. Attenuation of oxyradical chemistry. *J. Biol. Chem.* **277**, 37064–37069.
96 Fetter J, Cohen J, Danger D, Sanders-Loehr J & Theil EC (1997) The influence of conserved tyrosine 30 and tissue-dependent differences in sequence on ferritin function: use of blue and purple Fe(III) species as reporters of ferroxidation. *J. Biol. Inorg. Chem.* **2**, 652–661.
97 Pereira AS, Tavares P, Lloyd SG, Danger D, Edmondson DE, Theil EC & Huynh BH (1997) Rapid and parallel formation of Fe^{3+} multimers, including a trimer, during H-type subunit ferritin mineralization. *Biochemistry* **36**, 7917–7927.
98 Pereira AS, Small W, Krebs C, Tavares P, Edmondson DE, Theil EC & Huynh BH (1998) Direct spectroscopic and kinetic evidence for the involvement of a peroxodiferric intermediate during the ferroxidase reaction in fast ferritin mineralization. *Biochemistry* **37**, 9871–9876.
99 Jameson GNL, Jin W, Krebs C, Perreira AS, Tavares P, Liu X, Theil EC & Huynh BH (2002) Stoichiometric Production of Hydrogen Peroxide and Parallel Formation of Ferric Multimers through Decay of the Diferric−Peroxo Complex, the First Detectable Intermediate in Ferritin Mineralization. *Biochemistry* **41**, 13435–13443.
100 Bauminger ER, Treffry A, Quail MA, Zhao Z, Nowik I & Harrison PM (1999) Stages in iron storage in the ferritin of *Escherichia coli* (EcFtnA): analysis of Mössbauer spectra reveals a new intermediate. *Biochemistry* **38**, 7791–7802.

101 Bauminger ER, Treffry A, Quail MA, Zhao Z, Nowik I & Harrison PM (2000) Metal binding at the active centre of the ferritin of *Escherichia coli* (EcFtnA). A Mössbauer spectroscopic study. *Inorg. Chim. Acta* **297**, 171–180.
102 Bou-Abdallah F, Papaefthymiou GC, Scheswohl DM, Stanga SD, Arosio P & Chasteen ND (2002) μ-1,2-Peroxobridged di-iron(III) dimer formation in human H-chain ferritin. *Biochem. J.* **364**, 57–63.
103 Bauminger ER, Harrison PM, Hechel D, Hodson NW, Nowik I, Treffry A & Yewdall SJ (1993) Iron (II) oxidation and early intermediates of iron-core formation in recombinant human H-chain ferritin. *Biochem. J.* **296**, 709–719.
104 Hwang J, Krebs C, Huynh BH, Edmondson DE, Theil EC & Penner-Hahn JE (2000) A short Fe-Fe distance in peroxodiferric ferritin: control of Fe substrate versus cofactor decay? *Science* **287**, 122–125.
105 Turano P, Lalli D, Felli IC, Theil EC & Bertini I (2010) NMR reveals pathway for ferric mineral precursors to the central cavity of ferritin. *Proc. Natl. Acad. Sci. U.S.A.* **107**, 545–550.
106 López-Castro JD, Delgado JJ, Perez-Omil JA, Gálvez N, Cuesta R, Watt RK & Domínguez-Vera JM (2012) A new approach to the ferritin iron core growth: influence of the H/L ratio on the core shape. *Dalton Trans.* **41**, 1320–1324.
107 Luscieti S, Santambrogio P, Langlois d'Estaintot B, Granier T, Cozzi A, Poli M, Gallois B, Finazzi D, Cattaneo A, Levi S & Arosio P (2010) Mutant ferritin L-chains that cause neurodegeneration act in a dominant-negative manner to reduce ferritin iron incorporation. *J. Biol. Chem.* **285**, 11948–11957.
108 Levi S, Yewdall SJ, Harrison PM, Santambrogio P, Cozzi A, Rovida E, Albertini A & Arosio P (1992) Evidence of H- and L-chains have co-operative roles in the iron-uptake mechanism of human ferritin. *Biochem. J.* **288**, 591–596.
109 Bradley JM, Moore GR & Le Brun NE (2014) Mechanisms of iron mineralization in ferritins: one size does not fit all. *J. Biol. Inorg. Chem.* **19**, 775–785.
110 Funk F, Lenders JP, Crichton RR & Schneider W (1985) Reductive mobilisation of ferritin iron. *Eur. J. Biochem.* **152**, 167–172.
111 Sirivech S, Frieden E & Osaki S (1974) The release of iron from horse spleen ferritin by reduced flavins. *Biochem. J.* **143**, 311–315.
112 Watt GD, Jacobs D & Frankel RB (1988) Redox reactivity of bacterial and mammalian ferritin: is reductant entry into the ferritin interior a necessary step for iron release? *Proc. Natl. Acad. Sci. USA* **85**, 7457–7461.
113 Tosha T, Behera RK, Ng H-L, Bhattasali O, Alber T & Theil EC (2012) Ferritin protein nanocage ion channels: gating by N-terminal extensions. *J. Biol. Chem.* **287**, 13016–13025.
114 Takagi H, Shi D, Ha Y, Allewell NM & Theil EC (1998) Localized Unfolding at the Junction of Three Ferritin Subunits A MECHANISM FOR IRON RELEASE? *J. Biol. Chem.* **273**, 18685–18688.
115 Liu X, Jin W & Theil EC (2003) Opening protein pores with chaotropes enhances Fe reduction and chelation of Fe from the ferritin biomineral. *Proc. Natl. Acad. Sci. USA* **100**, 3653–3658.
116 Ilari A, Ceci P, Ferrari D, Rossi GL & Chiancone E (2002) Iron incorporation into *Escherichia coli* Dps gives rise to a ferritin-like microcrystalline core. *J. Biol. Chem.* **277**, 37619–37623.

117 Huang HQ, Lin QM, Kong B, Zeng RY, Qiao YH, Chen CH, Zhang FZ & Xu LS (1999) Role of phosphate and kinetic characteristics of complete iron release from native pig spleen ferritin-Fe. *J. Protein Chem.* **18**, 497–504.
118 Yasmin S, Andrews SC, Moore GR & Le Brun NE (2011) A new role for heme, facilitating release of iron from the bacterioferritin iron biomineral. *J. Biol. Chem.* **286**, 3473–3483.
119 Quail MA, Jordan P, Grogan JM, Butt JN, Lutz M, Thomson AJ, Andrews SC & Guest JR (1996) Spectroscopic and voltammetric characterisation of the bacterioferritin-associated ferredoxin of *Escherichia coli*. *Biochem. Biophys. Res. Commun.* **229**, 635–642.
120 Ceci P, Cellai S, Falvo E, Rivetti C, Rossi GL & Chiancone E (2004) DNA condensation and self-aggregation of *Escherichia coli* Dps are coupled phenomena related to the properties of the N-terminus. *Nucleic Acids Res.* **32**, 5935–5944.
121 Grove A & Wilkinson SP (2005) Differential DNA binding and protection by dimeric and dodecameric forms of the ferritin homolog Dps from *Deinococcus radiodurans*. *J. Mol. Biol.* **347**, 495–508.
122 Gupta S & Chatterji D (2003) Bimodal protection of DNA by *Mycobacterium smegmatis* DNA-binding protein from stationary phase cells. *J. Biol. Chem.* **278**, 5235–5241.
123 Ceci P, Ilari A, Falvo E, Giangiacomo L & Chiancone E (2005) Reassessment of protein stability, DNA binding, and protection of *Mycobacterium smegmatis* Dps. *J. Biol. Chem.* **280**, 34776–34785.
124 Ceci P, Mangiarotti L, Rivetti C & Chiancone E (2007) The neutrophil-activating Dps protein of *Helicobacter pylori*, HP-NAP, adopts a mechanism different from *Escherichia coli* Dps to bind and condense DNA. *Nucleic Acids Res.* **35**, 2247–2256.
125 Chiancone E (2010) Role of Dps (DNA-binding proteins from starved cells) aggregation on DNA. *Front. Biosci.* **15**, 122–131.
126 Tosha T, Ng H-L, Bhattasali O, Alber T & Theil EC (2010) Moving metal ions through ferritin-protein nanocages from three-fold pores to catalytic sites. *J. Am. Chem. Soc.* **132**, 14562–14569.
127 Uchida M, Kang S, Reichhardt C, Harlen K & Douglas T (2010) The ferritin superfamily: Supramolecular templates for materials synthesis. *Biochim. Biophys. Acta* **1800**, 834–845.
128 Butts CA, Swift J, Kang S-G, Di Costanzo L, Christianson DW, Saven JG & Dmochowski IJ (2008) Directing noble metal ion chemistry within a designed ferritin protein. *Biochemistry* **47**, 12729–12739.
129 Yamashita I, Iwahori K & Kumagai S (2010) Ferritin in the field of nanodevices. *Biochim. Biophys. Acta* **1800**, 846–857.
130 Jacobs JF, Hasan MN, Paik KH, Hagen WR & van Loosdrecht MCM (2010) Development of a bionanotechnological phosphate removal system with thermostable ferritin. *Biotechnol. Bioeng.* **105**, 918–923.
131 Kitagawa T, Kosuge H, Uchida M, Dua MM, Iida Y, Dalman RL, Douglas T & McConnell MV (2012) RGD-conjugated human ferritin nanoparticles for imaging vascular inflammation and angiogenesis in experimental carotid and aortic disease. *Mol. Imaging Biol.* **14**, 315–324.
132 Sun C, Yang H, Yuan Y, Tian X, Wang L, Guo Y, Xu L, Lei J, Gao N, Anderson GJ, Liang X-J, Chen C, Zhao Y & Nie G (2011) Controlling assembly of paired gold

clusters within apoferritin nanoreactor for in vivo kidney targeting and biomedical imaging. *J. Am. Chem. Soc.* **133**, 8617–8624.
133 MaHam A, Tang Z, Wu H, Wang J & Lin Y (2009) Protein-based nanomedicine platforms for drug delivery. *Small* **5**, 1706–1721.
134 Xing R, Wang X, Zhang C, Zhang Y, Wang Q, Yang Z & Guo Z (2009) Characterization and cellular uptake of platinum anticancer drugs encapsulated in apoferritin. *J. Inorg. Biochem.* **103**, 1039–1044.
135 Cypionka H (2000) Oxygen respiration by *Desulfovibrio* species. *Annu. Rev. Microbiol.* **54**, 827–848.
136 Gauthier MJ, Lafay B, Christen R, Fernandez L, Acquaviva M, Bonin P & Bertrand JC (1992) *Marinobacter hydrocarbonoclasticus* gen. nov., sp. nov., a New, Extremely Halotolerant, Hydrocarbon-Degrading Marine Bacterium. *Int. J. Syst. Bacteriol.* **42**, 568–576.
137 Johnson MS, Zhulin IB, Gapuzan ME & Taylor BL (1997) Oxygen-dependent growth of the obligate anaerobe *Desulfovibrio vulgaris* Hildenborough. *J. Bacteriol.* **179**, 5598–5601.
138 NZYTech (2011) NZYMiniprep kit. *NZYTech, Ed. Genes e enzymes*, Lisbon.
139 NZYTech (2011) NZYMidiprep kit. *NZYTech*, *Ed. Genes e enzymes*, Lisbon.
140 Laemmli UK (1970) Cleavage of structural proteins during the assembly of the head of bacteriophage T4. *Nature* **227**, 680–685.
141 Depart. of Chemistry, UTK (2004) Experiment 9: Determination of Iron with 1,10-Phenanthroline. 1–3.
142 Maloney KM, Quiazon EM & Indralingam R (2008) Measurement of Iron in Egg Yolk: An Instrumental Analysis Experiment Using Biochemical Principles. *J. Chem. Educ.* **85**, 399.
143 Noble RW & Gibson QH (1970) The reaction of ferrous horseradish peroxidase with hydrogen peroxide. *J. Biol. Chem.* **245**, 2409–2413.
144 Ausubel FM, Brent R, Kingston RE, Moore DD, Seidman JG, Smith JA & Struhl K (1989) *Current Protocols in Molecular Biology*, pp. 2.4.1–2.4.5. Wiley, New York.
145 Ravi N, Bollinger JM, Huynh BH, Stubbe J & Edmondson DE (1994) Mechanism of assembly of the tyrosyl radical-diiron(III) cofactor of *E. Coli* ribonucleotide reductase: 1. Mössbauer Characterization of the Diferric Radical Precursor. *J. Am. Chem. Soc.* **116**, 8007–8014.
146 Fischer DS DS & Price DC (1964) A simple serum iron method using the new sensitive chromogen tripyridyl-s-triazine. *Clin. Chem.* **10**, 21–31.
147 Abràmoff MD, Magalhães PJ & Ram SJ (2004) *Image processing with imageJ. Biophoton Int 11: 36–41.*
148 Frolow F, Gilboa AJK & Yariv J (1994) Structure of a unique twofold symmetric haem-binding site. *Nat. Struct. Mol. Biol.* **1**, 453–460.
149 Le Brun NE, Andrews SC, Guest JR, Harrison PM, Moore GR & Thomson AJ (1995) Identification of the ferroxidase centre of *Escherichia coli* bacterioferritin. *Biochem. J.* **312**, 385–392.
150 Gasteiger E, Hoogland C, Gattiker A, Duvaud S, Wilkins MR, Appel RD & Bairoch A (2005) Protein Identification and Analysis Tools on the ExPASy Server. In *The Proteomics Protocols Handbook* pp. 571–607. Humana Press, Totowa, NJ.
151 Andrews SC, Smith JM, Hawkins C, Williams JM, Harrison PM & Guest JR (1993) Overproduction, purification and characterization of the bacterioferritin of

Escherichia coli and a C-terminally extended variant. *Eur. J. Biochem.* **213**, 329–338.
152 Gouet P, Courcelle E, Stuart D & Metoz F (1999) ESPript: analysis of multiple sequence alignments in PostScript. *Bioinformatics* **15**, 305–308.
153 Larkin MA, Blackshields G, Brown NP, Chenna R, McGettigan PA, McWilliam H, Valentin F, Wallace IM, Wilm A, Lopez R, Thompson JD, Gibson TJ & Higgins DG (2007) Clustal W and Clustal X version 2.0. *Bioinformatics* **23**, 2947–2948.
154 Baaghil S, Lewin A, Moore GR & Le Brun NE (2003) Core formation in *Escherichia coli* bacterioferritin requires a functional ferroxidase center. *Biochemistry* **42**, 14047–14056.
155 Papaefthymiou GC (2010) The Mössbauer and magnetic properties of ferritin cores. *Biochim. Biophys. Acta* **1800**, 886–897.
156 Nguyen KH, Smith LT, Xiao L, Bhattacharyya G & Grove A (2012) On the stoichiometry of *Deinococcus radiodurans* Dps-1 binding to duplex DNA. *Proteins* **80**, 713–721.
157 Castruita M, Saito M, Schottel PC, Elmegreen LA, Myneni S, Stiefel EI & Morel FMM (2006) Overexpression and characterization of an iron storage and DNA-binding Dps protein from *Trichodesmium erythraeum*. *Appl. Environ. Microbiol.* **72**, 2918–2924.
158 Swinger KK & Rice PA (2004) IHF and HU: flexible architects of bent DNA. *Curr. Opin. Struct. Biol.* **14**, 28–35.
159 Guilherme MCM (2009) Estudos Mecanísticos e Estruturais da Oxidação e Armazenamento de Ferro por Ferritinas Rápidas. PhD Thesis, FCT-UNL.
160 NZYTech (2013) NZYMutagenesis kit. *NZYTech, Ed. Genes e enzymes*, Lisbon.
161 Chelikani P, Fita I & Loewen PC (2004) Diversity of structures and properties among catalases. *Cell. Mol. Life Sci.* **61**, 192–208.
162 Carter P (1986) Site-directed mutagenesis. *Biochem. J.* **237**, 1–7.
163 Erickson HP (2009) Size and shape of protein molecules at the nanometer level determined by sedimentation, gel filtration, and electron microscopy. *Biol. Proced. Online* **11**, 32–51.
164 Wertheim GK (1967) Mössbauer effect. *Physics Today* **20**, 31–37.
165 Münck E (2000) Aspects of ^{57}Fe Mössbauer Spectroscopy. In *Physical Methods in Bioinorganic Chemistry Spectroscopy and Magnetism* (Lawrence Que J, ed), 1st ed., pp. 287–319. Sausalito, United States.
166 Mössbauer Spectroscopy Group (2018) Introduction of Mösbauer Spectroscopy. *Royal Society of Chemistry RSC*. Last accessed on 3.06.2018. URL: http://www.rsc.org/membership/networking/interestgroups/mossbauerspect/intropart1.asp
167 Gütlich P, Bill E & Trautwein AX (2011) *Mössbauer Spectroscopy and Transition Metal Chemistry*, 1st ed. Springer-Verlag Berlin Heidelberg, Berlin, Heidelberg.
168 Tavares P & Folgosa F (2010) *Mössbauer Spectroscopy: principles and applications in biochemistry*, 2nd ed. Department of Chemistry, FCT-UNL.
169 Treffry A & Harrison PM (1984) Spectroscopic studies on the binding of iron, terbium, and zinc by apoferritin. *J. Inorg. Biochem.* **21**, 9–20.
170 Bozzi M, Mignogna G, Stefanini S, Barra D, Longhi C, Valenti P & Chiancone E (1997) A novel non-heme iron-binding ferritin related to the DNA-binding proteins of the Dps family in *Listeria innocua*. *J. Biol. Chem.* **272**, 3259–3265.

171 Tonello F, Dundon WG, Satin B, Molinari M, Tognon G, Grandi G, Del Giudice G, Rappuoli R & Montecucco C (1999) The *Helicobacter pylori* neutrophil-activating protein is an iron-binding protein with dodecameric structure. *Mol. Microbiol.* **34**, 238–246.
172 Yamamoto Y, Poole LB, Hantgan RR & Kamio Y (2002) An Iron-Binding Protein, Dpr, from *Streptococcus* mutans Prevents Iron-Dependent Hydroxyl Radical Formation In Vitro. *J. Bacteriol.* **184**, 2931–2939.
173 Zhao G, Ceci P, Ilari A, Giangiacomo L, Laue TM, Chiancone E & Chasteen ND (2002) Iron and hydrogen peroxide detoxification properties of DNA-binding protein from starved cells. A ferritin-like DNA-binding protein of *Escherichia coli*. *J. Biol. Chem.* **277**, 27689–27696.
174 Bevers LE & Theil EC (2011) Maxi- and mini-ferritins: minerals and protein nanocages. *Prog. Mol. Subcell. Biol.* **52**, 29–47.
175 Yang CY, Meagher A, Huynh BH, Sayers DE & Theil EC (1987) Iron(III) clusters bound to horse spleen apoferritin: an x-ray absorption and Mössbauer spectroscopy study that shows that iron nuclei can form on the protein. *Biochemistry* **26**, 497–503.
176 Pierre TGS, Bell SH, Dickson DPE, Mann S, Webb J, Moore GR & Williams RJP (1986) Mössbauer spectroscopic studies of the cores of human, limpet and bacterial ferritins. *Biochim. Biophys. Acta* **870**, 127–134.
177 Coey JMD, Meagher A, Kelly JM & Vos JG (1984) A Mössbauer study of polymers prepared from polyvinylpyridine and ferric chloride or ferric nitrate. *J. Polym. Sci. A Polym. Chem.* **22**, 303–318.
178 Bauminger ER, Harrison PM, Hechel D, Nowik I & Treffry A (1991) Iron (III) can be transferred between ferritin molecules. *Proc. Biol. Sci.* **244**, 211–217.
179 Bauminger ER, Harrison PM, Nowik I & Treffry A (1989) Mössbauer spectroscopic study of the initial stages of iron-core formation in horse spleen apoferritin: evidence for both isolated iron(III) atoms and oxo-bridged iron(III) dimers as early intermediates. *Biochemistry* **28**, 5486–5493.
180 Lynch JB, Juarez-Garcia C, Münck E & L Que J (1989) Mössbauer and EPR studies of the binuclear iron center in ribonucleotide reductase from *Escherichia coli*. A new iron-to-protein stoichiometry. *J. Biol. Chem.* **264**, 8091–8096.
181 DeWitt JG, Bentsen JG, Rosenzweig AC, Hedman B, Green J, Pilkington S, Papaefthymiou GC, Dalton H, Hodgson KO & Lippard SJ (1991) X-ray absorption, Mössbauer, and EPR studies of the dinuclear iron center in the hydroxylase component of methane monooxygenase. *J. Am. Chem. Soc.* **113**, 9219–9235.
182 Fox BG, Hendrich MP, Surerus KK, Andersson KK, Froland WA, Lipscomb JD & Münck E (1993) Mössbauer, EPR, and ENDOR studies of the hydroxylase and reductase components of methane monooxygenase from *Methylosinus trichosporium* OB3b. *J. Am. Chem. Soc.* **115**, 3688–3701.
183 Silvester E, Charlet L, Tournassat C, Géhin A, Grenèche J-M & Liger E (2005) Redox potential measurements and Mössbauer spectrometry of FeII adsorbed onto FeIII (oxyhydr)oxides. *Geochim.t Cosmochim. Acta* **69**, 4801–4815.
184 Williams AGB & Scherer MM (2004) Spectroscopic Evidence for Fe(II)−Fe(III) Electron Transfer at the Iron Oxide−Water Interface. *Environ. Sci. Technol.* **38**, 4782–4790.
185 Norambuena T & Melo F (2010) The Protein-DNA Interface database. *BMC Bioinformatics* **11**, 262.

186 Hellman LM & Fried MG (2007) Electrophoretic mobility shift assay (EMSA) for detecting protein-nucleic acid interactions. *Nat. Protoc.* **2**, 1849–1861.
187 Kerr LD (1995) Electrophoretic mobility shift assay. *Meth. Enzymol.* **254**, 619–632.
188 Huergo LF, Rahman H, Ibrahimovic A, Day CJ & Korolik V (2013) *Campylobacter jejuni* Dps protein binds DNA in the presence of iron or hydrogen peroxide. *J. Bacteriol.* **195**, 1970–1978.
189 Santos SP, Mitchell EP, Franquelim HG, Castanho MARB, Abreu IA & Romão CV (2015) Dps from *Deinococcus radiodurans*: oligomeric forms of Dps1 with distinct cellular functions and Dps2 involved in metal storage. *FEBS J.* **282**, 4307–4327.
190 Altenbach C, Flitsch SL, Khorana HG & Hubbell WL (1989) Structural Studies on Transmembrane Proteins. 2. Spin Labeling of Bacteriorhodopsin Mutants at Unique Cysteines. *Biochemistry* **28**, 7806–7812.
191 DeSensi SC, Rangel DP, Beth AH, Lybrand TP & Hustedt EJ (2008) Simulation of nitroxide electron paramagnetic resonance spectra from brownian trajectories and molecular dynamics simulations. *Biophys. J.* **94**, 3798–3809.
192 Hubbell WL, Mchaourab HS, Altenbach C & Lietzow MA (1996) Watching proteins move using site-directed spin labeling. *Structure* **4**, 779–783.
193 Bordignon E (2017) EPR Spectroscopy of Nitroxide Spin Probes. *eMagRes* **6**, 235–254.
194 Bordignon E & STEINHOFF H-J (2007) Membrane Protein Structure and Dynamics Studied by Site-Directed Spin-Labeling ESR. In *ESR Spectroscopy in Membrane Biophysics* pp. 129–164. Springer, Boston, MA, Boston, MA.
195 Belle V, Rouger S, Costanzo S, Liquière E, Strancar J, Guigliarelli B, Fournel A & Longhi S (2008) Mapping alpha-helical induced folding within the intrinsically disordered C-terminal domain of the measles virus nucleoprotein by site-directed spin-labeling EPR spectroscopy. *Proteins* **73**, 973–988.
196 Mchaourab HS, Lietzow MA, Hideg K & Hubbell WL (1996) Motion of spin-labeled side chains in T4 lysozyme. Correlation with protein structure and dynamics. *Biochemistry* **35**, 7692–7704.
197 Stoll S & Schweiger A (2006) EasySpin, a comprehensive software package for spectral simulation and analysis in EPR. *J. Magn. Reson.* **178**, 42–55.
198 Ma JW, Cunningham MF, McAuley KB, Keoshkerian B & Georges MK (2001) Nitroxide partitioning between styrene and water. *J. Polym. Sci. A Polym. Chem.* **39**, 1081–1089.
199 Gast P, Herbonnet RTL, Klare J, Nalepa A, Rickert C, Stellinga D, Urban L, Möbius K, Savitsky A, Steinhoff HJ & Groenen EJJ (2014) Hydrogen bonding of nitroxide spin labels in membrane proteins. *Phys. Chem. Chem. Phys.* **16**, 15910–15916.
200 Bordignon E, Brutlach H, Urban L, Hideg K, Savitsky A, Schnegg A, Gast P, Engelhard M, Groenen EJJ, Möbius K & Steinhoff H-J (2010) Heterogeneity in the Nitroxide Micro-Environment: Polarity and Proticity Effects in Spin-Labeled Proteins Studied by Multi-Frequency EPR. *Appl. Magn. Reson.* **37**, 391–403.
201 Jeschke G (2002) Distance measurements in the nanometer range by pulse EPR. *ChemPhysChem* **3**, 927–932.
202 Ward R, Bowman A, Sozudogru E, Mkami El H, Owen-Hughes T & Norman DG (2010) EPR distance measurements in deuterated proteins. *J. Magn. Reson.* **207**, 164–167.

203 Ward R, Bowman A, Mkami El H, Owen-Hughes T & Norman DG (2009) Long distance PELDOR measurements on the histone core particle. *J. Am. Chem. Soc.* **131**, 1348–1349.
204 Ward R, Keeble DJ, Mkami El H & Norman DG (2007) Distance determination in heterogeneous DNA model systems by pulsed EPR. *ChemBioChem* **8**, 1957–1964.
205 Sen KI, Logan TM & Fajer PG (2007) Protein Dynamics and Monomer−Monomer Interactions in AntR Activation by Electron Paramagnetic Resonance and Double Electron−Electron Resonance. *Biochemistry* **46**, 11639–11649.
206 Pannier M, Veit S, Godt A, Jeschke G & Spiess HW (2011) Dead-time free measurement of dipole-dipole interactions between electron spins. 2000. *J. Magn. Reson.* **213**, 316–325.
207 Jeschke G (2012) DEER Distance Measurements on Proteins. *Annu. Rev. Phys. Chem.* **63**, 419–446.
208 Milov AD, Maryasov AG & Tsvetkov YD (1998) Pulsed electron double resonance (PELDOR) and its applications in free-radicals research. *Appl. Magn. Reson.* **15**, 107–143.
209 Goldfarb D (2012) Metal-Based Spin Labeling for Distance Determination. In *Structural Information from Spin-Labels and Intrinsic Paramagnetic Centres in the Biosciences* pp. 163–204. Springer Berlin Heidelberg, Berlin, Heidelberg.
210 Giannoulis A, Ward R, Branigan E, Naismith JH & Bode BE (2013) PELDOR in rotationally symmetric homo-oligomers. *Mol. Phys.* **111**, 2845–2854.
211 Hagens von T, Polyhach Y, Sajid M, Godt A & Jeschke G (2013) Suppression of ghost distances in multiple-spin double electron-electron resonance. *Phys. Chem. Chem. Phys.* **15**, 5854–5866.
212 Valera S, Ackermann K, Pliotas C, Huang H, Naismith JH & Bode BE (2016) Accurate Extraction of Nanometer Distances in Multimers by Pulse EPR. *Chem. Eur. J.* **22**, 4700–4703.
213 Schmidt T, Ghirlando R, Baber J & Clore GM (2016) Quantitative Resolution of Monomer-Dimer Populations by Inversion Modulated DEER EPR Spectroscopy. *ChemPhysChem* **17**, 2987–2991.
214 Jeschke G & Polyhach Y (2007) Distance measurements on spin-labelled biomacromolecules by pulsed electron paramagnetic resonance. *Phys. Chem. Chem. Phys.* **9**, 1895–1910.
215 Fielding AJ, Concilio MG, Heaven G & Hollas MA (2014) New developments in spin labels for pulsed dipolar EPR. *Molecules* **19**, 16998–17025.
216 Hagelueken G, Ward R, Naismith JH & Schiemann O (2012) MtsslWizard: In Silico Spin-Labeling and Generation of Distance Distributions in PyMOL. *Appl. Magn. Reson.* **42**, 377–391.
217 Jeschke G, Chechik V, Ionita P, Godt A, Zimmermann H, Banham J, Timmel CR, Hilger D & Jung H (2006) DeerAnalysis2006—a comprehensive software package for analyzing pulsed ELDOR data. *Appl. Magn. Reson.* **30**, 473–498.
218 Carrondo MA (2003) Ferritins, iron uptake and storage from the bacterioferritin viewpoint. *EMBO J.* **22**, 1959–1968.

Appendix

A.1 DNA markers

A.1.1 Molecular weight NZYLadder II (NZYTech)

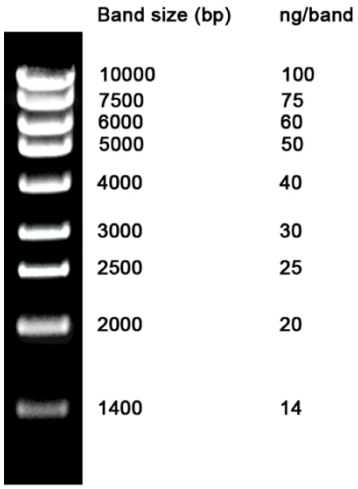

Figure A.1: Molecular weight NZYLadder II. 5 µl in a 1% agarose gel, 1xTAE buffer.

A.1.2 Molecular weight NZYLadder III (NZYTech)

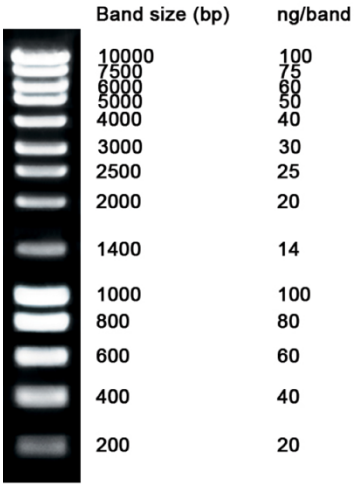

Figure A.2: Molecular weight NZYLadder III. 5 µL in a 1% agarose gel, 1xTAE buffer.

A.1.3 Molecular weight HyperLadder V (Bioline)

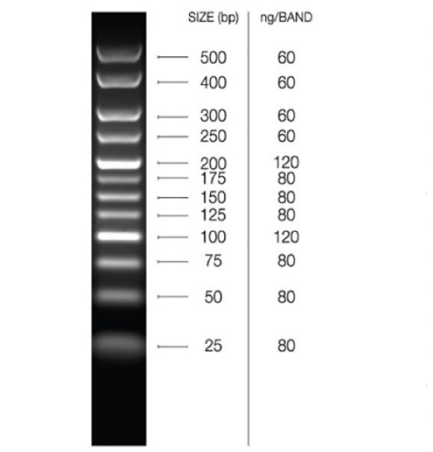

Figure A.3: Molecular weight HyperLadder V.5 µL in 3.5% agarose gel, 1xTAE buffer.

A.2 Protein markers

A.2.1 Molecular weight LMW (NZYTech)

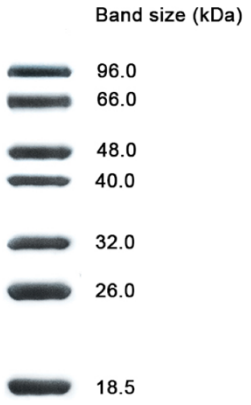

Figure A.4: Molecular weight LMW. 15 µL in a 14% Tris-glycine SDS-PAGE.

A.2.2 Molecular weight PageRuler Prestained Protein Ladder (Thermo Scientific)

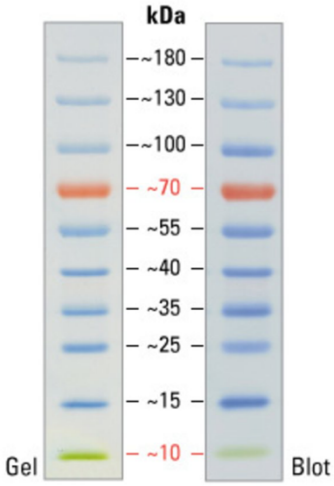

Figure A.5: Molecular weight PageRuler Prestained Protein Ladder. 5 µL in a 4–20% Tris-glycine SDS-PAGE.

A.3 Plasmid vector maps

A.3.1 pUC19 vector

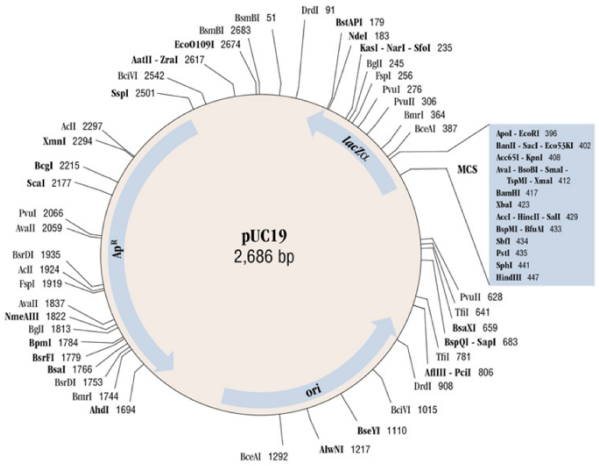

Figure A.6: Plasmid pU19 vector map.

A.3.2 pGEX-6P-1 vector (GE Healthcare)

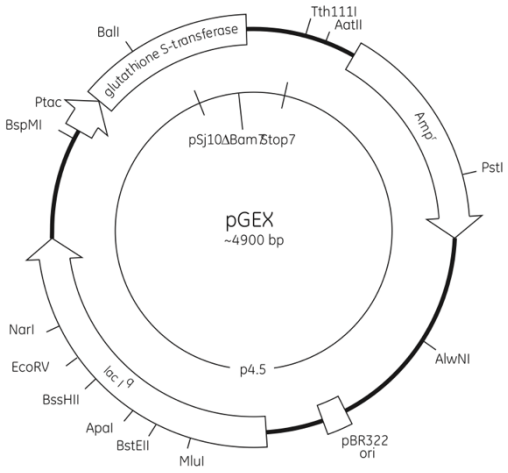

Figure A.7: Plasmid pGEX-6P-1 vector map.

A.3.3 pET-21c(+) vector (Novagen)

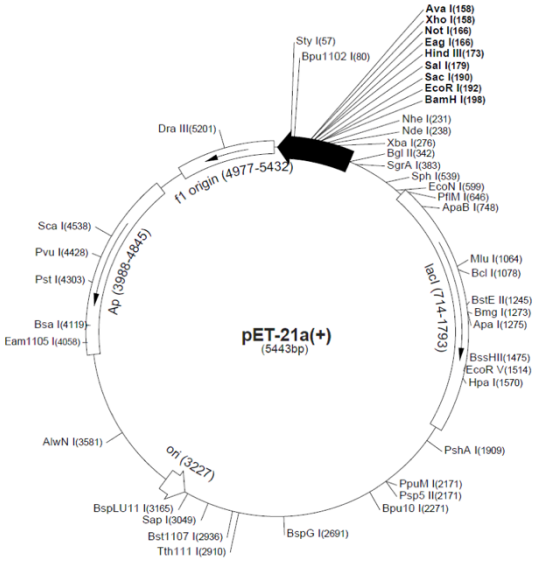

Figure A.8: Plasmid pET-21c(+) vector map.

A.3.4 pET-21c—Bfr vector

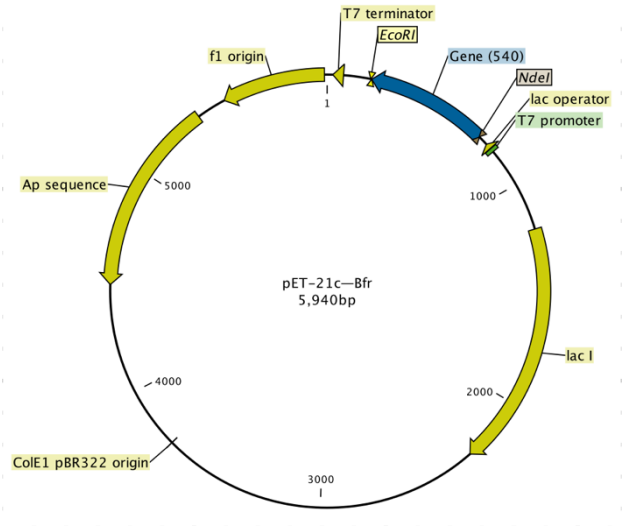

Figure A.9: Plasmid pET-21c—Bfr vector map.

A.3.5 pET-21c—Dps vector and variants

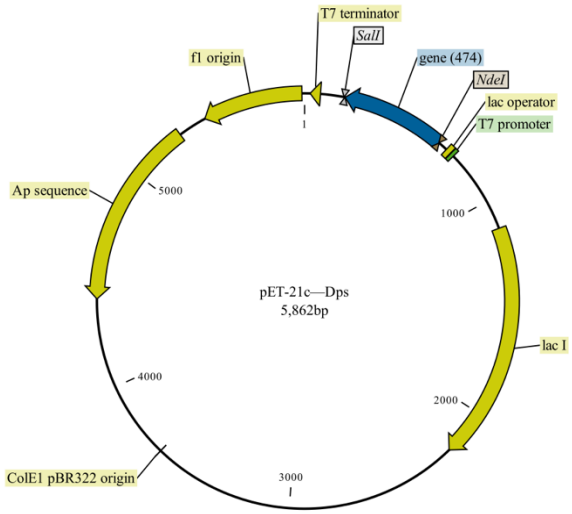

Figure A.10: Plasmid pET-21c—Dps vector map. Gene that code for Dps-WT and Dps-Q14E, Dps-T10C and Dps-F5C proteins contain 474 bp, while Dps-Δ15 protein variant is codified by a gene of 432 bp.

A.4 Data sheets of oligonucleotides primers used in site-directed mutagenesis

A.4.1 Dps-T10C protein variant

A

Researcher Name	MASP	Purification	HPLC
Manufactory date	2-10-2015 12:23:32	5'-Label:	No
Batch-No	584932	3'-Label:	No
Oligo Name	T10C-1	Internal Label	No
Comment		Method	High Purity
Scale	40 nmol	Dissolved	No
Chemistry	DNA	QC	Normal no extra

Sequence:
5'–GAA CTT TAT AGG TCT CGA CTG CGA CAA AAC CCA GAA GCT GG–3'

Number of bases:

A	C	G	T	N	Total	%GC
13	10	10	8	0	41	49

Melting Tempterature:	70,5	°C
Molecular Weight:	12627	gr/mol
Absorbance value (260 nm):	8,89	
Total Nucleic Acid:	22,09	nmol
in sample:	278,98	ug
for 100 µM Solution dissolve in:	220,93	µl

B

Researcher Name	MASP	Purification	HPLC
Manufactory date	2-10-2015 12:23:32	5'-Label:	No
Batch-No	584933	3'-Label:	No
Oligo Name	T10C-2	Internal Label	No
Comment		Method	High Purity
Scale	40 nmol	Dissolved	No
Chemistry	DNA	QC	Normal no extra

Sequence:
5'–CCA GCT TCT GGG TTT TGT CGC AGT CGA GAC CTA TAA AGT TC–3'

Number of bases:

A	C	G	T	N	Total	%GC
8	10	10	13	0	41	49

Melting Tempterature:	70,5	°C
Molecular Weight:	12582	gr/mol
Absorbance value (260 nm):	7,83	
Total Nucleic Acid:	20,39	nmol
in sample:	256,61	ug
for 100 µM Solution dissolve in:	203,95	µl

Figure A.11: Primers of Dps-T10C variant provided by NZYTech. (A) Forward oligonucleotide primer (T10C-1). (B) Reverse oligonucleotide primer (T10C-2).

A.4.2 Dps-F5C protein variant

A

Researcher Name	MASP	Purification	HPLC
Manufactory date	2-10-2015 12:23:32	5'-Label:	No
Batch-No	584930	3'-Label:	No
Oligo Name	F5C-1	Internal Label	No
Comment		Method	High Purity
Scale	40 nmol	Dissolved	No
Chemistry	DNA	QC	Normal no extra

Sequence:
5'–GAT ATA CAT ATG GGT AAG AAC TGT ATA GGT CTC GAC ACA GAC–3'

Number of bases:

A	C	G	T	N	Total	%GC
15	7	10	10	0	42	40

Melting Tempterature:	65,9	°C
Molecular Weight:	12994	gr/mol
Absorbance value (260 nm):	8,18	
Total Nucleic Acid:	18,93	nmol
in sample:	245,98	ug
for 100 µM Solution dissolve in:	189,30	µl

B

Researcher Name	MASP	Purification	HPLC
Manufactory date	2-10-2015 12:23:32	5'-Label:	No
Batch-No	584931	3'-Label:	No
Oligo Name	F5C-2	Internal Label	No
Comment		Method	High Purity
Scale	40 nmol	Dissolved	No
Chemistry	DNA	QC	Normal no extra

Sequence:
5'–GTC TGT GTC GAG ACC TAT ACA GTT CTT ACC CAT ATG TAT ATC–3'

Number of bases:

A	C	G	T	N	Total	%GC
10	10	7	15	0	42	40

Melting Tempterature:	65,9	°C
Molecular Weight:	12829	gr/mol
Absorbance value (260 nm):	6,49	
Total Nucleic Acid:	16,07	nmol
in sample:	206,21	ug
for 100 µM Solution dissolve in:	160,73	µl

Figure A.12: Primers of Dps-F5C variant provided by NZYTech. (A) Forward oligonucleotide primer (F5C-1). (B) Reverse oligonucleotide primer (F5C-2).